UNIVERSITÉ MONTPELLIER II
SCIENCES ET TECHNIQUES DU LANGUEDOC

ECOLE DOCTORALE I2S - INFORMATION, STRUCTURES, SYSTÈMES
SPÉCIALITÉ MATHÉMATIQUES ET MODÉLISATION

NUMERICAL STUDY OF MACH NUMBER EFFECTS ON COMBUSTION INSTABILITY.

THÈSE DE DOCTORAT

pour l'obtention du titre de

DOCTEUR DE L'UNIVERSITÉ MONTPELLIER II

présentée et soutenue publiquement par

Kerstin Wieczorek

le 8 Novembre 2010

COMPOSTION DU JURY

T. SCHULLER	MdC HDR, CNRS Ecole Centrale Paris	Rapporteur
A. MORGANS	Professeur, Imperial College London	Rapporteur
W. POLIFKE	Professeur, TU München	Examinateur
W. SCHRÖDER	Professeur, RWTH Aachen	Examinateur
B. MOHAMMADI	Professeur, Université Montpellier 2	Examinateur
S. MOREAU	Professeur, Université de Sherbrooke	Examinateur
F. NICOUD	Professeur, Université Montpellier 2	Directeur de Thèse

---

Abstract

The development of gas turbines towards lean combustion increases the susceptibility of the flame to flow perturbations, and leads more particularly to a higher risk of combustion instability. As these self-sustained oscillations may affect the performance of the combustion device or even cause structural damage, it is very important to be able to predict this behaviour at the design level. The methods used at present for the description of combustion instabilities are numerous and range from powerful yet very CPU time demanding LES and DNS calculations to low-order network models.
An intermediate method consists in solving a set of equations describing the acoustic field using a finite volume technique. This allows to take into account geometrical details that cannot be represented by network models, but needs less time and resources than a LES calculation. It is therefore this latter approach that has been used for conducting the present study.

This thesis discusses the impact of a non zero Mach number mean flow field on thermo-acoustic instability. The study is based on the linearized Euler equations, which are stated in the frequency domain in the form of an eigenvalue problem and solved using a finite volume technique. Using the linearized Euler equations rather than the Helmholtz equation avoids making the commonly used assumption of the mean flow being at rest, and thus allows to take into account convection effects and their impact on the stability of the system. Among the mechanisms that can be studied using the present approach is namely the impact of convected entropy waves. This is especially interesting in combustion applications, where hot spots are created in the flame zone and then transported downstream by the mean flow, where they may interact with the acoustic field in zones of non-uniform mean flow.

In order to investigate the problem of thermo-acoustic instability for quasi-1D and 2D configurations, two numerical solvers have been developed and are presented in this thesis. The results obtained with these codes are compared to results of a Helmholtz solver, analytical models and experimental data. In order to asses the effect of the mean flow terms on the modes' stability, an analysis of the disturbance energy budget is performed. Finally, the aspect of the eigenmodes being non-orthogonal and thus allowing for transient growth in linearly stable systems is adressed.

Keywords: Combustion Instability, Acoustics, Linearized Euler Equations, Mach number effects, Entropy waves, Eigenvalue Problem, Non-normality

Résumé

L'évolution des turbines à gaz vers des régimes de combustion en mélange pauvre augmente la sensibilité de la flamme aux perturbations de l'écoulement. Plus particulièrement, cela augmente le risque d'apparition d'instabilités de combustion. Comme ces oscillations auto-entretenues peuvent alors affecter le processus de combustion ou même causer des dommages structurels, il est très important d'être capable de prédire ce phénomène au niveau de la conception. Les méthodes utilisées à l'heure actuelle afin de décrire les instabilités de combustion sont nombreuses. Elles vont des Simulations aux Grands Echelles (SGE ou, plus couramment, LES), qui sont à la fois performantes et exigeantes en termes de mémoire et temps de calcul, jusqu'aux codes réseaux.
Une méthode intermédiaire consiste à résoudre un système d'équations simplifiées en utilisant des techniques de type éléments- ou volumes finis. Cela permet de prendre en compte des détails géométriques qui ne peuvent être représentés par des modèles réseaux, tout en diminuant le temps de calculs par rapport aux calculs de type LES. L'étude effectuée dans cette thèse repose sur cette dernière approche.

Cette thèse vise à discuter l'impact d'un écoulement moyen à vitesse non négligeable sur les instabilités thermo-acoustiques. La méthode utilisée consiste à résoudre les équations d'Euler linéarisées, qui sont écrites dans le domaine fréquentiel sous la forme d'un problème aux valeurs propres, et discrétisées avec un schema de type volumes finis. Comme les équations d'Euler linéarisées ne contiennent pas l'hypothèse d'un écoulement moyen à Mach nul (à la différence de l'équation de Helmholtz, qui est utilisée plus couramment pour décrire le phénomène consideré), la resolution de ce système d'équations permet de tenir compte des effets causés par la convection, et de leur impact sur la stabilité des modes. Parmi les mécanismes qui peuvent être étudiés se trouve notamment l'effet des ondes d'entropie convectées. Dans une chambre de combustion, ces ondes sont créées dans la flamme et puis transportées vers l'aval avec l'écoulement moyen, où elles peuvent interagir avec le champ acoustique dans des zones d'écoulement moyen non uniforme.

Afin d'étudier le phénomène des instabilités thermo-acoustiques dans des configurations quasi-1D et 2D, deux solveurs numériques ont été développés et sont presentés dans cette thèse. Les résultats obtenus avec ces deux codes sont comparés à des résultats d'un solveur Helmholtz et de modèles analytiques ainsi qu'à des données experimentales. Afin de déterminer l'effet des termes liés à la vitesse de l'écoulement moyen sur la stabilité des modes, une analyse de l'énergie contenue dans les perturbations est effectuée. Finalement, l'aspect de la non-orthogonalité des modes propres, qui permet une croissance d'énergie transitoire dans un système linéairement stable, est abordé.

Mots Clefs: Instabilité de combustion, Acoustique, Équations d'Euler linéarisées, Effets du nombre de Mach, Ondes entropiques, Problème aux valeurs propres

Contents

Nomenclature

Latin Symbols

C_v	heat capacity at constant volume	$[\mathrm{J}/(\mathrm{kg\ K})]$
C_p	heat capacity at constant pressure	$[\mathrm{J}/(\mathrm{kg\ K})]$
E	acoustic energy density	$\left[\mathrm{J}/\mathrm{m}^3\right]$
F	acoustic energy flux	$\left[\mathrm{W}/\mathrm{m}^2\right]$
G	transient amplification factor	$[-]$
M	Mach number	$[-]$
Q	heat release rate	$[\mathrm{J/s}]$
R	complex reflection coefficient	$[-]$
S	surface	$\left[\mathrm{m}^2\right]$
T	temperature	$[\mathrm{K}]$
T	period of oscillation	$[\mathrm{s}]$
Y	complex admittance	$[-]$
Z	complex impedance	$[-]$
c	speed of sound	$[\mathrm{m/s}]$
f	frequency	$[\mathrm{Hz}]$
i	standard imaginary unit	$[-]$
k	complex wave number	$[1/\mathrm{m}]$
n	interaction index (flame model)	$[-]$
$\mathbf{n}$	normal vector	$[-]$
p	pressure	$[\mathrm{Pa}]$
q	heat release rate per unit volume	$\left[\mathrm{J}/(\mathrm{s}\mathrm{m}^3)\right]$
r	specific gas constant	$[\mathrm{J}/(\mathrm{kg\ K})]$
s	entropy	$[\mathrm{J}/(\mathrm{kg\ K})]$
t	time	$[\mathrm{s}]$
$\mathbf{u}$	velocity vector	$[\mathrm{m/s}]$
u	velocity (1D)	$[\mathrm{m/s}]$

Greek Symbols

γ	adiabatic index (heat capacity ratio)	$[-]$
δ_f	flame length	$[\mathrm{m}]$
ϵ	error	$[-]$
λ	wavelength	$[\mathrm{m}]$
ω	complex angular frequency	$[\mathrm{rad/s}]$
ρ	density	$\left[\mathrm{kg/m^3}\right]$
τ	time delay (flame model)	$[\mathrm{s}]$

Indices

x	component in x-direction
y	component in y-direction
z	component in z-direction
r	real part of complex value
i	imaginary part of complex value
0	mean value
1	small amplitude fluctuation
f	concerning the flame
t	total / stagnation value
in	at domain inlet
out	at domain outlet
u	unburnt gas
b	burnt gas
ref	reference state

Superscripts

$\hat{}$	complex amplitude
$+$	concerning the downstream travelling acoustic wave
$-$	concerning the upstream travelling acoustic wave

Acronyms, Abbreviations & Proper Names

LEE	Linearized Euler Equations
LES	Large Eddy Simulation
AVBP	LES solver developed at CERFACS
AVSP	Helmholtz solver developed at CERFACS

Chapter 1

Introduction

Thermoacoustic instability is a term that covers a wide range of phenomena in which acoustic oscillations are caused and maintained by thermal sources. The so-called "singing flame", which refers to a flame producing sound when placed inside a tube of proper length, was observed by Higgins as early as in 1777 [44]. Among other early studies on the subject one may cite the works of Sondhauß, Rijke and Rayleigh [87, 89, 105]. The studies of Sondhauß examine the spontaneous excitation of acoustic oscillations that had been observed by glass blowers: a glass tube open on one end and with a closed bulb other end may produce sound when the bulb is heated. Rijke describes the onset of acoustic oscillations in a vertical tube that is open on both ends and which contains a heated metal grid. This heated grid causes an upstream air flow, that convects possible fluctuations in heat release rate. When the heat source is placed at a quarter of the tube length from the bottom end, the heat release rate fluctuations may couple with the acoustic field in a way as to cause self-excited oscillations.
It was Rayleigh who first stated a criterion about the possible existence of such oscillations [86]:

"If heat be given to the air at the moment of greatest condensation, or be taken from it at the moment of greatest rarefaction, the vibration is encouraged. On the other hand, if heat be given at the moment of greatest rarefaction, or abstracted at the moment of greatest condensation, the vibration is discouraged."

Rayleigh's criterion may be cast into a mathematical expression, stating that the unsteady heat source adds energy to the acoustic field if the unsteady heat release rate $q_1(\mathbf{x}, t)$ is in phase with the pressure fluctuations at the location of the heat source $p_1(\mathbf{x}, t)$. This necessary condition for the existence of combustion instability is satisfied if

$$\int\int\int p_1(\mathbf{x}, t) q_1(\mathbf{x}, t) \mathrm{d}V > 0. \tag{1.1}$$

While these early works were dedicated to sound produced by thermal sources, a somewhat opposite effect has been shown by Merkli & Thomann in 1975 [69]: They demonstrated that the wall temperature in an acoustic resonator decreases at the locations of acoustic velocity maxima.
Each of these two effects due to coupling between a heat source and an acoustic field can be exploited in so-called thermoacoustic engines. Subsequently to theoretical work of Rott [90]

in the 1970s and 1980s, such devices have been developed in several configurations. They are based either on the first phenomenon and use a heat source to create sound [110], or on the latter one, using sound waves to pump heat [118]. It is also possible to combine both effects, using a heat source to create sound waves that serve then as a source of power for a cooling device [1]. Besides, these devices can be designed in very small dimensions, which makes them conceivable as cooling devices in microelectronic circuits where they may remove heat by acoustic radiation [111].

Coming back to combustion-driven oscillations, the situation is somewhat different: These phenomena are in general rather detrimental, which is why extensive research about their appearance and avoidance is conducted.

1.1 Combustion Instabilities

1.1.1 Overview

Combustion instabilities have been observed in devices as different as blast furnaces, heating units, gas turbines or rocket engines [123]. While the mechanisms that lead to the excitation of acoustic oscillations are different and depend on the respective configuration, the instabilities have the common point of being in general unexpected, undesirable and often of significant amplitude.
One often cited example of impressing combustion instabilities is the F-1 engine, that was designed in the 1950s to power the Saturn V rocket. As reported by Zinn & Lieuwen [123], this engine "[...] encountered instabilities with amplitudes up to 100% of the mean combustor pressure, (i.e., more than 2000 psi [1])". The difficulty of describing the phenomenon at the design stage implicated the necessity of long and costly testing campaigns.

With the development of high performance combustion devices, in the energy supply sector as well as in the aerospace industry, the problem of unstable combustion came into focus and led to extensive research on the subject [12, 26, 50]. Combustion instability may occur in a variety of configurations, each with specific characteristics. The instabilities can hence be classified according to key criteria, such as frequency ranges, driving mechanisms or their extent in the system. Barrère & Williams [7] distinguish in a first place three "classes of instabilities":

1. instabilities that are restricted to the combustion chamber
2. instabilities that involve interaction with other parts of the system, such as feeding lines or the device's structure
3. instabilities that are inherent to the chemical reactants, depending for example on combustion kinetics.

Even though individual cases may bear characteristics of more than one of these categories, they give a first impression of the complexity of the problem. Concerning combustion chamber instabilities, Barrère & Williams differentiate further between

- acoustic instabilities, characterized by the appearance of resonant acoustic modes in the combustion chamber

[1] corresponds to $\approx$ 140 bar

- shock instabilities involving propagating shock or detonation waves due to high combustion intensity
- and fluid-dynamic instabilities, that are characterized by specific flow patterns such as vortices.

This thesis focusses on instabilities that may occur in gas turbine combustion chambers as a result of flame-acoustic coupling. The understanding of this kind of instabilities requires hence knowledge about the acoustic field and the flame as a source of heat, as well as their interaction via excitation and damping mechanisms.

1.1.2 Excitation Mechanisms

The process of thermoacoustic instabilities can be divided schematically into two parts [29]: For one, a driving process that relates an incoming flow perturbation to a fluctuation of the flame's heat release rate q_1. This leads subsequently to acoustic pressure perturbations. Secondly, a feedback mechanism that links perturbations in downstream regions to the flow upstream of the flame, which is generally based on acoustic propagation.

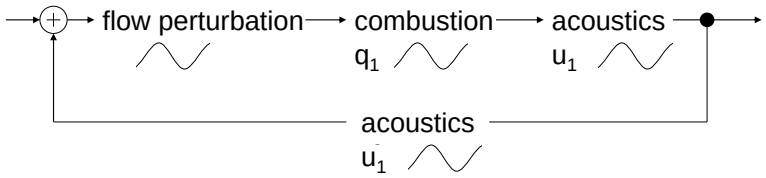

Figure 1.1: Feedback Loop leading to self-sustained oscillations. q_1: fluctuation of heat release rate; u_1: velocity fluctuation.

The feedback loop created this way may excite self-sustained oscillations when the processes involved lead to a situation where the Rayleigh criterion of Eq. (1.1) is satisfied, i.e. where the unsteady heat release rate of the flame is in phase with acoustic pressure perturbations and thus enhances the perturbations. In order to asses the stability of the system, it is thus necessary to identify the processes that link pressure and heat release rate fluctuations, in order to be able to evaluate their phase shift.
That this is not always simple is illustrated in a review by Culick [20], where an example of the processes leading to instability is discussed as follows: A pressure drop in the chamber at time t allows an increased fuel mass flow through the injector. Burning at the time $t + \tau$, the additional fuel causes an increased heat release rate. If this surplus in heat release rate occurs now at a moment where the pressure is reincreasing, it will enhance the pressure growth and destabilize the system. The important issue is therefore to evaluate the time lag τ, which represents in this example the time between the injection of the fuel and the heat release due to its combustion. This time lag is however composed of contributions resulting from separate mechanisms: in the present example, these are the time delay due to the transport of the fuel from the injector to the flame at a given velocity; and further a time delay due to combustion itself, i.e. linked to vaporization, reaction kinetics, and other factors. It is hence necessary not only to identify all processes that are involved in the combustion process, but also to determine their characteristic time scales.
As illustrated in Fig. 1.2, a positive feedback is obtained when the total time lag is of the order

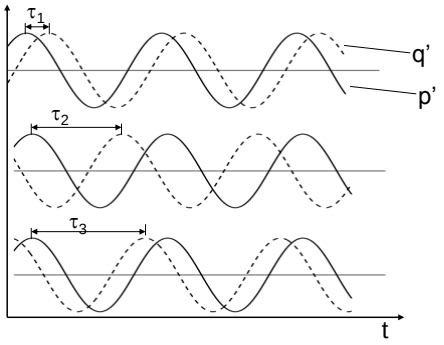

Figure 1.2: Response of flame to pressure fluctuation with different time lags τ. The Rayleigh criterion is satisfied if the time lag between pressure and heat release rate is $-\pi/(2\omega) < \tau < \pi/(2\omega)$.

of the acoustic period, or more precisely for $-\pi/(2\omega) < \tau < \pi/(2\omega)$. As pointed out by Zinn & Lieuwen [123], this means that the stability of different modes is governed by different mechanisms, in the sense that a driving process with a time scale suitable to excite one mode does not necessarily have an impact on another mode. At the same time, a change in operating conditions may change the time scale and thereby the effect of certain mechanisms. In the example cited above, a change in fuel injection velocity would directly modify the time delay. This, in turn, changes the frequencies for which positive feedback is possible.

The identification and characterisation of driving and feedback mechanisms is thus crucial for the understanding of combustion instability. Among the key mechanims one finds the following [11, 29, 123]:

- flame-vortex interaction:
  - vortex roll-up causes rapid changes in flame surface area, which in turn leads to an unsteady heat release rate
  - fresh gas is taken along in vortex structures and ignited further downstream, causing sudden increase in heat release rate
- flame-flame and flame-boundary interaction generates fluctuations in flame surface area and hence in heat release rate
- flame surface wrinkling can be caused by acoustic waves impinging on the flame and cause heat release rate fluctuations
- equivalence ratio fluctuations due to inhomogeneities in fuel composition cause unsteady combustion

As mentioned above, this list of mechanisms is not comprehensive. A further difficulty in the description of combustion instability lies in the fact that these mechanisms do in general not occur separately: It is then a challenging task to identify the processes responsible of the major contributions for a given configuration.

1.1.3 Damping Mechanisms

As a counterpart to the excitation mechanisms, a number of damping and loss mechanisms impede the appearance of instabilities or limit their growth. Among the most important processes

one finds the following [123]:

- radiation: some of the acoustic energy of resonant modes in cavities or ducts that have open outlets propagates to the far field (cf. for example organ pipes)
- convection: in cases where a mean flow is present in the domain, it will take some of the acoustic energy with it when leaving the system
- thermal and viscous dissipation:
  - boundary layers near rigid walls lead to imperfect reflection of acoustic waves, thus inducing loss of acoustic energy [88, 98, 123]: an acoustic wave that interacts with the thermal and acoustic boundary layers may transform some of its energy into vortical velocity fluctuations and entropy fluctuations.
  - flow separation and vortex shedding: at sharp egdes, the separation of the flow field from the surface and the consequential formation of vortices allows the transfer of acoustic energy into vorticity.
- transfer of energy between acoustic modes: the combustion chamber acting as a resonator, combustion instability occurs in general at specific frequencies. Nonlinear mechanism allow the transfer of energy from the unstable mode to other modes, such as its higher harmonics or subharmonics. This extraction of energy from the unstable mode has thus a stabilising effect for the system.

1.1.4 Criteria for Stability

As a result of the mechanisms discussed above, instability will eventually occur if the energy added to the system by driving mechanisms outbalances the energy lost by damping. It is hence of interest to be able to judge under which circumstances this is the case.
The Rayleigh criterion introduced before describes the conditions under which the flame will act as a source term. However, it is not sufficient to evaluate the stability of a system, as it does not account for loss terms. In order to estimate if a system is stable or unstable, the actual impact of energy sources and energy loss have to be compared.
To this end, the magnitude of the source term due to unsteady heat release rate is integrated over the domain's volume V and compared to the losses caused by acoustic energy flux across the domain's bounding surface A. Instability may then occur if the integrated source term outweighs the energy loss, i.e. if the following inequality is satisfied [75, 82]:

$$\int\int\int \frac{\gamma-1}{\gamma p_0} p_1(\mathbf{x},t) q_1(\mathbf{x},t) \mathrm{d}V > \int\int p_1(\mathbf{x},t)\mathbf{u}_1(\mathbf{x},t)\cdot\mathbf{n}\mathrm{d}A, \tag{1.2}$$

where γ and p_0 denote the heat capacity ratio and mean pressure, respectively, and p_1, $\mathbf{u}_1$ and q_1 perturbations of pressure, velocity and heat release rate. Furthermore, in cases where entropy fluctuations s_1 are susceptible to play an important role, the perturbations cannot be described in terms of acoustic energy, but require a more general definition that has been proposed as disturbance energy by Chu [16]. Following this approach, the flame acts as a source term if

$$\int\int\int T_1(\mathbf{x},t) q_1(\mathbf{x},t) \mathrm{d}V > 0,$$

i.e. if temperature fluctuations T_1 and heat release rate fluctuations q_1 are in phase, and not pressure and heat release rate fluctuations as required by the Rayleigh criterion. Equivalently to the expression of Eq. (1.2), an extended stability criterion predicts the growth of perturbations if [75]:

$$\int\int\int \left(\frac{T_1 q_1}{T_0} - \frac{p_0}{rC_p} s_1 \mathbf{u_1} \cdot \nabla s_0\right) \mathrm{d}V > \int\int p_1(\mathbf{x},t)\mathbf{u}_1(\mathbf{x},t) \cdot \mathbf{n} \mathrm{d}A \qquad (1.3)$$

where s_0 is the mean entropy, r the gas constant and C_p the heat capacity at constant pressure. In contrast to Eq. (1.2), the source (i.e. LHS) term of the above expression also takes into account the increase of mean entropy that occurs across the flame in combustion applications. Yet these criteria, though of increasing complexity, do not reflect all driving and damping mechanisms: for example, losses due to convection effects are not included in Eq. (1.2). Based on the consideration of Myers [72] on the balance of disturbance energy, more complete expressions have therefore been derived in the last years [40, 53]. They will be discussed in section 2.3.2.
The stability criteria stated above illustrate nevertheless that various factors are involved in the appearance of combustion instability, and that, in order to avoid this phenomenon, one may either increase the loss terms, or impede source mechanism. This balance is thus the basis for developing passive [106, 112] and active [11, 27, 68] control solutions.

1.1.5 Linear and Nonlinear Mechanisms

The mechanisms that control the stability of a system can be divided in linear or non-linear categories. Linear processes describe the behaviour of small amplitude oscillations, for which the strength of driving and damping processes is directly proportional to the amplitude. The onset and initial growth of instability is governed by linear processes [123], which justifies the use of linear stability models to determine whether combustion instability will occur or not.

However, linear theory predicts unlimited exponential growth of perturbations in the case of unstable systems, i.e. something that cannot exist in reality. As the perturbation amplitude increases, non linear processes, i.e. mechanisms that are not a linear function of the perturbation amplitude, start to govern driving and damping processes, and restrict the perturbation to a limit cycle amplitude. These mechanisms result from non linear terms in the governing equations of fluid dynamics, such as convective terms like $(\rho \mathbf{u} \nabla \mathbf{u})$ in the Navier Stokes equations or the non linear relationship between pressure and density $p(t)/p_0 = (\rho(t)/\rho_0)^\gamma$ [123]. Nonlinear terms are of importance when the amplitude of the perturbations approaches the order of the mean flow quantities, i.e when they exceed a threshold of about 10% of the mean flow values.

Another aspect to keep in mind is that a system that is predicted to be stable by linear theory may be nonlinearly unstable, i.e. it is stable when subjected to small amplitude perturbations, but may be unstable when subjected to large amplitude perturbations. This behaviour - in general referred to as triggering - has been observed in liquid and solid fuel rockets, where the high amplitude initial perturbations can occur due to batch-wise burning of fuel or when solid material is ejected through the exhaust nozzle [21]. However, according to Lieuwen [62], triggering may probably also occur in gas turbines, as a result of mechanisms driven by flame area-fluctuations.

1.2 Numerical Prediction of Thermoacoustic Instabilities

At present, several methods are used to describe combustion instabilities, ranging from Large Eddy Simulations (LES) to low-order network models. They differ in the degree of mathematical modelisation, geometrical simplifications, their ability to predict linear or non-linear instability and last but not least their computational cost.
Furthermore, time-domain and frequency-domain methods are distinguished. The former reproduce the physical processes following the order they actually take place in the system, in stages of initial, transient and long term behaviour. In contrast to that, the latter allow to describe the system in terms of periodical effects. In computations of thermo-acoustic instability, this is applied for example in the form of eigenmode computations, where the system is described in terms of resonant modes. Their form, frequency of oscillation and growth rate allows to identify patterns that are not necessarily clearly visible in a time-domain computation. The reason is that these latter reflect the actual behaviour of the system, which is governed by one single, more precisely the most unstable, mode. A disadvantage of eigenmode approaches is however that they do not allow to predict the actual amplitude of the perturbations in a simple way.

1.2.1 Large Eddy Simulations

As most elaborate method, Large Eddy Simulations (LES) solve the three-dimensional unsteady Navier-Stokes equations, and therefore include both a solution for the mean flow field and for the fluctuations in the sense of acoustic perturbations. Including the effects of chemical reactions, turbulence, compressibility and viscosity, this method allows to capture flame dynamics as well as flame acoustic interaction.
This method can be applied to very complex geometries and deal with a great number of flow configurations, which allows quite a realistic representation of industrial applications. While still limited in rocket engine calculations, LES is used successfully in the prediction of gas turbine instability [67, 100, 121]. Large Eddy Simulations do not only predict the onset of instability and its linear growth, but capture also non-linear mechanisms that lead to saturation and allow thus to deduce the limit cycle amplitudes of oscillations. However, when an LES predicts the appearance of combustion instability in a configuration, it is still a challenging task to determine its cause and find ways to control it.
The major inconvenience of this type of computation is their huge demand in computation time and memory, which results from the fact that not only the large scale acoustics are considered, but also small scale phenomena such as turbulence and combustion. This means that not only the resolution of the computational grid has to be extremely fine in order to capture all of the considered effects, but also that the system of equations to be solved is accordingly complex.

1.2.2 Acoustic Analysis based on Linearized Equations

As an alternative to LES computations, a number of less elaborate, yet very effective methods based on linearized equations exist. The linearisation is based on the conservation equations for mass, momentum and energy, in which the flow variables are decomposed into expressions for the mean flow field and small-amplitude perturbations. The conservation equations being satisfied for the mean flow field, one may deduce a set of equations for the perturbations, containing terms of first order only. These linearized equations for space-time evolution of small

perturbations can then be solved directly in the time domain, or modified by including additional assumptions about the mode shape or temporal evolution.
As the mean flow field is not part of the solution, the relevant mean flow quantities (such as the speed of sound) have to be determined beforehand. Besides, the interaction of the flame and the acoustic field needs to be described by a suitable model.
Some of the aspects concerning this kind of analysis, such as different ways of spatial discretisation of the computational domain, time or frequency domain approaches, or flame description, are adressed in the paragraphs below.

1.2.2.1 Galerkin Method

The linearization of the equations of conservation yields a system of partial differential equations for the perturbations. To solve these equations, different methods exist: one possibility is to apply a Galerkin method, as has been discussed by Culick [20] and later by Dowling [24]. In these works, the description of the acoustic is based on an inhomogeneous wave equation for pressure perturbations p_1

$$\nabla^2 p_1 - \frac{1}{c_0^2}\frac{\partial^2 p_1}{\partial t^2} = h, \tag{1.4}$$

where c_0 is the speed of sound and h denotes a source term. A boundary condition relates the pressure gradient normal to the wall to the flux term f:

$$\nabla p_1 \cdot \mathbf{n} = f \tag{1.5}$$

To simplify the analysis, the objective is then to replace the system of partial differential equations by a system of ordinary differential equations. This is achieved by expressing the pressure perturbations as function of the mean pressure p_0 in form of a Galerkin series

$$p_1(x,t) = p_0 \sum_{n=1}^{\infty} \eta_n(t)\Psi_n(x), \tag{1.6}$$

where the weight functions $\Psi_n(x)$ form a set of orthogonal basis functions and $\eta_n(t)$ describe the time variation of amplitude of the pressure perturbation. This allows, a number of steps later, to deduce an ordinary differential equation of the form

$$\frac{d^2\eta_n}{dt^2} + \omega_n^2 \eta_n = F(h,f). \tag{1.7}$$

The challenging part of this method is to determine a set of orthogonal basis functions $\Psi_n(x)$ that are suitable to describe the system and satisfy the boundary conditions. An obvious choice are the acoustic eigenmodes of the system. However, this ansatz is only justified if the terms h and f are small enough to be negligible. If this is not the case, for example when the boundaries are characterized by a complex valued impedance, the eigenmodes of the system are not orthogonal [74] and the set of basis functions has to be determined by other means.
Nevertheless, this method provides an efficient framework for formal studies of thermoacoustic systems. It can be used to describe the acoustic field in network models, and may be extended to include non-linear effects by keeping higher order terms [21].

1.2.2.2 Network Models

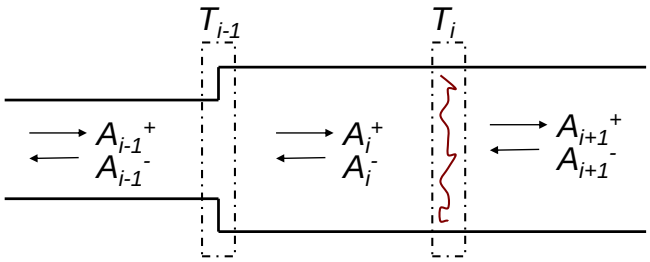

Figure 1.3: Description of Configurations in Terms of an Acoustic Network. A_i^+, A_i^-: Forward and backward travelling acoustic wave in subdomain i. T_i: Transfer Matrix between subdomains i and $i+1$.

The basic concept of a network code is to describe the configuration to be analysed as a succession (or network) of 1D components with piecewise uniform mean flow properties (see Fig. 1.3). Changes in geometrical or mean flow properties, e.g. variations in the domain's cross section, temperature increase across a flame, etc., are described as discontinuities across which step conditions are applied in order to assure the conservation of mass, momentum and energy. Though time domain network models exist [108], the larger part is based on a frequency domain formulation [32, 82, 107]. The pressure field in each subdomain i is expressed analytically. The solution is most commonly deduced from the homogeneous wave equation and yields

$$p_{1_i}(x,t) = A_i^+ e^{i(kx-\omega t)} + A_i^- e^{i(-kx-\omega t)},$$

where k is the wave vector, ω the frequency and A^+ and A^- the amplitudes of down- and upstream travelling waves. However, more complex expressions can be deduced, e.g. by basing the analysis on the linearized Euler equations [122]. The equations for the acoustic field are then solved for each element of the network, the boundary conditions being provided by matching conditions with the neighbouring subdomain. The discontinuities between the separate elements of the network are described by transfer matrices T, that establish relations between the amplitudes of forward and backward travelling waves on both sides:

$$\begin{bmatrix} A_{i+1}^+ \\ A_{i+1}^- \end{bmatrix} = T_i \begin{bmatrix} A_i^+ \\ A_i^- \end{bmatrix}$$

The essential difficulty of this method is thus the correct determination of the transfer matrices that describe all relevant non-uniformities of the configuration. This left aside, the method is rather straightforward in its implementation and use, and therefore constitutes a valuable means of analysis that is widely used for the description of acoustics in (research type) combustion devices [32, 107, 122]. The system of equations solved in a network code may include the effects of a uniform mean flow as well as flame-acoustic interaction, and can be formulated in a way as to describe both resonant modes and responses to frequency forcing. However, this method suffers from the drawback of being limited to rather simple geometries.

1.2.2.3 Finite Element & Finite Volume Methods

If the acoustic field is to be computed for rather complex geometries, well suited techniques are those combining the solution of a set of linearized equations with a finite volume or finite element discretisation of the computational domain: This allows to represent details of the geometry, while the mesh can be conceived considerably coarser than it would be necessary for a Large Eddy Simulation.
As viscous effects can be neglected in the description of acoustic wave propagation, the system of equations to be solved is in general based on the linearized Euler equations. Flame acoustic interaction is modelled using a flame transfer function. Depending on the configuration to be analysed, the system of equations may be simplified or adapted, e.g. to yield the acoustic perturbation equations [33, 80], which neglect the convection of entropy and vorticity modes, or to yield one single wave equation [78].
One noteworthy point is that solving the linearized Euler equations in the time domain leads to numerical problems in the sense that non-physical instability waves are propagated [2]. This can be bypassed by solving for example the acoustic perturbation equations, which are hydrodynamically stable [33]. When maintaining the linearized Euler equations as the system to solve, instability may be avoided by assuming the perturbations to be harmonic in time and passing to the frequency domain, a technique proposed by Rao & Morris [85] for wave propagation problems. Another advantage of the frequency domain approach is the fact that it allows to analyse not only the most unstable mode, but also less amplified or damped modes. As this is of interest in the evaluation of combustion instability, various frequency domain approaches have been proposed in this domain. They take different forms, e.g. based on the Helmholtz equation [74] or the linearized Navier-Stokes equations [14].

This latter approach is therefore also the one adopted in this thesis: Using a finite volume technique to discretise the computational domain, combustion instability is described by the linearized Euler equations in the frequency domain together with a transfer function that describes the interaction of the flame with the acoustic field. Extending the work of Benoit [9] and Nicoud et al. [74] from a Helmholtz solver to a solver for the linearized Euler equations, the presented work allows to take into account mean flow effects and therefore contributes to an improved prediction of combustion instability.

1.2.2.4 Description of the Flame

A key element in linear analysis of combustion instability is the description of the unsteady behaviour of the flame and its interaction with the acoustic field. This description is based on observations on acoustically compact flames [39, 97], which are subjected to perturbations, e.g. of flow velocity, and whose response to these perturbations is recorded. This can be achieved both by experiment [8, 30, 55], numerical simulation [41, 52, 116] or semi-analytical models [96].
According to the type of method used to describe the system, the formulation of the flame response may have the form of a transfer matrix (cf. network model, section 1.2.2.2, [38, 84]) or a flame transfer function (cf. finite volume approach, section 1.2.2.3, [77, 96]). In the former case, the flame itself is a black box and the pressure and velocity fluctuations upstream of the flame are linked to those downstream of the flame. In the latter case, a relation between the acoustic velocity upstream of the flame and the unsteady heat release rate of the flame is established. It should be noted that the two formulations are a priori not equivalent, as the flame

transfer function does usually not include information about the acoustic pressure field [115]. A flame transfer function, which is the approach used in the study presented here, has the general form

$$\mathcal{F}(\omega) = \frac{q_1(\omega)/q_{\mathrm{norm}}}{u_{1,x_{\mathrm{ref}}}(\omega)/u_{\mathrm{bulk}}},$$

where q_1 is the unsteady heat release rate, $u_{1,x_{\mathrm{ref}}}$ the acoustic velocity at the reference point and ω the angular frequency of the perturbation. The fluctuating quantities q_1 and u_1 are normalized using the bulk velocity u_{bulk} and a reference value for the mean heat release rate q_{norm}.
Flame transfer functions are usually expressed as complex quantities in terms of their gain and phase. The simplest approach to describe the flame's unsteady behaviour is therefore the $n-\tau$-model [18, 19], which approximates the flame transfer function in the form

$$\mathcal{F}(\omega) = ne^{i\omega\tau},$$

where n, the so-called interaction index, is a measure for the intensity of the flame response and the time lag τ describes the delay between the incoming velocity perturbation and the resulting fluctuation in heat release rate. This description reflects hence the time-lagged behaviour of the flame as described in section 1.1.
Beyond the rather simple $n-\tau$-model, various expression for flame transfer functions describing specific cases exist, such as V-shaped and conical flames [96], non linear effects [25, 77], or equivalence ratio fluctuations [93].

1.3 Impact of the Mean Flow Field

In the description of thermoacoustic instability, an assumption that is commonly made is that of the mean flow velocity being small enough to be considered zero. This assumption allows to considerably simplify the system of equations that describes the acoustic field, and to derive one single wave equation. However, this zero Mach number assumption may lead to significant changes in the evaluation of the thermo-acoustic modes present in the combustion chamber. This is especially true when the mean flow is not isentropic, which is always given in combustion applications.
In the following, different effects of the mean flow velocity are discussed considering two main aspects: firstly, the way it impacts on the physical mechanisms occurring in the system is addressed. A second subsection describes the consequences for the mathematical description of the system in terms of an eigenvalue problem.

1.3.1 Driving and Damping Mechanisms

Considering acoustic phenomena in moving media, one aspect is that the flow field itself may act as a source of sound. The way that sound is created and radiated by flow fields that contain fluctuations or turbulence has been described in detail by Lighthill [63, 64]. Other mechanisms of sound generation include interaction of flow with solid walls or inhomogeneities of the medium, or the interaction of pairs of vortices [17, 46].
These aeroacoustic phenomena are subject to extensive research, as they are of great relevance in predicting the noise produced by all kinds of vehicles, like for example the noise emitted by aircraft engine exhaust jets, flows over cavities or around obstacles. For these cases, the aspect of interest is the way the sound propagates and is perceived in the far field. The description of the acoustic field is then based on acoustic analogies [23, 34, 71] or the linearized Euler equations [4, 10], the noise generation due to the (turbulent) velocity field being introduced as an aeroacoustic source term into the system of equations.
These studies are hence very different from the analysis of combustion instability, where the acoustic field is confined and interacts with the source region, i.e. the flame. Besides, it has been shown that the source term related to unsteady combustion is far more important than aerodyamic sources [43], which are therefore not explicitly taken into account in the study that follows.

Other than acting as a source, the mean flow field has an impact on the acoustic field present in the domain, e.g. by convection, refraction or coupling with vorticity and entropy fluctuations [79, 88]. Convection leads for example to losses of acoustic energy at the outlet of open ended ducts: Ingard et al. [51] showed that for open ended ducts, the reflection coefficient R is 0.95 when the mean flow is at rest, 5% of the wave amplitude being lost by radiation (see also [123]). In presence of a mean flow however, the reflection coefficient is drastically reduced to about $R = 0.85$ at Mach numbers as low as $M = 0.05$. At Mach numbers exceeding 0.4, "[...] losses are so large that axial duct resonances are almost completely suppressed." [51]. In the same way, the reflection coefficient describing compact subcritical nozzles decreases with growing mean flow mach number at the nozzle inlet, following a relation deduced by Marble & Candel [66].
The mean flow may also enhance other damping mechanisms, such as the dissipation of acoustic energy at sharp edges due to vortex shedding [47, 88], which is exploited in acoustic liners:

when a perforated plate is placed perpendicular to a planar sound wave, the harmonic pressure difference across the plate leads to flow across the perforations, and subsequently to periodic shedding of vortices from the edges of the perforations. This way, energy of the acoustic field is transferred into vortical energy which is then dissipated. This mechanism, a priori also effective in quiescent media, has been found to be enhanced by a bias flow across the liner [31, 42].

Finally, an important aspect linked to the mean flow in combustion applications is the convection and acceleration of entropy inhomogeneities created in the flame. Also referred to as entropy waves or hot spots, these fluctuations are transported downstream by the mean flow. They may interact with the acoustic field in zones of accelerated mean flow as for example in the high pressure distributor downstream of the combustion chamber. There, the entropy spots can partly be converted into acoustic waves, which may then propagate upstream again [22, 66], thus closing a feedback loop between the flame and the acoustic field.
At the same time, acoustic waves generated as a result of entropy fluctuations may propagate downstream and into the far field, thus contributing to the noise emission of the engine as so called indirect combustion noise [5, 61], as opposed to the direct noise resulting from the acoustic field generated by the unsteady heat release rate of the flame. The effect of accelerated hot spots intervene hence both in combustion instability and noise emission. Therefore, this mechanism is not negligible in combustion applications and subject to both experimental [5] and numerical studies [61, 83].

1.3.2 Mathematical Formulation

When the acoustic field is to be described for an arbitrary mean flow field with non-zero mean flow velocity, the appropriate set of equations to solve are the Linearized Euler Equations (cf. section 2.1). However, when solved in the time domain, these equations account not only for the propagation of acoustic waves, but also of that of instability waves such as Kelvin-Helmholtz instabilities. The problematic aspect therein is that these instabilities are actually limited in growth by viscous and non-linear effects, which are precisely the ones neglected in the linearized Euler equations. The instability waves can therefore grow in a non-physical way and thereby obscure the solution for the acoustic field [2]. As mentioned before, the problem can be avoided by either modifying the system of equations, e.g. using the hydrodynamically stable acoustic perturbation equations [33], or by solving the linearized Euler equations in the frequency domain [85]. Yet, as a result of the structure of the linearized Euler equations, numerical instability is observed also in the frequency domain in the form of odd-even decoupling between pressure and velocity terms.

The description of thermoacoustic instabilitiy in the frequency domain requires to state the equation in the form of an eigenvalue problem. The resulting eigenvectors are in general not orthogonal [74], a phenomenon that is enhanced by the mean flow velocity [37]. However, non orthogonal eigenvectors may interact in ways that lead to transient amplification, even if a system is linearly stable [95]. This means that in configurations that are characterized by high mean flow Mach numbers, the amplitudes of perturbations in the system might be bigger than predicted by linear theory.

1.4 Thesis Outline

This thesis presents a study that deals with the computation of eigenmodes in combustion chambers using the Linearized Euler Equations in the frequency domain. To this end, a 1D and a 2D code solving this system of equations are developed. The objective is to investigate the impact of a non zero Mach number mean flow on the frequency of oscillation, growth rate and form of the eigenmodes.

The document is structured as follows:

Firstly, the mathematical description of the problem is introduced in Chapter 2. This comprises the governing equations for the description of the acoustic field, i.e. the Linearized Euler Equations, as well as the model used to reproduce the unsteady heat release rate of the flame and its coupling to the acoustic field.

Subsequently, a brief overview of the techniques necessary to solve the resulting eigenvalue problem is given in Chapter 3. This refers for one to the Arnoldi algorithm, which is the procedure used to solve the eigenvalue problem in the narrower sense. Yet, the way this algorithm is applied, i.e. the so called shift-invert-method, requires additionally the solution of a linear system. This is hence the second aspect to be discussed in this chapter.

Using the means introduced in these first two chapters, the problem of thermoacoustic instability has been investigated separately for 1D and 2D configurations. The major difference between these two cases is the way that the domain and equations are discretized:

1. In the 1D case, the domain is represented by a grid of equidistant points, and the equations are discretized using a central finite difference scheme for the acoustic variables and an upwind difference scheme for entropy fluctuations. Numerical instability is avoided by using a staggered grid formulation.

2. In the 2D case, a finite volume method is used on a mesh of unstructured tetrahedral cells. An artificial viscosity term is introduced to suppress numerical instability.

The main aspects of the numerical description and the results obtained for different test cases are presented in Chapters 4 and 5 concerning the 1D and 2D study, respectively.

In Chapter 6 the results obtained from the 1D solver are subjected to further analysis: the first aspect is to determine the disturbance energy contained in the separate modes. This allows not only to verify the accuracy of the results, but also to evaluate the origin of differences between cases with zero and non-zero Mach number mean flow. The second aspect considered is the effect of the eigenmodes being not orthogonal, and hence their possible interaction to cause transient growth of energy. It is shown how this effect can be evaluated in the framework of this study as a post-processing analysis of the results of the 1D solver.

The last chapter is dedicated to the conclusions that can be drawn from this work.

Chapter 2

Equations

The description of the acoustic field is based on the conservation equations for mass, momentum and energy, which are written for perturbations of small amplitude. As discussed in Chapter 1, the onset and initial growth of combustion instability may be described by linear theory. Such a linear approximation of the acoustic equations is obtained by neglecting second- and higher-order disturbance terms in the conservation equations. The resulting set of equations are the Linearized Euler Equations. They constitute the basis of the study presented in this thesis and are therefore discussed in this chapter.
Besides, the simulation of combustion instability using a system of linearized equations requires the use of a model to mimic the flame-acoustic interaction. In the present study, the time-lagged behaviour of the flame is described using an $n - \tau$-model, which is presented in a second section of this chapter.
Finally, it can be of some interest to evaluate the energy contained in the perturbations. To this end, a description of the acoustic energy as well as of a more generalized disturbance energy is included in this chapter.

2.1 Governing Equations for the Acoustic Field

2.1.1 Linearisation of the Conservation Equations

The equations used to describe the acoustic field are derived from the conservation laws for mass, momentum and energy. In order to derive the system of equations used for the present study, the following hypotheses have been made:

- the medium is a gas mixture that acts as a perfect gas. Multi-species effects are neglected
- volume forces (such as gravity) are neglected
- viscous terms (molecular diffusion of momentum and heat) are neglected

With the above assumptions, the conservation equations for mass, momentum and energy read (cf. [82]):

$$\frac{D\rho}{Dt} = -\rho\nabla\cdot\mathbf{u} \tag{2.1}$$

$$\rho\frac{D\mathbf{u}}{Dt} = -\nabla p \tag{2.2}$$

$$\frac{Ds}{Dt} = \frac{rq}{p} \tag{2.3}$$

where ρ denotes the mean density, p the static pressure, $\mathbf{u}$ the velocity vector and s the entropy per mass unit. The quantity $r = C_p - C_v$ is the specific gas constant of the mixture and q the rate of heat release per unit of volume.

The acoustic field is then commonly described in terms of perturbations of small amplitude, that are superimposed on the mean flow field. The instantaneous values of pressure, density, velocity vector, entropy and heat release rate are therefore decomposed into two contributions, i.e. each of these quantities can be written as $\phi(\mathbf{x},t) = \phi_0(\mathbf{x}) + \phi_1(\mathbf{x},t)$, where indeces 0 and 1 denote mean flow quantities and small amplitude fluctuations respectively. Introducing this decomposition into the Eqs. (2.1) - (2.3) yields:

$$\frac{\partial(\rho_0+\rho_1)}{\partial t} + (\mathbf{u_0}+\mathbf{u_1})\nabla(\rho_0+\rho_1) + (\rho_0+\rho_1)\nabla\cdot(\mathbf{u_0}+\mathbf{u_1}) = 0 \tag{2.4}$$

$$(\rho_0+\rho_1)\frac{\partial(\mathbf{u_0}+\mathbf{u_1})}{\partial t} + (\rho_0+\rho_1)(\mathbf{u_0}+\mathbf{u_1})\cdot\nabla(\mathbf{u_0}+\mathbf{u_1}) + \nabla(p_0+p_1) = 0 \tag{2.5}$$

$$\frac{\partial(s_0+s_1)}{\partial t} + (\mathbf{u_0}+\mathbf{u_1})\nabla(s_0+s_1) = r\frac{(q_0+q_1)}{p_0+p_1} \tag{2.6}$$

The derivation of a linearized set of equations is then based on the following hypotheses:

- the perturbations are small compared to the mean flow values, i.e. $p_1 << p_0$, $\rho_1 << \rho_0$, $s_1 << s_0$ and $u_1 << c_0$.

- the mean flow field is not time-dependant. It may depend on space though, and does not need to be quiescent, i.e. no assumptions are made about $\mathbf{u_0}(\mathbf{x})$

In addition to the above assumptions, the mean flow field is of course supposed to satisfy the conservation equations, i.e. Eqs. (2.1) - (2.3) hold for $p = p_0$, $\rho = \rho_0$, $s = s_0$ and $\mathbf{u} = \mathbf{u_0}$:

$$\frac{D\rho_0}{Dt} = -\rho_0 \nabla \cdot \mathbf{u_0} \tag{2.7}$$

$$\rho_0 \frac{D\mathbf{u_0}}{Dt} = -\nabla p_0 \tag{2.8}$$

$$\frac{Ds_0}{Dt} = \frac{rq_0}{p_0} \tag{2.9}$$

As the perturbations are assumed to be small, it is justified to apply a linear approximation and keep only perturbation terms of first order, while second and higher- order terms are neglected. The resulting set of equations reads thus

$$\frac{\partial \rho_1}{\partial t} + \mathbf{u_0} \nabla \rho_1 + \mathbf{u_1} \nabla \rho_0 + \rho_0 \nabla \cdot \mathbf{u_1} + \rho_1 \nabla \cdot \mathbf{u_0} = 0 \tag{2.10}$$

$$\rho_0 \frac{\partial \mathbf{u_1}}{\partial t} + \rho_0 \mathbf{u_0} \cdot \nabla \mathbf{u_1} + \rho_0 \mathbf{u_1} \cdot \nabla \mathbf{u_0} + \rho_1 \mathbf{u_0} \cdot \nabla \mathbf{u_0} + \nabla p_1 = 0 \tag{2.11}$$

$$\frac{\partial s_1}{\partial t} + \mathbf{u_0} \nabla s_1 + \mathbf{u_1} \nabla s_0 = \frac{rq_1}{p_0} - \frac{rq_0 p_1}{p_0^2} \tag{2.12}$$

2.1.2 Quasi-1D Formulation of the Linearized Euler Equations

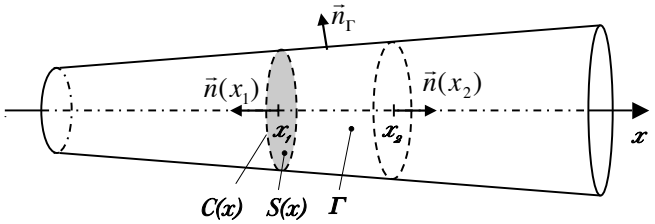

Figure 2.1: Notation used for derivation of quasi-1D form of the linearized Euler equations.
$\mathcal{S}(x)$: cross section of the domain at position x; Γ: lateral surface of the domain between two limits x_1 and x_2; $\mathcal{C}(x)$: contour line on the lateral surface at position x.

A part of this study is dedicated to a quasi-1D analysis. An example for a geometry that can be considered with the quasi-1D theory is plotted in Fig. 2.1: The cross section of the domain, noted $\mathcal{S}$ in the following, varies slowly and can be described as a function of the x-direction. The equations for the acoustic field are therefore derived in their quasi 1D formulation (cf. [76]). To this end, the conservation equations for mass, momentum and energy are first stated in conservative form [94]:

$$\frac{\partial \rho}{\partial t} + \frac{\partial}{\partial x_i}(\rho u_i) = 0 \tag{2.13}$$

$$\frac{\partial}{\partial t}(\rho u_i) + \frac{\partial}{\partial x_j}(\rho u_i u_j + p) = 0 \tag{2.14}$$

$$\frac{\partial}{\partial t}(\rho s) + \frac{\partial}{\partial x_j}(\rho u_j s) = \frac{q}{T} \tag{2.15}$$

The equations have hence the form of transport equations

$$\frac{\partial}{\partial t}(\rho\Phi) + \nabla \cdot \mathcal{F}(\Phi) = \mathcal{Q} \tag{2.16}$$

where Φ is a conserved variable, $\mathcal{F}(\Phi)$ the flux of Φ and $\mathcal{Q}$ a possible source term. The following shows the transformation into quasi-1D form for the general case of the above transport equation. Yet, all steps can be applied to the conservation equations Eq. (2.13) -(2.15).
Integrating Eq. (2.16) over the domain's volume V, one obtains

$$\int\int\int_V \big(\frac{\partial}{\partial t}(\rho\Phi) + \nabla \cdot \mathcal{F}(\Phi)\big)\mathrm{d}V = \int\int\int_V \mathcal{Q}\mathrm{d}V \tag{2.17}$$

Concerning the first term on the left hand side, one may consider that the domain's volume is constant over time. Besides, the volume integral can be rewritten in terms of the domain's cross section $\mathcal{S}(x)$ and its extension along x, such that (cf. Fig. 2.1):

$$\int\int\int_V \frac{\partial}{\partial t}(\rho\Phi)\mathrm{d}V = \frac{\partial}{\partial t}\int_{x_1}^{x_2}\big(\int\int_{\mathcal{S}}(\rho\Phi\mathrm{d}\mathcal{S})\big)\mathrm{d}x \tag{2.18}$$

Defining a cross sectional average of the quantity $\rho\Phi$ of the form

$$\overline{\rho\Phi} = \frac{1}{\mathcal{S}}\int\int_{\mathcal{S}}\rho\Phi\mathrm{d}\mathcal{S} \tag{2.19}$$

one can further rewrite Eq. (2.18) as

$$\int\int\int_V \frac{\partial}{\partial t}(\rho\Phi)\mathrm{d}V = \frac{\partial}{\partial t}\int_{x_1}^{x_2}\overline{\rho\Phi}\mathcal{S}\mathrm{d}x. \tag{2.20}$$

The second term on the left hand side of Eq. (2.17) can be converted into a surface integral using the divergence theorem:

$$\int\int\int_V \big(\nabla \cdot \mathcal{F}(\Phi)\big)\mathrm{d}V = \int\int_\Omega \big(\mathcal{F}(\Phi)\big)\mathbf{n}\mathrm{d}\Omega \tag{2.21}$$

where Ω is the total surface of the domain. As illustrated in Fig. 2.1, it can be separated into the inlet and outlet surface $\mathcal{S}(x_1)$ and $\mathcal{S}(x_2)$ and a lateral surface Γ. The normal vectors associated to the separate surfaces are oriented outwards of the domain, i.e. aligned with the negative x-direction for $\mathcal{S}(x_1)$ and the positive x-direction for $\mathcal{S}(x_2)$. The normal vector associated to the lateral surface is noted n_Γ. Equation (2.21) expands thus to

$$\int\int_\Omega \big(\mathcal{F}(\Phi)\big)\mathbf{n}\mathrm{d}\Omega = \int\int_\Gamma \mathcal{F}(\Phi)\mathbf{n_\Gamma}\mathrm{d}\Gamma + \int\int_{\mathcal{S}(x_2)}\mathcal{F}_x(\Phi)\mathrm{d}\mathcal{S} - \int\int_{\mathcal{S}(x_1)}\mathcal{F}_x(\Phi)\mathrm{d}\mathcal{S} \tag{2.22}$$

where $\mathcal{F}_x$ is the x-component of the flux term $\mathcal{F}$. Using the definition of the surface average Eq. (2.19), the last two terms of Eq. (2.22) can be transformed into:

$$\int\int_{\mathcal{S}(x_2)}\mathcal{F}_x(\Phi)\mathrm{d}\mathcal{S} - \int\int_{\mathcal{S}(x_1)}\mathcal{F}_x(\Phi)\mathrm{d}\mathcal{S} = \overline{\mathcal{F}_x}(\Phi, x_2)\mathcal{S}(x_2) - \overline{\mathcal{F}_x}(\Phi, x_1)\mathcal{S}(x_1) \tag{2.23}$$

Finally, Eq. (2.17) reads after these conversions:

$$\frac{\partial}{\partial t}\int_{x_1}^{x_2}\overline{\rho\Phi}\mathcal{S}\mathrm{d}x+\int\int_{\Gamma}\mathcal{F}(\Phi)\mathbf{n}_{\mathbf{\Gamma}}\mathrm{d}\Gamma+\overline{\mathcal{F}_x}(\Phi,x_2)\mathcal{S}(x_2)-\overline{\mathcal{F}_x}(\Phi,x_1)\mathcal{S}(x_1)=\int\int\int_{V}\mathcal{Q}\mathrm{d}V \tag{2.24}$$

For an infinitely thin slice of surface $\mathcal{S}$, where $x_2=x_1+\mathrm{d}x$, one may then write the balance

$$\frac{\partial}{\partial t}\overline{\rho\Phi}\mathcal{S}+\int_{\mathcal{C}}\mathcal{F}(\Phi)\mathbf{n}_{\mathbf{\Gamma}}\mathrm{d}\mathcal{C}+\frac{\partial}{\partial x}\overline{\mathcal{F}_x}(\Phi)\mathcal{S}=\int\int_{\mathcal{S}}\mathcal{Q}\mathrm{d}\mathcal{S}, \tag{2.25}$$

where $\mathcal{C}$ denotes the contour that marks the infinitesimally thin part of the lateral surface Γ at position x (cf. Fig. 2.1).
The expression of Eq. (2.25) allows then to deduce the quasi-1D equivalents of Eqs. (2.13) - (2.15) by introducing $\Phi=1$, $\Phi=u$ and $\Phi=s$, respectively, together with the respective flux terms. In the following, it will be assumed that the mean value of a product equals the product of the mean values of the factors, i.e. that $\overline{\rho\Phi}(x)=\overline{\rho}(x)\overline{\Phi}(x)$ etc. This way, the averaging permits to express all quantities as function of the x-direction only. As flux terms depending on velocity are parallel to the surface Γ, the only contribution of the integral in $\mathcal{C}$ in Eq. (2.25) concerns the flux term related to pressure in the momentum equation. Therefore, Eqs. (2.13) - (2.15) can be transformed into

$$\mathcal{S}\frac{\partial\overline{\rho}}{\partial t}+\frac{\partial}{\partial x}(\overline{\rho}\,\overline{u}\mathcal{S})=0 \tag{2.26}$$

$$\mathcal{S}\frac{\partial}{\partial t}(\overline{\rho}\,\overline{u})-\overline{p}\frac{\partial\mathcal{S}}{\partial x}+\frac{\partial}{\partial x}(\overline{\rho}\,\overline{u}^2\mathcal{S}+\overline{p}\mathcal{S})=0 \tag{2.27}$$

$$\mathcal{S}\frac{\partial}{\partial t}(\overline{\rho}\,\overline{s})+\frac{\partial}{\partial x}(\overline{\rho}\,\overline{u}\,\overline{s}\mathcal{S})=\mathcal{S}\frac{\overline{q}}{\overline{T}} \tag{2.28}$$

Finally, the above equations may be written in non-conservative form (the overbars indicating cross-sectional averaging of the quantities are omitted for clarity):

$$\frac{\partial\rho}{\partial t}+\frac{\partial}{\partial x}(\rho u)+\frac{\rho u}{\mathcal{S}}\frac{\partial\mathcal{S}}{\partial x}=0 \tag{2.29}$$

$$\rho\frac{\partial u}{\partial t}+(\rho u)\frac{\partial u}{\partial x}+\frac{\partial p}{\partial x}=0 \tag{2.30}$$

$$\frac{\partial s}{\partial t}+u\frac{\partial s}{\partial x}=\frac{q}{\rho T} \tag{2.31}$$

While the continuity equation contains an additional term referring to the geometry of the domain, the momentum and energy equations are found to be the 1D restrictions of the 3D equations Eq. (2.2) and (2.3). These equations are then linearized in the same way as the 3D equations, and yield:

$$\frac{\partial\rho_1}{\partial t}+u_0\frac{\partial\rho_1}{\partial x}+u_1\frac{\partial\rho_0}{\partial x}+\rho_0\frac{\partial u_1}{\partial x}+\rho_1\frac{\partial u_0}{\partial x}+\frac{u_1\rho_0}{\mathcal{S}}\frac{\partial\mathcal{S}}{\partial x}+\frac{u_0\rho_1}{\mathcal{S}}\frac{\partial\mathcal{S}}{\partial x}=0 \tag{2.32}$$

$$\rho_0\frac{\partial u_1}{\partial t}+\rho_0u_0\frac{\partial u_1}{\partial x}+\rho_0u_1\frac{\partial u_0}{\partial x}+\rho_1u_0\cdot\frac{\partial u_0}{\partial x}+\frac{\partial p_1}{\partial x}=0 \tag{2.33}$$

$$\frac{\partial s_1}{\partial t}+u_0\frac{\partial s_1}{\partial x}+u_1\frac{\partial s_0}{\partial x}=\frac{rq_1}{p_0}-\frac{rq_0p_1}{p_0^2} \tag{2.34}$$

2.1.3 Entropy Expression

The objective of the present study being the analysis of configurations that include heat release, the mean flow is not isentropic, i.e. $\nabla s_0 \neq 0$, and fluctuations of entropy s_1 may exist in the domain. The commonly used relation between pressure and density fluctuations derived for isentropic conditions, i.e. $\frac{p_1}{p_0} = \gamma \frac{\rho_1}{\rho_0}$, is hence not applicable.
In order to establish a valid relation between the quantities p_1, ρ_1 and s_1, a suitable expression for the entropy of the flow has thus to be found and linearized.

Taking a reference state noted with index "ref", the specific entropy of a fluid is defined as [36]:

$$s - s_{\text{ref}} = C_v \ln\left(\frac{p}{p_{\text{ref}}}\right) - C_p \ln\left(\frac{\rho}{\rho_{\text{ref}}}\right) \tag{2.35}$$

Solved for pressure, the relation reads:

$$\frac{p}{p_{\text{ref}}} = \left(\frac{\rho}{\rho_{\text{ref}}}\right)^{\gamma} \exp\left(\frac{s - s_{\text{ref}}}{C_v}\right) \tag{2.36}$$

Again, the flow variables p, ρ and s are decomposed into mean flow and small amplitude perturbations. In order to obtain a linearized form of this equation, a Taylor series is developed around the mean state, and only terms of first order in perturbation are kept:

$$p(\rho_0 + \rho_1, s_0 + s_1) = p(\rho_0, s_0) + \frac{\partial p}{\partial \rho}\Big|_{\rho_0,s_0}(\rho - \rho_0) + \frac{\partial p}{\partial s}\Big|_{\rho_0,s_0}(s - s_0) \tag{2.37}$$

The partial derivatives of pressure with respect to density and entropy read:

$$\frac{\partial p}{\partial \rho}\Big|_{\rho_0,s_0} = \gamma\frac{p_0}{\rho_0} \qquad \text{and} \qquad \frac{\partial p}{\partial s}\Big|_{\rho_0,s_0} = \frac{p_0}{C_v}. \tag{2.38}$$

Inserting Eqs. (2.38) into Eq. (2.37), a relation between pressure, entropy and density fluctuations can be established:

$$\frac{p_1}{p_0} = \gamma\frac{\rho_1}{\rho_0} + \frac{s_1}{C_v} \tag{2.39}$$

which simplifies to the isentropic relation if $s_1 = 0$.

2.1.4 Equation of State

In the same way as the entropy equation, the state equation for a perfect gas

$$p = \rho r T \tag{2.40}$$

can be linearized for small perturbations of pressure, density and temperature. (The gas constant is not subject to fluctuations.) The Taylor series developed around the mean state, keeping terms of first order only, reads:

$$p(\rho_0 + \rho_1, T_0 + T_1) = p(\rho_0, T_0) + \frac{\partial p}{\partial \rho}\Big|_{\rho_0,T_0}(\rho - \rho_0) + \frac{\partial p}{\partial T}\Big|_{\rho_0,T_0}(T - T_0) \tag{2.41}$$

with

$$\frac{\partial p}{\partial \rho}\Big|_{\rho_0,T_0} = rT_0 \qquad \text{and} \qquad \frac{\partial p}{\partial T}\Big|_{\rho_0,T_0} = r\rho_0. \tag{2.42}$$

The linearized equation of state reads thus:

$$\frac{p_1}{p_0} = \frac{\rho_1}{\rho_0} + \frac{T_1}{T_0}. \tag{2.43}$$

2.1.5 Wave Equation for the Acoustic Field in Quiescent Media

When the mean flow is at rest, it is possible to reduce the system of linearized equations Eqs. (2.10) - (2.12) to a scalar wave equation. Firstly, setting $u_0 = 0$ obviously simplifies these equations to:

$$\frac{\partial \rho_1}{\partial t} + \mathbf{u_1}\nabla\rho_0 + \rho_0 \nabla \cdot \mathbf{u_1} = 0 \tag{2.44}$$

$$\rho_0 \frac{\partial \mathbf{u_1}}{\partial t} + \nabla p_1 = 0 \tag{2.45}$$

$$\frac{\partial s_1}{\partial t} + \mathbf{u_1}\nabla s_0 = \frac{r q_1}{p_0} \tag{2.46}$$

Besides, using the thermodynamic relation [82]

$$ds = C_v dT - \frac{p}{\rho^2} d\rho \tag{2.47}$$

and the linearized state equation in the form:

$$\frac{dT}{T} = \frac{dp}{p} - \frac{d\rho}{\rho} \tag{2.48}$$

one may write

$$\frac{Ds}{Dt} = \frac{C_v}{p}\frac{Dp}{Dt} - \frac{C_p}{\rho}\frac{D\rho}{Dt}. \tag{2.49}$$

As the mean flow quantities are independant of time, one obtains the following expression for the mean entropy gradient:

$$\nabla s_0 = \frac{C_v}{p_0}\nabla p_0 - \frac{C_p}{\rho_0}\nabla \rho_0 \tag{2.50}$$

However, if the mean flow is assumed to be at rest, the mean pressure gradient is zero (cf. Eq. (2.8)). Thus, the mean entropy gradient simplifies to $\nabla s_0 = -\frac{C_p}{\rho_0}\nabla\rho_0$. Introducing this relation into Eq. (2.46), and using the linearized state and entropy expressions Eqs. (2.39) and (2.43), one may eliminate ρ_1 from Eq. (2.44). The system of equations Eqs. (2.44) - (2.46) simplifies then to:

$$\frac{1}{\gamma p_0}\frac{\partial p_1}{\partial t} + \nabla \cdot \mathbf{u_1} = \frac{r q_1}{C_p p_0} \tag{2.51}$$

$$\frac{\partial \mathbf{u_1}}{\partial t} + \frac{1}{\rho_0}\nabla p_1 = 0 \tag{2.52}$$

Taking the time derivative of Eq. (2.51) and adding the divergence of Eq. (2.52) allows finally to write a wave equation that describes the propagation of pressure fluctuations:

$$\frac{1}{\gamma p_0}\frac{\partial^2 p_1}{\partial t^2} - \nabla \cdot \left(\frac{1}{\rho_0}\nabla p_0\right) = \frac{\gamma - 1}{\gamma p_0}\frac{\partial q_1}{\partial t} \tag{2.53}$$

It should be noted that Eq. (2.53) differs from the wave equation for stagnant fluids commonly derived [79, 88]: it includes the effect of a mean entropy gradient, an aspect that is of importance in combustion applications.

2.1.6 Flame Model

The interaction between the flame and the acoustic field is described using a model that allows to account for the time lagged response of the flame to upstream flow perturbations as described in Chapter 1. Based on the work of Crocco [18, 19], such models have been developed in various forms and are referred to as $n - \tau$-models.

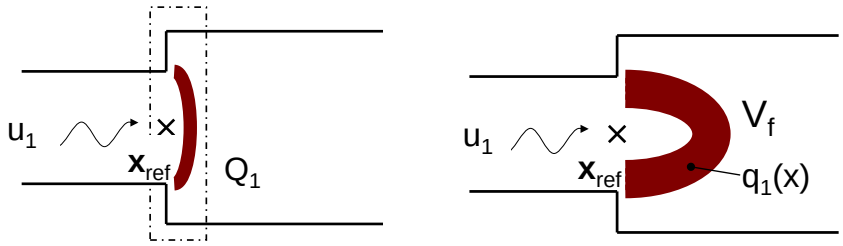

(a) Description in terms of global unsteady heat release rate

(b) Description in terms of local unsteady heat release rate

Figure 2.2: Description of flame-acoustic interaction via Flame Transfer Function. u_1: incoming velocity perturbation, $\mathbf{x_{ref}}$: reference position; V_f: volume of the flame; Q_1: global (i.e. volume integrated) fluctuation in heat release rate; q_1: local fluctuation in heat release rate (per unit volume)

The basic idea is to link the unsteady heat release emitted by the flame at time t to the acoustic velocity at an upstream reference point $\mathbf{x}_{\mathrm{ref}}$ (usually at the burner exit) at an earlier time $t - \tau$ (see Fig. 2.2). In a global view, the system is thus confronted with a fluctuation in heat release rate that can be written as

$$Q_1(t) = n\frac{Q_{\mathrm{norm}}}{U_{\mathrm{bulk}}}\mathbf{u_1}(\mathbf{x}_{\mathrm{ref}}, t-\tau)\cdot\mathbf{n}_{\mathrm{ref}}. \tag{2.54}$$

In this expression, $Q_1(t)$ denotes the fluctuating heat release rate integrated over the whole flow domain, Q_{norm} a reference value for the mean heat release rate of the flame, U_{bulk} the bulk velocity of the mean flow field and $\mathbf{n}_{\mathrm{ref}}$ is a unitary vector defining the direction of the reference velocity. The factor n is referred to as interaction index and is a measure of the strength of the flame's response to a perturbation, and τ is the time delay between the passage of the acoustic perturbation at the reference position and the response of the flame. These global parameters can be determined experimentally [28, 96].
However, introducing this kind of model into a finite volume solver requires a local formulation, as the flame is resolved by the mesh, and thus all quantities - including the unsteady heat release rate - are defined locally at each grid point. Besides, a description in terms of the global response of the flame is only well adapted when the flame is acoustically compact, i.e. when the acoustic wavelength is much smaller than the length of the flame, which is not always the case. In particular, it should be noted that the parameter τ directly impacts on the phase difference between the fluctuations of pressure and heat release rate, which means that τ controls the role of the flame as a source or a sink of acoustic energy (as stated in the Rayleigh criterion, cf. Eq. (1.1)). For these reasons, a more general description of flame acoustic interaction in the form of a local flame model (see Fig. 2.2(b)) is derived. In this approach, the response of the flame is expressed in terms of the local unsteady heat release rate per unit volume $q_1(\mathbf{x}, t)$ [74]. Expressed in a form equivalent to Eq. (2.54), the unsteady heat release rate per unit volume is

defined locally as:

$$q_1(\mathbf{x},t) = n_{\mathrm{loc}}(\mathbf{x})\frac{q_{\mathrm{norm}}}{U_{\mathrm{bulk}}}\mathbf{u_1}(\mathbf{x}_{\mathrm{ref}}, t-\tau(\mathbf{x}))\cdot\mathbf{n}_{\mathrm{ref}}. \tag{2.55}$$

In this local definition, the interaction index $n_{\mathrm{loc}}(\mathbf{x})$ and the time delay $\tau(\mathbf{x})$ are defined as fields of parameters rather than as the two real numbers n and τ, that are used in the global model Eq. (2.54). This allows hence to describe the response of the flame locally, provided that the two parameter fields are known, which can be achieved using LES computations [116, 117].

The link between the global and the local formulation is given by the relation between the total unsteady heat release rate $Q_1(t)$ and the local unsteady heat release rate per unit volume $q_1(\mathbf{x},t)$:

$$\int_{V_f} q_1(\mathbf{x},t)dV = Q_1(t), \tag{2.56}$$

i.e. the parameter fields $n_{\mathrm{loc}}(\mathbf{x})$ and $\tau(\mathbf{x})$ have to be designed in a way that the integrated flame response of the local model Eq. (2.55) corresponds to that of the global approach Eq. (2.54).

In this present study, the time delay is chosen as a constant value $\tau(\mathbf{x}) = \tau$, while the local interaction index is assumed to be constant throughout the flame region and zero everywhere else. The local interaction index is then related to the global interaction index n by:

$$\begin{aligned} n_{\mathrm{loc}} &= \frac{nQ_{\mathrm{norm}}}{q_{\mathrm{norm}}V_f} \qquad \text{in the reaction zone} \\ n_{\mathrm{loc}} &= 0 \qquad\qquad\quad \text{otherwise.} \end{aligned} \tag{2.57}$$

It should be noted here that the quantities Q_{norm} and q_{norm} are reference values employed for scaling in Eqs. (2.54) and (2.55), and that they do *not* necessarily satisfy the relation $q_{\mathrm{norm}}V_f = Q_{\mathrm{norm}}$. As Q_{norm} corresponds usually to the total heat release rate of the flame obtained experimentally, whereas q_{norm} and V_f are definitions used for describing the flame in an acoustic solver, requiring this latter relation to be fulfilled is neither convenient nor necessary. Thus, in order to assure that Eq. (2.56) is satisfied, the scaling values Q_{norm} and q_{norm} have to be maintained in Eq. (2.57).

Even though the flame is described in terms of its local response, the model expressed in Eq. (2.55) is still a rather simplified description, as it links the unsteady heat release rate only to fluctuation of acoustic velocity. The description can be improved by including relations between unsteady heat release rate and acoustic pressure or fuel ratio fluctuations [49, 115]. If the flame is related to the complete acoustic field, the flame transfer function approach becomes equivalent to a transfer matrix formulation, that relates upstream acoustic fluctuations to downstream acoustic fluctuations [115].

2.2 Formulation as an Eigenvalue Problem

In order to solve the thermo-acoustic problem stated by the linearized Euler equations and the flame related source term, the fluctuating quantitites are assumed to be harmonic in time, i.e. to vary periodically with a complex frequency $\omega = \omega_r + i\omega_i$. The fluctuating quantities can then be expressed in terms of an amplitude that depends on position $\hat{\phi}(\mathbf{x})$, and a temporal variation with ω, as

$$\phi_1(\mathbf{x}, t) = \Re\left(\hat{\phi}(\mathbf{x})e^{-i\omega t}\right), \tag{2.58}$$

This expression allows to pass to a frequency domain formulation. As a result, the system of equations can be written in the form of an eigenvalue problem.
The formulation retained for the present study is presented in its 3D as well as its quasi-1D form in the following. Besides, the Helmholtz-equation is briefly recalled: This equation can be used to describe thermo-acoustic instability in quiescent media and serves in this study as a reference method.

2.2.1 Linearized Euler Equations in the Frequency Domain

In order to derive the linearized Euler equations in a frequency domain formulation, the assumption of harmonic perturbations is introduced into their time domain equivalents Eq. (2.10) - (2.12). The time derivatives of the fluctuating quantities simplify to

$$\frac{\partial}{\partial t}\phi_1(\mathbf{x}, t) = -i\omega\hat{\phi}(\mathbf{x})e^{-i\omega t},$$

so that the system of equations Eq. (2.10) - (2.12) is transformed into:

$$\mathbf{u_0}\nabla\hat{\rho} + \hat{\mathbf{u}}\nabla\rho_0 + \rho_0\nabla\cdot\hat{\mathbf{u}} + \hat{\rho}\nabla\cdot\mathbf{u_0} = i\omega\hat{\rho} \tag{2.59}$$

$$\rho_0\mathbf{u_0}\cdot\nabla\hat{\mathbf{u}} + \rho_0\hat{\mathbf{u}}\cdot\nabla\mathbf{u_0} + \hat{\rho}\mathbf{u_0}\cdot\nabla\mathbf{u_0} + \nabla\hat{p} = i\omega\rho_0\hat{\mathbf{u}} \tag{2.60}$$

$$\mathbf{u_0}\nabla\hat{s} + \hat{\mathbf{u}}\nabla s_0 + \frac{rq_0\hat{p}}{p_0^2} - \frac{r\hat{q}}{p_0} = i\omega\hat{s} \tag{2.61}$$

The frequency domain formulations for the linearized entropy expression and state equation are deduced from their time domain form in Eqs. (2.39) and (2.43), respectively, and read:

$$\frac{\hat{p}}{p_0} = \gamma\frac{\hat{\rho}}{\rho_0} + \frac{\hat{s}}{C_v} \tag{2.62}$$

and

$$\frac{\hat{p}}{p_0} = \frac{\hat{\rho}}{\rho_0} + \frac{\hat{T}}{T_0}. \tag{2.63}$$

The system of equations (2.59) - (2.61) can now be transformed into an eigenvalue problem $\mathcal{A}\mathcal{V} = i\omega\mathcal{V}$, with an eigenvector $\mathcal{V}$ comprised of $(\hat{\rho}, \hat{\mathbf{u}}, \hat{s})^T$. Solving for an eigenvector containing this particular set of variables is a choice among several possibilities. Other options are

for example a description in terms of fluctuating mass flux and stagnation enthalpy.
In order to derive an eigenvalue problem with the eigenvector $\mathcal{V} = (\hat{\rho}, \hat{\mathbf{u}}, \hat{s})^T$, $\hat{p}$ and $\hat{q}$ need to be expressed as function of these three quantities. First, $\hat{p}$ is eliminated from the equations using the relation stated in Eqs. (2.62). The resulting system of equations reads:

$$(\nabla \cdot \mathbf{u_0} + \mathbf{u_0} \cdot \nabla)\hat{\rho} + (\nabla\rho_0 + \rho_0\nabla) \cdot \hat{\mathbf{u}} = i\omega\hat{\rho} \tag{2.64}$$

$$\left(\frac{\nabla c_0^2}{\rho_0} + \frac{\mathbf{u_0} \cdot \nabla \mathbf{u_0}}{\rho_0} + \frac{c_0^2}{\rho_0}\nabla\right)\hat{\rho} + (\nabla \mathbf{u_0} \cdot + \mathbf{u_0} \cdot \nabla)\hat{\mathbf{u}} + (\gamma - 1)T_0\left(\frac{\nabla p_0}{p_0} + \nabla\right)\hat{s} = i\omega\hat{\mathbf{u}} \tag{2.65}$$

$$\frac{\gamma r q_0}{\rho_0 p_0}\hat{\rho} + \nabla s_0 \cdot \hat{\mathbf{u}} + \left(\mathbf{u_0} \cdot \nabla + (\gamma - 1)\frac{q_0}{p_0}\right)\hat{s} - \frac{r}{p_0}\hat{q} = i\omega\hat{s} \tag{2.66}$$

Secondly, the amplitude of the unsteady heat release rate per unit volume $\hat{q}$ is expressed as a function of the amplitude of the acoustic velocity at a reference location $\hat{\mathbf{u}}_{\mathbf{x_{ref}}}$ using the $n - \tau$-model. The frequency domain equivalent of Eq. (2.55) reads:

$$\hat{q}(\mathbf{x}) = \frac{q_{\mathrm{norm}}}{U_{\mathrm{bulk}}} n_{\mathrm{loc}}(\mathbf{x}) e^{(i\omega\tau)} \hat{\mathbf{u}}_{\mathbf{x}_{\mathrm{ref}}} \cdot \mathbf{n}_{\mathrm{ref}} \tag{2.67}$$

Formally, this can be written as $\hat{q} = q_{\hat{\mathbf{u}}}\hat{\mathbf{u}}$. Introducing this expression into Eq. (2.66), one can thus write the eigenvalue problem

$$\mathcal{A}\mathcal{V} = i\omega\mathcal{V} \tag{2.68}$$

with the eigenvector $\mathcal{V} = (\hat{\rho}, \hat{\mathbf{u}}, \hat{s})^T$ and the complex eigenvalue $\omega = \omega_r + i\omega_i$. The matrix $\mathcal{A}$ is a linear operator applied to the eigenvector, which reads thus:

$$\mathcal{A} = \begin{bmatrix} (\nabla \cdot \mathbf{u_0} + \mathbf{u_0} \cdot \nabla) & (\nabla\rho_0 + \rho_0\nabla) & 0 \\ \left(\frac{\nabla c_0^2}{\rho_0} + \frac{\mathbf{u_0}\cdot\nabla\mathbf{u_0}}{\rho_0} + \frac{c_0^2}{\rho_0}\nabla\right) & (\nabla\mathbf{u_0} \cdot + \mathbf{u_0} \cdot \nabla) & (\gamma - 1)T_0\left(\frac{\nabla p_0}{p_0} + \nabla\right) \\ \frac{\gamma r q_0}{\rho_0 p_0} & \nabla s_0 \cdot - \frac{r}{p_0} q_{\hat{\mathbf{u}}} & \left(\mathbf{u_0} \cdot \nabla + (\gamma - 1)\frac{q_0}{p_0}\right) \end{bmatrix} \tag{2.69}$$

The quasi-1D formulation of the problem is deduced equivalently from Eqs. (2.32) - (2.34). The velocity vector being reduced to its component in the x-direction, the eigenvector contains the three unknowns $\mathcal{V} = (\hat{\rho}, \hat{u}, \hat{s})^T$. The operator matrix $\mathcal{A}$ corresponds to the 1D equivalent of the 3D version, with the additional terms accounting for variations of the cross section area $\mathcal{S}$ and reads:

$$\mathcal{A} = \begin{bmatrix} (\frac{\partial u_0}{\partial x} + u_0\frac{\partial}{\partial x} + \frac{u_0}{\mathcal{S}}\frac{\partial \mathcal{S}}{\partial x}) & (\frac{\partial \rho_0}{\partial x} + \rho_0\frac{\partial}{\partial x} + \frac{\rho_0}{\mathcal{S}}\frac{\partial \mathcal{S}}{\partial x}) & 0 \\ \left(\frac{1}{\rho_0}\frac{\partial c_0^2}{\partial x} + \frac{u_0}{\rho_0}\frac{\partial u_0}{\partial x} + \frac{c_0^2}{\rho_0}\frac{\partial}{\partial x}\right) & (\frac{\partial u_0}{\partial x} + u_0\frac{\partial}{\partial x}) & (\gamma - 1)T_0\left(\frac{1}{p_0}\frac{\partial p_0}{\partial x} + \frac{\partial}{\partial x}\right) \\ \frac{\gamma r q_0}{\rho_0 p_0} & \frac{\partial s_0}{\partial x} - \frac{r}{p_0} q_{\hat{u}} & \left(u_0\frac{\partial}{\partial x} + (\gamma - 1)\frac{q_0}{p_0}\right) \end{bmatrix} \tag{2.70}$$

2.2.2 Medium at Rest: Helmholtz Equation

Introducing the assumption of harmonic perturbations as stated in Eq. (2.58) into the wave equation (2.53) yields the inhomogeneous Helmholtz equation

$$\nabla \cdot \left(\frac{1}{\rho_0} \nabla \hat{p} \right) + \frac{\omega^2}{\gamma p_0} \hat{p} = i\omega \frac{\gamma - 1}{\gamma p_0} \hat{q} \tag{2.71}$$

The RHS term of this equation expresses the contribution of the unsteady heat release rate $\hat{q}$, which can be linked to the amplitude of the pressure perturbation $\hat{p}$ using the $n - \tau$-model. As the momentum equation for first order perturbations in a medium at rest (cf. Eq. (2.60)) states that $\nabla \hat{p} = i\omega \rho_0 \hat{u}$, the expression of Eq. (2.67) can be rewritten as function of the pressure perturbation at a reference location $\mathbf{x}_{\mathrm{ref}}$:

$$\hat{q}(\mathbf{x}) = \frac{q_{\mathrm{norm}}}{i\omega \rho_{\mathbf{x}_{\mathrm{ref}}} U_{\mathrm{bulk}}} n_{\mathrm{loc}}(\mathbf{x}) e^{(i\omega\tau)} \nabla \hat{p}_{\mathbf{x}_{\mathrm{ref}}} \cdot \mathbf{n}_{\mathrm{ref}}. \tag{2.72}$$

After spatial discretization, equation (2.71) can then be written in the form of a quadratic eigenvalue problem of the form [74, 101]

$$\mathcal{A}\mathcal{V} + \omega \mathcal{B}\mathcal{V} + \omega^2 \mathcal{C}\mathcal{V} = \mathcal{D}(\omega)\mathcal{V}, \tag{2.73}$$

where the eigenvector $\mathcal{V}$ is reduced to one single unknown, i.e. the amplitude of the pressure perturbation $\mathcal{V} = \hat{p}$ and $\mathcal{A}$, $\mathcal{B}$, $\mathcal{C}$ and $\mathcal{D}$ are operator matrices that describe the impact of the mean flow field, the boundary conditions and the source term. A detailed description of these operator matrices can be found in Nicoud et al. [74].

2.3 Energy of the Perturbations

In order to understand the mechanisms that lead to stability or instability of a thermo-acoustic system, it is of some interest to evaluate the energy contained in the field of perturbations. Care has to be taken in the description of this energy, as it is composed of second order terms in the perturbations: by way of example, the kinetic energy density of the acoustic field is given by the term $\frac{1}{2}\rho_0 u_1^2$. It is therefore a difficult task to derive a consistent conservation law for the energy of these perturbations, which are themselves described by first order equations.
The situation gets even more complex when entropy fluctuations and convection processes are involved, which is the case in the present study. Then, the classic definition of acoustic energy is not sufficient anymore, and a generalized expression for the energy of the disturbances has to be used.
In the following, the definition of the acoustic energy for fluids at rest is briefly recalled. The focus of this section lies however on the introduction of the generalized perturbation energy, whose derivation is presented subsequently.

2.3.1 Acoustic Energy in Quiescent Media

The simplest case to consider is that of the acoustic field in a medium at rest and without any sources and mean flow gradients. The governing equations are then the linearized continuity and momentum equations that read for these conditions (cf. Eqs (2.10)-(2.11)):

$$\frac{1}{c_0^2}\frac{\partial p_1}{\partial t} + \rho_0 \nabla \cdot \mathbf{u_1} = 0 \tag{2.74}$$

$$\rho_0 \frac{\partial \mathbf{u_1}}{\partial t} + \nabla p_1 = 0 \tag{2.75}$$

In order to derive an expression for the acoustic energy, these two equations are combined as follows: Eq. (2.74) is multiplied by p_1/ρ_0 and Eq. (2.75) is multiplied by $\mathbf{u_1}$. The resulting expressions are then added, resulting in (cf. [82, 88]):

$$\frac{\partial}{\partial t}\left(\frac{1}{2}\rho_0 \mathbf{u_1}^2 + \frac{1}{2}\frac{p_1^2}{\rho_0 c_0^2}\right) + \nabla \cdot (p_1 \mathbf{u_1}) = 0 \tag{2.76}$$

Equation (2.76) states a conservation law for the acoustic energy of the form

$$\frac{\partial}{\partial t} E + \nabla \cdot \mathbf{F} = 0 \tag{2.77}$$

where the acoustic energy E is defined as

$$E = \frac{1}{2}\rho_0 \mathbf{u_1}^2 + \frac{1}{2}\frac{p_1^2}{\rho_0 c_0^2} \tag{2.78}$$

and the flux of acoustic energy across the system's boundaries $\mathbf{F}$ reads

$$\mathbf{F} = p_1 \mathbf{u_1} \tag{2.79}$$

Being derived from Eq. (2.74) and Eq. (2.75), these expressions are of course only valid in situations where these latter equations are satisfied, i.e. in absense of mean flow terms, entropy fluctuations and source terms.

2.3.2 Generalized Disturbance Energy

For cases where mean flow terms and entropy fluctuations are not negligible, generalized expressions for disturbance energy have been derived. The study presented in Chapter 6 of this work is based on the energy corollary by Myers [72], which describes the energy of perturbations in arbitrary steady flow. Rather than deriving a conservation law for the energy of perturbations from the continuity and momentum equation by "algebraic manipulation" as employed in section 2.3.1, Myers derives such an expression directly from the energy equation. This derivation is summed up here in order to introduce the terms used in the evaluation of the disturbance energy budget in Chapter 6. Otherwise following the notation used in the reference paper by Myers [72], the source term of the energy equation is adapted to the case considered in this study, and viscous terms are omitted from the beginning.

Formulation of the Conservation Equations for n-th order Fluctuations

The starting point of the derivation are the conservation equations for mass, momentum and energy for a fluid in motion:

$$\frac{\partial \rho}{\partial t} + \nabla \cdot (\rho \mathbf{u}) = 0 \tag{2.80}$$

$$\frac{\partial \mathbf{u}}{\partial t} + (\mathbf{u} \cdot \nabla)\mathbf{u} + \frac{1}{\rho}\nabla p = 0 \tag{2.81}$$

$$\frac{\partial s}{\partial t} + (\mathbf{u} \cdot \nabla)s = \frac{q}{\rho T} \tag{2.82}$$

As mentioned before, viscous terms and body forces are neglected in these equations. This set of equations is therefore exactly the same as that used for the derivation of the Linearized Euler Equations shown in section 2.1 (cf. Eqs. (2.1)- (2.3)).

For the derivation of the disturbance energy corollary, these equations are then noted in terms of specific stagnation enthalpy H and mass flux $\mathbf{m}$. These quantities are defined by

$$H = h + \frac{\mathbf{u}^2}{2} \qquad \text{and} \qquad \mathbf{m} = \rho \mathbf{u}, \tag{2.83}$$

respectively, where h is the specific enthalpy. This latter can further be expressed in terms of the inner energy e via

$$h = e + \frac{p}{\rho} \tag{2.84}$$

Furthermore, the thermodynamic relations

$$\mathrm{d}e = T\mathrm{d}s + \frac{p}{\rho^2}\mathrm{d}\rho \qquad \mathrm{d}p = \frac{c^2 \rho \beta T}{C_p}\mathrm{d}s + c^2 \mathrm{d}\rho \qquad \mathrm{d}T = \frac{T}{C_p}\mathrm{d}s + \frac{\beta T}{\rho C_p}\mathrm{d}p \tag{2.85}$$

are recalled [72]. In the above expressions, $\beta = (-\partial\rho/\rho\partial T)_p$ is the coefficient of thermal expansion. Using Eq. (2.84) together with Eq. (2.85), one may write

$$\frac{\nabla p}{\rho} = \nabla h - T \nabla s \tag{2.86}$$

Besides, the convective acceleration term $(\mathbf{u} \cdot \nabla)\mathbf{u}$ is transformed using the vector identity

$$(\mathbf{u} \cdot \nabla)\mathbf{u} = (\nabla \times \mathbf{u}) \times \mathbf{u} + \nabla(\frac{\mathbf{u}^2}{2}) = \zeta + \nabla(\frac{\mathbf{u^2}}{\mathbf{2}}) \tag{2.87}$$

with $\zeta = (\nabla \times \mathbf{u}) \times \mathbf{u}$ a vector that comprises the impact of the vorticity $\xi = \nabla \times \mathbf{u}$.

Finally, the conservation equations Eqs. (2.80) - (2.82) can be rewritten in the form

$$\frac{\partial \rho}{\partial t} + \nabla \cdot \mathbf{m} = 0 \tag{2.88}$$

$$\frac{\partial \mathbf{u}}{\partial t} + \zeta + \nabla H - T\nabla s = 0 \tag{2.89}$$

$$\frac{\partial(\rho s)}{\partial t} + \nabla \cdot (\mathbf{m}s) = Q \tag{2.90}$$

Note that, for the sake of simplicity, the source term in the energy equation is noted Q in the following, and is related to the source term of Eq. (2.82) via $Q = \frac{q}{T}$.

In a next step, the flow quantities are expressed as a sum of a steady mean value and n-th order fluctuations:

$$\phi(x,t) = \phi_0(x) + \sum_{n=1}^{\infty} \delta^n \phi_n(x,t) \tag{2.91}$$

where Myers [72] uses the parameter δ to designate the order of magnitude of the fluctuations.

Using this decomposition, the conservation equations can then be written separately for flow quantities of order $n = 0, 1, 2, ...$ As the mean flow quantities are assumed to be independent of time, the system of equations for $n = 0$ reads:

$$\nabla \cdot \mathbf{m_0} = 0 \tag{2.92}$$

$$\zeta_0 + \nabla H_0 - T_0 \nabla s_0 = 0 \tag{2.93}$$

$$\nabla \cdot (\mathbf{m_0} s_0) = Q_0 \tag{2.94}$$

As mentioned before, the conservation equations for first order fluctuations correspond to a alternative formulation of the linearized Euler equations and read:

$$\frac{\partial \rho_1}{\partial t} + \nabla \cdot \mathbf{m_1} = 0 \tag{2.95}$$

$$\frac{\partial \mathbf{u_1}}{\partial t} + \zeta_1 + \nabla H_1 - T_0 \nabla s_1 - T_1 \nabla s_0 = 0 \tag{2.96}$$

$$\frac{\partial}{\partial t}(\rho_0 s_1 + \rho_1 s_0) + \nabla \cdot (\mathbf{m_0} s_1 + \mathbf{m_1} s_0) = Q_1 \tag{2.97}$$

Finally, the conservation laws for second order fluctuations are obtained as:

$$\frac{\partial \rho_2}{\partial t} + \nabla \cdot \mathbf{m_2} = 0 \tag{2.98}$$

$$\frac{\partial \mathbf{u_2}}{\partial t} + \zeta_2 + \nabla H_2 - T_0 \nabla s_2 - T_1 \nabla s_1 - T_2 \nabla s_0 = 0 \tag{2.99}$$

$$\frac{\partial}{\partial t}(\rho_0 s_2 + \rho_1 s_1 + \rho_2 s_0) + \nabla \cdot (\mathbf{m_0} s_2 + \mathbf{m_1} s_1 + \mathbf{m_2} s_0) = Q_2 \tag{2.100}$$

The system of equations for the n-th order terms is completed by expressions that allow to decompose the quantities (ρe) and h into a mean value and perturbations of order n. Therefore, these quantities are expanded in Taylor series, and the relations (2.85) are used to determine the correct expression for the involved derivatives:

$$\begin{aligned}\rho e =& \rho_0 e_0 + \frac{\partial(\rho e)}{\partial \rho}\Big|_0(\rho - \rho_0) + \frac{\partial(\rho e)}{\partial s}\Big|_0(s - s_0) \\ &+ \frac{\partial^2(\rho e)}{\partial \rho^2}\Big|_0 \frac{(\rho - \rho_0)^2}{2} + \frac{\partial^2(\rho e)}{\partial \rho \partial s}\Big|_0(\rho - \rho_0)(s - s_0) + \frac{\partial^2(\rho e)}{\partial s^2}\Big|_0 \frac{(s - s)^2}{2} + ...\end{aligned} \tag{2.101}$$

i.e.

$$\begin{aligned}\rho e =& \rho_0 e_0 + \delta(h_0 \rho_1 + \rho_0 T_0 s_1) \\ &+ \delta^2(h_0 \rho_2 + \rho_0 T_0 s_2 + \rho_1 T_0 s_1 + \frac{p_1^2}{2\rho_0 c_0^2} + \frac{\rho_0 T_0 s_1^2}{2C_p}) + \mathcal{O}(\delta^3)\end{aligned} \tag{2.102}$$

and for the specific enthalpy, one obtains

$$h = h_0 + \delta\left(\frac{p_1}{\rho_0} + T_0 s_1\right) + \mathcal{O}(\delta^2) \tag{2.103}$$

where, as introduced with Eq. (2.91), the parameter δ^n denotes the order of the perturbations.

Derivation of the Energy Corollary

The expressions deduced so far are then used to derive an exact energy equation of second order in the perturbations. This is done starting from an equation that expresses the conservation of internal and kinetic energy in absence of body forces and viscosity, and which reads

$$\frac{\partial}{\partial t}(\rho H - p) + \nabla \cdot (\mathbf{m} H) - TQ = 0 \tag{2.104}$$

where all terms are noted according to what has been introduced before.

The disturbance energy being expressed by an equation of second order in the perturbations, Eq. (2.104) is decomposed into contributions of order $n = 0, 1, 2, ...$ using the expression Eq. (2.91). The conservation law for $n = 2$ reads:

$$\frac{\partial}{\partial t}(\rho H - p)_2 + \nabla \cdot (\mathbf{m_0} H_2 + \mathbf{m_1} H_1 + \mathbf{m_2} H_0) - T_0 Q_2 - T_1 Q_1 - T_2 Q_0 = 0 \tag{2.105}$$

It is then shown that the terms of Eq. (2.105) can be arranged in such a way as to yield an expression that involves *first order terms of perturbations* only, and this without any additional assumptions. The basic steps of this transformation are given in the following.

Firstly, the second order fluctuation term $(\rho H - p)_2$ is expressed in terms of primitive variables using Eqs. (2.83) and (2.84) and transformed according to the relation expressed in Eq. (2.102):

$$\begin{aligned}(\rho H - p)_2 =&(\rho e + \rho\frac{\mathbf{u}^2}{2})_2 = (\rho e)_2 + \frac{1}{2}\rho_0 {\mathbf{u_1}}^2 + \rho_1 \mathbf{u_1}\cdot\mathbf{u_0} + \rho_0 \mathbf{u_0}\cdot\mathbf{u_2} + \frac{1}{2}\rho_2 {\mathbf{u_0}}^2 \\ =&\frac{p_1^2}{2\rho_0 c_0^2} + \frac{1}{2}\rho_0 {\mathbf{u_1}}^2 + \rho_1 \mathbf{u_1}\cdot\mathbf{u_0} + \frac{\rho_0 T_0 s_1^2}{2C_p} + H_0\rho_2 + T_0(\rho_0 s_2 + \rho_1 s_1) + \mathbf{m_0}\cdot\mathbf{u_2}\end{aligned} \tag{2.106}$$

The term $(\rho H - p)_2$ occurs in Eq. (2.105) as a derivative w.r.t. time. The objective of the following transformation is then to arrange the different terms of Eq. (2.105) in a way that allows to exploit the relations stated by the conservation equations for the second order fluctuations Eqs. (2.98) - (2.100). The time derivative is therefore splitted into separate parts: the terms that correspond to the time derivatives on the left hand side of Eqs. (2.98) - (2.100), and a remainder. As the mean flow quantities, i.e. the quantities of order zero, are not time dependant, this yields:

$$\begin{aligned}\frac{\partial}{\partial t}(\rho e + \rho\frac{\mathbf{u}^2}{2})_2 = &(H_0 - T_0 s_0)\frac{\partial \rho_2}{\partial t} + \mathbf{m_0}\frac{\partial \mathbf{u_2}}{\partial t} + T_0\frac{\partial}{\partial t}(\rho_0 s_2 + \rho_1 s_1 + \rho_2 s_0) \\ &+ \frac{\partial}{\partial t}\left[\frac{p_1^2}{2\rho_0 c_0^2} + \frac{1}{2}\rho_0 {\mathbf{u_1}}^2 + \rho_1 \mathbf{u_1}\cdot\mathbf{u_0} + \frac{\rho_0 T_0 s_1^2}{2C_p}\right]\end{aligned} \tag{2.107}$$

The four remaining terms are then summarized in the term E_2:

$$E_2 = \frac{p_1^2}{2\rho_0 c_0^2} + \frac{1}{2}\rho_0 {\mathbf{u_1}}^2 + \rho_1 \mathbf{u_1}\cdot\mathbf{u_0} + \frac{\rho_0 T_0 s_1^2}{2C_p} \tag{2.108}$$

The time derivative of Eq. (2.107) is then introduced into Eq. (2.105). After a few cumbersome but rather straightforward transformations, one may finally rewrite this equation as:

$$\begin{aligned}&\frac{\partial E_2}{\partial t} \\ &+(H_0 - T_0 s_0)\left[\frac{\partial \rho_2}{\partial t} + \nabla\cdot\mathbf{m_2}\right] \\ &+\mathbf{m_0}\cdot\left[\frac{\partial u_2}{\partial t} + \zeta_2 + \nabla H_2 - T_0\nabla s_2 - T_1\nabla s_1 - T_2\nabla s_0\right] \\ &+T_0\left[\frac{\partial}{\partial t}(\rho_0 s_2 + \rho_1 s_1 + \rho_2 s_0) + \nabla\cdot(\mathbf{m_0}s_2 + \mathbf{m_1}s_1 + \mathbf{m_2}s_0) - Q_2\right] \\ &+\nabla\cdot(\mathbf{m_1}H_1) + T_1\nabla\cdot(\mathbf{m_0}s_1) - T_0\nabla\cdot(\mathbf{m_1}s_1) - \mathbf{m_0}\cdot\zeta_2 - \mathbf{m_2}\cdot\zeta_0 - T_1 Q_1 = 0\end{aligned} \tag{2.109}$$

The second, third and fourth term of Eq. (2.109) are zero, as the terms in brackets correspond exactly to the conservation equations for second order flucutating flow quantities stated in Eqs. (2.98) - (2.100).

Thus, the final energy balance is retained in the form:

$$\begin{aligned}\frac{\partial E_2}{\partial t} + \nabla \cdot \underbrace{[\mathbf{m_1}(H_1 - T_0 s_1) + \mathbf{m_0} T_1 s_1]}_{W_2} \\ = \underbrace{-\mathbf{m_1} s_1 \cdot \nabla T_0 + \mathbf{m_0} s_1 \cdot \nabla T_1 + \mathbf{m_0} \cdot \zeta_2 + \mathbf{m_2} \cdot \zeta_0 + T_1 Q_1}_{D_2}\end{aligned} \tag{2.110}$$

Eq. (2.110) expresses hence a conservation law for the disturbance energy E_2 as stated in Eq. (2.108), with W_2 the flux of disturbance energy across the domain boundaries and D_2 the source term.

Using the relations $H_1 = h_1 + \mathbf{u_0} \cdot \mathbf{u_1}$ and Eq. (2.103), one may further rewrite W_2 in the form:

$$W_2 = \mathbf{m_1}\left(\frac{p_1}{\rho_0} + \mathbf{u_0 u_1}\right) + \mathbf{m_0} T_1 s_1 \tag{2.111}$$

Furthermore, it can be shown that the vorticity terms in D_2 can be simplified as follows:

$$\rho_0 \mathbf{u_0} \cdot \zeta_2 + \mathbf{m_2} \cdot \zeta_0 = \rho_0 \mathbf{u_0} \cdot (\xi_1 \times \mathbf{u_1}) + \rho_1 \mathbf{u_1} \cdot (\xi_0 \times \mathbf{u_0})$$

where $\xi = \nabla \times \mathbf{u}$ denotes the vorticity, and $\zeta = \xi \times \mathbf{u}$. D_2 is then obtained as a function of first order terms as well and reads:

$$D_2 = -\mathbf{m_1} s_1 \cdot \nabla T_0 + \mathbf{m_0} s_1 \cdot \nabla T_1 + \rho_0 \mathbf{u_0} \cdot (\xi_1 \times \mathbf{u_1}) + \rho_1 \mathbf{u_1} \cdot (\xi_0 \times \mathbf{u_0}) + T_1 Q_1 \tag{2.112}$$

Thus, as a result of the derivation, an exact energy corollary involving only first order perturbation terms is obtained. Furthermore, it is straightforward to show that Eq. (2.110) corresponds to the acoustic energy balance of Eq. (2.76) as soon as mean flow velocity and entropy fluctuations are neglected.

Expressions for Energy, Flux & Source Terms as used in the 1D Analysis

The analysis in Chapter 6 is conducted for a 1D flow, which is described by the system of Equations (2.32) - (2.34) for constant values of cross section area $\mathcal{S}$. The expressions for E_2, W_2 and D_2 are therefore the 1D equivalents of the terms derived above. This means that the velocity vector $\mathbf{u}$ is replaced by its 1D equivalent u, and vorticity can be neglected. The source term Q is expressed as stated in the governing system of Equations, i.e.

$$Q = \frac{q}{T},$$

which yields for the product of first order perturbations:

$$T_1 Q_1 = T_1 \left(\frac{q}{T}\right)_1 = T_1 \left(\frac{q_1}{T_0} - \frac{q_1 T_1}{T_0^2}\right)$$

The energy corollary for a 1D flow, where viscous terms have been neglected, reads thus:

$$\frac{\partial E_2}{\partial t} + \frac{\partial W_2}{\partial x} = D_2 \tag{2.113}$$

with

$$E_2 = \frac{p_1^2}{2\rho_0 c_0^2} + \frac{\rho_0 u_1^2}{2} + \rho_1 u_0 u_1 + \frac{\rho_0 T_0 s_1^2}{2c_{p_0}} \tag{2.114}$$

$$W_2 = \frac{u_0}{\rho_0} p_1 \rho_1 + p_1 u_1 + u_0^2 \rho_1 u_1 + u_0 \rho_0 u_1^2 + \rho_0 u_0 T_1 s_1 \tag{2.115}$$

$$D_2 = -s_1 \rho_1 u_0 \cdot \nabla T_0 - s_1 \rho_0 u_1 \cdot \nabla T_0 + s_1 \rho_0 u_0 \cdot \nabla T_1 + T_1 \left(\frac{q_1}{T_0} - \frac{q_0 T_1}{T_0^2} \right) \tag{2.116}$$

Chapter 3

Numerical Solution of Large Eigenvalue Problems

This chapter presents some aspects of numerical linear algebra that are necessary to solve the eigenvalue problem arising from the discretized system of equations presented in Chapter 2. While the methods of spatial discretization are different for the 1D and 2D study and are therefore presented in the respective chapters, the solution of the resulting eigenvalue problem is in both cases based on the Arnoldi method [3]. For the 1D study, this method is available as part of the MATLAB^{TM}- environment. In the 2D solver, the Arnoldi-algorithm is directly accessed via the software library ARPACK [60].

This chapter addresses the solution of large eigenvalue problems the way it is implemented in the 2D solver. This comprises the use of the Arnoldi algorithm in shift-invert mode as well as the algorithm used for the matrix inversion.

3.1 Reducing the Size of the Eigenvalue Problem

As shown in Chapter 2, the description of thermoacoustic instabilities using the Linearized Euler Equations in the frequency domain can be expressed in the form of an eigenvalue problem. In discretized form, this problem reads

$$[\mathcal{A}][\mathcal{V}] = i\omega[\mathcal{V}], \tag{3.1}$$

with $[\mathcal{V}]$ the discrete eigenvector that contains the unknown values of $(\hat{\rho}, \hat{\mathbf{u}}, \hat{s})$ for each grid point and $[\mathcal{A}]$ the linear operator matrix as derived in section 2.2.1. It should be noted that in cases including an unsteady heat release rate, the operator matrix $[\mathcal{A}]$ depends on ω via the heat release model as introduced in section 2.2.1.

The size m of the discrete eigenvealue problem can easily be estimated as a function of the number of mesh points N: in the 1D case, the eigenvector contains values of three variables, ($\hat{\rho}$, $\hat{u}$, $\hat{s}$), at each node, compared to four variables in 2D cases ($\hat{\rho}$, $\hat{u}_x$, $\hat{u}_y$, $\hat{s}$). The overall size of the eigenvalue problem is therefore of about $m \approx 4N$ for a 2D mesh with N grid points. This implies that an accordingly large number of eigenvalues and -vectors exists. However, only very few of these solutions are of interest, namely those that represent the low frequency resonant modes of the configuration: these are the modes that are susceptible to be involved in combustion instability.

Based on this consideration, the objective is hence not to solve the full eigenvalue problem of size $m \approx 4N$, but to solve an appropriate problem of considerably smaller size n, that nevertheless allows to determine the eigenpairs of the original problem. This can be achieved by projecting the original m-dimensional problem into a suitable lower-dimensional subspace [113], and solve the resulting problem of lower dimension as an approximation of the original one. This technique is used in this study in the form of a projection on a so-called Krylov subspace, which refers to a subspace spanned by matrix-vector products of the first powers of a matrix A and a vector b [91]:

$$\mathcal{K}_n = \mathrm{span}\{b, Ab, A^2b, ..., A^{n-1}b\} \tag{3.2}$$

As can be deduced from the above definition, the dimension of the Krylov subspace is not fixed, but depends on n. If n denotes the steps of an iterative algorithm, the dimension of the subspace increases hence continously as more iterations of the process are carried out.
Methods that involve a projection on a Krylov subspace exist in various forms, depending on the characteristics of the problem to be solved. The most well known techniques for eigenvalue problems are the Lanczos algorithm, that is applicable if the matrix A is hermitian, and the Arnoldi algorithm, that can be used with non-hermitian matrices. Furthermore, Krylov subspace methods are also used to solve linear systems of the form $Ax = b$, as a part of the conjugate gradient or GMRES (Generalized Minimal Residuals) algorithms [113].

3.1.1 The Arnoldi Iteration

In the present study, solutions of the eigenvalue problem arising from the spatial discretization of Eq. (3.1) are determined using the Arnoldi algorithm. This method allows to project the operator matrix $[\mathcal{A}]$ into a Krylov subspace following the procedure stated in Table 3.1.
Starting from a random input vector b, the algorithm generates a Krylov subspace spanned by the vectors q, and simultaneously reduces the matrix A to a matrix H_n of upper Hessenberg

b = arbitrary vector
$q_1 = b/||b||_2$

for $n = 1, 2, 3, ...$
$v_n = Aq_n$

for $j = 1$ **to** n
$h_{jn} = q_j^* v_n$
$v_n = v_n - h_{jn} q_j$
end

$h_{n+1,n} = ||v_n||_2$
$q_{n+1} = v_n / h_{n+1,n}$
end

Table 3.1: Algorithm of the Arnoldi Iteration (cf. [113]). * denotes the conjugate transpose.

form and dimension $n \times n$ by generating the coefficients h_{ij}. The process can be stopped after any number of iterations n. If the number of iterations corresponds to the dimension of the matrix A, this latter will hence be transformed into a Hessenberg matrix of the same size; however, the objective is a partial reduction of A to a Hessenberg matrix of smaller dimension.

As can be seen in the algorithm stated in Table 3.1, the matrix A appears only in the form of a matrix-vector product. This is a very useful feature, since in the study presented here the matrix A corresponds to the linear operator $A = [\mathcal{A}]$ introduced in section 2.2.1. In the present case, the matrix $A = [\mathcal{A}]$ is hence not known explicitly, but rather defined as part of a matrix-vector product. Thus, the algorithm corresponds conveniently to the way the problem is defined.
Each iteration of the process adds another vector q_n to the basis of orthonormal vectors. These vectors are related to each other via the coefficients h_{ij} and the matrix A as follows:

$$\begin{aligned} Aq_1 &= h_{11}q_1 + h_{21}q_2 \\ Aq_2 &= h_{12}q_1 + h_{22}q_2 + h_{32}q_3 \\ Aq_n &= h_{1n}q_1 + h_{2n}q_2 + h_{3n}q_3 + ... + h_{nn}q_n + h_{n+1,n}q_{n+1} \end{aligned} \tag{3.3}$$

After n iterations, the algorithm has generated $n + 1$ vectors q, that can be gathered in a matrix $Q_{n+1} = (q_1; ...; q_{n+1})$, and the coefficients of a non-square Hessenberg matrix $\tilde{H}_n$ of dimension $(n + 1) \times n$. Thus, the following notation holds for the relations of Eqs. (3.3):

$$AQ_n = Q_{n+1}\tilde{H}_n \tag{3.4}$$

where Q_n is a matrix of size $m \times n$ whose columns contain the vectors $(q_1; ...; q_n)$. A square Hessenberg matrix noted H_n can be obtained by removing the last line of $\tilde{H}_n$, which corresponds to the matrix operation [113]

$$H_n = Q_n^* Q_{n+1}\tilde{H}_n \tag{3.5}$$

where Q_n^* is the conjugate transpose of Q_n. Inserting Eq. (3.4) into Eq. (3.5) yields

$$H_n = Q_n^* A Q_n \tag{3.6}$$

i.e. the square matrix H_n contains an orthogonal projection of the matrix A on the Krylov subspace spanned by the vectors q that constitute the matrix Q_n. The relation of Eq. (3.4) can then be reformulated in terms of the quadratic Hessenberg matrix H_n :

$$AQ_n = Q_n H_n + h_{n+1,n} q_{n+1} e_n^T \tag{3.7}$$

where the last term on the right hand side describes the residual, which is expressed in terms of a matrix of rank one (see Fig. 3.1), e_n^T being a unitary vector.

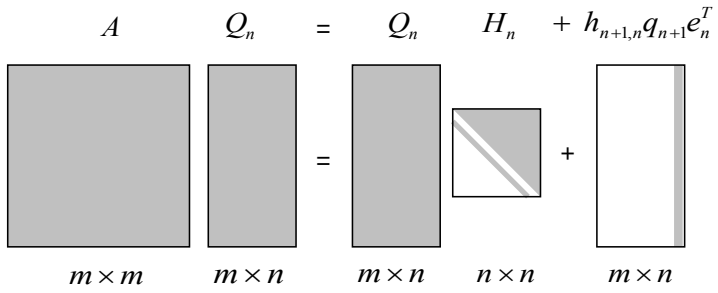

Figure 3.1: Reduction of matrix A to Hessenberg form

The asset of this transformation of A to H_n is the following: it has been observed that *some* of the eigenvalues of the Hessenberg matrix H_n, which are referred to as *Ritz values*, are very accurate approximations of the eigenvalues of the initial matrix A. This means that the time- and memory-demanding task of computing the eigenpairs of the large matrix A can be avoided and replaced by the computation of the eigenpairs of the much smaller matrix H_n. The eigenvalues and -vectors of this small matrix can be computed by direct methods such as the QR algorithm [113]. In order to detect the eigenvalues of interest, the search can be directed towards the desired area in the frequency spectrum, an aspect that will be covered lateron. The accuracy of the approximations improves with an increasing number of iterations n: in the case where $n = m$, all eigenvalues of H correspond to eigenvalues of A.
However, as usually the matrix A is not completely reduced to Hessenberg form, it is necessary to determine which of the Ritz values are good approximates of the eigenvalues of A, and how good an approximate they are. Such an assessment can be achieved via the following considerations [91]: The value λ_i^n denotes the i-th eigenvector of the $n \times n$- Hessenberg matrix H_n, with y_i^n the associated eigenvector of length n, such that $H_n y_i^n = \lambda_i^n y_i^n$. The Ritz vector u_i^n is a vector of length m that *approximates* an eigenvector of A. It is related to y_i^n via

$$u_i^n = Q_n y_i^n \tag{3.8}$$

One can then write

$$\begin{aligned} AQ_n y_i^n &= Q_n H_n y_i^n + h_{n+1,n} q_{n+1} e_n^T y_i^n \\ &= Q_n \lambda_i^n y_i^n + h_{n+1,n} q_{n+1} e_n^T y_i^n \end{aligned} \tag{3.9}$$

and thus

$$(A - \lambda_i^n \mathcal{I}) u_i^n = h_{n+1,n} e_n^T y_i^n q_{n+1} \tag{3.10}$$

where $\mathcal{I}$ is the unitary matrix. The pair (λ_i, u_i^n) is then a good approximation of an eigenpair of A, if the norm of the RHS term of Eq. (3.10) is smaller than a certain threshold value. Since $|q_{n+1}| = 1$ by construction, the estimation of this residual norm is rather simple, as it corresponds to the product of the last component of the vector y_i^n with $h_{n+1,n}$:

$$\left|\left|(A - \lambda_i^n \mathcal{I})u_i^n\right|\right|_2 = h_{n+1,n}\left|e_n^T y_i^n\right| \tag{3.11}$$

Based on such an error estimation, stopping criteria for eigenvalue solvers can then be derived [91, 113].

3.1.2 The Shift & Invert - Method

The eigenvalues that are found by the Arnoldi algorithm are those located at the extrema of the frequency spectrum, i.e. either the very large eigenfrequencies or those close to zero [113]. The eigenvalue problem considered here is expressed as

$$[\mathcal{A}][\mathcal{V}] = \lambda[\mathcal{V}] = i\omega[\mathcal{V}],$$

i.e. the eigenvalues are related to the eigenfrequency by

$$\lambda = i\omega = -\omega_i + i\omega_r.$$

In the considered case of acoustic eigenmodes in combustion chambers, the results of physical interest are the first resonant modes of the configuration, i.e. the results that are characterized by small positive values of ω_r. High values of ω_r correspond to higher order modes, which contain less energy and are therefore of less interest for this analysis. The Arnoldi algorithm should therefore be oriented towards the eigenvalues λ with smallest positive imaginary part, which corresponds to small positive real parts of ω (see schematic view in Fig. 3.3).
However, as a result of the formulation of the problem, a large number of purely mathematical solutions with eigenfrequencies very close to zero exist. The problem is related to the fact that the system of equations allows the presence of point-to-point instability as only first order derivatives are considered and the system is discretized by centered schemes. The eigenvectors associated to these solutions reveal their non-physical character, as the distributions of fluctuating quantities do not follow any mode shape, but are distributed randomly (with exception of the values imposed by boundary conditions). This difference between a physical and a non-physical solution can be observed in Fig. 3.2.

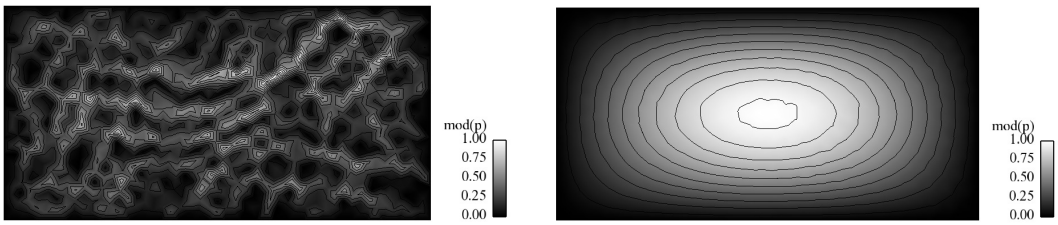

(a) Non-physical Mode. $f = 9.77 \cdot 10^{-14} - 6.01i$ Hz (b) Physical Mode. $f = 193.30 - 1.66 \cdot 10^{-3}i$ Hz

Figure 3.2: Module of $\hat{p}(x, y)$ for a non-physical and a physical solution obtained by the 2D LEE solver. Mean flow is uniform and at rest; the boundary condition $\hat{p} = 0$ is imposed on all boundaries.

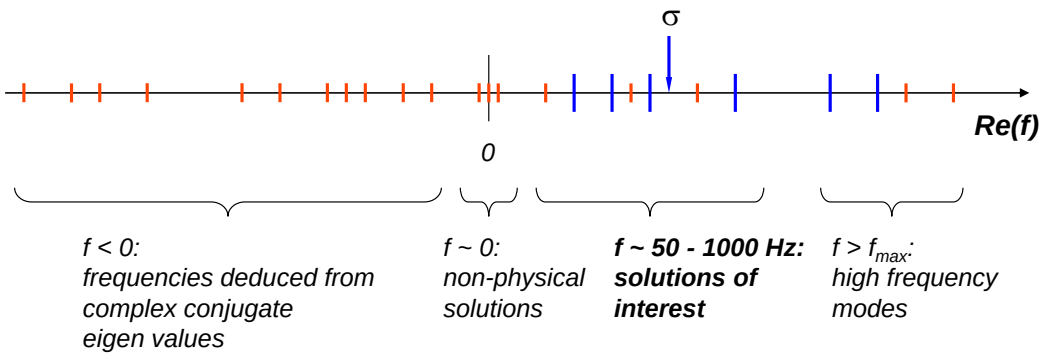

Figure 3.3: Schematic view of possible solutions for $f_r = \omega_r/(2\pi)$. Long markers: physical solutions. Short markers: non-physical solutions. σ denotes a user-defined shift (or target frequency).

A way to by-pass this kind of solution and achieve convergence of the algorithm towards the eigenvalues of physical interest is to apply the Arnoldi method to a shifted and inverted form of the original problem. This means that the original problem

$$[\mathcal{A}][\mathcal{V}] = i\omega[\mathcal{V}]$$

is rewritten as

$$[\mathcal{A} - i\sigma\mathcal{I}]^{-1}[\mathcal{V}] = i(\omega - \sigma)^{-1}[\mathcal{V}] = i\mu[\mathcal{V}] \tag{3.12}$$

where σ is a target value near the eigenvalue of interest, $\mathcal{I}$ a unitary matrix and μ the eigenvalue of the shifted and inverted problem.

The Arnoldi algorithm is then applied to the problem of Eq. (3.12), the search for eigenvalues being directed towards large values of μ. As μ is related to ω via

$$\omega = \sigma + 1/\mu,$$

this allows to obtain values for ω close to the indicated target value σ.

While making the search for eigenvalues more convenient, the use of the shift-and-invert-method introduces a supplementary step into the solution process: Instead of the eigenvalues of $[\mathcal{A}]$, the Arnoldi process has now to determine eigenvalues of $[\mathcal{A} - i\sigma\mathcal{I}]^{-1}$. This means that instead of generating the matrix-vector product $v_n = \mathcal{A}q_n$ (cf. Table 3.1), the algorithm requires an input vector of the form $v_n = [\mathcal{A} - i\sigma\mathcal{I}]^{-1}q_n$, or in other words, a vector v_n that is solution of the linear system of equations $[\mathcal{A} - i\sigma\mathcal{I}]v_n = q_n$.
Thus, in order to determine the vector v_n, a linear system of equations of size m has to be solved at each iteration n of the algorithm. The way this is done in the present study is described in the following section.

3.2 Solution of Linear Systems of Equations

As described in section 3.1.2, the shift-and-invert-method that is applied to the eigenvalue problem in the 2D LEE solver requires the solution of a linear system of equations in order to generate the input vector for the Arnoldi algorithm. The numerous algorithms that exist to solve linear systems of equations $Ax = b$ can be separated into two categories:

- Direct methods must carry out the complete inversion of the matrix A in order to obtain a solution. Furthermore, they require the matrix A to be explicitly available, i.e. in the case where A is an operator and defined as part of a matrix vector product, an explicit form of the matrix has to be generated first.

- By contrast, so-called iterative methods are based on matrix-vector products Aq in the same way as the Arnoldi algorithm. They can thus be applied when the matrix itself is not known explicitly, but the result of its product with any vector can be determined. Besides, iterative methods allow to obtain results of good accuracy after a limited number of iterations. This is especially advantageous when large matrices are involved and a complete inversion of the matrix is too demanding in terms of memory and processing time.

In the study presented here, where A is an operator matrix and hence not explicitly available and the problem is of large dimensions, the latter methods are doubtlessly better suited. However, their use is not as straightforward as that of a direct method: The convergence of the algorithm towards the solution depends on properties of the matrix A. In order to ensure fast convergence, the problem has to be posed in a suitable way, which means that it usually must be transformed in order to improve the properties of the problem's matrix. This is achieved by so called preconditioning, which denotes the transformation of the system $Ax = b$ by multiplication with a preconditioning matrix M on both sides into a system $MAx = Mb$. This leaves the solution of the system unchanged, but modifies the system in the way that the convergence does no longer depend on the properties of A, but on those of MA [113, 92]. However, as Y. Saad puts it [92], "Finding a good preconditioner [...] is often viewed as a combination of art and science."

Thus, for the sake of simplicity, the solver developed in the present study uses a direct method to find the input vector required by the Arnoldi algorithm at each iteration n to solve a shifted and inverted eigenvalue problem. The method chosen to solve the system of the type $Ax = b$ consists in performing an LU factorization of the matrix A and subsequently computing the solution vector x. An algorithm designed for the solution of sparse complex unsymmetric systems is implemented in the software package ME38 of the HSL software library [48].

3.2.1 LU Factorization

The linear system to be solved reads $[\mathcal{A} - i\sigma\mathcal{I}]v_n = q_n$ (cf. section 3.1.2). Firstly, in order to be able to apply an LU factorization, the matrix $[\mathcal{A} - i\sigma\mathcal{I}]$ has to be determined explicitely. This is achieved by applying the operator matrix $[\mathcal{A}]$ as derived in section 2.2.1 to m orthogonal unitary input vectors, and substracting $i\sigma\mathcal{I}$ from the result.
The LU factorization of the resulting matrix consists then in its decomposition into a lower

and an upper triangular matrix, L and U with elements l_{ij} and u_{ij}, respectively, of the form $A = LU$. This is achieved using the algorithm stated in Table 3.2 [113]:

```
U = A, L = I

for k = 1 to m − 1
    for j = k + 1 to m
        l_jk = u_jk / u_kk
        for n = k to m
            u_jn = u_jn − l_jk u_kn
        end
    end
end
```

Table 3.2: Algorithm of the LU Factorization (cf. [113])

As initial condition, the matrices U and L are filled with the system matrix $A = [\mathcal{A} - i\sigma\mathcal{I}]$ and a unitary matrix $\mathcal{I}$, respectively. The following steps eliminate the values of U below the diagonal, while at the same time L is filled with elements below the diagonal.
The factorization $[\mathcal{A} - i\sigma\mathcal{I}] = LU$ being completed, the solution vector v_n of the system $[\mathcal{A} - i\sigma\mathcal{I}]v_n = q_n$ is computed in two steps. Denoted forward and back substitution, they consist in rewriting the system in terms of the vector $y = Uv_n$ and solving two triangular systems, the first for the vector y and the second for v_n:

$$\begin{aligned} LUv_n &= q_n & & \\ Ly &= q_n & \text{forward substitution} & \\ Uv_n &= y & \text{back substitution} & \end{aligned} \tag{3.13}$$

While being rather straightforward to use, this method of solving a linear system has several drawbacks in terms of computation time and use of memory:
Solving a system of equations of size m by a direct method requires work of the order of $\mathcal{O}(m^3)$ flops [113]. Besides, additional work is necessary to generate an explicit form of the matrix $[\mathcal{A} - i\sigma\mathcal{I}]$. The time needed for this process is in a lot of cases the major part of the whole computation time. However, in the present study, the limiting aspect of this direct method is not the computation time, but the memory that is required to solve the linear system of equations: In order to invert a matrix of size $m \approx 20000$, the linear solver demands a workspace of about 2 GB. Even though processors that provide memory of this order are widely available, this high demand in memory is unnecessary and limits the computation to relatively small cases. A crucial step in the further development of the Linerized Euler Equation solver is therefore the implementation of an iterative method for the solution of the linear system of equations.

3.2.2 Generalized Minimal Residuals (GMRES)

GMRES is an iterative method for the solution of linear systems of equations. This algorithm is used in the context of the Helmholtz-solver AVSP developed at CERFACS [35, 103]. It is

therefore conceivable to apply this method to the LEE solver as well.

The GMRES algorithm is based on the generation of a basis of orthogonal vectors using the Arnoldi algorithm (cf. Table 3.1). The objective is then to approximate the solution of a linear problem $Ax = b$ at each iteration n by a vector x_n that minimizes the residual $r_n = Ax_n - b$. Using the notation introduced in section 3.1.1, this minimisation problem can be expressed in terms of the orthogonal basis Q_n and the Hessenberg matrix H_n generated by the Arnoldi algorithm [113]:
Expressing the vector x_n to be found at the n-th iteration as

$$x_n = Q_n y,$$

the problem to be solved consists in finding a vector y such that

$$||Ax_n - b|| = ||AQ_n y - b|| = \text{minimum} \tag{3.14}$$

Using Eq. (3.4), the problem is further transformed into:

$$||Q_{n+1}\tilde{H}_n y - b|| = \text{minimum} \tag{3.15}$$

Finally, multiplication with Q^*_{n+1} on the left allows to write:

$$||\tilde{H}_n y - Q^*_{n+1} b|| = \text{minimum} \tag{3.16}$$

As the Arnoldi algorithm was initialized with $q_1 = b/||b||$, the relation $Q^*_{n+1}b = ||b||e_1$ with $e_1 = (1, 0, 0, ...)$ holds. Thus, the problem consists in finding a vector y that minimizes

$$||\tilde{H}_n y - ||b||e_1|| = ||r_n|| = \text{minimum} \tag{3.17}$$

The size of the problem is determined by the matrix $\tilde{H}_n$, which is of dimension $(n + 1) \times n$ at the n-th iteration of the Arnoldi algorithm.

Compared to direct methods, iterative methods require considerably less work to solve a system of size m, typically of the order of $\mathcal{O}(m)$ to $\mathcal{O}(m^2)$ flops [113]. More importantly for the case studied here, however, they also drastically reduce the size of the system that is considered, and thereby the memory necessary to store intermediate results.

Chapter 4

Quasi-1D Study: Method and Results

In a first step, the calculation of eigenmodes as described in chapters 2 and 3 was carried out for 1D and quasi-1D configurations. Results have been published in [76, 119].
To this end, the Linearized Euler Equations (Eqs. 2.64-2.66) are rewritten in a quasi-1D formulation. The study is hence restricted to purely longitudinal modes, excluding modes with a two- or three-dimensional spatial structure. This assumption of plane-wave configurations implies also that only frequencies below the cut-off frequency of the duct may be considered.

The following chapter shows the mathematical formulation of the quasi-1D problem, its numerical implementation and results obtained with this method. The presentation of the numerical method used to solve the system of equation focusses on the particularities of the 1D study, viz. the use of a central finite difference method and a staggered grid discretization.

Results are presented for three academic configurations. The first configuration to be considered consists in a tube with constant cross section connected to an isentropic nozzle. This setup, which does not contain any entropy perturbations, shows the effects of moving and accelerated mean flow on the acoustic field. As a second test case, a tube of constant cross section containing a 1D flame will be analysed. In addition to the acoustic waves, entropy fluctuations have to be considered in this case. Interaction of the acoustic field with the flame may be taken into account via an unsteady heat release term based on the description in section 2.1.6. Finally, a combination of these two configurations, i.e. a tube containing a 1D flame followed by a nozzle, will be presented. This third test case allows to capture the effect of convected hot spots and their interaction with the acoustic field, which may occur in regions of accelerated mean flow.

The LEE calculations show that the prediction of instabilities obtained from zero Mach number calculations may be misleading already for Mach numbers as low as $Ma_0^{in} = 0.05$. Besides, the form of the modes downstream of the flame changes considerably when the convection of entropy waves is taken into account.

4.1 Numerical Implementation in 1D

The test cases considered in this chapter are 1D or quasi-1D configurations of rather basic geometry. This means that a certain number of aspects, such as vorticity perturbations or 2D mean flow phenomena (shear layers, vortices, etc.) and their effect on the acoustic field are not taken into account.
However, the 1D formulation allows to take into account the production and convection of entropy perturbations (hot spots), as well as their interaction with the acoustic field in regions of non-uniform mean flow, i.e. the flame region and the nozzle.

The system of equations as derived in Chapter 2 is recalled and reads:

$$\left(\frac{\partial u_0}{\partial x} + u_0\frac{\partial}{\partial x} + \frac{u_0}{S}\frac{\partial S}{\partial x}\right)\hat{\rho} + \left(\frac{\partial \rho_0}{\partial x} + \rho_0\frac{\partial}{\partial x} + \frac{\rho_0}{S}\frac{\partial S}{\partial x}\right)\hat{u} = i\omega\hat{\rho} \tag{4.1}$$

$$\begin{aligned}&\left(\frac{1}{\rho_0}\frac{\partial c_0^2}{\partial x} + \frac{u_0}{\rho_0}\frac{\partial u_0}{\partial x} + \frac{c_0^2}{\rho_0}\frac{\partial}{\partial x}\right)\hat{\rho} + (\frac{\partial u_0}{\partial x} + u_0\frac{\partial}{\partial x})\hat{u}\\ &+ (\gamma-1)T_0\left(\frac{1}{p_0}\frac{\partial p_0}{\partial x} + \frac{\partial}{\partial x}\right)\hat{s} = i\omega\hat{u}\end{aligned} \tag{4.2}$$

$$\frac{\gamma r q_0}{\rho_0 p_0}\hat{\rho} + \frac{\partial s_0}{\partial x}\hat{u} + \left(u_0\frac{\partial}{\partial x} + (\gamma-1)\frac{q_0}{p_0}\right)\hat{s} - \frac{r}{p_0}\hat{q} = i\omega\hat{s} \tag{4.3}$$

The unsteady heat release term is described by an $n-\tau$-model as introduced in section 2.1.6. The expression for the unsteady heat release rate in the frequency domain as given by Eq. (2.67) reads in a 1D formulation:

$$\hat{q}(x) = \frac{q_\mathrm{t}}{U_\mathrm{bulk}} n_\mathrm{loc}(x) e^{i\omega\tau}\hat{u}_{x_\mathrm{ref}} \tag{4.4}$$

In the above expression, the local interaction index is defined as (cf. Eq. (2.57)):

$$\begin{aligned}&n_\mathrm{loc}(x) = \tfrac{n}{\delta_f}\,\tfrac{U_\mathrm{bulk}}{q_\mathrm{t}}\,\tfrac{\gamma}{\gamma-1}\,p_0 && \text{for} \quad x_f - \tfrac{\delta}{2} < x < x_f + \tfrac{\delta}{2};\\ &n_\mathrm{loc}(x) = 0 && \text{otherwise}\end{aligned} \tag{4.5}$$

with x_f the position of the flame and δ_f the length of the flame zone.

4.1.1 Discretization in 1D: Finite Difference Method

For the one-dimensional study, the system of partial differential equations described by Eqs. (4.1) - (4.3) is discretized using the finite difference method. A general way to obtain the expression of the approximation for the gradient is to develop $\Phi(x+\Delta x)$ in a Taylor series around x [45]:

$$\Phi(x+\Delta x) = \Phi(x) + \Delta x\Phi_x(x) + \frac{(\Delta x)^2}{2}\Phi_{xx}(x) + \frac{(\Delta x)^3}{6}\Phi_{xxx}(x) + ...$$

$$\frac{\Phi(x+\Delta x) - \Phi(x)}{\Delta x} = \Phi_x(x) + O(\Delta x) \tag{4.6}$$

This Taylor series development then allows to evaluate the truncation error $O(\Delta x^n)$, with $n \in \mathbf{N}$ being the order of the finite difference approximation. In the case of the forward

difference quotient of Eq. (4.6), this error is of the order of Δx, the approximation hence of first order.
Instead of using information about the quantity Φ at a position x and a downstream position $x + \Delta x$ as in the forward difference quotient, one may also use a backward formulation:

$$\Phi(x - \Delta x) = \Phi(x) - \Delta x \Phi_x(x) + \frac{(\Delta x)^2}{2}\Phi_{xx}(x) - \frac{(\Delta x)^3}{6}\Phi_{xxx}(x) + ...$$

$$\frac{\Phi(x) - \Phi(x - \Delta x)}{\Delta x} = \Phi_x(x) + O(\Delta x) \tag{4.7}$$

From a combination of the forward and backward formulation results the central finite difference formulation for the gradient:

$$\Phi(x + \Delta x) - \Phi(x - \Delta x) = 2\Delta x \Phi_x(x) + \frac{(\Delta x)^3}{3}\Phi_{xxx}(x) + ...$$

$$\frac{\Phi(x + \Delta x) - \Phi(x - \Delta x)}{2\Delta x} = \Phi_x(x) + O(\Delta x)^2 \tag{4.8}$$

As indicated by Eq. (4.8), the central finite difference approximation is of higher accuracy, the truncation error being of second order in Δx.

The scheme used to discretize a system of equations should correspond to its physical properties [45]: isotropic phenomena should be discretized by a centered scheme, i.e. a scheme that does not have a preferential direction. For the discretization of the quasi-1D linearized Euler equations stated in Eqs. (4.1) - (4.3), two different schemes are used in the present study: In order to account for the fact that acoustic waves travel upstream as well as downstream, gradients of fluctuating velocity and density are approximated with central finite differences. Entropy fluctuations only being convected downstream, an upwind finite difference scheme is used for this quantity.

4.1.2 Staggered Grid Method

As described above, the system of equations Eqs. (4.1) - (4.3) is discretized using a central finite difference scheme for the acoustic quantities. However, in the discretized form of the system, the individual equations are decoupled, in the sense that separate solutions for the odd and even grid points exist. This decoupling is then observerd in the solutions in the form of the point-to-point instability shown in Fig. 4.1: The solutions for the amplitude of the fluctuating quantities do not follow sine-functions as expected, but oscillate between two sinusoidal envelope curves - one being the solution for the odd, the other for the even grid points. The

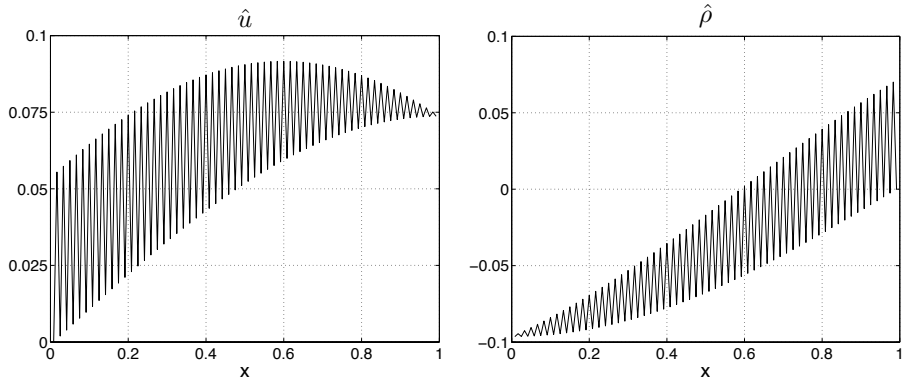

(a) $\left|\hat{u}(x)\right|$ (b) $\left|\hat{\rho}(x)\right|$

Figure 4.1: Point-to-point oscillation in the first eigenmode

reason of this behaviour can be understood by having a look on the set of equations that is being solved in one of the most simplified cases (see Fig. 4.2). This configuration consists in a tube filled with a uniform medium at rest. The boundary conditions for the acoustic field were chosen to $\hat{u} = 0$ at the inlet $x = 0$ and $\hat{\rho} = 0$ at the outlet $x = L$. Entropy fluctuations are not considered in this case.

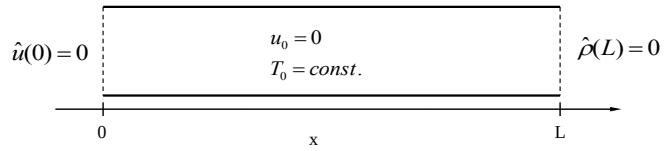

Figure 4.2: Simple Configuration in 1D

For this case, the system of equations (4.1) - (4.3) simplifies to the following two equations:

$$\rho_0 \frac{\partial \hat{u}}{\partial x} = i\omega\hat{\rho} \tag{4.9}$$

$$\frac{c_0^2}{\rho_0} \frac{\partial \hat{\rho}}{\partial x} = i\omega\hat{u} \tag{4.10}$$

These are the two equations that are commonly used to obtain the Helmholtz-equation. However, the method used for this study consists in solving the two equations as part of an eigenvalue problem.

The spatial discretization of the calculation domain is realised as a grid of equidistant points along the x-axis.
The 'standard' discretization method consists in defining the unknown quantities ($\hat{u}$ and $\hat{\rho}$) at the grid points. The use of a central finite difference expression for both unknowns leads to the situation shown in Fig. 4.3: via Eq. (4.9), the value of $\hat{\rho}$ at point i is linked to the gradient of $\hat{u}$ at this point. This gradient is expressed by a central finite difference approximation, i.e. as a function of $\hat{u}$ at points $i-1$ and $i+1$. The values of $\hat{u}$ at points $i-1$ and $i+1$, in turn, are related to the gradient of $\hat{\rho}$ at the respective locations via Eq. (4.10). These gradients of $\hat{\rho}$ are once again expressed by central finite difference quotients involving the values of $\hat{u}$ at the neighbouring points, and so on.
As a result, there is no link between neighbouring values of the unknown quantities $\hat{\rho}$ and $\hat{u}$, but only between the values at every second grid point. This is what allows the appearance of the two envelope curves in the solution (see Fig. 4.1), one being the result for even grid points, the other one for the odd grid points.

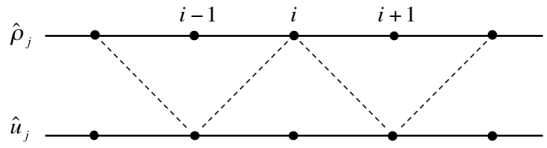

Figure 4.3: Node based discretization in 1D

There are several methods that allow to avoid this kind of oscillations, like using an upwind finite difference scheme, introducing an artificial viscosity term or using a staggered grid discretization. The latter technique has the advantage of not introducing any numerical viscosity, which is why it has been used in the present study.
In a 1D framework, the implementation of a staggered grid method is rather simple: instead of defining both $\hat{\rho}$ and $\hat{u}$ at the grid points, one of the quantities (here: $\hat{u}$) is defined in between two points. The values of $\hat{u}$ at the grid points not being directly part of the problem any more, they have to be interpolated using the values at the 'cell centers' when needed.

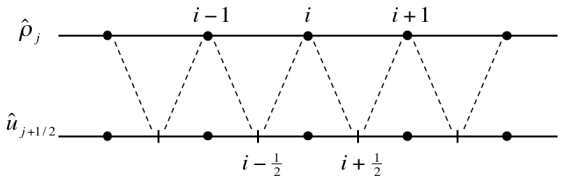

Figure 4.4: Staggered Grid in 1D

Using the staggered grid method, the discretization of Eqs.(4.9) and (4.10) using central finite differences for both $\hat{\rho}$ and $\hat{u}$ leads to the configuration shown in Fig. 4.4. As neighbouring values of the unknown quantities are linked now, the formation of the point-to-point oscillations is prevented and smooth sine-functions are obtained for the distributions of $\hat{\rho}(x)$ and $\hat{u}(x)$.

4.2 Results of the 1D Study

The following sections present the results that were obtained for several academic configuration using the method described above.
Numerical errors due to insufficient grid resolution may be excluded, as grid convergence has been obtained for all calculations. The computational grids used to discretize the domain consist of around 1000 to 5000 points, depending on the configurations. As the grid nodes are supposed to be equidistant, local mesh refinement (for example in the flame zone in configuration II) is not possible. In such cases, the mesh has to be refined globally.
As only longitudinal modes are considered in the following section, the height of the ducts being considered in the different configurations is not specified.

4.2.1 Configuration I: Nozzle Flow

The first configuration to be analysed consists in a tube of length L_c with constant cross section, which is connected to an isentropic nozzle of length $L - L_c$ (cf. Fig. 4.5). The nozzle may be unchoked or choked and therefore of convergent or convergent-divergent shape, respectively.

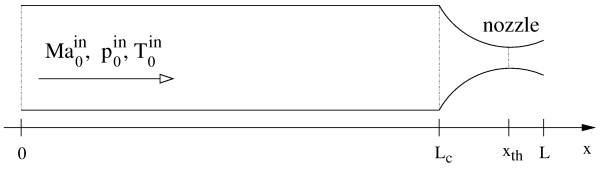

Figure 4.5: Configuration I

The mean flow in the chamber is uniform and characterised by its static pressure p_0^{in}, static temperature T_0^{in} and the mean flow Mach number M_0^{in}. The main geometric and mean flow parameters used for the following calculations are gathered in Table 4.1.

L(m)	L_c (m)	p_0 (Pa)	T_0 (K)	γ	r (J/kgK)
1.0	0.9	101325	300	1.4	287

Table 4.1: Parameters used for the calculations

The mean flow field inside the nozzle is described by an analytical distribution of the mean flow Mach number of the form:

$$M_0(x) = M_0^{in} + (M_0^{out} - M_0^{in}) \left(\frac{x - L_c}{L - L_c} \right)^3 \tag{4.11}$$

In this equation, M_0^{in} is the mean flow Mach number at the nozzle inlet, i.e. the Mach number of the chamber flow; and M_0^{out} is the Mach number that is imposed at position $x = L$. When an outlet Mach number greater than 1 is imposed, the nozzle flow is choked with the throat being located at x_{th}. All other flow quantities are deduced using the classical isentropic nozzle flow equations.

The boundary conditions for the acoustic field have to be defined in a way that all waves entering the domain are specified.
In the case of a subsonic configuration with a non zero mean flow velocity, the computational domain contains two downstream travelling waves, i.e an acoustic wave and a convected entropy wave, and one upstream travelling acoustic wave. It is therefore necessary to specify two boundary conditions for the downstream travelling waves at the inlet boundary, and one boundary condition for the upstream travelling wave at the outlet boundary.
However, if the nozzle is choked and the flow therefore supersonic at the outlet section, it is not necessary or meaningful to define an outlet boundary condition, as downstream of the throat no upstream travelling acoustic wave exists. In this case, the boundary condition for the resonant acoustic field is set by the flow conditions at the nozzle throat.

In the configuration to be considered, the boundary conditions at the inlet $x = 0$ were set to $\hat{u}(0) = 0$ and $\hat{s}(0) = 0$. As the mean flow is isentropic throughout the domain, Eq. (4.3) reduces to

$$u_0 \frac{\partial \hat{s}}{\partial x} = i\omega \hat{s}$$

leading to the result that $\hat{s}(x) = 0$ for the whole domain. The system of equations to solve is therefore reduced to Eqs. (4.1) and (4.2), describing a purely acoustic configuration.
For the case of a subsonic nozzle, the boundary condition at the outlet $x = L$ is set to $\hat{p}(L) = 0$.

4.2.1.1 Reference Method: Helmholtz Solver

In order to validate the results obtained by solving the eigenvalue problem of Eqs. (4.1) and (4.2) and to asses the effect of taking into account the mean flow Mach number, the configuration of Fig. 4.5 has been analysed with a second method.
This method consists in solving the eigenvalue problem resulting from the Helmholtz equation, i.e. an equation assuming the mean flow to be at rest. This equation is solved for the part of the domain where this zero Mach number assumption is reasonable, which is the case in the part upstream of the nozzle ($0 \leq x \leq L_c$). The influence of the nozzle on the acoustic field is represented by a complex impedance, that is imposed as outlet boundary condition at $x = L_c$.
The problem to be solved reads hence:

$$\begin{array}{ll} \nabla \cdot (c_0^2 \nabla \hat{p}) + \omega^2 \hat{p} = 0 & \text{inside the domain;} \\ \nabla \hat{p} = 0 & \text{on the boundary } x = 0 \\ Z = i\omega \hat{p} / (c_0 \nabla \hat{p}) & \text{on the boundary } x = L_c \end{array} \tag{4.12}$$

The set of equations Eq. (4.12) is solved by the CERFACS-developed code AVSP, which uses a central finite volume discretization on unstructured triangular grids [74]. The impedance Z describing the nozzle downstream of the domain outlet is determined numerically, using the technique described in the following.

Numerical Calculation of the Nozzle Impedance:

The tool "NOZZLE" developed at CERFACS [57] computes the impedance at the inlet of non-compact isentropic nozzles, requiring information about the mean flow conditions, the

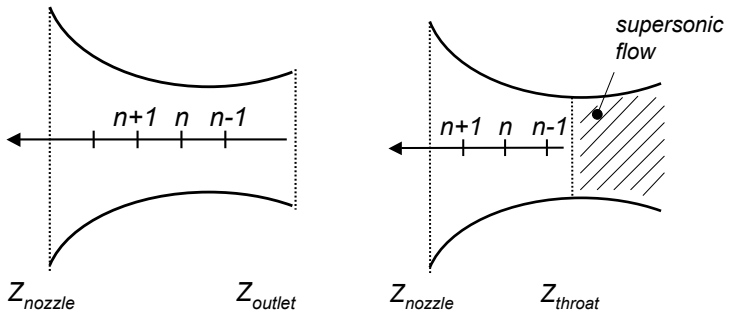

(a) subsonic nozzle (b) choked nozzle

Figure 4.6: Computation of the impedance at the nozzle inlet as function of the impedance at its outlet (subsonic case) or its throat (supersonic case).

form of the nozzle and an acoustic outlet condition (see Fig. 4.6).
The code solves the linearized Euler equations for purely acoustic configurations, i.e. the set of equations Eqs. (4.1) and (4.2). Eq. (4.3) is not relevant, as the mean flow is assumed to be isentropic, and the convection of entropy waves is not taken into account.
However, unlike the LEE solver described so far, the code NOZZLE does not solve these equations in the form of an eigenvalue problem, but rather as a linear system of equations:

$$[A] \begin{bmatrix} \hat{p} \\ \hat{u} \end{bmatrix} - i\omega \begin{bmatrix} \hat{p} \\ \hat{u} \end{bmatrix} = 0$$

The equations are discretized using an upwind finite difference scheme, in a way that the fluctuations at each grid point n are expressed in terms of their *downstream* neighbouring value (see Fig. 4.6), in the form

$$[D_n] \begin{bmatrix} \hat{u}_n \\ \hat{p}_n \end{bmatrix} = \begin{bmatrix} f_u(\hat{u}_{n-1}) \\ f_p(\hat{p}_{n-1}) \end{bmatrix}$$

with $[D_n]$ a 2×2-matrix and f_u, f_p expressions that result from discretizing Eqs. (4.1) and (4.2) (see detailed description in [59]).
In order to solve the systems of equations, a value for the (real valued) frequency ω and an outlet boundary condition have to be set. Starting with the point $n = 1$ at the domain outlet, the code determines then the impedance $Z = \hat{p}/(\rho_0 c_0 \hat{u})$ at the domain inlet.

The outlet boundary conditions used by the code NOZZLE correspond to those that are used by the LEE solver that is to be validated: For subsonic nozzles, the outlet boundary condition is set to $\hat{p} = 0$ in both codes. In the case where the nozzle is choked, the tool described here uses the impedance at the troat Z_{th} as outlet boundary condition:

$$Z_{th} = \frac{2\frac{du_0}{dx} - i\omega}{(\gamma - 1)\frac{du_0}{dx} - i\omega} \tag{4.13}$$

The impedance at the nozzle inlet determined by the code NOZZLE depends on the eigenfrequency ω. Therefore, a frequency sweep is carried out and the impedance Z is determined for all values of ω in the interval of interest. This concerns frequencies in a range from $f = 0$Hz to $f = 1500$Hz in steps of $\Delta f \approx 0.3$ Hz.

4.2.1.2 Case with Unchoked Nozzle

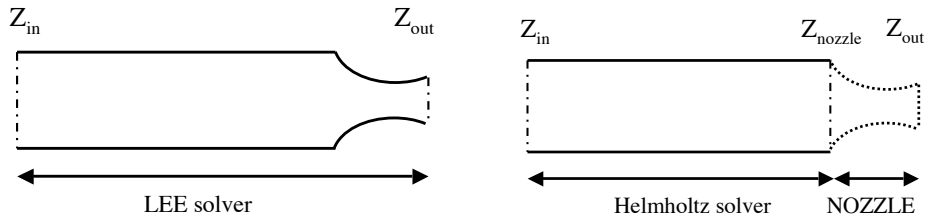

(a) LEE solver: Computational domain includes nozzle

(b) Helmholtz solver: Nozzle is replaced by a boundary condition that reflects its impedance.

Figure 4.7: Computational domain of LEE and Helmholtz solver.

In a first time, results for the case of an unchoked nozzle are presented. The Mach number at the outlet is set to $M_0^{out} = 0.9$, whereas for the Mach number at the inlet several values are considered, i.e. $M_0^{in} = 0.01;\ 0.1;\ 0.2;\ 0.3;\ 0.4$. The results for the complex eigenfrequencies obtained for the first mode using the Linearized Euler Equations and the Helmholtz-Equation respectively are gathered in Table 4.2.
The relative error between the results is defined with reference to the arithmetic mean of the two values

$$\epsilon = \frac{2(\phi_{LEE} - \phi_{Helmholtz})}{\phi_{LEE} + \phi_{Helmholtz}}$$

and noted ϵ_{Re} and ϵ_{Im} for the real and imaginary part respectively.

The difference in real frequency between the computations based on the Linearized Euler Equations and the Helmholtz equations being due to the fact that the latter neglects the mean flow velocity, it can be assessed by the following consideration: The first eigenmode of the configuration is composed of a downstream and an upstream travelling wave. When the mean flow is at rest, both waves traverse the combustion chamber of length L_c at the speed of sound c_0, leading to equal transit times in the downstream and upstream direction of $t^+ = t^- = L_c/c_0$. The frequency of oscillation of this first mode can then be found to

$$f_0 = \frac{1}{T} = \frac{1}{t^+ + t^-} = \frac{c_0}{2L_c} = \frac{c_0}{\lambda}$$

The same reasoning applied to a meanflow at mean velocity u_0 leads to different propagation times for the downstream and upstream travelling waves:

$$t^+ = \frac{L_c}{c_0 + u_0} = \frac{L_c}{c_0(1 + M_0)} \qquad \text{and} \qquad t^- = \frac{L_c}{c_0 - u_0} = \frac{L_c}{c_0(1 - M_0)}$$

This leads to an estimate for the resonance frequency of

$$f \approx \frac{1}{t^+ + t^-} = \frac{c_0(1 - M_0^2)}{2L_c}$$

M_0^{in}	f (Hz) LEE	f (Hz) Helmholtz	ϵ_{Re} (%)	ϵ_{Im} (%)	$\epsilon_{Re,\,theor.}$ (%)
0.01	$187.39 - 0.29i$	$187.39 - 0.29i$	0.0	0.0	0.0
0.10	$180.65 - 2.80i$	$182.33 - 2.88i$	0.9	2.8	1.0
0.20	$173.62 - 5.41i$	$180.30 - 5.80i$	3.8	6.9	4.1
0.30	$163.92 - 7.90i$	$178.83 - 9.00i$	8.7	13.0	9.4
0.40	$151.15 - 10.30i$	$177.51 - 12.84i$	16.0	22.0	17.4

Table 4.2: Frequency of first eigenmode for subsonic nozzle.

The relative error between these two frequencies can then be expressed as function of the mean flow Mach number M_0:

$$\epsilon_{Re,theor.} = \frac{2(f_0 - f)}{f_0 + f} = \frac{2M_0^2}{(2 - M_0^2)} \tag{4.14}$$

The error in real frequency estimated this way is noted in the last column of Table 4.2.

At very low Mach number, the frequencies computed by the Linearized Euler Equation solver and by the Helmholtz solver are, as expected, the same. For growing Mach numbers in the part upstream of the nozzle, both methods predict a decrease in real and imaginary frequency. However, as the assumption of a mean flow at rest is not fulfilled anymore, the differences between the Helmholtz solver and the LEE solver become considerable. The error in real frequency is very well estimated using the term $\epsilon_{Re,\,theor.}$, which predicts closely the difference observed between the two computations.
As no sources of acoustic energy are present in the domain, the eigenmodes of this configuration are marginally stable when the mean flow is at rest (i.e. $\omega_i = 0$), or damped when the the mean flow Mach number is not zero (i.e. $\omega_i < 0$). This increasing damping rate can be explained by losses at the boundaries. The acoustic flux across the domains boundaries can be expressed as [13]

$$F = (\hat{u} + \frac{u_0}{\rho_0 c_0^2}\hat{p})(\hat{p} + \rho_0 u_0 \hat{u}) \tag{4.15}$$

As in the presented case, the boundary conditions read $\hat{u} = 0$ and $\hat{p} = 0$ at inlet and outlet respectively, the flux of acoustic energy across the boundaries is zero when $u_0 = 0$. For increasing values of u_0, the losses at the boundaries increase, leading to higher damping rates.

The spatial shape of this first eigenmode is shown in Fig. 4.8 for low and high inlet Mach number. Module and phase of the pressure fluctuations computed by the LEE solver are compared to those predicted by the Helmholtz solver. This latter, of course, does not allow to describe the structure of the mode inside the nozzle, i.e. results are limited to $x \leq L_c$.
As expected, the results of the two codes agree very well for the case where the Mach number inside the domain is negligible (Fig. 4.8 (a) and (b)). At $M_0^{in} = 0.4$, the distribution of $|\hat{p}(x)|$ computed by the Helmholtz solver still follows closely that computed by the LEE solver, considerable differences being only visible in the vicinity of the nozzle inlet. However, the Helmholtz solver fails to capture the linear decrease in phase that is predicted by the LEE solver.

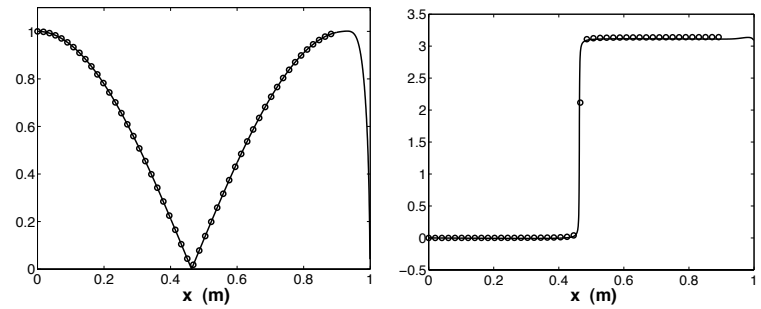

(a) $|\hat{p}|(x)$ at $M_0^{in} = 0.01$ (b) $\arg(\hat{p}(x))$ at $M_0^{in} = 0.01$

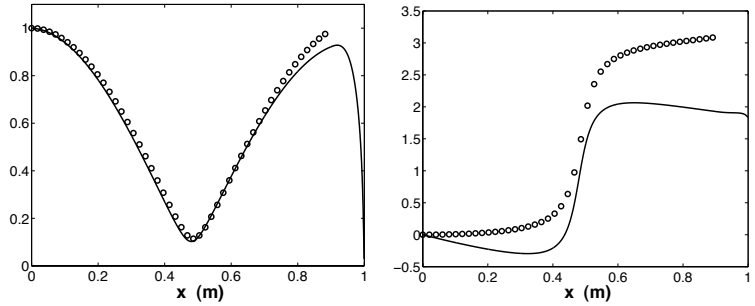

(c) $|\hat{p}(x)|$ at $M_0^{in} = 0.4$ (d) $\arg(\hat{p}(x))$ at $M_0^{in} = 0.4$

Figure 4.8: Structure of the first eigenmode for the configuration with subsonic nozzle. —— : LEE solver ○ : Helmholtz solver

4.2.1.3 Case with Choked Nozzle

M_0^{in}	f (Hz) LEE	f (Hz) Helmholtz	ϵ_{Re} (%)	ϵ_{Im} (%)	$\epsilon_{Re,\,theor.}$ (%)
0.01	$187.69 - 0.14i$	$187.70 - 0.15i$	0.0	6.7	0.0
0.10	$180.77 - 1.35i$	$182.51 - 1.44i$	1.0	6.5	1.0
0.20	$173.30 - 2.54i$	$180.08 - 2.85i$	3.8	11.5	4.1
0.30	$163.10 - 3.55i$	$177.98 - 4.31i$	8.7	19.3	9.4
0.40	$149.77 - 4.31i$	$175.88 - 5.74i$	16.0	28.5	17.4

Table 4.3: Frequency of first eigenmode for choked nozzle configuration.

Subsequently to the subsonic nozzle case, the configuration of described in section 4.2.1 is analyzed for a case where the nozzle is choked. The outlet Mach number is now set to $M_0^{out} = 1.1$, while the values for the inlet Mach number remain at $M_0^{in} = 0.01;\ 0.1;\ 0.2;\ 0.3;\ 0.4$. The results obtained with the LEE solver and the method based on Helmholtz calculations as described in section 4.2.1.1 together with the relative errors of Eqs. (4.2.1.2) and (4.14) are gathered in Table 4.3.

As mentioned before, the Linearized Euler Equation solver takes into account the whole domain, including the supersonic part downstream of the nozzle. This means that no boundary condition needs to be set at the domain outlet, as the acoustically resonant domain is restricted by the nozzle throat. In order to verify if this boundary condition is correctly captured by the

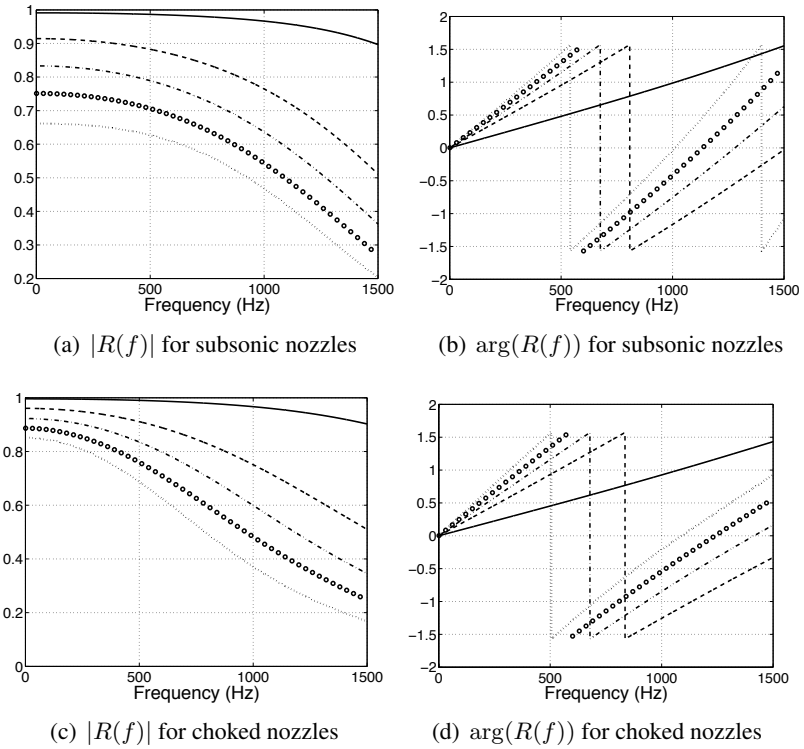

(a) $|R(f)|$ for subsonic nozzles (b) $\arg(R(f))$ for subsonic nozzles

(c) $|R(f)|$ for choked nozzles (d) $\arg(R(f))$ for choked nozzles

Figure 4.9: Reflection Coefficient computed by the tool "Nozzle" corresponding to the impedance boundary condition imposed at $x = L_c$ for the Helmholtz computations.
——: $M_0^{in} = 0.01$ – – –: $M_0^{in} = 0.1$ —·—: $M_0^{in} = 0.2$ ∘: $M_0^{in} = 0.3$ ·····: $M_0^{in} = 0.4$

code, calculations have been carried out with the domain being extended beyond $x = L$. As expected, this modification in the supersonic part of the domain did not have an impact on the resonant frequencies, confirming that the position and impact of the sonic nozzle throat is well represented.

The results gathered in Table 4.3 confirm those presented for the case with a subsonic nozzle. For a mean flow virtually at rest the two methods predict again the same result. Besides, the evolution of the values ϵ_{Re} and ϵ_{Im} with increasing inlet Mach number is very similar to that of the unchoked nozzle computations. Again, the error in real frequency is well estimated by the term $\epsilon_{Re,\, theor.}$ of Eq. (4.14).

Compared to the results obtained for the configuration with subsonic nozzle, the first eigenmode is less damped when the nozzle is choked. This observation is confirmed by the reflection coefficient $R = (Z-1)/(Z+1)$ equivalent to the boundary impedance represented by the nozzles. (The values of Z have been determined using the tool "Nozzle" described in section 4.2.1.1). Module and argument of the reflection coefficient are illustrated in Fig. 4.9 for the different Mach numbers at the nozzle inlet that are used in the calculation, and for the subsonic as well as for the choked case. While the choked and unchoked nozzles tend to similar values for the reflection coefficient at high frequencies, their behaviour at low frequencies is quite different. At the frequency of the first eigenmode, i.e. at $f \approx 180$Hz, the reflection coefficient of the choked nozzles remains above $|R| = 0.8$ even for the highest inlet Mach number, while that of the unchoked nozzle drops to $|R| \approx 0.65$ for $M_0^{in} = 0.4$.

4.2.1.4 Comparison to Analytical Solutions

For the simple configuration considered here, a semi-analytical solution can be obtained for the part of the configuration upstream of the nozzle, while the nozzle itself can be expressed as an impedance.
As the mean flow in this part of the configuration is uniform and entropy perturbations are not considered, the equations describing the acoustic perturbations read

$$\hat{p}(x) = A^{+}exp(ik^{+}x) + A^{-}exp(-ik^{-}x) \tag{4.16}$$

and

$$\hat{u}(x) = \frac{1}{\rho_0 c_0}\left[A^{+}exp(ik^{+}x) - A^{-}exp(-ik^{-}x)\right] \tag{4.17}$$

with A^{+} and A^{-} the amplitudes and k^{+} and k^{-} the wavenumbers of the forward and backward travelling waves respectively.
The inlet boundary condition $\hat{u}(x=0)$ imposes $A^{+} = A^{-}$. The impedance imposed as outlet boundary condition at $x = L_c$ establishes a relation between pressure and velocity fluctuations of the form $Z = \hat{p}/(\rho_0 c_0 \hat{u})$, such that the following dispersion relation can be derived:

$$exp(ik^{+}x) + exp(-ik^{-}x) = Z\left[exp(ik^{+}x) - exp(-ik^{-}x)\right] \tag{4.18}$$

The equivalent impedance of the nozzle is determined numerically using the method described in section 4.2.1.1. As mentioned there, the impedance is frequency-dependant, i.e. $Z = Z(\omega)$. This means that the dispersion relation Eqn. (4.18) has to be solved iteratively, adjusting the value of $Z(\omega)$ at every iteration.
Solving Eq. (4.18) with a numerically calculated impedance for non compact nozzles is equivalent to solving the Linearized Euler Equations equations for the complete domain. At the same time, the results of the Helmholtz calculations can be verified by solving the dispersion relation Eq. (4.18) while assuming the mean flow to be at rest, which means that $k^{+} = k^{-} = \omega/c_0$.

The results of this comparison are presented in Table 4.4. As expected, the eigenfrequencies computed by the Helmholtz solver, which were obtained using the numerically calculated impedance $Z(\omega)$, are the same as those obtained by solving Eq. (4.18).
Comparing the results of the LEE solver to those of Eq. (4.18), one finds good agreement for the values of real frequency. However, for the imaginary frequency the values predicted by the two methods differ by about $6-7\%$. This can be explained as follows: The computation of the equivalent impedance is based on an upwind finite difference scheme. However, this kind of numerical scheme is dissipative, and may induce damping behaviour. In contrast to that, the LEE solver uses a central finite difference scheme, and predicts thus slightly smaller damping rates.

Finally, one may solve Eq. (4.18) with an analytically calculated value for the impedance. Using the compact nozzle assumption, i.e. assuming the length of the nozzle to be small compared to the acoustic wavelength, the reflection coefficient of an isentropic nozzle can be expressed as function of the inlet Mach number of the nozzle [66]:

$$R = \frac{1 - \frac{1}{2}(\gamma - 1)M}{1 + \frac{1}{2}(\gamma - 1)M} \tag{4.19}$$

M_0^{in}	f (Hz) Helmholtz	f (Hz) Eq. (4.18) at $M = 0$	ϵ_{Re} (%)	ϵ_{Im} (%)
0.01	$187.70 - 0.15i$	$187.69 - 0.15i$	0.0	0.0
0.10	$182.51 - 1.44i$	$182.51 - 1.44i$	0.0	0.0
0.20	$180.08 - 2.85i$	$180.08 - 2.85i$	0.0	0.0
0.30	$177.98 - 4.31i$	$178.01 - 4.31i$	0.0	0.0
0.40	$175.88 - 5.74i$	$175.88 - 5.74i$	0.0	0.0
M_0^{in}	f (Hz) LEE	f (Hz) Eq. 4.18 at $M \neq 0$	ϵ_{Re} (%)	ϵ_{Im} (%)
0.01	$187.69 - 0.14i$	$187.68 - 0.15i$	0.0	6.7
0.10	$180.77 - 1.35i$	$180.79 - 1.42i$	0.0	5.1
0.20	$173.30 - 2.54i$	$173.33 - 2.71i$	0.0	6.5
0.30	$163.10 - 3.55i$	$163.10 - 3.83i$	0.0	7.6
0.40	$149.77 - 4.31i$	$149.84 - 4.64i$	0.0	7.4

Table 4.4: Comparison with semi-analytical solution, numerical impedance

M_0^{in}	R	Z	f (Hz) LEE	f (Hz) of Eq. (4.18) at $M \neq 0$	ϵ_{Re} (%)	ϵ_{Im} (%)
0.01	0.997	500.0	$187.69 - 0.14i$	$192.86 - 0.12i$	2.7	15.4
0.10	0.968	50.0	$180.77 - 1.35i$	$190.76 - 1.21i$	5.4	10.9
0.20	0.938	25.0	$173.30 - 2.54i$	$184.43 - 2.35i$	6.2	7.8
0.30	0.907	16.7	$163.10 - 3.55i$	$173.96 - 3.33i$	6.4	6.4
0.40	0.878	12.5	$149.77 - 4.31i$	$159.49 - 4.07i$	6.3	5.7

Table 4.5: Resonant frequencies obtained analytically using compact nozzle assumption

or in terms of impedance

$$Z = -\frac{R+1}{R-1} = \frac{2}{(\gamma-1)M} \tag{4.20}$$

The real valued reflection coefficient and impedance obtained from Eqs. (4.19) and (4.20) are noted in Table 4.5, together with the eigenfrequencies computed from Eq. (4.18) using this impedance. It should be noted that the reflection coefficients calculated using the compact nozzle assumption are the low frequency limit of the numerically determined curves plotted in Fig. 4.9 (c).

Comparing the results obtained by the LEE solver to those obtained analytically using the compact nozzle assumption, two aspects can be observed: As the latter calculations neglect the length of the nozzle, and thereby underpredict the overall length of the domain, they tend to overpredict the resonance frequency. At the same time, the mean flow in the chamber being taken into account, the trend towards lower real frequencies with increasing mean flow velocity is well captured.

4.2.2 Configuration II: 1D Flame

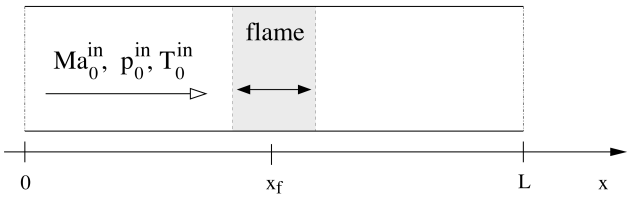

Figure 4.10: Configuration II

As second configuration, a tube of length L with constant cross section, which contains a 1D-flame of thickness δ_f at position x_f, is considered (see Fig. 4.10).
The mean flow field is imposed via an analytical distribution of static temperature of the form:

$$T_0(x) = \frac{T_0^{out} + T_0^{in}}{2} + \frac{T_0^{out} - T_0^{in}}{2} \tanh\left(3\frac{x - x_f}{\delta_f/2}\right) \tag{4.21}$$

The conservation laws for mass flux, momentum and total temperature provide the conditions

$$\rho_0 u_0 = \text{const.}$$

$$p_0 + \rho_0 u_0^2 = \text{const.}$$

and

$$q_0 = \rho_0 u_0 C_p dT_{t0}/dx.$$

The flow field is then entirely defined by the choice of inlet pressure p_0^{in}, temperature T_0^{in}, Mach number $\mathrm{M}_0^{\mathrm{in}}$ and a temperature step $T_0^{out} - T_0^{in}$. The mean flow parameters used for the computations are gathered in Table 4.6.

p_0^{in} (Pa)	T_0^{in} (K)	T_0^{out} (K)	γ	r (J/kgK)	L (m)	x_f/L
101325	300	1200	1.4	287	1	0.5

Table 4.6: Parameters used for the calculations

As for the configuration of section 4.2.1, two boundary conditions have to be set at the inlet, and one at the outlet, in order to provide information about the waves entering the domain.
The conditions at the domain inlet are set to $\hat{s} = 0$ and $\hat{u} = 0$, while at the domain outlet $\hat{p} = 0$ is imposed. Thus, as in the first configuration, no entropy fluctuations are entering the domain. However, in this second configuration, entropy fluctuations are created in the flame zone and then convected downstream.

The results of the calculations carried out with the LEE solver are validated using a semi-analytical model presented by Dowling [24], which solves the problem for the limit case $\delta_f \to 0$. This method is described in the following section.

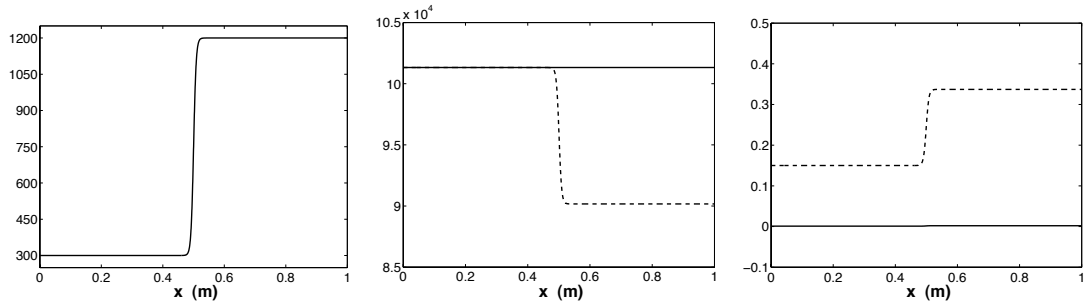

(a) Temperature in K (b) Pressure in Pa (c) Mach number

Figure 4.11: Mean flow field of Configuration II. —— : $M_0^{in} = 0.001$ - - - : $M_0^{in} = 0.15$

4.2.2.1 Validation via Semi-Analytical Solution

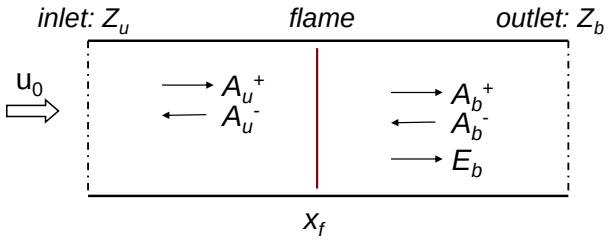

Figure 4.12: Description of the system as used in the reference model [24]: an infinitely thin flame sheet separates unburnt and burnt gas. Entropy waves are not present upstream of the flame.

For the limit case of a infinitely thin flame front, the problem can be solved semi-analytically (cf. [24]). The domain is split into two subdomains with uniform isentropic meanflow, which are seperated by the flame at position $x = x_f$. In the following, these two subdomains are noted with index *u* for the part upstream of the flame filled with unburnt gas and with index *b* for the part downstream of the flame filled with burnt gas (see Fig. 4.12).
The solution for density, velocity and entropy fluctuations can be determined by calculating the amplitudes of the waves that are present in the two subdomains, i.e. the amplitudes of right-going acoustic wave, left-going acoustic wave and entropy wave in the unburnt gas $\mathcal{A}_u^+$, $\mathcal{A}_u^-$ and $\mathcal{E}_u$ and in the burnt gas $\mathcal{A}_b^+$, $\mathcal{A}_b^-$ and $\mathcal{E}_b$.
The inlet boundary condition $\hat{s}(0) = 0$ imposes directly that $\mathcal{E}_u = 0$, as no entropy can be created upstream of the flame. The other amplitudes can then be calculated from the remaining two boundary conditions and three step conditions that need to be satisfied at the flame sheet. The boundary conditions at $x = 0$ and $x = L$ are expressed as impedances:

$$Z_u = \left.\frac{\hat{p}}{\rho_0 c_0 \hat{u}}\right|_{x=0} \tag{4.22}$$

$$Z_b = \left.\frac{\hat{p}}{\rho_0 c_0 \hat{u}}\right|_{x=L} \tag{4.23}$$

The jump conditions are derived from the conservation equations for mass, momentum and

energy and impose a relation between the conditions on both sides of the infinitely thin flame

$$\Big[\rho_0\hat{u} + u_0\hat{\rho}\Big]_{x=x_f,u} = \Big[\rho_0\hat{u} + u_0\hat{\rho}\Big]_{x=x_f,b} \tag{4.24}$$

$$\Big[\hat{p} + 2\rho_0 u_0\hat{u} + u_0^2\hat{\rho}\Big]_{x=x_f,u} = \Big[\hat{p} + 2\rho_0 u_0\hat{u} + u_0^2\hat{\rho}\Big]_{x=x_f,b} \tag{4.25}$$

$$\begin{aligned}&\Big[(C_pT_0 + \frac{1}{2}u_0^2)(\rho_0\hat{u} + u_0\hat{\rho}) + \rho_0 u_0(C_p\hat{T} + u_0\hat{u})\Big]_{x=x_f,u}\\ &= \Big[(C_pT_0 + \frac{1}{2}u_0^2)(\rho_0\hat{u} + u_0\hat{\rho}) + \rho_0 u_0(C_p\hat{T} + u_0\hat{u})\Big]_{x=x_f,b} + \hat{Q}\end{aligned} \tag{4.26}$$

The amplitudes of fluctuating pressure, velocity and density can then be expressed in terms of harmonic waves:

$$\hat{p}(x) = \mathcal{A}^+ e^{ik^+x} + \mathcal{A}^- e^{-ik^-x} \tag{4.27}$$

$$\hat{u}(x) = \frac{1}{\rho_0 u_0}\Big[\mathcal{A}^+ e^{ik^+x} - \mathcal{A}^- e^{-ik^-x}\Big] \tag{4.28}$$

$$\hat{s}(x) = \mathcal{E} e^{ik_s x} \tag{4.29}$$

where the wavenumbers associated to forward acoustic, backward acoustic and entropy waves are noted $k^+ = \frac{\omega}{c_0(1+M)}$, $k^- = \frac{\omega}{c_0(1-M)}$ and $k_s = \frac{\omega}{u_0}$ respectively.
The amplitudes of density and temperature fluctuations can be derived to (cf. Eqs. (2.39) and (2.43))

$$\hat{\rho} = \frac{\hat{p}}{c_0^2} - \frac{\rho_0\mathcal{E}}{C_p}e^{ik_s x}$$

$$\hat{T} = T_0\Big(\frac{\gamma-1}{\rho_0 c_0^2}\hat{p} + \frac{\mathcal{E}}{C_p}e^{ik_s x}\Big)$$

and the unsteady heat release rate reads

$$\hat{Q} = \frac{\gamma p_0}{\gamma - 1} n e^{j\omega\tau}\hat{u}\Big|_{x=x_f,u}$$

Introducing the above expressions for the fluctuating quantities into Eqs. (4.22) - (4.26), the equations may be rewritten in the form

$$\mathcal{X}\begin{bmatrix} \mathcal{A}_u^+ \\ \mathcal{A}_u^- \\ \mathcal{A}_b^+ \\ \mathcal{A}_b^- \\ \frac{\rho_b c_b^2}{C_p}\mathcal{E}_b e^{ik_s x_f} \end{bmatrix} = 0, \tag{4.30}$$

with $\mathcal{X}$ a 5×5 matrix :

$$\mathcal{X} = \begin{bmatrix} (1+M_u)e^{ik_u^+ x_f} & (M_u-1)e^{-ik_u^- x_f} & -(1+M_b)\frac{c_u}{c_b}e^{ik_b^+ x_f} & -(M_b-1)\frac{c_u}{c_b}e^{-ik_b^- x_f} & M_b\frac{c_u}{c_b} \\ (1+M_u)^2 e^{ik_u^+ x_f} & (M_u-1)^2 e^{-ik_u^- x_f} & -(1+M_b)^2 e^{ik_b^+ x_f} & -(M_b-1)^2 e^{-ik_b^- x_f} & M_b^2 \\ \mathcal{X}_{3,1} & \mathcal{X}_{3,2} & \mathcal{X}_{3,3} & \mathcal{X}_{3,4} & M_b^3/2 \\ 1-Z_u & 1+Z_u & 0 & 0 & 0 \\ 0 & 0 & (1-Z_b)e^{ik_b^+ L} & (1+Z_b)e^{-ik_b^- L} & 0 \end{bmatrix} \tag{4.31}$$

with

$$\begin{aligned} \mathcal{X}_{3,1} &= \frac{c_u}{c_b}\left((1+M_u)\left[M_u + \tfrac{1}{\gamma-1} + M_u^2/2\right] + \tfrac{1}{\gamma-1}ne^{i\omega\tau}\right)e^{ik_u^+ x_f} \\ \mathcal{X}_{3,2} &= \frac{c_u}{c_b}\left((1-M_u)\left[M_u - \tfrac{1}{\gamma-1} - M_u^2/2\right] - \tfrac{1}{\gamma-1}ne^{i\omega\tau}\right)e^{-ik_u^- x_f} \\ \mathcal{X}_{3,3} &= -(1+M_b)\left[M_b + \tfrac{1}{\gamma-1} + M_b^2/2\right]e^{ik_b^+ x_f} \\ \mathcal{X}_{3,4} &= -(1-M_b)\left[M_b - \tfrac{1}{\gamma-1} - M_b^2/2\right]e^{-ik_b^- x_f} \end{aligned} \tag{4.32}$$

Equation (4.30) has a non trivial solution when the matrix $\mathcal{X}$ is singular. Hence, by requiring $\det\mathcal{X} = 0$, a dispersion relation can be obtained, whose complex roots are the semi-analytical solutions for ω.

4.2.2.2 Case without Unsteady Heat Release Rate: $\hat{q} = 0$

Firstly, the configuration is analyzed without an unsteady heat release rate. The flame does hence not interact directly with the acoustic field. However, entropy fluctuations are created in the flame zone and then convected downstream, which may have an impact on the form of the acoustic modes and the loss of disturbance energy at the domain outlet.

The calculations of configuration of Fig. 4.10 are carried out with the flow parameters and boundary conditions as summarized in section 4.2.2. In the LEE computations, the flame zone covers a length of $\delta_f = 0.05L$, $\delta_f = 0.10L$ or $\delta_f = 0.15L$, respectively (cf Eq. (4.21)). The results obtained by the LEE solver are compared to those of the semi-analytical model presented in section 4.2.2.1, which solves the problem for the limit case of an infinitely thin flame.

In addition to that, for the particular case where the mean temperatures of burnt and unburnt gases are related by a factor $T_{0,b}/T_{0,u} = 4$ (which is given here, cf. Table 4.6), an analytical solution can be found under the assumptions that the mean flow is at rest and the flame is infinitely thin [54]. As described in section 4.2.2.1, the configuration is split into two subdomains upstream and downstream of the flame. Assuming continuity in mass, momentum and energy across the flame leads to following the jump conditions:

$$\left[\hat{u}\right]_{x=x_f,u} = \left[\hat{u}\right]_{x=x_f,b} \tag{4.33}$$

$$\left[\hat{p}\right]_{x=x_f,u} = \left[\hat{p}\right]_{x=x_f,b} \tag{4.34}$$

These are equivalent of Eqs. (4.24) - (4.26) for the case where the mean flow is at rest and fluctuations in heat release rate are not considered. The passage from Eqs. (4.24) - (4.26) to the zero mean flow equivalents however is not straightforward and is derived in detail in [24].

Expressing pressure and velocity fluctuations in terms of harmonic waves as in Eqs. (4.27) and (4.28), and neglecting mean flow and entropy fluctuations, Kaufmann et al. [54] derive the following dispersion relation:

$$\Lambda = \frac{\Gamma - 1}{\Gamma + 1} = e^{2ik_u x_f} \frac{R_1 - R_2 e^{-3ik_u x_f}}{1 - R_1 R_2 e^{ik_u x_f}} \tag{4.35}$$

with $\Gamma = \frac{\rho_{0,b} c_{0,b}}{\rho_{0,u} c_{0,u}}$ the ratio of mean density times sound speed of burnt to unburnt gases, $k_u = \omega / c_{0,u}$ the wavenumber in the unburnt gases, and R_1 and R_2 the reflection coefficients at inlet and outlet respectively.

In the case presented here, the boundary conditions $\hat{u}(x = 0)$ and $\hat{p}(x = L)$ imply that the reflection coefficients at the domain inlet and outlet are $R_1 = 1$ and $R_2 = -1$ respectively. Introducing R_1 and R_2 into Eq. (4.35), one finds:

$$\Lambda = e^{2ik_u x_f} \frac{1 + e^{-3ik_u x_f}}{1 + e^{ik_u x_f}} = \frac{e^{\frac{3}{2} ik_u x_f} + e^{-\frac{3}{2} ik_u x_f}}{e^{\frac{1}{2} ik_u x_f} + e^{-\frac{1}{2} ik_u x_f}}$$

$$\Lambda \cos\left(\frac{1}{2} k_u x_f\right) = \cos\left(\frac{3}{2} k_u x_f\right) = 4\cos^3\left(\frac{1}{2} k_u x_f\right) - 3\cos\left(\frac{1}{2} k_u x_f\right)$$

The resonant frequencies are thus the solutions of the following expression:

$$\cos\left(\frac{k_u x_f}{2}\right) \left[\cos^2\left(\frac{k_u x_f}{2}\right) - \frac{3}{4} - \frac{\Lambda}{4}\right] = 0 \tag{4.36}$$

The authors separate the results then into two families, being solutions of the left and right factor of Eq. (4.36) respectively. It is pointed out that the modes which are solution of the left hand side term represent the half wave mode of the part of the duct upstream of the flame (and its harmonics). These modes have velocity nodes at the location of the flame, and can therefore not be excited using the $n - \tau$ -model of Eq. (4.4).
As at $M = 0$ the pressure is constant across the flame, the density decreases by factor 4 across the flame, while the speed of sound increases by factor 2. Thus, one finds $\Gamma = \frac{1}{3}$ and $\Lambda = \frac{2}{3}$. The real valued frequencies of the first three modes can then be determined to:

$$f_1 = \frac{2c_{0,u}}{x_f} \cos^{-1}\left(\sqrt{2/3}\right) = 136.04\text{Hz}$$

$$f_2 = \frac{\pi c_{0,u}}{x_f} = 347.19\text{Hz}$$

$$f_3 = \frac{2c_{0,u}}{x_f} \cos^{-1}\left(-\sqrt{2/3}\right) = 588.34\text{Hz}$$

The first and third mode are hence results of the right hand term of Eq. (4.36), while the second mode is due to the left hand term, therefore being one of the modes with a velocity node at the

	$\delta_f \to 0$ semi-analytical solver of section 4.2.2.1	$\delta_f = 0.05L$	$\delta_f = 0.10L$ 1D LEE solver	$\delta_f = 0.15L$
$M_0^{in} = 0.001$				
1	$136.04 - 0.26i$	$136.01 - 0.24i$	$137.51 - 0.15i$	$138.34 - 0.15i$
2	$347.19 - 0.23i$	$347.31 - 0.23i$	$347.33 - 0.23i$	$347.36 - 0.23i$
3	$558.34 - 0.26i$	$561.64 - 0.15i$	$565.47 - 0.14i$	$569.29 - 0.13i$
$M_0^{in} = 0.15$				
1	$121.43 - 48.49i$	$123.35 - 50.52i$	$126.41 - 52.54i$	$129.80 - 54.25i$
2	$325.04 - 35.52i$	$324.41 - 34.06i$	$323.57 - 33.88i$	$322.85 - 33.77i$
3	$538.48 - 50.89i$	$552.43 - 44.84i$	$559.71 - 36.02i$	$562.38 - 29.10i$

Table 4.7: Eigenfrequencies of first three modes at $M_0^{in} = 0.001$ and $M_0^{in} = 0.15$

location of the flame.

Table 4.7 shows the first three eigenfrequencies of the configuration obtained by the semi-analytical method of section 4.2.2.1 and by the LEE solver for three values of flame length δ_f at a very low and a high Mach number at the domain inlet. The computations at very low inlet Mach number reproduce very well the analytical results of Kaufmann et al., predicting marginally stable modes at the correct frequencies. The modes are all expected to be neither amplified nor damped when the mean flow is at rest, as in this case the acoustic flux across the inlet and outlet boundaries is defined as $F = \hat{p}\hat{u}$ and equals zero due to the boundary conditions that are imposed. Besides, as fluctuations in heat release rate are not considered here, the flame does not generate any amplification or damping.
When the mean flow in the domain is at a higher Mach number (here: $M_0^{in} = 0.15$), all modes are damped. This is due to the fact that loss terms at the boundaries do now play an important role, while still no source of acoustic energy is present. In contrast to the computations for the mean flow being virtually at rest, the length of the flame zone does now slightly modify the results, especially the growth rates. This aspect is discussed in more detail later on. The results found by the LEE solver tend however towards those found by the semi-analytical method when the length of the flame is decreased.

The evolution of the complex eigenfrequencies of the first three modes with increasing Mach number at the domain inlet are shown in Fig. 4.13. The plot contains both results of the semi-analytical model of section 4.2.2.1, which assumes a flame length of $\delta_f \to 0$, and of the 1D LEE solver, with this parameter being set to $\delta_f = 0.05$. The semi-analytical model and the LEE computations predict both a trend towards slightly lower real frequencies and stronger damping with increasing Mach number. The differences between the results obtained by the two methods increase with the mean flow Mach number, and concern especially the imaginary frequencies of the first and third mode.

The structure of the third eigenmode of this configuration is shown in Fig. 4.14 at low and high inlet Mach numbers. For $M_0^{in} = 0.001$ and $M_0^{in} = 0.15$, module and phase of pressure, velocity and entropy fluctuations are plotted.
The figures show that the mean flow speed does not have an important effect on the struc-

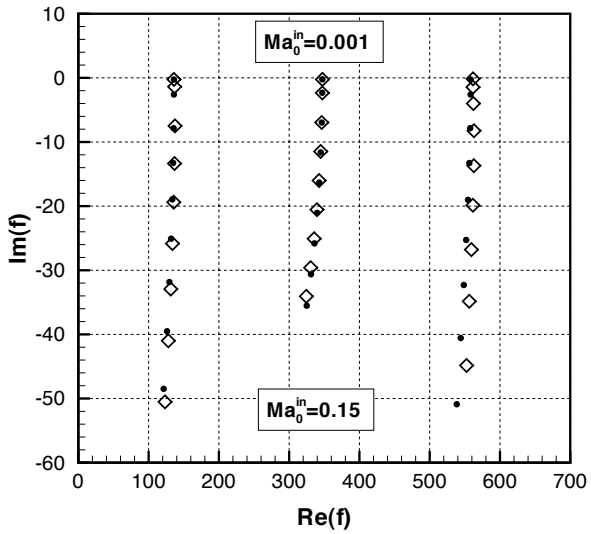

Figure 4.13: Eigenfrequencies of the first three modes obtained by semi-analytical method and LEE solver. •: $\delta_f \to 0$ $\quad \diamond : \delta_f = 0.05L$

ture of the mode upstream of the flame. However, the mode shape changes clearly within the flame region and downstream of the flame. The most noticeable change can be observed in the distribution of fluctuating entropy (see Fig. 4.14 (e)). When the mean flow is at rest, these fluctuations are confined to the flame zone. In contrast to that, the computation with a non zero mean flow velocity predicts their convection towards the outlet of the domain. The presence of the entropy fluctuations downstream of the flame, together with the fact that the flame accelerates the mean flow to about twice its speed at the inlet, does then in turn modify the distributions of pressure and velocity fluctuations.

The impact of the mean flow speed is also visible in the evolution of the phase of the fluctutating quantities (see Fig. 4.14 (b), (d), (f)). When the mean flow is at rest, the argument of the complex quantities $\hat{p}$ and $\hat{s}$ is constant along x at zero or $\pm\pi$ and at $\pm\pi/2$ for $\hat{u}$, with steps at the respective node positions. At non zero Mach number however, the phase is not piecewise constant anymore. This difference can be illustrated by coming back to the definitions of $\hat{p}$, $\hat{u}$ and $\hat{s}$ as defined in Eqs. (4.27) - (4.29):

$$\hat{p}(x) = \mathcal{A}^+ e^{ik^+x} + \mathcal{A}^- e^{-ik^-x}$$

$$\hat{u}(x) = \frac{1}{\rho_0 c_0}\left[\mathcal{A}^+ e^{ik^+x} - \mathcal{A}^- e^{-ik^-x}\right]$$

$$\hat{s}(x) = \mathcal{E} e^{ik_s x}$$

Replacing the complex wavenumbers k in the above expressions by their respective definitions yields:

$$\hat{p}(x) = \mathcal{A}^+ e^{i\frac{\omega_r + i\omega_i}{c+u}x} + \mathcal{A}^- e^{-i\frac{\omega_r + i\omega_i}{c-u}x} = \mathcal{A}^+ e^{-\frac{\omega_i}{c+u}x} e^{i\frac{\omega_r}{c+u}x} + \mathcal{A}^- e^{\frac{\omega_i}{c-u}x} e^{-i\frac{\omega_r}{c-u}x} \tag{4.37}$$

$$\hat{u}(x) = = \frac{1}{\rho_0 c_0}\left[\mathcal{A}^+ e^{-\frac{\omega_i}{c+u}x} e^{i\frac{\omega_r}{c+u}x} - \mathcal{A}^- e^{\frac{\omega_i}{c-u}x} e^{-i\frac{\omega_r}{c-u}x}\right] \tag{4.38}$$

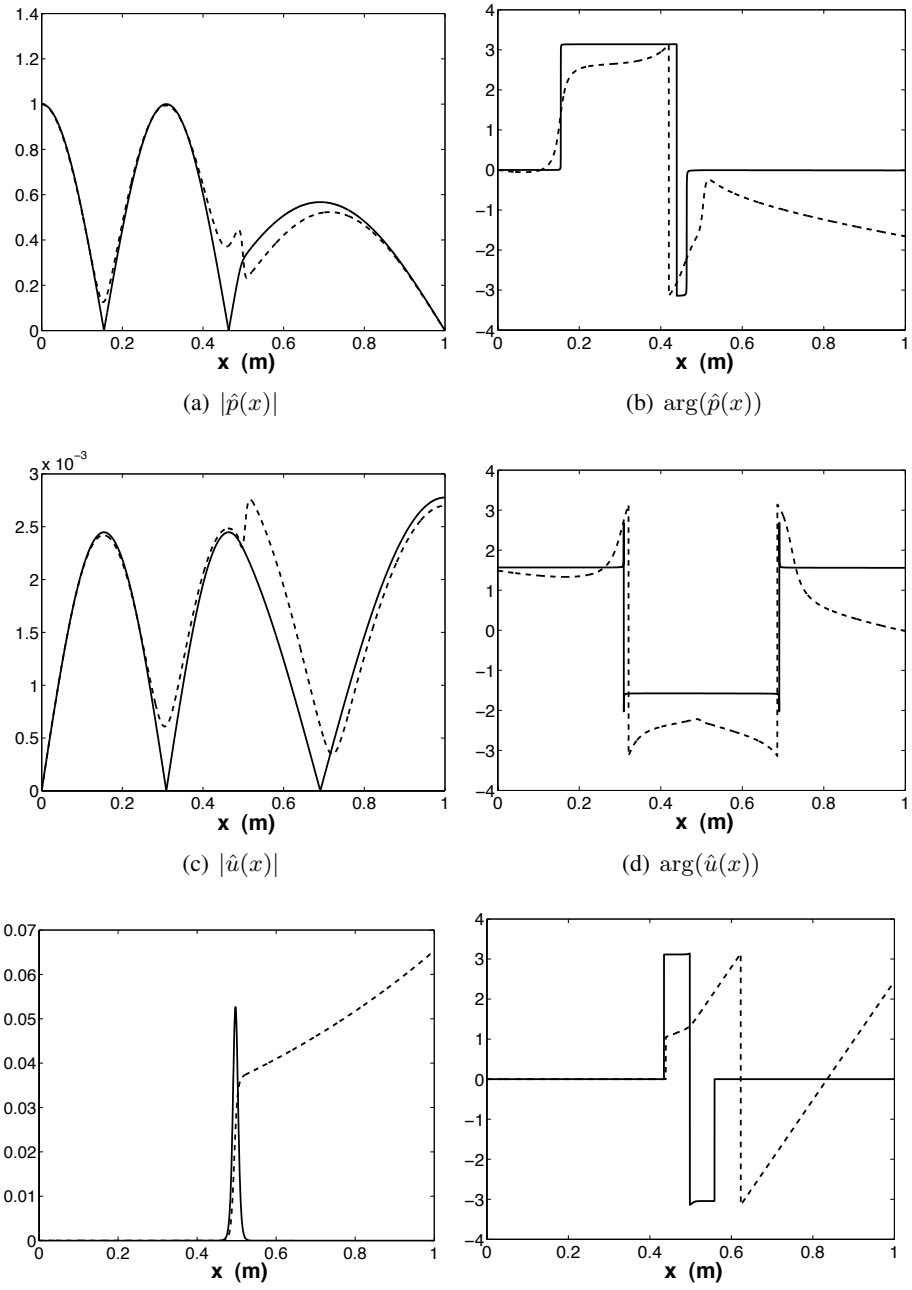

(a) $|\hat{p}(x)|$ (b) $\arg(\hat{p}(x))$

(c) $|\hat{u}(x)|$ (d) $\arg(\hat{u}(x))$

(e) $|\hat{s}(x)|$ (f) $\arg(\hat{s}(x))$

Figure 4.14: Structure of the third eigenmode at low and high Mach numbers as obtained numerically by the LEE solver for $\delta_f = 0.05L$. Normalization is such that $\hat{p}(x=0) = 1$.
—— : $M_0^{in} = 0.001$, $f = 561.64 - 0.15i$ Hz - - - : $M_0^{in} = 0.15$, $f = 552.43 - 44.84i$ Hz.

and

$$\hat{s}(x) = \mathcal{E} e^{i\frac{\omega_r + i\omega_i}{u}x} = \mathcal{E} e^{-\frac{\omega_i}{u}x} e^{i\frac{\omega_r}{u}x} \tag{4.39}$$

Using this notation allows to identify module and phase of the fluctuating quantities more clearly. At zero Mach number, the eigenfrequencies observed here are purely real, and the

boundary conditions impose that $\mathcal{A}^+ = \mathcal{A}^-$. The pressure perturbation reads hence

$$\hat{p} = \mathcal{A}^+ \left(e^{i\frac{\omega_r}{c}x} + e^{-i\frac{\omega_r}{c}x} \right)$$

i.e. module and phase read

$$|\hat{p}(x)| = 2\mathcal{A}^+ \cos\left(\frac{\omega_r}{c}x\right) \qquad \text{and} \qquad \arg(\hat{p})(x) = \pm\pi$$

However, as soon as the mean flow velocity is non zero, this simplifications are not possible anymore, which precludes finding analytical expressions for module and phase for pressure and velocity perturbations. For the entropy perturbations however, one finds

$$|\hat{s}(x)| = \mathcal{E}e^{-\frac{\omega_i}{u}x} \qquad \text{and} \qquad \arg(\hat{s})(x) = \frac{\omega_r}{u}x$$

The phase of the entropy perturbations is hence supposed to increase linearly with $\frac{\omega_r}{u}$, which can easily be verified in Fig. 4.14(e): with $f_r = 552.4$Hz and a mean flow velocity downstream of the flame of $u = 234.1$m/s, the phase curve should increase with $\frac{\omega_r}{u} = 14.8\frac{1}{\text{m}}$. As the phase passes from $arg(\hat{s}) = -\pi$ at $x \approx 0.62$ to $arg(\hat{s}) = 0$ at $x \approx 0.83$, the actual slope of the curve is $\approx \frac{\pi}{0.21\text{m}} = 15.0\frac{1}{\text{m}}$, which corresponds well to the expected result.

Using the expressions of Eqs. (4.27) - (4.29) recalled above, one may also recover the factors $\mathcal{A}^+$, $\mathcal{A}^-$ and $\mathcal{E}$ as

$$\mathcal{A}^+ = \frac{1}{2}\Big[\hat{p}(x) + \rho_0 c_0 \hat{u}(x)\Big] e^{-ik^+x} \tag{4.40}$$

$$\mathcal{A}^- = \frac{1}{2}\Big[\hat{p}(x) - \rho_0 c_0 \hat{u}(x)\Big] e^{ik^-x} \tag{4.41}$$

$$\mathcal{E} = \hat{s}(x) e^{-ik_s x} \tag{4.42}$$

It should be noted that these factors are deduced from harmonic wave solutions that are valid in isothermal, isobaric flow conditions. Their interpretation is hence meaningful only in the parts of the flow outside of the flame.
In these regions upstream and downstream of the flame, the factors $\mathcal{A}^+$, $\mathcal{A}^-$ and $\mathcal{E}$ are supposed to be constant. This is effectively the case, as shown in Fig. 4.15, where these factors are plotted for the eigenvectors at $M_0^{in} = 0.001$ (left) and $M_0^{in} = 0.15$ (right) of Fig. 4.14. When the mean flow is virtually at rest, the entropy factor is zero outside of the flame, but negligible even in the part of the flow where entropy is present. The coefficients $\mathcal{A}^+$ and $\mathcal{A}^-$ attributed to the forward and backward travelling acoustic wave have the same amplitude, which is a result of the boundary conditions at inlet and outlet.
For zero Mach number limit, the coefficients $\mathcal{A}^+$ and $\mathcal{A}^-$ can be understood as the amplitudes of the characteristic waves, as $\omega_i = 0$ for the corresponding eigenmode. However, in general, the characteristic wave amplitudes read $|\mathcal{A}^+ e^{-\frac{\omega_i}{c(1+M)}x}|$, $|\mathcal{A}^- e^{\frac{\omega_i}{c(1-M)}x}|$ and $|\mathcal{E}e^{-\frac{\omega_i}{u}x}|$. This means that the amplitudes of the characteristic waves are - unlike the factors $\mathcal{A}^+$ and $\mathcal{A}^-$ - not constant in the zones outside of the flame, as soon as the eigenmode is amplified or damped.
The same behaviour can be observed for the convected entropy wave at non zero Mach number: Fig. 4.14(e) shows that $|\hat{s}|$ increases downstream of the flame, which may give the misleading impression that entropy perturbations could be produced downstream of the flame. This being

not the case of course, the factor $\mathcal{E}$ is well constant outside of the flame (Fig. 4.15(e)). Finally, on may recover the temporal signal of the entropy perturbations that reads

$$s'(x,t) = \Re(\hat{s}(x)e^{-i\omega t}) = \Re(\mathcal{E}e^{\omega_i(t-\frac{x}{u})}e^{-i\omega_r(t-\frac{x}{u})})$$

This expression illustrates how entropy perturbations are expressed as part of a damped mode: The maximum amplitude of $s'(x,t)$ is expected to be constant downstream of the flame, while a damped mode induces a decay in amplitude during the convection time from an upstream to a downstream position, which is in turn compensated by an increase in space of $|\hat{s}|$.

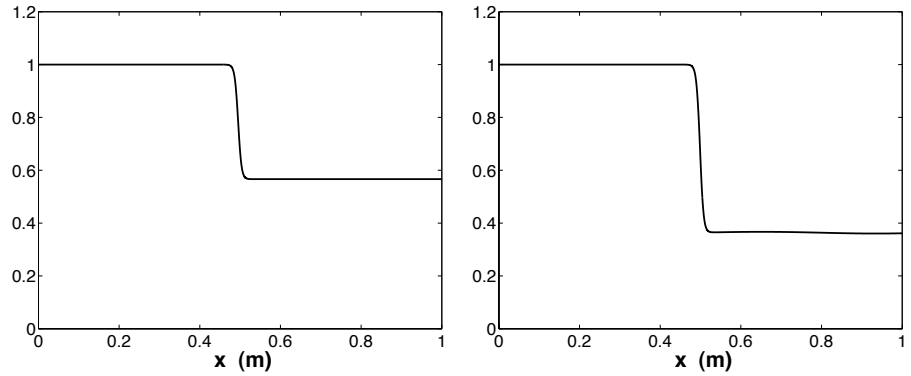

(a) $\mathcal{A}^+$ for $M_0^{in} = 0.001$ (b) $\mathcal{A}^+$ for $M_0^{in} = 0.15$

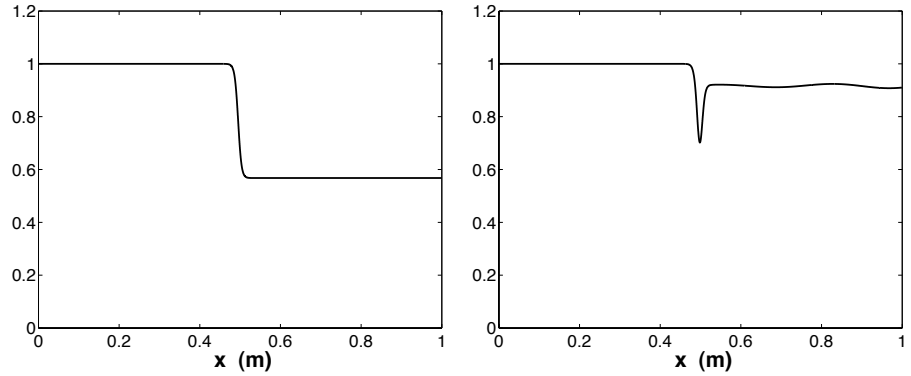

(c) $\mathcal{A}^-$ for $M_0^{in} = 0.001$ (d) $\mathcal{A}^-$ for $M_0^{in} = 0.15$

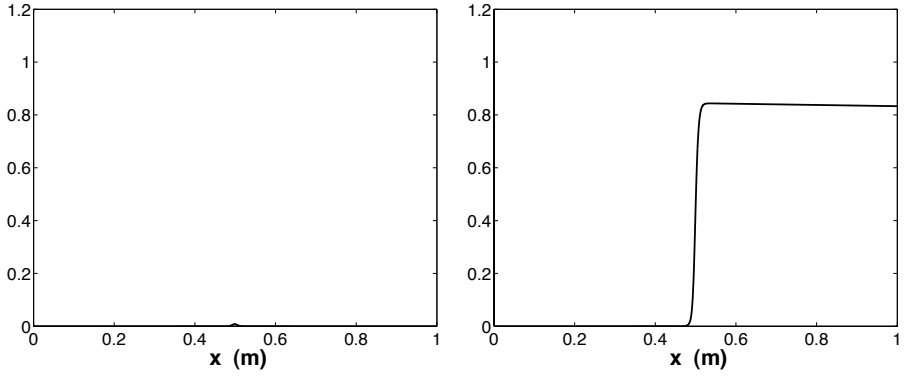

(e) $\mathcal{E}$ for $M_0^{in} = 0.001$ (f) $\mathcal{E}$ for $M_0^{in} = 0.15$

Figure 4.15: Structure of the third eigenmode in terms of pre-exponential factors $\mathcal{A}^+$, $\mathcal{A}^-$ and $\mathcal{E}$ as defined in Eqs (4.40) - (4.42).
left: $M_0^{in} = 0.001$, $f = 561.64 - 0.15i$ Hz right: $M_0^{in} = 0.15$, $f = 552.43 - 44.84i$ Hz.

Impact of Boundary Conditions

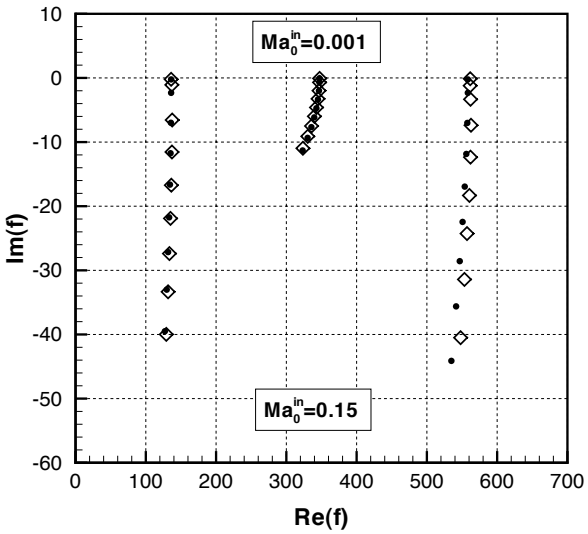

Figure 4.16: Eigenfrequencies of the first three modes obtained by semi-analytical method and LEE solver for boundary conditions "no acoustic flux". •: $\delta_f \rightarrow 0$ $\quad \diamond : \delta_f = 0.05L$

The results presented in Fig. 4.16 show that an increasing mean flow Mach number leads to higher damping rates for the observed eigenmodes. One reason for this is the loss of acoustic energy by its transport out of the domain, an aspect that can be influenced by the choice of boundary conditions: The same computations as those shown so far can be carried out with boundary conditions that set the flux of acoustic energy at the domain inlet and outlet to zero (cf. Eq. (4.15)). The boundary condition at the inlet reads then $\hat{u} + \frac{u_0}{\rho_0 c_0^2}\hat{p} = 0$, that at the outlet $\hat{p} + \rho_0 u_0 \hat{u} = 0$.
However, entropy fluctuations may still leave the domain at the domain outlet, i.e. losses of disturbance energy cannot be completely avoided.

The results for the complex eigenfrequencies found by the LEE solver and the semi-analytical method for these boundary conditions are plotted in Fig. 4.16 for mean flow Mach numbers increasing from $M_0^{in} = 0.001$ to $M_0^{in} = 0.15$. Again, good agreement between the two methods is obtained. As for the initial set of boundary conditions, a trend towards slightly lower real frequencies and more stable modes is predicted for increasing mean flow Mach numbers.
Compared to the computations with the boundary conditions that allow a flux of acoustic energy across the inlet and outlet borders, the damping rates predicted for a given inlet Mach number are lower now (cf. Fig 4.13). This confirms the idea that the losses of disturbance energy are lower, as they are only due to entropy terms. However, the impact is not the same on the three modes: While the second mode is significantly less damped now, the changes in damping rates for the first and third mode are much smaller.

These observations are discussed in more detail in Chapter 6, where an analysis of the disturbance energy contained in the different modes is carried out for this configurations.

Impact of the Flame Thickness

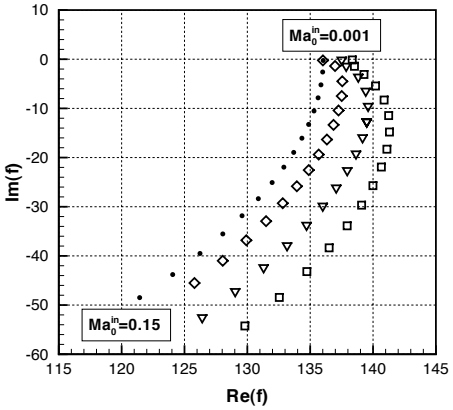

(a) Mode 1

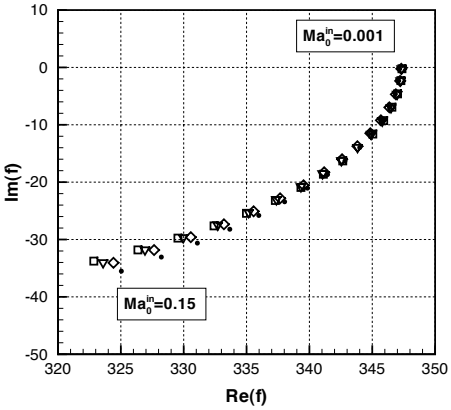

(b) Mode 2

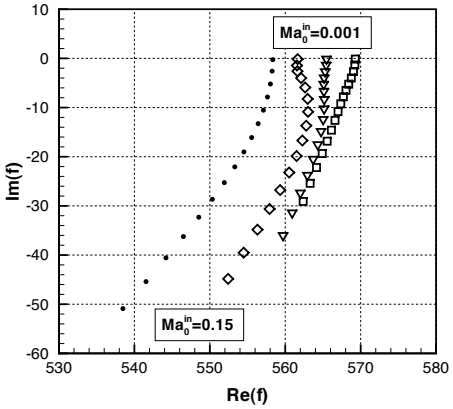

(c) Mode 3

Figure 4.17: Impact of the flame length on the eigenfrequency. •: $\delta_f \rightarrow 0$; ⋄: $\delta_f = 0.05L$ ▽: $\delta_f = 0.10L$ □ : $\delta_f = 0.15L$

As has been mentioned before (cf. Table 4.7), the length of the flame zone may have an impact on the eigen frequency. In order to evaluate this effect, the eigenfrequencies of the first three modes of the configuration shown in Fig. 4.10 have been computed using the infinitely thin flame assumption and the 1D LEE solver for $\delta_f = 0.05L$, $\delta_f = 0.10L$ and $\delta_f = 0.15L$. The results are plotted in Fig. 4.17. One observes that the impact of an increasing flame length is not the same for the three modes: the real frequency of the first mode is little affected at low Mach number, whereas at higher Mach number increasing flame thickness leads to higher real frequencies. For the third mode, this trend towards higher real frequencies can be observed both at high and low Mach number, whereas the second mode shows a slight decrease in real frequency with increasing δ_f. In the same way, the damping rate at a given mean flow speed is found to slightly increase with δ_f for the first mode, left unchanged for the second and decreases for the third mode.

The reason why the second mode is left almost unchanged when the flame thickness is varied is due to the fact that this mode contains a velocity node and a pressure maximum at the position of the flame. The mode being thus nearly symmetric with respect to the flame position, a symmetric change in mean flow conditions has very little effect on its structure. This is however not the case for the first and third mode, where the change in mean flow conditions impacts (slightly) on the structure of the mode. This in turn may change the decay rate, as the damping is (among others) due to losses of disturbance energy at the domain boundaries, i.e. on the amplitudes of pressure, velocity and entropy perturbations at those positions. This illustrates that the impact of a change of δ_f depends largely on the spatial structure of the mode at the position of the flame and can therefore not be predicted in a general way.
The situation becomes even more complex when heat release rate fluctuations are taken into account using the $n - \tau$- model of Eq. (4.4): As this model links the source term $\hat{q}$ to the acoustic velocity at a point immediately upstream of the flame $\hat{u}_{x_{ref}}$, a change in δ_f not only leads to small changes in the mode's structure, but shifts the location of the reference point x_{ref}. If the flame is placed near to a velocity node, i.e. in a zone where the gradient of $|\hat{u}(x)|$ is strong, a small shift of x_{ref} leads to important differences in $\hat{u}_{x_{ref}}$ and therefore $\hat{q}$. For the configuration being considered here, this applies to the second mode: unlike in the case where $\hat{q} \neq 0$, this mode is expected to be susceptible on changes in δ_f as soon as fluctuations in heat release rate are considered.

4.2.2.3 Case with Unsteady Heat Release Rate: $\hat{q} \neq 0$

	$\delta_f \to 0$ semi-analytical solver of section 4.2.2.1	$\delta_f = 0.05L$	$\delta_f = 0.10L$ 1D LEE solver	$\delta_f = 0.15L$
$M_0^{in} = 0.001$				
1	$92.56 - 7.51i$	$91.27 - 7.86i$	$94.24 - 7.62i$	$95.02 - 7.66i$
2	$347.12 - 0.08i$	$360.69 + 6.70i$	$374.48 + 15.64i$	$383.13 + 23.01i$
3	$582.50 + 53.10i$	$581.84 + 54.46i$	$580.22 + 51.23i$	$579.48 + 42.30i$
$M_0^{in} = 0.15$				
1	$70.94 - 47.61i$	$70.91 - 45.87i$	$71.15 - 44.96i$	$70.70 - 44.02i$
2	$325.04 - 9.49i$	$337.45 - 4.50i$	$350.03 + 1.42i$	$359.09 + 6.14i$
3	$565.30 - 7.55i$	$598.56 - 56.56i$	$614.19 - 137.54i$	$689.37 - 99.24i$

Table 4.8: First three modes at $M_0^{in} = 0.001$ and $M_0^{in} = 0.15$

The configuration of Fig. 4.10 is now analyzed including an unsteady heat release rate. This term is modeled as function of the acoustic velocity at a reference point immediately upstream of the flame, as described in section 4.1. The parameters of the heat release model of Eq. 4.4 are set to $n = 3$ and $\tau = 0.5$ ms in the following. The mean flow parameters remain those of Table 4.6.

As before, the results of the LEE solver are compared to those of the semi-analytical model described in section 4.2.2.1. The results obtained by the two methods for complex eigen frequencies of the first three modes at very low and high inlet velocity are gathered in Table 4.8. Besides, the evolution of the eigenfrequencies between the two values $M_0^{in} = 0.001$ and $M_0^{in} = 0.15$ is plotted in Fig. 4.18 for the infinitely thin flame computations and the LEE computations with $\delta_f = 0.05L$.

The results obtained by the two methods show overall good agreement. At low Mach number, both the semi-analytical model and the LEE solver predict now the first mode as stable, and the third mode as unstable. However, for the second mode the length of the flame zone has an impact on the result even at low Mach numbers, which is due to its spatial structure: Comparing the complex frequencies of this mode obtained by the semi-analytical model at $M_0^{in} = 0.001$ to that obtained without the unsteady heat release term (cf. Tab. 4.7), the observation that the second mode cannot be excited using the present heat release model is confirmed. As this mode contains a velocity node at the middle of the domain, i.e. at the position of the flame, the unsteady heat release rate computed by Eq. (4.4) equals zero. However, this is only strictly true for the infinitely thin flame computations. If the flame covers a certain length, the velocity is not strictly zero, and thus an unsteady heat release term occurs. This explains why this second mode is particularly sensitive to changes in flame thickness.

The third mode now being unstable at low Mach number indicates that the flame acts as a source of disturbance energy, i.e. the phase shift between pressure and heat release rate fluctuations is such that the Rayleigh criterion is satisfied. At the same time, the energy losses at low Mach number are small enough in order not to outbalance the energy gain due to the unsteady heat release rate. As shown in Fig. 4.18, this is not the case at high Mach number: for the three

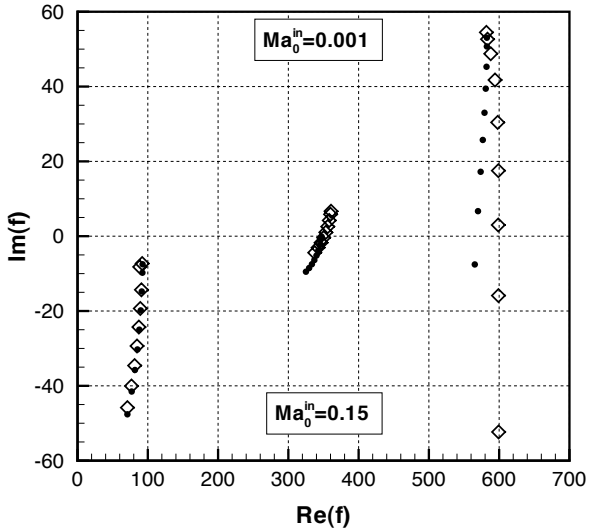

Figure 4.18: Eigenfrequencies of the first three modes obtained by semi-analytical method and LEE solver. •: $\delta_f \to 0$ $\quad \diamond : \delta_f = 0.05L$

modes shown here, the computations predict again a general trend towards more stable modes with increasing mean flow velocity, This indicates that the loss terms, among others due to flux of disturbance energy across the domain borders, outbalance the source terms related to the flame. A detailed analysis of these mechanisms is presented in Chapter 6.

The structure of the third eigenmode is shown in Fig. 4.19. Similarly to the computations without unsteady heat release rate (cf. Fig. 4.14), the impact of the mean flow speed is especially visible in the flame zone and downstream of the flame.

The unsteady heat release rate in the flame zone leads to a modified distribution of entropy compared to the case without unsteady heat release rate: At low Mach number, this quantity is non zero throughout the flame zone, with very steep gradients at its beginning and end. Besides, the amplitude of the entropy fluctuations is now underpredicted at low Mach number. Similarly, the curve of $|\hat{u}(x)|$ shows a much stronger impact of the flame than in the case without unsteady heat release rate, both at low and high Mach number.
Furthermore, the phase of the pressure and velocity perturbations is not constant along x anymore at low Mach number, but one observes rather an opposite behaviour between the low and high Mach number case: in the parts of the domain where the phase of the pressure signal increases for $M_0 = 0.001$ it decreases for $M_0 = 0.15$. This might be related to the growth rates, which are of similar values for the two Mach numbers, but with opposite signs: $\omega_i = 54.5\mathrm{s}^{-1}$ at $M_0 = 0.001$, whereas $\omega_i = -56.5\mathrm{s}^{-1}$ at $M_0 = 0.15$.

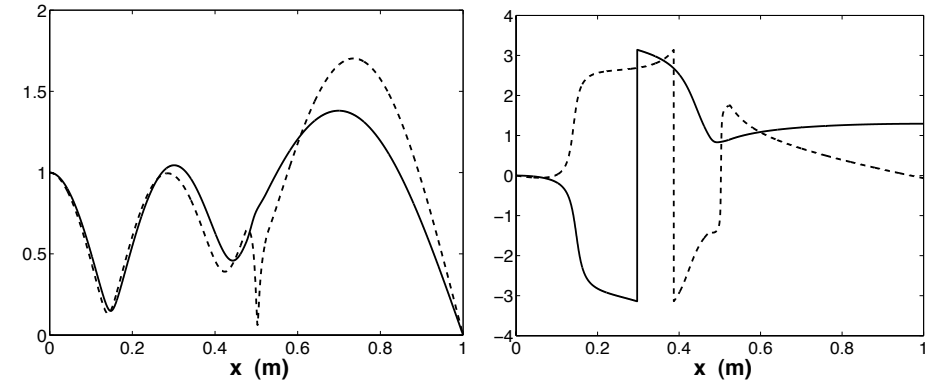

(a) $|\hat{p}(x)|$ (b) $\arg(\hat{p}(x))$

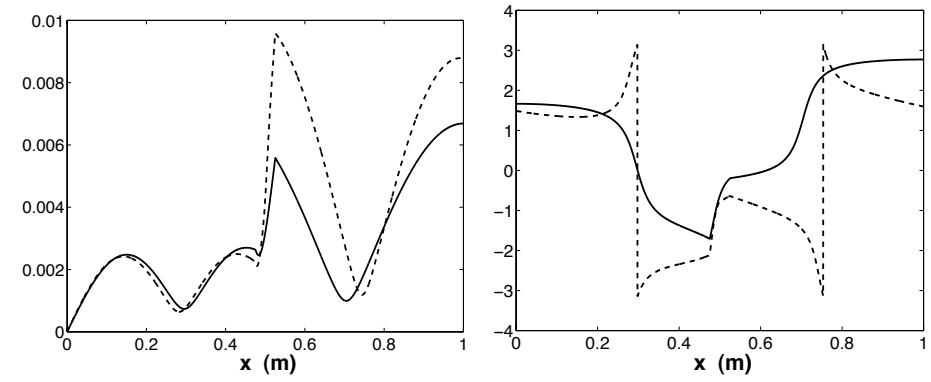

(c) $|\hat{u}(x)|$ (d) $\arg(\hat{u}(x))$

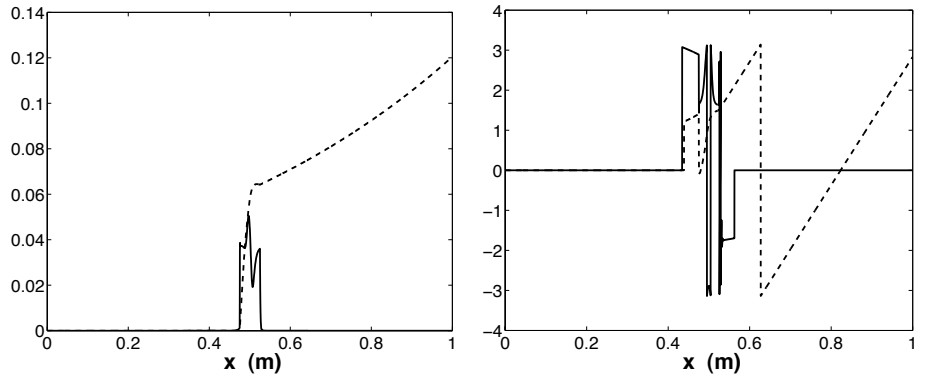

(e) $|\hat{s}(x)|$ (f) $\arg(\hat{s}(x))$

Figure 4.19: Structure of the 3rd Eigenmode at low and high Mach numbers for $\delta_f = 0.05L$.
—— : $M_0^{in} = 0.001$, $f = 581.84 + 54.46i$ Hz; - - - : $M_0^{in} = 0.15$, $f = 598.56 - 56.56i$ Hz

Impact of the Parameters of the $n-\tau$-model

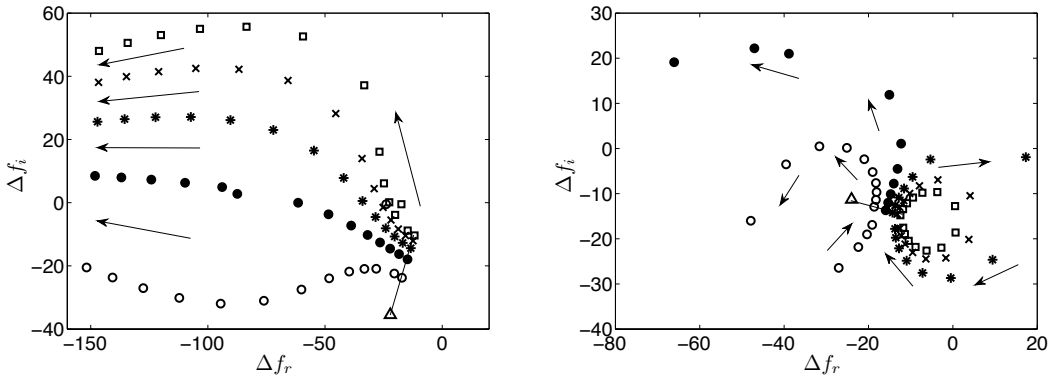

(a) Boundary Conditions 'simple'

(b) Boundary Conditions 'no acoustic flux'

Figure 4.20: Frequency shift between results at $M_0^{in} = 0.15$ and $M_0^{in} = 0.001$: $f_{0.15} - f_{0.001}$.
Δ: $n = 0$; $\circ$: $n = 1$; $\bullet$: $n = 2$; *: $n = 3$; $\times$: $n = 4$; $\square$: $n = 5$. For each n, the time delay τ varies from $\tau = 0$ms to $\tau = 2.6$ms with $\Delta\tau = 0.2$ms in direction of the arrows (starting from $\tau = 0$ms indicated by the solid line). For $M_0^{in} = 0$, the eigenfrequency is real valued and equals 347.19 Hz.

In the following, the impact of the parameters n and τ used in the unsteady heat release model on the complex eigenfrequency is discussed . Therefore, the eigenfrequency of the second mode of the configuration is computed at $M_0^{in} = 0.001$ and $M_0^{in} = 0.15$ for values of n ranging from 0 to 5, and values for τ increasing from $\tau = 0$ms to $\tau = 2.6$ms. In order to save computational time, the frequencies are computed using the semi-analytical model described in section 4.2.2.1. As shown before, the results obtained by the 1D LEE solver and the semi-analytical model are very similar when the flame is short.
In this parameter study, the two sets of boundary conditions introduced before are considered: the simple boundary conditions that impose $\hat{u} = \hat{s} = 0$ at the inlet and $\hat{p} = 0$ at the outlet, and the set of boundary conditions that blocks the acoustic flux by setting $\hat{u} + \frac{u_0}{\rho_0 c_0^2}\hat{p} = \hat{s} = 0$ at the inlet and $\hat{p} + \rho_0 u_0 \hat{u} = 0$ at the outlet. The results are finally presented in Fig. 4.20 in the form of the shift in frequency between the result at $M_0^{in} = 0.15$ and $M_0^{in} = 0.001$, i.e. $f_{0.15} - f_{0.001}$.
As mentioned before, at $M_0^{in} = 0$ the second mode of the considered configuration contains a velocity node at the $x = 0.5L$, i.e. at the position of the (infinitely thin) flame. For a mean flow at rest, this mode can hence not be influenced by the $n-\tau$-model used here and has a real valued frequency of $f = 347.19$Hz for all values of n and τ. The results shown in Fig. 4.20 indicate hence in how the eigenfrequency at $M_0^{in} = 0.15$ differs from this "fix point" as a function of the parameters n and τ and the boundary conditions.

The results show that it is not possible to predict the eigen frequency at non zero Mach number from the zero Mach number result: the way the frequency changes depends strongly on n, τ and the boundary conditions, without following a predictable pattern. For the simple set of boundary conditions (Fig. 4.20(a)), the high Mach number result has a lower real frequency in all cases ($\Delta f_r < 0$ for all n and τ). However, the imaginary frequency can change from $f_i = 0$ at $M_0^{in} = 0$ to both negative and positive values, i.e. the initially marginally stable

mode can become both stable or unstable when the mean flow velocity is taken into account. In the case shown here, only $n = 1$ leads to a shift towards a stable mode for all values of τ considered; for higher values of n, the mode will eventually become unstable when τ is high enough ($\tau > 1.4$ms for $n = 2$ and $\tau > 0.8$ms for $n = 5$).
In the case where the boundary conditions were set to block the acoustic flux (Fig. 4.20(b)), the shift in real frequency can be either negative or positive. More importantly however, the imaginary frequency as well can change towards both positive and negative values. Even though a shift towards an unstable mode occurs only for one value of n, the problem that the behaviour at higher Mach number cannot be predicted from a zero Mach number computation persists.

4.2.3 Configuration III: 1D Flame followed by Isentropic Nozzle

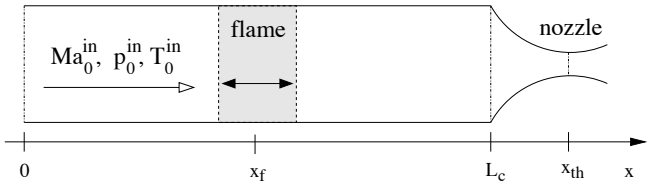

Figure 4.21: Configuration III

Finally, the configurations presented in sections 4.2.1 and 4.2.2 are combined in a third configuration, which consists in a tube of constant cross section that contains a 1D flame, followed by an isentropic nozzle (see Fig. 4.21).
The mean flow is described by a temperature distribution as in Eq. (4.21) for the part $0 < x < L_c$ and by a Mach number distribution as in Eq. (4.11) for the nozzle. As the mean flow accelerates across the flame, the Mach number at the inlet of the nozzle can be estimated to about twice the value at the inlet of the domain.
The main parameters of the computation are presented in Table 4.9. Keeping the main parameters of the previous test cases, the temperature downstream of the flame is set to $T = 1200$ K, and the Mach number at the outlet of the nozzle is $M_0^{out} = 1.1$. The flame is linked to the acoustic field via the unsteady heat release model of Eq. (4.4) with the parameters $n = 3$ and $\tau = 0.5$ms.

L(m)	L_c (m)	x_f (m)	δ_f/L	n	τ	p_0^{in} (Pa)	T_0^{in} (K)	γ	r (J/kgK)
1.1	1.0	0.5	0.05	3	0.5 ms	101325	300	1.4	287

Table 4.9: Parameters used for the calculations

The boundary conditions at the inlet are set to $\hat{u} = 0$ and $\hat{s} = 0$, whereas the outlet is defined by the sonic nozzle throat: As no waves can travel upstream as soon as the flow is supersonic, none of the unknown quantities may be imposed at a supersonic outlet.
Computations are carried out for three inlet Mach numbers: $M_0^{in} = 0.001$, $M_0^{in} = 0.05$ and $M_0^{in} = 0.10$. The frequencies and mode shapes of the first eigenmode of this configuration are indicated in Table 4.10 and Fig. 4.23. The results show that the mode is unstable when the mean flow at rest, and gets stable as the mean flow Mach number increases. This means that at low Mach number, the unsteady heat release term adds energy to the system, while at higher Mach number losses exceed any energy input. These losses can be due to convection, or result from the unsteady heat release rate: The Rayleigh criterion states that this term acts as a source term if the maximum heat release rate occurs simultaneously with a pressure maximum in the flame region; whereas it acts as a energy sink if the maximum heat release rate coincides with a pressure minimum. In the following, the results obtained for this third configuration are used to evaluate if the Rayleigh criterion is satisfied.
The flame model stated in Eq. (4.4) links the unsteady heat release rate $\hat{q}(x)$ to the acoustic velocity perturbation at a reference position immediately upstream of the flame $\hat{u}_{x_{\mathrm{ref}}}$. This can be written compactly as

$$\hat{q} = \alpha \hat{u}_{x_{\mathrm{ref}}} e^{i\omega\tau}$$

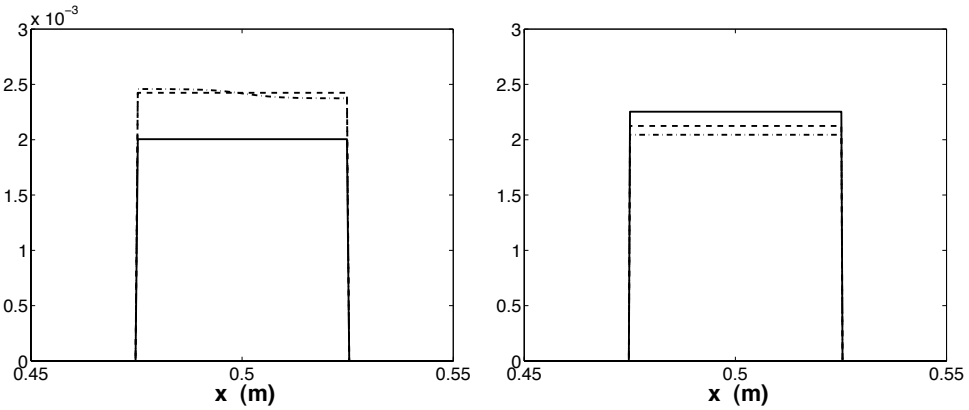

(a) $|\hat{q}(x)|/\alpha$ (b) $\arg(\hat{q}(x))$

Figure 4.22: Structure of the unsteady heat release rate at different Mach numbers.
α refers to the value $\alpha = \frac{n\gamma p_0}{\delta_f(\gamma-1)}$ determined using the pressure upstream of the flame.
——: $Ma_0^{in} = 0.001$ – – –: $Ma_0^{in} = 0.05$: -·- $Ma_0^{in} = 0.10$

where $\alpha = \frac{n\gamma p_0}{\delta_f(\gamma-1)}$ is a real valued quantity, that depends on x only via the mean pressure p_0. This means that $|\hat{q}(x)|$ is constant across the flame zone for low Mach numbers, as p_0 is constant in this case, and decreases slightly at higher Mach numbers, as the mean pressure drops across the flame. This is illustrated in Fig. 4.22, which shows module and phase of the unsteady heat release rate. The phase of the unsteady heat release rate can further be verified using the connection to the acoustic pressure. As

$$\hat{q} = \alpha \hat{u}_{x_{\text{ref}}} e^{i\omega\tau} = \alpha |\hat{u}_{x_{\text{ref}}}| e^{(i \arg(\hat{u}_{x_{\text{ref}}}))} e^{i\omega_r\tau} e^{-\omega_i\tau},$$

the phase of the unsteady heat release rate is given as

$$\arg(\hat{q}) = \arg(\hat{u}_{x_{\text{ref}}}) + \omega_r\tau.$$

Figure 4.23 shows that the phase of the acoustic velocity at the reference position is of about 1.5 for the three Mach numbers. Using $\tau = 0.5$ms and the frequencies indicated in Table 4.10, it can be shown that the above relation is satisfied for the three cases discussed here.

As described in the Chapter 1, the Rayleigh criterion is satisfied if the perturbations of pressure and heat release rate are in phase at the position of the flame, i.e. if the phase difference between heat release rate and pressure fluctuations $\Delta\phi = \phi_q - \phi_p$ in the flame zone is comprised between

$$-\frac{\pi}{2}(+2\pi\ n) < \Delta\phi < \frac{\pi}{2}(+2\pi\ n).$$

As the time delay τ is set to a constant value, the phase of $\hat{q}$ is constant across the flame as plotted in Fig. 4.22(b). The phase of $\hat{p}$ varies across the flame (see Fig. 4.23(b)); it is approximated using the value that covers the larger part of the flame zone.
The values for the phase of pressure and heat release rate fluctuations and the resulting phase difference determined for the three Mach numbers are indicated in Table 4.10. The phase difference is of $\approx \frac{3}{2}\pi$ for $M_0^{in} = 0.05$; slightly higher than this at $M_0^{in} = 0.001$ and slightly lower at $M_0^{in} = 0.10$. This estimation suggests thus that the flame is feeding energy into

	$M_0^{in} = 0.001$	$M_0^{in} = 0.05$	$M_0^{in} = 0.10$
Frequency [Hz]	$249.13 + 19.15i$	$203.21 - 1.20i$	$175.72 - 26.28i$
$\arg(\hat{u}_{x_{\text{ref}}})$	1.5	1.5	1.5
$\phi_q = \arg(\hat{q})$	2.3	2.1	2.0
$\phi_p = \arg(\hat{p})$	-2.9	-2.5	-1.8
$\Delta\phi = \phi_q - \phi_p$	5.2	4.6	3.8
impact	energy input	neutral	energy loss

Table 4.10: Estimation of Rayleigh criterion: The flame is feeding energy to the system if $-\frac{\pi}{2}(+2\pi\ n) < \Delta\phi < \frac{\pi}{2}(+2\pi\ n)$, and extracting energy if $\frac{\pi}{2}(+2\pi\ n) < \Delta\phi < \frac{3\pi}{2}(+2\pi\ n)$

the system in the case where $M_0^{in} = 0.001$ and extracting energy for $M_0^{in} = 0.10$, while in the intermediate case at $M_0^{in} = 0.05$ the phase lag between pressure and heat release rate fluctuations is such that the Rayleigh term should be neutral.
This simple evaluation matches very well the actual growth rates of the modes, which indicate the mode to be unstable at low Mach number, marginally stable at the intermediate Mach number and stable at the highest Mach number. This shows that the difference in growth rate at low and high Mach numbers is not only caused by losses due to convection, but the contribution of the unsteady heat release term may change as the Mach number is varied.

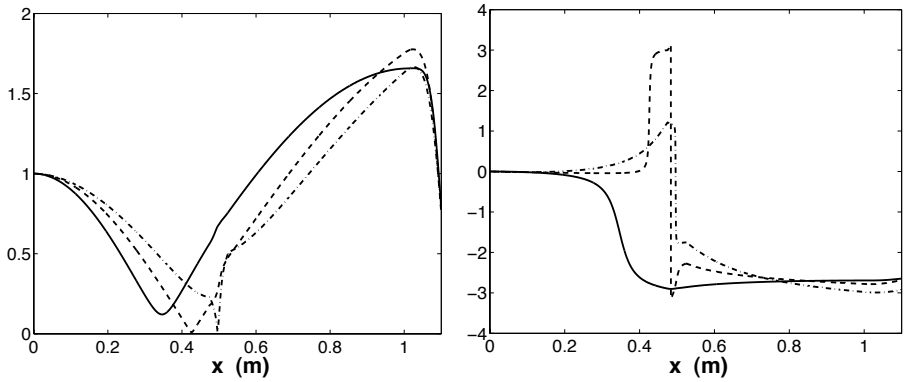

(a) $|\hat{p}(x)|$ (b) $\arg(\hat{p}(x))$

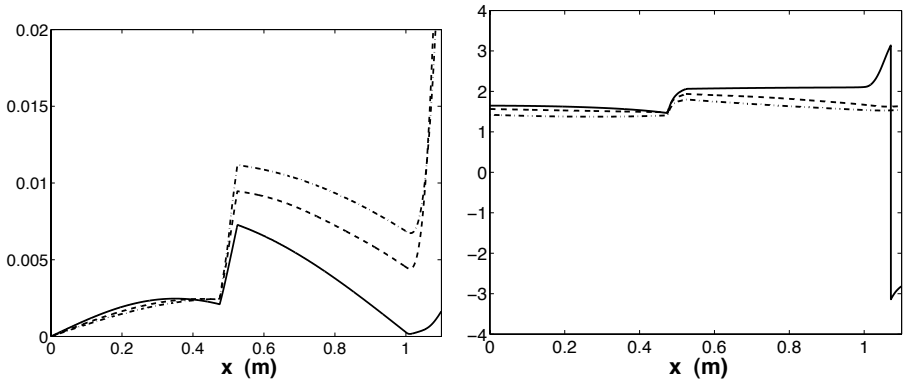

(c) $|\hat{u}(x)|$ (d) $\arg(\hat{u}(x))$

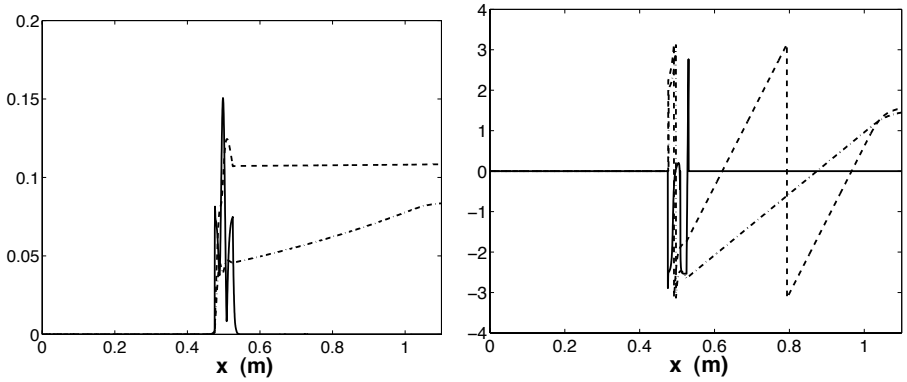

(e) $|\hat{s}(x)|$ (f) $\arg(\hat{s}(x))$

Figure 4.23: Structure of the eigenmode at low and medium Mach numbers.
——: $M_0^{in} = 0.001, f = 249.13 + 19.15i$ Hz; – – –: $M_0^{in} = 0.05$, $f = 203.21 - 1.20i$ Hz;
–·–: $M_0^{in} = 0.10$, $f = 175.72 - 26.28i$ Hz

Chapter 5

2D Study: Method and Results

Subsequently to the study of eigenmodes in quasi-1D configurations, the approach described in chapters 2 and 3 is extended to 2D cases. The eigenvalue problem stated in Eq. (2.68) is now solved using a finite volume technique on unstructured grids. In addition to acoustic and entropy waves that could be observed in the 1D study, a 2D formulation also allows for vorticity waves to occur and be convected with the mean flow.

This chapter presents firstly the main aspects of the numerical implementation of the Linearized Euler Equations into a finite volume solver. Alongside an overview of the discretization techniques applied to gradient and divergence terms, the boundary conditions that can be applied are described. Furthermore, the concept of artificial viscosity and its use in order to avoid spurious waves is introduced.

Secondly, results obtained for several academic test cases as well as the respective validation methods are presented. As first test case, the computation of the 1D flame configuration has been reconducted with the 2D solver, which allowed to show the equivalence of the 1D and the 2D solver for the Linearized Euler Equations. Subsequently, an isentropic nozzle configuration is presented. The results of the 2D LEE solver are in this case validated by a time domain flow solver. Details of the validation approach are presented together with the results of this test case. Finally, the 2D LEE solver is applied to a configuration for which experimental data is available: the Continously Variable Resonance Combustor studied at Purdue University. In addition to a comparison with the experimental results, the results obtained by the 2D LEE solver are compared to results of a Helmholtz solver.

5.1 Numerical Implementation in 2D

For the two-dimensional solver, the Linearized Euler Equations are discretized using a finite volume approach on unstructured triangular grids. This method, originally chosen for the development of the LES solver AVBP [15], has been taken over during the implementation of a first acoustic code that solves the Helmholtz-equation (AVSP, [9]), and is now applied to the Linearized Euler Equation solver.
The use of unstructured grids allows an efficient representation of complex geometries and flow fields, which is of major importance for the simulation of industrial configurations: the grid can easily be refined in zones of steep gradients in flow parameters such as the flame or injection zones, while it may be coarsened in regions of relatively uniform flow.
However, the use of unstructured grids impedes the use of higher order numerical schemes when applying a Finite Volume discretization. The scheme used for the present solver is of second order accuracy.

5.1.1 Discretization in 2D: Finite Volume Method

The finite volume discretization of the governing equations can be realized in different ways (see Fig. 5.1): In the cell centered approach (Fig. 5.1(a)), the variables are defined at the centers of the grid cells, who themselves serve as control volumes, whereas in a vertex centered approach (Fig. 5.1(b)) the variables are defined at the nodes and the control volume is constituted by a so-called dual cell, that is delimited by the center points of the surrounding cells.
In the present study, the discretization of flow quantities is based on a cell-vertex formulation as used in AVBP (Fig. 5.1c). In this approach, the grid cells serve as control volume, with the variables being stored at the nodes. This latter formulation differs hence from the former two in the sense that the variables are not defined at the center of the control volume anymore, but at its corner points. As a result, this formulation is closely related to the finite element method [58]. For the Helmholtz solver AVSP, the finite element formulation which is equivalent to the finite volume formulation used in the code has been derived in [101].

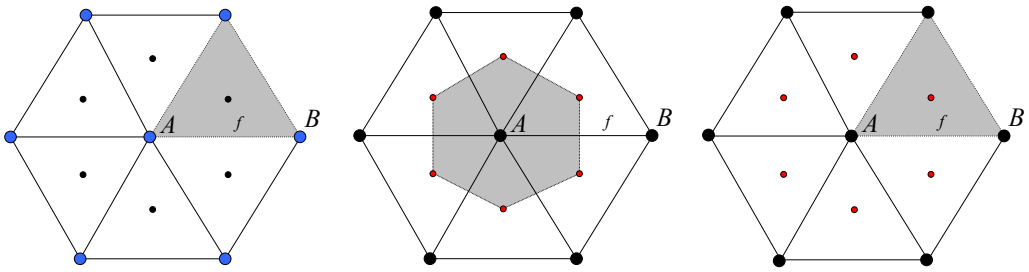

(a) cell centered (b) vertex centered (c) cell vertex

Figure 5.1: Different approaches of finite volume discretization. A, B: nodes. f: cell face. Grey shaded area: control volume. Black markers: Location where variables are stored.

In the following, the formulation used for the two basic operators used in the LEE solver, i.e. gradient and divergence operator, are presented.

5.1.1.1 Calculation of Gradients

Gradients of a quantity Φ are assumed to be constant over one cell. The value for the gradient of Φ in a cell is calculated using the values of that quantity at the surrounding vertices. The passage of this cell-defined gradient to a value defined at the grid nodes is achieved via a so-called scatter operation (cf. [15]).

The approximation of the gradient of a scalar quantity Φ for the cell Ω_j is defined as a mean value over the cell area S_{Ω_j}. Using the gradient theorem, this definition reads:

$$\vec{\nabla}\Phi\big|_{\Omega_j} \approx \frac{1}{S_{\Omega_j}} \int\int_{\Omega_j} \vec{\nabla}\Phi \mathrm{d}S = \frac{1}{S_{\Omega_j}} \oint_{\partial\Omega_j} \Phi\vec{n}\mathrm{d}x \tag{5.1}$$

with S_{Ω_j} the surface of the cell, $\partial\Omega_j$ its circumference and $\vec{n}$ the vector normal to the cell boundary. In discretised form, the above expression is transformed into a sum over the cells faces:

$$\vec{\nabla}\Phi\big|_{\Omega_j} = \frac{1}{S_{\Omega_j}} \sum_{i=1}^{n_{face}} \Phi_i \vec{n_i} \mathrm{d}S_i \tag{5.2}$$

with Φ_i being the mean value of Φ on face i, n_i the vector normal to face i and dS_i its length.

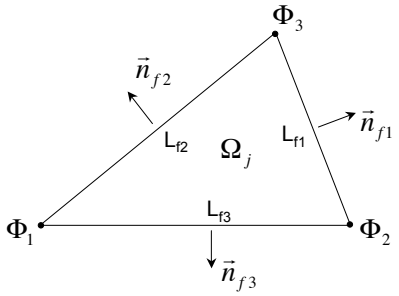

Figure 5.2: Triangular Element

For a triangular grid cell Ω_j as shown in Fig. 5.2, Eq. 5.2 reads:

$$\vec{\nabla}\Phi\big|_{\Omega_j} = \frac{1}{S_{\Omega_j}} \left[\Phi_{f1}\vec{n}_{f1}L_{f1} + \Phi_{f2}\vec{n}_{f2}L_{f2} + \Phi_{f3}\vec{n}_{f3}L_{f3}\right] \tag{5.3}$$

The mean values of Φ on each face, Φ_{f_i}, are defined as arithmetic mean of the values of Φ at the two adjacent nodes, i.e.

$$\begin{aligned} \Phi_{f1} &= \frac{1}{2}(\Phi_2 + \Phi_3) \\ \Phi_{f2} &= \frac{1}{2}(\Phi_1 + \Phi_3) \\ \Phi_{f3} &= \frac{1}{2}(\Phi_1 + \Phi_2) \end{aligned} \tag{5.4}$$

The cell-based value for the gradient $\vec{\nabla}\Phi\big|_{\Omega_j}$ can then be expressed in terms of the nodal values of Φ by introducing the above relations Eq. (5.4) into Eq. (5.3). Further simplification is

achieved by using the following relation that is satisfied for any triangle:

$$\vec{n}_{f1}L_{f1} + \vec{n}_{f2}L_{f2} + \vec{n}_{f3}L_{f3} = 0 \tag{5.5}$$

The gradient of Φ at cell Ω_j is finally obtained to

$$\vec{\nabla}\Phi\big|_{\Omega_j} = -\frac{1}{2\,S_{\Omega_j}}\left[\Phi_1\vec{n}_{f1}L_{f1} + \Phi_2\vec{n}_{f2}L_{f2} + \Phi_3\vec{n}_{f3}L_{f3}\right] \tag{5.6}$$

In a second step, this cell-defined gradient is transformed into a node-based value: To this end, the value determined in each cell Ω_j is distributed to the vertices surrounding this cell via a scatter operation (see Fig. 5.3). Each node receives contributions of all the cells it is surrounded by, such that the value for the node-based gradient can be seen as a mean value of the gradient for the dual cell.

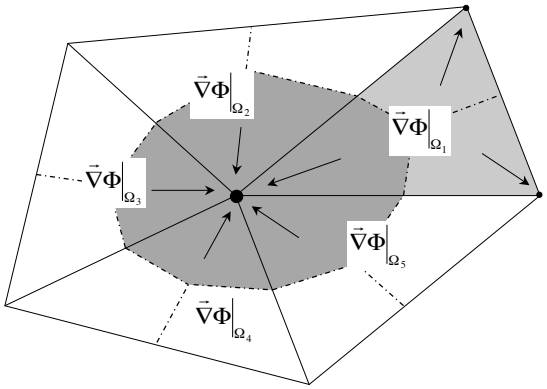

Figure 5.3: Scatter operation

5.1.1.2 Calculation of the Divergence

The calculation of the divergence operator is carried out in the same way, i.e. by first determining a cell-based value which is then scattered to the nodes. The definition of a mean value of the divergence at cell Ω_j for a given quantity $\vec{\Phi}$ (which is now a quantity in vector form) can hence be stated by using the divergence theorem as follows:

$$\nabla\cdot\vec{\Phi}\big|_{\Omega_j} \approx \frac{1}{S_{\Omega_j}}\int\!\!\int_{\Omega_j}\nabla\cdot\vec{\Phi}\mathrm{d}S = \frac{1}{S_{\Omega_j}}\oint_{\partial\Omega_j}\vec{\Phi}\cdot\vec{n}\mathrm{d}x \tag{5.7}$$

where, again, S_{Ω_j} is the surface of the cell, $\partial\Omega_j$ its circumference and $\vec{n}$ the vector normal to the cell boundary. In discretized form, the cell based divergence reads

$$\nabla\cdot\vec{\Phi}\big|_{\Omega_j} = \frac{1}{S_{\Omega_j}}\sum_{i=1}^{n_{face}}\vec{\Phi}_i\cdot\vec{n_i}\mathrm{d}S_i \tag{5.8}$$

Equivalently to what has been derived for the gradient, for a triangular cell Eq. (5.8) can be expressed in termes of nodal values as follows:

$$\nabla\cdot\vec{\Phi}\big|_{\Omega_j} = -\frac{1}{2\,S_{\Omega_j}}\left[\vec{\Phi}_1\cdot\vec{n}_{f1}L_{f1} + \vec{\Phi}_2\cdot\vec{n}_{f2}L_{f2} + \vec{\Phi}_3\cdot\vec{n}_{f3}L_{f3}\right] \tag{5.9}$$

This expression can then be further developed by expressing the vectors $\vec{\Phi}$ and $\vec{n}$ in terms of their separate components. After having determined the mean value for the grid cells, the nodal values of the divergence are obtained via a scatter operation as shown in Fig. 5.3.

5.1.2 Domain Borders and Boundary Conditions

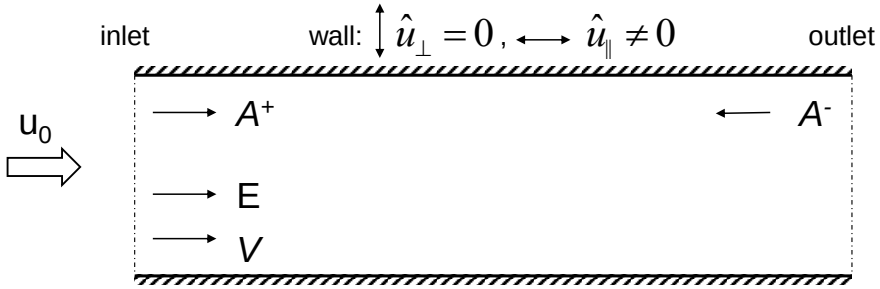

Figure 5.4: Boundary Conditions for 2D solver: Defining the incoming waves: A^+, A^-: down- and upstream travelling acoustic waves; E: entropy wave; V: vorticity wave.

At the boundaries of the domain information about the incoming waves has to be specified. In the present case, three types of waves have to be taken into account, namely acoustic, entropy and vorticity waves [56]. The incoming waves are defined at each boundary using Dirichlet conditions, i.e. the values required for the unknown variables of the vector $\mathcal{V} = (\hat{\rho}, \hat{u}_x, \hat{u}_y, \hat{s})^T$ are directly imposed at the boundary nodes. The number of conditions to be imposed on each boundary depends on its character, i.e. on the way that waves are reflected or may enter or leave the domain (see Fig. 5.4): For instance, at a boundary that represents a mean flow inlet, information about the downstream travelling acoustic wave as well as about entropy and vorticity waves has to be provided. In contrast to that, a mean flow outlet allows only the upstream travelling acoustic wave to enter the domain, while entropy and vorticity waves are convected out of the domain, which means that only one boundary condition is required.
The boundary conditions implemented in the 2D solver impose conditions on the vector of unknowns $(\hat{\rho}, \hat{u}_x, \hat{u}_y, \hat{s})^T$ as follows:

- **Inlet "Velocity Node":** All inlet boundary conditions specify that neither entropy nor vorticity waves may enter the domain. Suppressing entropy waves at the domain inlet is achieved by imposing

  $$\hat{s} = 0.$$

  In order to prevent vorticity waves from entering the domain, the component of fluctuating velocity parallel to the inlet cross section is imposed to zero, i.e.:

  $$\hat{\mathbf{u}}_\parallel = 0.$$

  Finally, the "velocity node" inlet sets the component of fluctuating velocity normal to the wall to zero, i.e.

  $$\hat{\mathbf{u}}_\perp = 0$$

  As a result, the vector of fluctuating velocity $\hat{\mathbf{u}} = \hat{\mathbf{u}}_\parallel + \hat{\mathbf{u}}_\perp$ is completely cancelled at this inlet.

- **Inlet "Pressure Node":** As introduced above, entropy and vorticity waves are suppressed at flow inlets by imposing

$$\hat{\mathbf{u}}_{\parallel} = 0 \qquad \text{and} \qquad \hat{\mathrm{s}} = 0.$$

  As can be deduced from Eq. (2.62), a pressure node can then be imposed by setting

$$\hat{\rho} = 0$$

  as third inlet boundary condition.

- **Inlet "Constant Flow Rate":** Again, the two conditions suppressing entropy and vorticity waves are maintained:

$$\hat{\mathbf{u}}_{\parallel} = 0 \qquad \text{and} \qquad \hat{\mathrm{s}} = 0.$$

  A constant flow rate at the inlet of the domain relates velocity and density fluctuations: $\dot{m}_1 = (\rho\mathbf{u})_1 = 0$, which reads, when expressed in the frequency domain formulation, $\rho_0\hat{\mathbf{u}} + \mathbf{u_0}\hat{\rho} = 0$ with $\mathbf{u}$ the velocity vector. As the mass flow rate across the inlet section is defined as normal to this section, this expression can be rewritten as $\rho_0\hat{\mathbf{u}}_{\perp} + \mathbf{u_0}_{\perp}\hat{\rho} = 0$. This condition can then be implemented by expressing the fluctuating density as function of the velocity perturbations:

$$\hat{\rho} = -\frac{|\hat{\mathbf{u}}_{\perp}|\rho_0}{|\mathbf{u_0}_{\perp}|} \qquad \text{with} \qquad |\mathbf{u_0}_{\perp}| = \mathbf{u_0}\cdot\mathbf{n} \quad \text{and} \quad |\hat{\mathbf{u}}_{\perp}| = \hat{\mathbf{u}}\cdot\mathbf{n}$$

  where $\mathbf{n}$ is the vector normal to the inlet cross section.

- **Outlet "Pressure Node":** This boundary conditions represents an outlet that is open to the atmosphere, which impedes pressure fluctuations. At a flow outlet, vorticity and entropy waves are convected out of the domain. Thus, entropy fluctuations are not necessarily zero. A pressure node establishes therefore a relation between density and entropy fluctuations (cf. Eq. (2.39)):

$$\hat{\rho} = -\frac{\rho_0}{C_p}\hat{s}$$

- **Outlet "Supersonic":** When the mean flow is supersonic at the outlet section no waves may enter the domain. Therefore, none of the variables $(\hat{\rho}, \hat{u}_x, \hat{u}_y, \hat{s})^T$ must be imposed.

- **Wall:** As boundary condition for the acoustic field, a wall impedes velocity fluctuations normal to the wall. At the same time, velocity fluctuations in wall-tangential direction are allowed ('slip walls'), as the system of equations neglects viscous effects. As for the entropy and vorticity waves, it is not necessary to impose any conditions: these waves are convected with the meanflow, and may thus neither enter nor leave across a wall.
  The condition imposed in the code reads hence:

$$\hat{\mathbf{u}}_{\perp} = 0 \qquad \text{i.e.} \qquad \hat{\mathbf{u}} = \hat{\mathbf{u}}_{\parallel} = \hat{\mathbf{u}} - \hat{\mathbf{u}}_{\perp} = \hat{\mathbf{u}} - (\hat{\mathbf{u}}\cdot\mathbf{n})\cdot\mathbf{n}$$

5.1.3 Artificial Viscosity

As already discussed in section 4.1.2, the system of equations to be solved permits the appearance of point-to-point instability. In the 1D solver, this problem was avoided by discretising the equations on a so-called staggered grid. However, the implementation of a staggered grid formulation is much more complex for a two- or three-dimensional unstructured grid than for a one-dimensional grid of equidistant points: As in the 1D case, variables of fluctuating density and entropy are stored at the cell centers, while the velocity fluctuations are defined at the faces (see Fig. 5.5). The velocity vector is expressed in terms of face-normal and tangential components and depends thus on the form and alignment of the grid cell. The formulation of the velocity at each cell is therefore not straightforward and requires the solution of a separate system of equations [65].

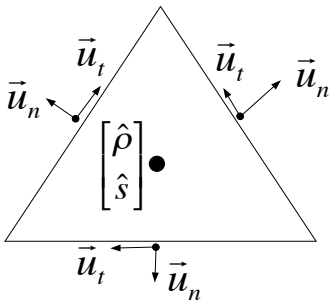

Figure 5.5: Schematic View of Staggered Grid Formulation in 2D

An alternative to the staggered grid formulation consists in the use of an artificial viscosity term. The introduction of a term that contains 2^{nd} or 4^{th} order derivatives into the system of equations to be solved prevents the appearance of point-to-point instability, as a relation between neighbouring grid points is established.
The introduction of an artificial viscosity term in an otherwise inviscid problem is certainly not without controversy. This method therefore has to be used with caution, in order to not modify the behaviour of the system. The approach is nonetheless justified, as the presented study is concerned with resonant modes rather than acoustic propagation. Unlike in propagation problems, where waves may traverse distances much larger than their wavelength, the wavelengths of the resonant eigenmodes considered in this study are of the same order as the dimensions of the computational domain. Errors due to the introduction of an artificial viscosity term are therefore small enough so as to not be prohibitive for the presented analysis.

The artificial viscosity for the 2D Euler Equation solver has been adapted from the formulation used in the LES solver AVBP (code developed at CERFACS [15, 109]). This formulation provides two viscosity operators: a 2^{nd} order operator that smoothes strong gradients, and a 4^{th} order operator that dissipates high-frequency spurious waves (”wiggles”). In AVBP, several sensors are used to determine the areas of the flow field where artificial viscosity needs to be applied. In most cases, a blend of 2^{nd} and 4^{th} order artificial viscosity is then used.
As the problem of point-to-point instability in the Euler Equation solver is not locally confined but concerns the whole domain, a 4^{th} order artificial viscosity term will be introduced uniformly throughout the domain. In addition to that, a 2^{nd} order artificial viscosity term may be used.

5.1.3.1 2nd order Operator

The artificial viscosity term added to the equation of the quantity Φ at node n is denoted $d\Phi_n^{AV}$. The 2nd order operator computes at first a contribution $d\Phi_k^{AV}$ for each of the vertices k of the cells Ω_j that surround the node n (cf. Fig. 5.6). The operator is defined as [15]:

$$d\Phi_k^{AV} = -\epsilon_2 \frac{1}{N_v} \frac{V_{\Omega_j}}{\Delta t_{\Omega_j}} (\Phi_{\Omega_j} - \Phi_k) \tag{5.10}$$

with N_v the number of vertices per cell (i.e. $N_v = 3$ for triangular cells as used in this study), V_{Ω_j} the volume of cell Ω_j and Φ_{Ω_j} and Φ_k the values of the quantity Φ for the cell Ω_j and the vertex k, respectively. Furthermore, Δt_{Ω_j} is a cell-defined time step, that represents the time required for an acoustic wave to traverse the cell, i.e. it is defined as the ratio of the cells characteristic length and the mean propagation speed in the cell. Finally, ϵ_2 is a user-defined factor that controls the amplitude of the artificial viscosity term.

Based on the values determined for all vertices k surrounding the node n, the contribution of the artificial viscosity at node n is then calculated as the sum of the values found for surrounding vertices:

$$d\Phi_n^{AV} = \sum_{k=1}^{N_v=3} d\Phi_k^{AV} \tag{5.11}$$

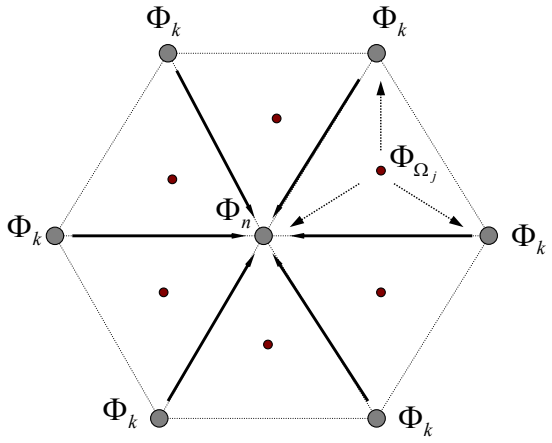

Figure 5.6: Stencil for 2nd order Artificial Viscosity Operator

The way the operator is defined leads to the use of a three-point stencil centered around the node n: The values Φ_k at the vertices surrounding n require the use of the value of Φ at the node n (see Fig.5.6). The right hand side term of Eq. (5.11) contains thus contributions of Φ at the vertices k around the node n, and the node n itself. This can be illustrated by developing the definition of Eq. (5.11) for a simple example: For a uniform 1D mesh with a cell size of Δx, Eq. (5.11) for a node n surrounded by the vertices $k = n - 1$ and $k = n + 1$ reads:

$$
\begin{aligned}
d\Phi_n^{AV} &= d\Phi_{n-1}^{AV} + d\Phi_{n+1}^{AV} \\
&= \left(-\frac{1}{2}\frac{\Delta x}{\Delta t_{\Omega_j}}\epsilon_2\right)\left[\left(\frac{\Phi_{n-1}+\Phi_n}{2} - \Phi_{n-1}\right) + \left(\frac{\Phi_{n+1}+\Phi_n}{2} - \Phi_{n+1}\right)\right] \\
&= \left(\frac{1}{2}\frac{\Delta x}{\Delta t_{\Omega_j}}\epsilon_2\right)\left[\frac{\Phi_{n-1} - 2\Phi_n + \Phi_{n+1}}{2}\right]
\end{aligned}
$$

The 2^{nd} order artificial viscosity operator has thus the form of a second order derivative in a central finite difference formulation. Establishing a link between neighbouring grid points, the problem of point-to-point instability can be handled by introducing such a term in the system of equations. However, the impact of the artificial term can be minimized by increasing the order of the operator to a fourth order derivative.

5.1.3.2 4^{th} order Operator

The formulation of the 4^{th} order term uses the same technique as the 2^{nd} order operator and computes at first contributions at all the vertices k surrounding node n. The value at node n is then computed as the sum of these vertex defined values:

$$
d\Phi_n^{AV} = \sum_{k=1}^{N_v} d\Phi_k^{AV} \tag{5.12}
$$

with the vertex based values being defined as:

$$
d\Phi_k^{AV} = \epsilon_4 \frac{1}{N_v}\frac{V_{\Omega_j}}{\Delta t_{\Omega_j}}\left[\vec{\nabla}\Phi\big|_{\Omega_j} \cdot (\vec{x}_{\Omega_j} - \vec{x}_k) - (\Phi_{\Omega_j} - \Phi_k)\right] \tag{5.13}
$$

As introduced before, the term N_v denotes the number of vertices per cell, V_{Ω_j} the volume of cell Ω_j, Φ_{Ω_j} and Φ_k the values of the quantity Φ for the cell Ω_j and the vertex k, respectively, Δt_{Ω_j} a cell-defined time step and ϵ_4 the user-defined amplitude of the artificial viscosity term.

In addition to these terms that also occur in the 2^{nd} order operator, the 4^{th} order operator uses the gradient of the quantity Φ at the cell Ω_j, noted here $\vec{\nabla}\Phi\big|_{\Omega_j}$. The key aspect in the definition of the fourth order artificial viscosity operator is now the fact that there are two ways to obtain this value: either directly in the way explained in section 5.1.1.1, i.e. based on the values of Φ at the vertices surrounding the cell Ω_j. The second option is to determine the gradient at a given cell in an "indirect" manner, by averaging the values of that gradient $\vec{\nabla}\Phi$ that has been computed for the surrounding vertices beforehand. The difference between the two approaches is explained using a 1D mesh of equidistant grid points as shown in Fig. 5.7:

Starting from the values of Φ at the nodes, a cell averaged value of the gradient can be determined immediately. Via a scatter operation, this gradient is redistributed to the nodes. Finally, a cell averaged gradient can then again be obtained by a supplementary averaging step. Following the scheme displayed in Fig 5.7, a "direct" definition of the gradient of Φ for the cell Ω_{-1} reads:

$$
\vec{\nabla}\Phi\big|_{\Omega_{-1}} = \frac{\Phi_k - \Phi_{k-1}}{\Delta x} \tag{5.14}
$$

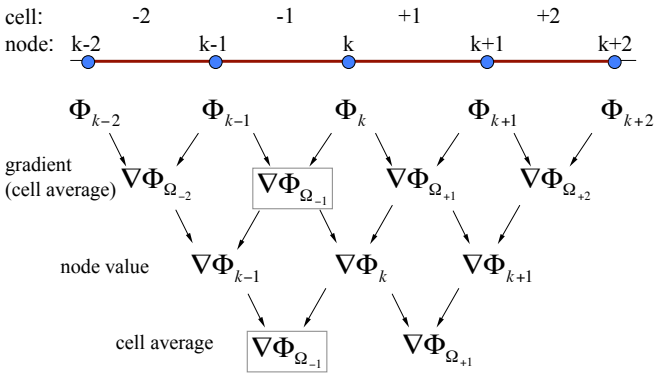

Figure 5.7: Stencil for 4th order Artificial Viscosity Operator

In contrast to that, the "indirect" method leads to:

$$\begin{aligned}
\vec{\nabla}\Phi\big|_{\Omega_{-1}} &= \frac{1}{2}\vec{\nabla}\Phi\big|_{k-1} + \frac{1}{2}\vec{\nabla}\Phi\big|_{k} \\
&= \frac{1}{2}\left(\frac{1}{2}\vec{\nabla}\Phi\big|_{\Omega_{-2}} + \frac{1}{2}\vec{\nabla}\Phi\big|_{\Omega_{-1}}\right) + \frac{1}{2}\left(\frac{1}{2}\vec{\nabla}\Phi\big|_{\Omega_{-1}} + \frac{1}{2}\vec{\nabla}\Phi\big|_{\Omega_{+1}}\right) \\
&= \frac{1}{2}\left(\frac{\Phi_{k-1}-\Phi_{k-2}}{2\Delta x} + \frac{\Phi_{k}-\Phi_{k-1}}{2\Delta x}\right) + \frac{1}{2}\left(\frac{\Phi_{k}-\Phi_{k-1}}{2\Delta x} + \frac{\Phi_{k+1}-\Phi_{k}}{2\Delta x}\right) \\
&= \frac{\Phi_{k+1}+\Phi_{k}-\Phi_{k-1}-\Phi_{k-2}}{4\Delta x}
\end{aligned} \tag{5.15}$$

Finally, in order to compute the artificial viscosity term at the node n, the operator uses the gradients of the two cells adjacent to this node (cf. Eq. (5.12)). This means that in addition to the gradient at cell Ω_{-1}, the value at cell Ω_{+1} is required:

$$\vec{\nabla}\Phi\big|_{\Omega_{+1}} = \frac{\Phi_{k+2}+\Phi_{k+1}-\Phi_{k}-\Phi_{k-1}}{4\Delta x} \tag{5.16}$$

As a result of these repeated gather and scatter operations, the 4th order operator uses a stencil of 5 points centered around the node n. For a 1D mesh of equidistant points, the artificial viscosity term for node n is obtained to:

$$d\Phi_n^{AV} = \epsilon_4 \frac{\Delta x}{16\Delta t}(\Phi_{n-2} - 4\Phi_{n-1} + 6\Phi_n - 4\Phi_{n+1} + \Phi_{n+2}) \tag{5.17}$$

which corresponds to a fourth order derivative.

5.1.3.3 Introduction of the Artificial Viscosity Term into the System of Equations

The artificial viscosity operator is applied to each of the components of the discrete eigenvector $\mathcal{V}_n = (\hat{\rho}, \hat{\mathbf{u}}, \hat{s})_n^T$, allowing to compute a term $d\mathcal{V}_n^{AV}$ for each grid point n. This term is then introduced into the system of equations (2.64) - (2.66). The discrete formulation reads then:

$$[\mathcal{A}]_n[\mathcal{V}]_n + \frac{1}{V_n} d\mathcal{V}_n^{AV} = i\omega[\mathcal{V}]_n \tag{5.18}$$

with $[\mathcal{A}]_n$ the linear operator matrix as derived in chapter 2.2.1 and V_n the volume associated to node n i.e. the volume of the dual cell around this node.

5.1.3.4 Amplitude of the Artificial Viscosity Term

The amplitude of the artificial viscosity terms is controlled by the factors ϵ_2 and ϵ_4. These parameters must be set in a way that two key criteria are satisfied:
On the one hand, the artificial viscosity term needs to be big enough to attenuate the point-to-point oscillations. On the other hand, the term must not have an influence on the overall behaviour of the solution, i.e. the growth rates of the eigenmodes must not be changed.
While the precise values of ϵ_2 and ϵ_4 may differ from case to case, their order of magnitude can be evaluated by considering a 1D configuration. (For the sake of simplicity, terms containing mean flow gradients are not taken into account in this example):
When a 4^{th} order artificial viscosity term is applied to the fluctuating density $d\hat{\rho}^{AV}$ and introduced into the continuity equation, this equation reads:

$$\rho\frac{\partial\hat{u}}{\partial x}+u\frac{\partial\hat{\rho}}{\partial x}+\underbrace{\frac{1}{dx}d\hat{\rho}^{AV}}_{\text{term AV}}=\underbrace{i\omega\hat{\rho}}_{\text{term RHS}} \tag{5.19}$$

One may now have a closer look on the separate terms of this equation and compare their respective order of magnitude. This is done in the following for artificial viscosity term and the right hand side term, which are both function of $\hat{\rho}(x)$. Considering a harmonic perturbation of the quantity $\hat{\rho}(x)$, i.e. a sine-function $\hat{\rho}(x)=\sin(kx)$, one may develop the two terms as follows: Expressing ω as $\omega=kc$, the RHS term can be replaced by

$$i\omega\hat{\rho}=ikc\sin(kx)).$$

The artificial viscosity term corresponds to a fourth order derivative, such that:

$$d\hat{\rho}^{AV}=\epsilon_4\frac{\Delta x}{16\Delta t}(\Delta x)^4\frac{\partial^4\hat{\rho}}{\partial x^4}=\epsilon_4\frac{|u+c|}{16}(\Delta x)^4\frac{\partial^4\hat{\rho}}{\partial x^4}.$$

In the above equation, the ratio of characteristic length scale to characteristic time scale $\Delta x/\Delta t$ is replaced by the propagation speed $|u+c|$. For a sinusoidal distribution $\hat{\rho}(x)=\sin(kx)$, the artificial viscosity term can thus be expressed as

$$\frac{1}{dx}d\hat{\rho}^{AV}=\frac{1}{\Delta x}\epsilon_4\frac{|u+c|}{16}(\Delta x)^4k^4\sin(kx).$$

One may deduce from these considerations that the physical terms of Eq. (5.19), i.e. the RHS term, is proportional to $k\Delta x$, while the artificial viscosity term is proportional to $(k\Delta x)^4$. This means that the scaling of physical to artificial terms depend on the wavelength of the considered modes, and the way they are resolved by the grid (see Fig. 5.8):

- The low frequency eigenmodes that are correct solutions of the system of equations follow sine-distribution of the form $\hat{\rho}(x)=\sin(kx)$, with wavenumbers k of the order $k\approx\frac{n\pi}{L}$, $n=1,2,3,...$ and L the length of the domain. The domain is discretized by N gridpoints separated by Δx, such that $L\approx N\Delta x$, and hence $k\approx\frac{n\pi}{N\Delta x}$. The factor $k\Delta x$ is therefore proportional to $\frac{n\pi}{N}$. In order to correctly capture the n-th mode, $\frac{n\pi}{N}<<1$ must be satisfied. The artificial viscosity term scaling by $(k\Delta x)^4\approx(\frac{n\pi}{N})^4$, its

influence can be considered negligible for the first n modes. However, for higher order modes which are less well discretized by a given mesh and for whom $\frac{n\pi}{N} << 1$ does not hold anymore, the artificial viscosity term will cause errors. This means that for one, the shape of the respective mode will change slightly, and what is more important, the predicted growth rate will be found to be more stable than it should be.

- In this sense, a point-to-point oscillation can be compared to a mode of very high frequency: if they are considered as waves with a wavelength of $\lambda = 2\Delta x$ (cf. Fig. 5.8), the factor $k\Delta x$ is found to $k\Delta x = \frac{2\pi}{\lambda}\Delta x = \pi$. The artificial viscosity term, weighted with $(k\Delta x)^4$, becomes then the preponderant term.

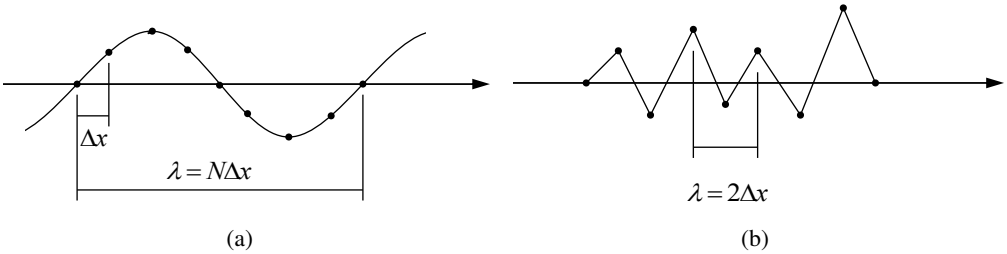

Figure 5.8: Eigenmode and spurious wave

Thus, the formulation of the artificial viscosity term as a fourth order derivative means that structures of short wavelengths are more affected than those with big wavelengths. Besides, it is possible to control the amplitude of the artificial viscosity term and the waves on which it will act by adjusting the factor ϵ_4. As its value may depend on the case that is considered (flow parameters, quality of the mesh, etc.) it is not possible to determine an universal optimum value. However, the above considerations allow to ensure that the artificial viscosity term is small enough in order to be negligible for the calculation of the first eigenmodes: Using the expressions derived for the artificial viscosity term and the physical RHS term of Eq. (5.19), one may determine the value of ϵ_4 that leads to the two terms being equally large:

$$\epsilon_4 \frac{|u+c|}{16\Delta x}(k\Delta x)^4 = (k\Delta x)\frac{c}{\Delta x}.$$

Using the considerations about the wavelength and resolution of physical and spurious waves, one may thus deduce a minimal and maximal order of magnitude for ϵ_4 (assuming that $M << 1$, i.e. $|c+u| \approx |c|$):

- for $k\Delta x = \frac{2\pi}{\lambda}\Delta x = \frac{2\pi}{N}$ as required for physical modes, one finds a maximum value of $\epsilon_4 = \frac{16N^3}{(2\pi)^3}$. An artificial viscosity term of this amplitude will affect modes discretized with N gridpoints such that $\lambda = N\Delta x$ (see Fig. 5.8(a))
- for $k\Delta x = \pi$, which characterizes spurious waves, one finds the minimum value $\epsilon_4 = \frac{16}{\pi^3}$. In order to affect point-to-point oscillations, the artificial viscosity should thus be of this order of magnitude.

5.2 Results of the 2D Study

The following sections present the results that have been obtained with the 2D LEE solver implemented according to the description of section 5.1. The results for the different test configurations are validated by the 1D solver of Chapter 4, a time domain flow solver and experimental data, respectively.

5.2.1 Configuration I: 1D Flame

As a first test case, the 1D-flame configuration presented in the 1D study is computed with the 2D LEE solver. This way, the results of section 4.2.2 serve as reference for the 2D computations.
The computations of the 1D solver are carried out on a grid of 1000 equidistant points, which corresponds to a uniform cell size of $\Delta x = 0.001$ m. In contrast to that, the 2D domain is discretized using about 8700 triangular cells, the mesh being refined in the flame zone (see Fig. 5.9). For the 2D mesh, a cell size of about $\Delta x = 0.001$ m is only reached in the flame zone, whereas near the boundaries the mesh is coarser with a cell size of the order of $\Delta x = 0.01$ m.

Figure 5.9: Mesh used for the 2D computation. Marker: reference point for $n-\tau$-model at $x = 0.47$.

The mean flow field, flame model parameters and boundary conditions correspond to those of section 4.2.2: at the domain inlet, pressure and temperature amount to $p_0^{in} = 101325$ Pa and $T_0^{in} = 300$ K, respectively. At $x = 0.5L$, a flame covering a zone of $\delta_f = 0.05L$ heats the flow up to $T_0^{out} = 1200$ K. Computations have been carried out for inlet Mach numbers of $M_0^{in} = 0.001$ and $M_0^{in} = 0.15$. The resulting distributions of Mach number, pressure and Temperature are displayed in Fig. 5.10.
The parameters of the flame model are set to the values $n = 3$ and $\tau = 0.5$ ms. Finally, the boundary conditions that are imposed read

$$(\hat{u}_x + \frac{u_0}{\rho_0 c_0^2})\big|_{x=0} = 0 \quad , \quad \hat{u}_y\big|_{x=0} = 0 \qquad \text{and} \qquad \hat{s}\big|_{x=0} = 0$$

at the domain inlet, whereas the outlet is defined by

$$(\hat{p} + \rho_0 u_u \hat{u})\big|_{x=L} = 0.$$

For the computations with the 2D solver, spurious point-to-point oscillations are suppressed by the use of 4^{th} order artificial viscosity. As described in section 5.1.3.4, the amplitude of this term is set to a value that ensures that only spurious wiggles are affected, while the eigenmodes are left unchanged. In this computation, 2^{th} order artificial viscosity is not used.

The comparison between the 2D and the 1D solver is illustrated for the results of the third eigenmode of the domain. The eigenfrequencies obtained for this mode by the two codes are noted in Table 5.1.

The results of the 1D and 2D solvers show very good agreement: The real frequencies determined by the 2D solver are virtually the same as those computed by the 1D solver. The

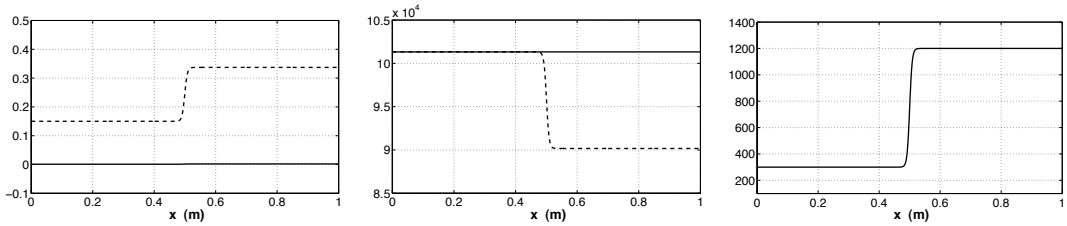

(a) Mach number M_0 (b) pressure p_0 in Pa (c) Temperature p_0 in K

Figure 5.10: Mean flow field of the 1D flame configuration. —— : $M_0^{in} = 0.001$; - - - : $M_0^{in} = 0.15$

	f (Hz) 1D Solver	f (Hz) 2D Solver
$Ma = 0.001$	$582.0 + 55.1i$	$581.9 + 54.0i$
$Ma = 0.15$	$540.6 - 19.5i$	$539.2 - 20.7i$

Table 5.1: 3rd mode at $\delta_f = 0.05L$ at low and high Mach . Comparison of 1D and 2D solver.

growth rates predicted by the 2D solver are slightly more stable than those predicted by the 1D solver. This is probably due to the coarser discretization of the computational domain in the 2D computation.

A comparison of the mode shapes obtained with the 1D and 2D solver is shown in Fig. 5.11. The spatial distribution of the modules of pressure, velocity and entropy fluctuations is shown for the case where the mean flow velocity is close to zero.

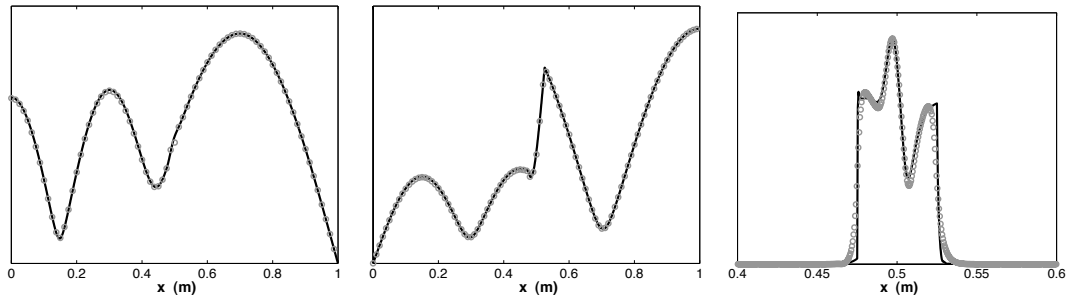

(a) $\left|\hat{p}(x)\right|$ (b) $\left|\hat{u}_x(x)\right|$ (c) $\left|\hat{s}(x)\right|$. Zoom on Flame Zone

Figure 5.11: Mode shape at $M_0 = 0.001$. Solid Line: 1D solver. Circles: 2D solver

Again, the predictions of the 1D and 2D code are virtually the same. As illustrated in Fig. 5.11(c), the entropy fluctuations are more or less restricted to the flame zone when the mean flow velocity is very low. Their spatial distribution involves steep gradients on both sides of the flame zone, that have to be captured appropriately. The convected entropy waves are structures with a wavelength much shorter than the acoustic wavelength, by a factor that corresponds to the mean flow mach number $\lambda_e/\lambda_{ac} = u/c = M$. This emphasizes that especially at low Mach numbers, discretization is an important issue.

5.2.2 Configuration II: Nozzle Flow

As a second test case for the 2D LEE solver, the flow through a tube connected to a choked isentropic nozzle is investigated [120]. A flame and therefore entropy fluctuations are not considered here, which allows to discretize the domain with a coarser mesh. The domain has a total length of $L = 2\mathrm{m}$ and is discretized using about 2800 triangular cells, the mesh being refined around the nozzle throat (see Fig. 5.12).
The mean flow field of this configuration is determined numerically. The mean flow Mach number at the domain inlet is of about $M_0^{in} = 0.11$. After an acceleration in the nozzle, the flow reaches $M = 1$ at the nozzle throat and is supersonic across the complete outlet section. The distribution of mean Mach number, temperature and pressure along the x-direction are shown in Fig. 5.13. It should be noted that the walls of the configuration are described by boundary conditions that allow a tangential velocity component ('slip walls'). The boundary layers are hence not taken into account, which is reflected by the coarse mesh in that region.

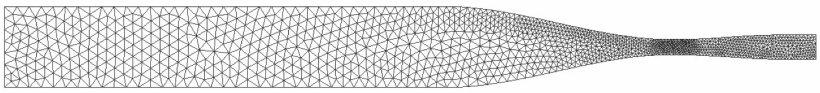

Figure 5.12: Mesh used for the computation of a choked nozzle flow.

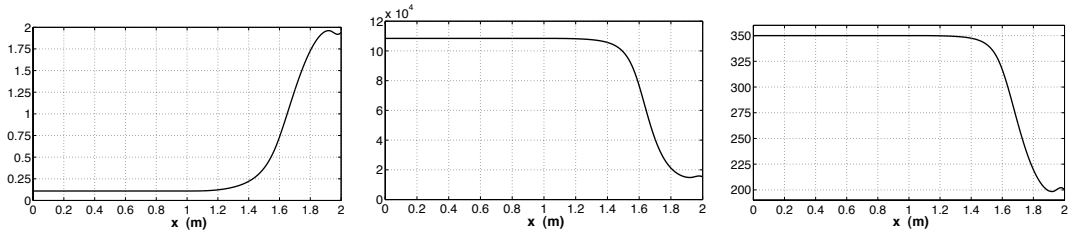

(a) Mach number M_0 (b) Pressure p_0 in Pa (c) Temperature T_0 in K

Figure 5.13: Mean flow field

5.2.2.1 Validation of 2D Computations using the Code AVBP

The results obtained by the LEE solver are validated by time domain computations carried out with the flow solver AVBP [15] . This code provides the possibility to solve the compressible Euler equations on unstructured grids. The approach used for comparison of the results between the two codes is the following:

1. The mean flow field is determined using the time domain solver.
2. Based on the mean flow field determined by the time domain flow solver, the LEE solver computes resonant frequencies, growth rates and mode shapes of the first resonant modes.
3. At the same time, the frequencies of the resonant modes are determined using the time domain flow solver. To this end, the flow field has to be excited in a suitable way. One

possibility is to run the calculation imposing a perturbation on one single node in the region upstream of the nozzle throat, e.g. an increased value for mean pressure. Another option is to excite the field at its inlet boundary, adding a time-periodic signal of small amplitude to one of the inlet conditions. This time-periodic signal is composed of a sum of N sinusoids covering the frequency range to be investigated, i.e. a finite Fourier series with a sufficiently small fundamental frequency f_0 and harmonics of equal amplitude ϵ up to the maximum frequency of interest $f_{max} = N f_0$, of the form

$$\phi(\mathbf{x}_{inlet}, t) = \phi_0(\mathbf{x}_{inlet}, t)\big(1 + \epsilon \sum_{n=1}^{N} \sin(2\pi n f_0 t)\big)$$

The perturbation needs to be of small amplitude, so that the error due to disturbing the boundary condition can be considered negligible.
In order to determine the resonant frequencies of the domain, it is then sufficient to capture the temporal evolution of a flow variable, e.g. pressure or velocity, at a suitable location. Those are the areas where the flucuations in the respective quantities are expected to be maximal. Adapted positions are indicated in the mode shapes determined by the LEE solver. The temporal evolution of these quantities contains information about the frequencies that respond to the excitation. These frequencies can then be determined by applying a Fourier transform to the respective result signal.

4. Finally, the time domain solver is used to verify the growth rate of one of the modes computed by the LEE solver. As the flow field of the time domain flow solver is dominated by the least damped mode, only the growth rate of this latter can be determined. To this end, the distribution of fluctuating quantities at an initial time $t_0 = 0$ is reconstructed from the mode shape and resonant frequency determined by the LEE solver (step 2). As introduced in section 2.2, the expression that links the frequency domain and the time domain fields reads $\phi_1(\mathbf{x}, t) = \Re(\hat{\phi}(\mathbf{x})e^{-i\omega t})$. The field $\phi_1(\mathbf{x}, t_0)$ being determined this way, it is superimposed to the mean flow as initial perturbation of small amplitude ϵ, such that $\phi(\mathbf{x}, t_0) = \phi_0(\mathbf{x}) + \epsilon\phi_1(\mathbf{x}, t_0)$. As the frequency domain LEE solver does not give any information about the amplitude of the perturbations, an arbitrary but small value for ϵ, of the order of 1-5% of the mean flow values, is applied.
Starting the time domain computation with this initial field, the decay rate of the mode that is investigated can directly be determined by following the temporal evolution of the perturbation.

In order to realize this comparison and interaction of a time-domain flow solver and a frequency-domain code for acoustics, the boundary conditions used in the two codes have to be compatible.
At the outlet, the supersonic mean flow sets the boundary condition for both the time domain and frequency domain solvers. As no information can travel upstream in a supersonic flow, it is not meaningful to impose any boundary values at the outlet. This means also that for the acoustic solver, the domain is implicitly restricted to the part upstream of the nozzle throat. Even though the part of the domain downstream of the nozzle throat is included in the computation, it does not have an influence on the results for the resonant frequencies.
At the inlet, the time domain solver requires information about the mass flow rate $\dot{m}(t)$ that enters the domain. In terms of acoustic variables, fixing the mass flow rate means suppressing any fluctuations of that quantity, i.e. $\dot{m}_1 = (\rho u)_1 = 0$. As no entropy fluctuations are supposed

to enter the domain, this corresponds to a boundary condition for the acoustic solver that sets the acoustic flux to zero, i.e. $u_0\hat{\rho} + \rho_0\hat{u} = 0$.
In order to capture the resonant frequencies of the domain and to verify the growth rate of a mode (steps 3 and 4), the boundary conditions of the time-domain flow solver have to be reflecting for acoustic waves. This issue is adressed in the solver AVBP by the use of characteristic boundary conditions (NSCBC [81]).

5.2.2.2 Application to the Frequency Domain Results

Based on the mean flow field described above, the results for the steps 2-4 are the following:

Step 2:

The values obtained by the 2D LEE solver for the complex eigenfrequencies of the first three modes are gathered in Table 5.2. As no source terms for acoustic energy are present in the domain, but acoustic energy is convected outside of the domain, all modes are damped.

	f (Hz) (domain Fig. 5.12)	f (Hz) (extended domain)
1	$132.79 - 7.50i$	$132.74 - 7.42i$
2	$259.31 - 17.60i$	$259.32 - 17.53i$
3	$375.36 - 35.93i$	$375.38 - 35.85i$

Table 5.2: First Eigenvalues obtained by the 2D LEE solver

These results have been checked by a second computation, for which the domain was extended by $0.5\mathrm{m}$ beyond the initial outlet (see Table 5.2, right column). As this extension is situated beyond the sonic nozzle throat, it may not have an influence on the resonant frequencies of the domain. The results obtained for the extended domain being virtually the same as those of the initial computation, they confirm that the passage to supersonic flow is correctly captured by the solver.

Step 3:

The resonant frequencies of the domain are then computed by the time domain flow solver. The excitation of the flow field is achieved by adding the small amplitude signal described above to the mass flow rate at the inlet. The response is captured by recording the pressure signal near the domain inlet, as all modes feature a pressure maximum at this position. After the mean pressure is substracted from the signal, a discrete Fourrier transform is carried out, yielding the result displayed in Fig. 5.14.

The resonant frequencies of the domain determined this way are of $f_1 = 131$ Hz, $f_2 = 259$ Hz and $f_3 = 379$ Hz. These values correspond very well to those determined by the LEE solver. The high damping rates for the higher order modes are reflected in the Fourier transform plottet in Fig. 5.14 by less pronounced peaks for the 2nd and 3rd mode.

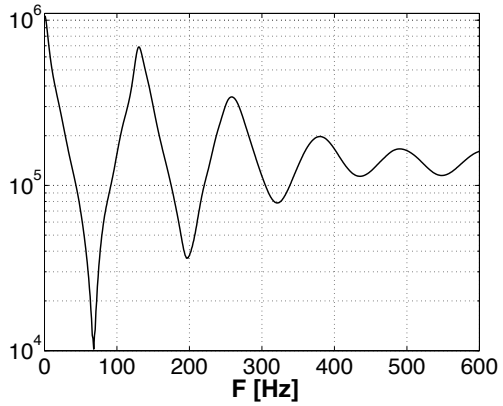

Figure 5.14: Discrete Fourier Transform of the pressure signal at the domain inlet. Maximum response is obtained at the frequencies $f_1 = 131$Hz, $f_2 = 259$Hz, $f_3 = 379$Hz.

Step 4:

Finally, the damping rate of the least damped mode is verified by the time-domain flow solver. In this case, this is the first longitudinal mode of the configuration, whose shape is illustrated via $|\hat{\rho}(\mathbf{x})|$ in Fig. 5.15.

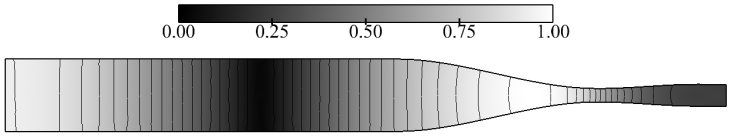

(a) Module $|\hat{\rho}(\mathbf{x})|$

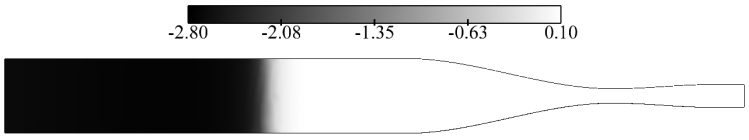

(b) Phase $\arg(\hat{\rho}(\mathbf{x}))$

Figure 5.15: Spatial structure of the first eigenmode.

The mode being superimposed to the mean flow field, the pressure signal is again recorded at the domain inlet, i.e. at a point of maximum pressure. Fitting an envelope curve of the form $e^{\omega_i t}$ to this signal allows to deduce the damping rate (see Fig. 5.16).

The first mode has a cycle increment of $\zeta = \exp(\frac{2\pi\omega_i}{\omega_r}) - 1 = -0.299$, meaning that the amplitude of the perturbation decreases by about 30% per period. Thus, the signal is damped after very few oscillations, which limits the precision of the damping rate determined this way. The value deduced from the flow solver is of $f_i \approx -8.5$ Hz, which is still in good agreement

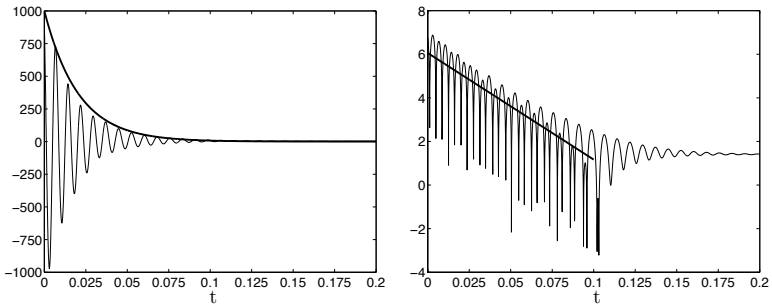

(a) pressure signal and fitted curve $p'_0 e^{\omega_i t}$ (b) logarithm of pressure signal $\ln(p')$ and fitted curve

Figure 5.16: Temporal evolution of pressure signal at domain inlet for first eigenmode.

with the value predicted by the LEE solver.
Besides, the fact that the pressure signal at the inlet follows very neatly a function of the form $\cos(\omega_r t)e^{\omega_i t}$ indicates that the first mode that is introduced as initial condition oscillates without irregularities. This way, the transfer of the field of fluctuating quantities from the LEE solver to the time domain flow solver confirms the mode shape that has been determined.

The results found by the time domain solver show hence overall good agreement with those of the LEE solver, confirming that all relevant terms are correctly taken into account.

5.2.3 Configuration III

The third test case for the 2D LEE solver is based on the CVRC (Continuously Variable Resonance Combustor) experiment conducted at Purdue University [104, 122], which allows to compare the results of the LEE computations to measured frequencies and mode shapes. Besides, the configuration is computed with the Helmholtz solver AVSP, showing the differences between a zero and a non zero Mach number approach.
The basic setup being that shown in Fig. 5.17, the CVRC experiment can be adjusted to various forms in terms of geometries, fuels and operating conditions: the length of the oxidizer tube and the combustion chamber as well as the devices that determine the inlet boundary condition can be varied; besides, both gaseous and liquid fuel may be used. The conditions that are the basis for the computations are those used by Sisco et al. [104] and are summarized in the following.

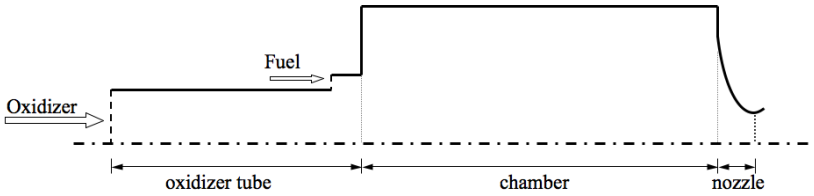

Figure 5.17: Schematic view of the Configuration

Figure 5.17 shows a schematic view of the configuration: The setup is composed of an oxidizer tube that leads into the combustion chamber, the fuel being injected shortly upstream of the combustion chamber inlet. Downstream, the configuration ends in a short sonic nozzle. The characteristics of these three main components are gathered in Table 5.3:

Oxidizer Tube	Length 9.2 ” = 23.37 10^{-2}m	Diameter 0.81” = 2.05 10^{-2}m	Cross section 3.3 10^{-4} m^2
Chamber	Length 15.0 ” = 38.10 10^{-2}m	Diameter 1.77” = 4.50 10^{-2}m	Cross section 15.9 10^{-4} m^2
Nozzle	Length 0.35 ” = 0.89 10^{-2}m		Cross section at throat 3.4 10^{-4} m^2

Table 5.3: Main parameters of the geometry

As the LEE solver is designed for handling 2D configurations only, all calculations are carried out on the 2D planar equivalent of this 3D radial geometry.

The boundary conditions of the configuration are characterized as follows:

- **inlet:** from the designs available for the inlet of the oxidizer tube, two have been retained for the presented comparison: the acoustically open inlet, that produces a pressure node at the inlet position, and the choked inlet, that defines a constant mass flow rate

- **outlet:** the outlet is defined acoustically by the sonic nozzle throat. However, the nozzle being short, it may be represented by a condition that produces a velocity node at the chamber outlet

5.2.3.1 Experimental Data and Mean Flow Conditions

The mean flow conditions are characterised by the following experimental settings [104]:

- the oxidizer consists of 42% by weight of oxygen gas, and 58% by weight of water vapour; the mass flow rate is of $\dot{m}_{oxi} = 0.53$ kg/s
- the fuel is the kerosene-based JP-8, with a mass flow rate of $\dot{m}_{fuel} = 0.08$ kg/s
- the nominal oxidizer-to-fuel ratio is of 6.2, the combustion efficiency of 90%
- the pressure in the combustion chamber and oxidizer tube is of ca. 2.6 MPa

Using this information, the conditions describing the unburnt and burnt gas that are relevant for the computations with the Helmholtz solver and the LEE solver can be deduced. The parameters retained for the computations are gathered in Table 5.4:

$\dot{m}_u$ [kg/s]	T_u [K]	p_u [MPa]	ρ_u [kg/m^3]	R_u [J/(kg K)]	γ_u	c_u [m/s]	u_u [m/s]	M_u
0.53	871.4	2.58	8.791	336.8	1.210	595.9	183.14	0.307
$\dot{m}_b$ [kg/s]	T_b [K]	p_b [MPa]	ρ_b [kg/m^3]	R_b [J/(kg K)]	γ_b	c_b [m/s]	u_b [m/s]	M_b
0.61	2717.8	2.59	2.435	389.8	1.184	1120.0	157.85	0.141

Table 5.4: Parameters of unburnt (index u) & burnt (index b) gas

The parameters gathered in Table 5.4 allow to generate a simplified mean flow field for the computations with the Helmholtz and LEE solver. According to Sisco et al. [104], the flame can be assumed to be situated at around 3.8 cm downstream of the chamber inlet. The mean flow field is thus set up in a way that the transition from cold to hot gas conditions occurs at that position. Temperature, density, pressure, speed of sound and gas constant are prescribed in a very simple manner as function of the x-position only. While the Helmholtz solver assumes $\mathbf{u} = 0$ throughout the whole domain, the LEE solver requires in addition information about a velocity field. It should be noted that the velocity of the hot gas in the combustion chamber is smaller than the velocity of the cold gas in the oxidizer tube. This results from the change in cross section, which decreases the flow velocity at the passage from the oxidizer tube into the chamber. The acceleration of the flow caused by the flame is not sufficient to compensate for the area change.

5.2.3.2 Computation with the Helmholtz Solver AVSP

Firstly, the configuration described above is computed with the Helmholtz solver AVSP. This code solves the problem stated by Eq. (2.71) for a mean flow that is considered to be at rest. As this condition is not satisfied near the choked outlet of the configuration, the nozzle is not included in the computational domain. Instead, its effect is described by an appropriate boundary condition.
The boundaries of the domain are described by the following conditions:

- **choked inlet:** The choked inlet is represented by a real valued impedance:
  This condition impedes fluctuations in mass flow rate, i.e. $\dot{m}_1 = (\rho u)_1 = 0$, or in other terms, $\rho_0 u_1 = -\rho_1 u_0$. At the same time, no entropy fluctuations are present, such that $p_1 = c_0^2 \rho_1$. From that, one may deduce an impedance Z:

$$Z = \frac{p_1}{\rho_0 c_0 u_1} = \frac{p_1}{-u_0 c_0 \rho_1} = \frac{c_0^2 \rho_1}{-u_0 c_0 \rho_1} = -\frac{c_0}{u_0}$$

- **open inlet:** The open inlet is represented by a pressure node boundary condition
- **walls:** All walls impose a zero velocity perpendicular to the wall, while tangential velocity is admitted
- **outlet:** The choked outlet is represented by a complex impedance at the position of the chamber outlet, the nozzle itself being not included in the computational domain. The impedance is computed using the tool "NOZZLE" described in section 4.2.1.1. The effect of the choked nozzle is shown in Figure 5.18 in terms of its reflection coefficient. For the frequency spectrum of interest, the reflection coefficient of the nozzle is very close to $|R| = 1$, i.e. the nozzle acts very much like a velocity node boundary condition.

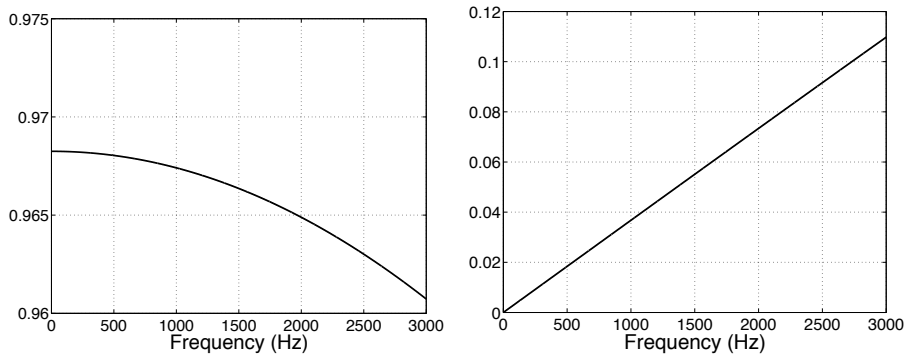

(a) $|R|$ (b) $\arg(R)$

Figure 5.18: Reflection Coefficient of the Choked Outlet Nozzle

5.2.3.3 Computation with the 2D LEE Solver

Secondly, the configuration is analyzed with the 2D LEE solver. As mentioned above, this requires an appropriate description of the velocity field. While the distribution of density, pressure, temperature, speed of sound and gas constant can be described as function of x-position only, this is not possible for the velocity field. Attention has to be paid to the aspect that flow may enter or leave the domain only at the correct positions, i.e. that wall normal velocity components vanish at all solid boundaries. Otherwise, losses due to convection of acoustic energy might considerably change the growth rate and presumably also the shape of the mode. The velocity field is thus function of x- and y-position, even though it still a very simple description: For the present calculations, the velocity in x-direction corresponds to the field shown in Fig. 5.19, while the velocity in y-direction is neglected. The velocity field of Fig. 5.19 is generated based on the flow velocities of cold gas in the oxidizer tube and hot gas in the chamber, and ensures that the mass flow rate is constant across area changes. This leads

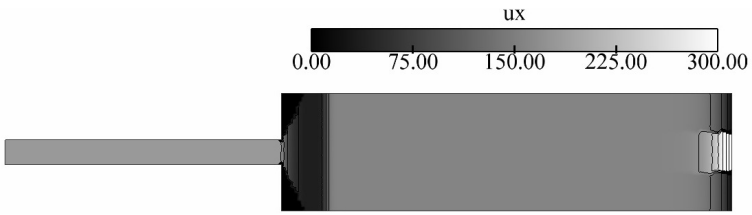

Figure 5.19: Velocity in x-direction

to the deceleration at the chamber inlet, and the acceleration towards the nozzle at the chamber exit. As indicated by Fig. 5.19, the LEE computations are first carried out for the same domain as used for the Helmholtz computations, i.e. the nozzle is not included in the computational domain.

The boundary conditions used for the LEE computations correspond to those imposed by the Helmholtz solver. As convection is taken into account, three conditions have to be imposed at inflow boundaries, and one condition at outflow boundaries. In the present case, the boundaries are described by the conditions below:

- **choked inlet:** as described above, the choked inlet impedes fluctuations of mass flow rate, i.e. $\dot{m}_1 = (\rho u)_1 = 0$. The mean flow is considered to be 1D at this position, such that the choked inlet condition is imposed as

  $$\hat{u}_x = -\frac{u_{0,x}}{\rho_0}\hat{\rho}.$$

  Vorticity waves are suppressed at the inlet by imposing $\hat{u}_y = 0$. Besides, no entropy fluctuations are assumed to enter the domain, i.e. $\hat{s} = 0$.

- **open inlet:** As for the Helmholtz solver, the open inlet is described in terms of a pressure node. In terms of the unknowns of the 2D problem, this corresponds to imposing $\hat{\rho} = 0$, $\hat{u}_y = 0$ and $\hat{s} = 0$

- **outlet:** The outlet is represented by a node of acoustic velocity $\hat{u}_x = 0$ at the position of the nozzle inlet

- **walls:** The wall boundary condition inhibits velocity perturbations normal to the wall, but allows tangential velocity fluctuations. No condition is imposed for entropy fluctuations. This condition allows to describe a solid wall provided that the mean flow velocity field is imposed correctly, i.e. that convection across the wall is not possible.

5.2.3.4 Comparison of Results

In the following, the results of the 2D LEE solver are compared to those of the Helmholtz solver AVSP as well as those obtained in the experimental campaign. The modes of interest in this configuration are those with high pressure fluctuations inside the chamber ("chamber modes"); modes that are characterized by high amplitudes of pressure fluctuations in the oxidizer tube while the level of pressure perturbation inside the chamber is low are not considered. Experimental data is available for the first of these chamber modes. It is therefore this mode that is discussed in the following.

Experiment	Helmholtz solver	LEE solver
1375 / 1390 Hz	$1423.64 - 27.55i$ Hz	$1382.62 - 68.85i$ Hz

Table 5.5: Eigenfrequency of the first chamber mode, choked inlet

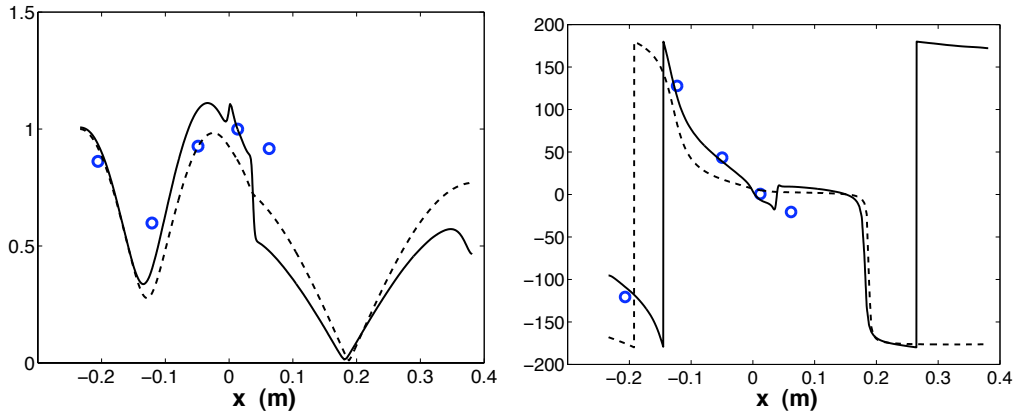

(a) mod $(\hat{p})$ (b) arg$(\hat{p})$

Figure 5.20: Comparison of results for choked inlet: —— : LEE solver − − − : Helmholtz solver. Symbols: experiment. Position $x = 0$ marks the inlet of the chamber.

Firstly, the results obtained for the choked inlet boundary condition are presented. The frequencies obtained experimentally from two measurements as well as those predicted by the two numerical tools are gathered in Table 5.5.

As flame acoustic interaction is not taken into account here, the Helmholtz solver as well as the LEE solver predict damped modes, while the first chamber mode is observed to be unstable in the experiments. Yet, the real frequency of the first chamber mode is captured with acceptable accuracy by the two codes. The LEE solver predicts a slightly lower frequency of oscillation than the Helmholtz solver. This observation is in agreement with the observations made in the 1D study between zero and non zero Mach number computations. In the present case, the LEE solver predicts the frequency of the first chamber mode quite exactly (at least within the experimental uncertainty), while the Helmholtz solver overpredicts it by about 3%.

Figure 5.20 shows a comparison of the mode shape of the first chamber mode as obtained from the 2D LEE solver, the Helmholtz solver and the experiments, i.e. the modulus and phase of the fluctuating pressure as observed along the axis of the oxidizer tube and the chamber. Both codes predict very similar mode shapes, which are in good agreement with the experimental results. Unlike the result of the Helmholtz solver, the mode shape predicted by the LEE solver is characterized by a noticeable step at the position where the flame is imposed, i.e. at around $x = 0.038$m. This suggests that the LEE computations are rather sensitive to the description of the mean flow field.

The phase of the pressure signal as predicted by the LEE solver is in good agreement with the experimental data. The result of the Helmholtz solver is very similar to that of the LEE solver in the chamber part of the configuration, i.e. for $x > 0$. However, the Helmholtz solver does not correctly predict the overall phase difference between the inlet of the oxidizer tube and the chamber inlet. The results of the LEE solver show a better agreement with the measurements

Experiment	Helmholtz solver	LEE solver
1440/1450 Hz	$1517.33 - 6.13i$ Hz	$1501.42 - 79.97i$ Hz

Table 5.6: Eigenfrequency of the first chamber mode, open inlet

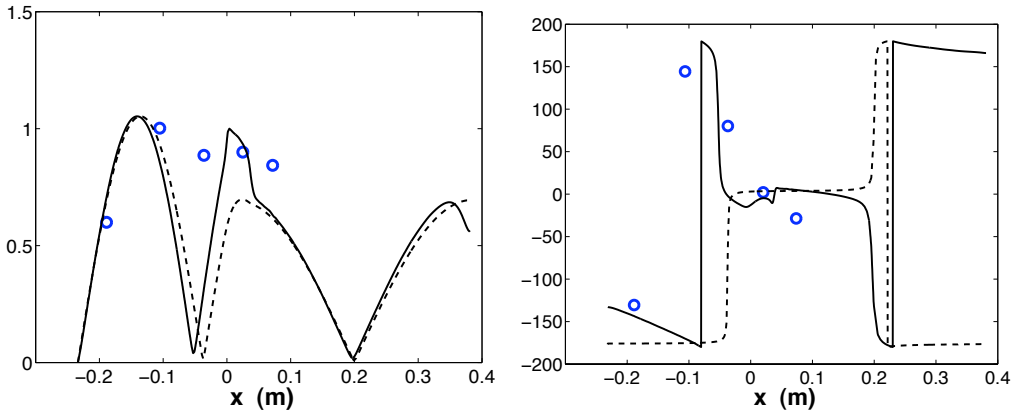

(a) mod $(\hat{p})$ (b) arg$(\hat{p})$

Figure 5.21: Comparison of results for open inlet: —— : LEE solver – – – : Helmholtz solver. Symbols: experiment

in this part of the configuration.

The second set of results concerns the case where the inlet is acoustically open, i.e. corresponding to a pressure node at the inlet of the oxidizer tube. The frequencies obtained for the first chamber mode under these conditions are noted in Table 5.6.

In this case, the boundary conditions are set in a way that only very little losses of acoustic energy are accounted for in the Helmholtz calculation: The inlet boundary condition $\hat{p} = 0$ impedes flux of acoustic energy, and the outlet nozzle acting very much as a velocity node, losses are small here, too. As a result, the mode determined by the Helmholtz solver has a imaginary frequency close to zero. The LEE computation takes into account loss of acoustic energy due to convection effects, and predicts thus a mode with a higher damping rate.
Again, both codes allow to capture the real frequency of the first chamber mode with acceptable accuracy. Similarly to what is observed for the case with choked inlet, the real frequencies predicted by the LEE solver are slightly lower than those predicted by the Helmholtz solver, and thereby closer to the measured result.

Figure 5.21 shows the modulus and phase of the pressure fluctuations in oxidizer tube and combustion chamber. In this case, the amplitude of the pressure perturbations determined by the two codes differ considerably in the zone of the chamber inlet around $x = 0$, and are less well capturing the experimental results: Those latter predict a continously high level of pressure perturbations from the second half of the oxidizer tube to the part near the chamber inlet, whereas the computational results obtained by both codes contain a pressure node in this zone. Concerning the phase of the pressure perturbations, it is predicted as piecewise constant by the Helmholtz solver. In contrast to that, the LEE results are in better agreement with the experiment. It should be noted here that capturing the phase of the pressure perturbation correctly is an important part of thermo-acoustic calculations: The phase difference between fluctuations in pressure and heat release rate at the position of the flame impacts on the role of the flame-

acoustic interaction as a source or sink of acoustic energy.

The following focusses on the results of the LEE solver. In order to evaluate the sensitivity of its results on boundary conditions, the description of both inlet and outlet are modified. The eigenfrequencies and mode shapes are then compared to those obtained in the above sections.

Variation of the Outlet Boundary Condition

Subsequently to the LEE computations carried out without the outlet nozzle as described so far, the domain is extended to include the nozzle. The following shows the results of the LEE solver from computations with and without the outlet nozzle. This comparison is carried out for the configuration with choked inlet, i.e. the inlet boundary is described by the conditions $\hat{u}_x = -\frac{u_{x,0}}{\rho_0}\hat{\rho}$, $\hat{u}_y = 0$ and $\hat{s} = 0$. The outlet is then either described by imposing a node of acoustic velocity at the nozzle inlet in the case where the nozzle itself is not included in the computational domain. In the case where the nozzle is part of the domain, the acoustic boundary condition is defined by the sonic nozzle throat.
Changing the description of the domain outlet leads to a slight change in eigenfrequency predicted by the LEE solver. Without the nozzle, an eigenfrequency of $f = 1382.62 - 68.85i$ Hz was obtained, whereas the computation including the nozzle predicts a frequency of $f = 1368.10 - 139.33i$ Hz. The modified description impacts thus above all the damping rate, while the frequency of oscillation is only little affected.
The shape of the first chamber mode as obtained by the LEE solver for the two descriptions of the outlet is shown in Fig. 5.22. Reflecting the limited impact observed in the frequency of oscillation, the distribution of $|\hat{p}(x)|$ is virtually unchanged. However, the phase of the pressure perturbation is modified in the second part of the chamber. While the computations without the nozzle predict a decrease from $\arg(\hat{p}) = 0$ to $\arg(\hat{p}) = -\pi$, the computations that include the nozzle predict rather an increase. Nevertheless, the two descriptions predict a constant phase at $+/-\pi$ near the outlet. However, as experimental results are not available for this part of the configuration, an assessment of this observation is not possible.

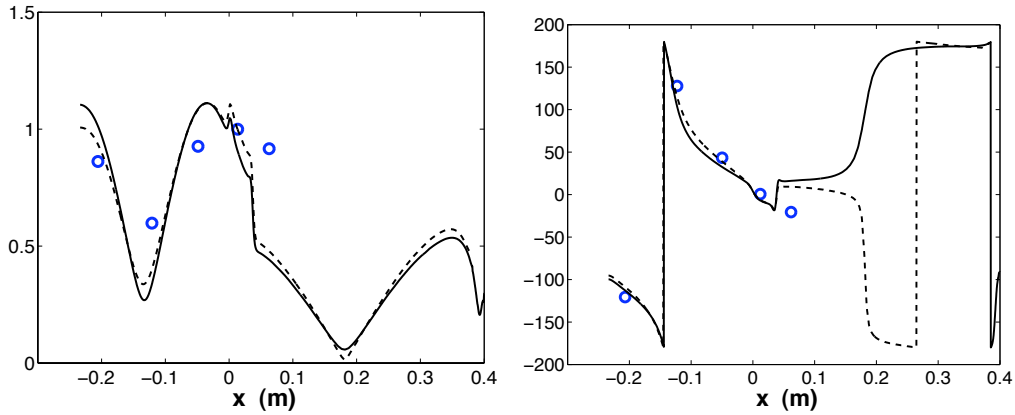

(a) mod $(\hat{p})$ (b) $\arg(\hat{p})$

Figure 5.22: Results of LEE solver for different outlet boundary descriptions. —— : LEE computation including the outlet nozzle − − − : LEE computation without the outlet nozzle. Symbols: experiment

Variation of the Inlet Boundary Condition

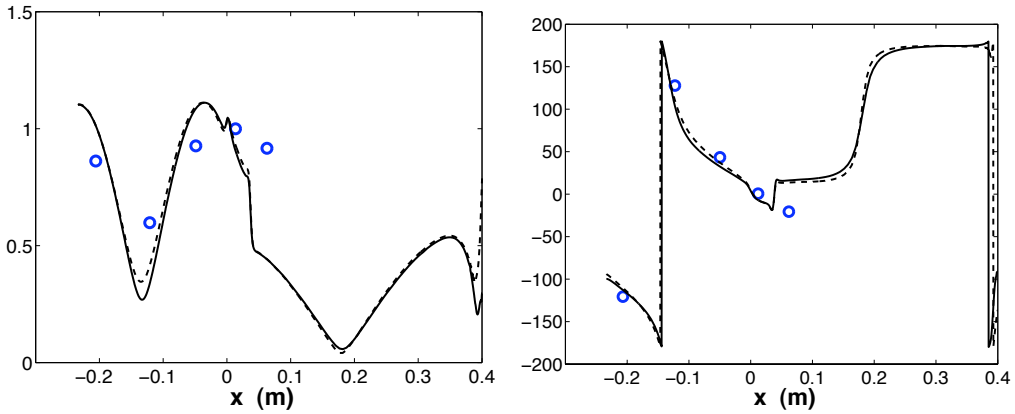

(a) mod $(\hat{p})$ (b) arg$(\hat{p})$

Figure 5.23: Comparison of results for closed inlet: —— : LEE solver with $\hat{s} = 0$ at the inlet. − − − : LEE solver with $\hat{H} = 0$ at the inlet. Symbols: experiment

Finally, the inlet boundary condition is modified in order to reach an improved description of a choked inlet. While the condition that imposes a constant mass flow rate is obviously maintained, the assumption that no entropy waves may enter the domain is dismissed. In the case of a choked nozzle as an inlet boundary, the upstream travelling acoustic wave interacts with the shock that defines the inlet. Though, this interaction allows the creation of entropy waves [61], which are then convected by the flow downstream. While this aspect is negligible in a Helmholtz solver, where convection effects are not taken into account, it may be of importance in a LEE solver.
Therefore, the condition that no entropy waves may enter the domain is replaced by a condition that imposes a constant total enthalpy at the inlet [104]. This means that the expression $\hat{s} = 0$ is replaced by $\hat{H} = C_p\hat{T} + u_x\hat{u}_{0_x} = 0$, while all other conditions at inlet and outlet are left unchanged. Imposing a constant total enthalpy $\hat{H} = 0$ corresponds to imposing a entropy perturbation of the form $\hat{s} = -\frac{1}{T_0}\left(\frac{\hat{p}}{\rho_0} + u_x\hat{u}_{0_x}\right)$.

The results show only a very small impact of this modified boundary condition: The frequency of the first chamber mode changes from $f = 1368.10 - 139.33i$ Hz for the case where the constant entropy boudary condition $\hat{s} = 0$ was used, to $f = 1376.94 - 139.29i$ Hz when the total enthalpy was imposed to $\hat{H} = 0$. Accordingly, modulus and phase of the pressure perturbation are virtually unchanged (see Fig. 5.23).
Nevertheless, the constant total enthalpy boundary condition leads to entropy fluctuations entering the domain, as can be seen in Fig. 5.24. The plots show that $|\hat{s}|$ is clearly non zero at the domain inlet when this boudary condition is used. However, the level of entropy fluctuations decreases very quickly along the oxidizer tube, and reaches about zero at the chamber inlet at $x = 0$ (see Fig. 5.24(a)). The situation is then very similar to the one created by the boundary condition that imposes $\hat{s} = 0$ at the inlet, in the sense that all entropy perturbations present in the domain originate from the flame. As can be observed in Fig. 5.24, modulus and phase of the entropy perturbations are virtually the same for the two computations downstream of the flame (the phase of $\hat{s}$ is not plotted in the oxidizer tube part $x < 0$ for the boundary condition

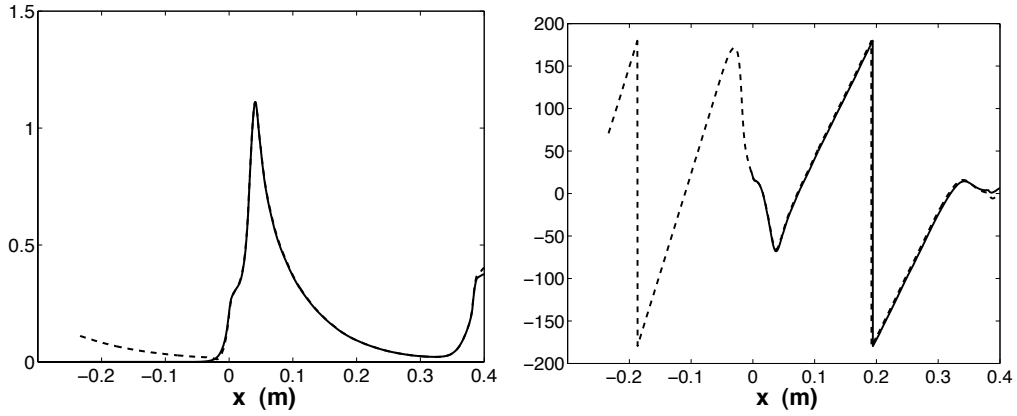

(a) mod $(\hat{s})$ (b) arg$(\hat{s})$

Figure 5.24: Comparison of module and phase of entropy perturbation for the two inlet boundary conditions: —— : LEE solver with $\hat{s} = 0$ at the inlet. − − − : LEE solver with $\hat{H} = 0$ at the inlet.

imposing $\hat{s} = 0$ at the inlet (solid line), as the modulus of $\hat{s}$ is zero in this zone).

The observation of this decaying curve for $|\hat{s}(x)|$ for a mode that is damped disagrees with what is expected to result from Eq. (4.39). That latter equation predicts an increasing envelope curve for convected hot spots in damped configurations, as the perturbations present at a downstream position have been released from the flame at an earlier time, when the overall level of perturbation was higher (cf. Fig. 4.14). The results shown in Fig. 5.24 do hence not satisfy Eq. (4.39) in the sense that the amplitude of the convected entropy hot spots $\mathcal{E}$ is not constant in uniform flow regions. The reason for this is the introduction of an artificial viscosity term into the system of equations, which is acting as a damping term on oscillations of small wavelength. As the wavelength of the entropy waves is much smaller than that of the acoustic waves, scaling by a factor $\lambda_e/\lambda_{ac} \approx M$, the former are susceptible to be affected by artificial viscosity while the considerations of section 5.1.3.4 ensure that the acoustic waves are left unchanged.
Even though this behaviour seems undesirable at a first view, it can be used to recover the decay of the amplitude of entropy waves on their way downstream that occurs in realistic systems. This damping is caused by dissipation, which is not taken into account in the system of equations solved in this study. The artificial viscosity term that was introduced to stabilize the system of equations from a numerical point of view could thus be adjusted to represent the physical impact of viscosity on convected entropy.

Chapter 6

Extended Analysis of Results

In the following chapter, the results obtained with the 1D LEE solver presented in chapter 4 are further analyzed. The objective is to discuss in more detail the mechanisms that occur in the system and their impact on its stability.
To this end, the eigenfrequencies and eigenmodes obtained from the 1D LEE solver are studied in postprocessing evaluations. In separate sections, the following two aspects are discussed:
In a first time, the budget of disturbance energy that can be attributed to a given eigenmode is analyzed. Reconstructing the temporal evolution of the amplitudes of the fluctuating quantities allows to assess the processes that lead to energy gain or loss in the system. By separately evaluating flux terms at the boundaries and several source terms, the impact of boundary conditions, mean flow parameters and flame-acoustic interaction can be assessed.
In a second time, the issue of the system being non normal is discussed. It is shown how the fact that the eigenvectors obtained from the preceding computation are in general not orthogonal may lead to short term energy growth in the system.

6.1 Balance of Disturbance Energy Budget

In this section, the modes that have been computed by the 1D LEE solver as presented in Chapter 4 are evaluated in terms of the energy they contain. This analysis allows to better understand the origin of differences between zero and non zero Mach number mean flow computations, and the mechanisms that lead to stable or instable modes.

Descriptions of the energy of acoustic perturbations exist in various forms, the definitions being derived for different applications: among the most known works are those of Cantrell & Hart [13] who state an acoustic energy definition for irrotational flows at uniform entropy. This description is later extended by Morfey [70] to be applicable to arbitrary uniform flows. However, when it comes to configurations that include combustion processes, the energy term must be extended from the purely acoustic energy to a more general definition of disturbance energy, which takes into account entropy fluctuations. Equations for such a generalized energy term have been derived by Chu [16] and Pierce [79] for mean flows at rest and later by Myers [72] for arbitrary steady flows. The corollary for disturbance energy derived by Myers [72] has later been extended by Karimi et al. [53] to include combustion terms. This definition of energy contained in disturbances is of course closely linked to the Rayleigh criterion stated in Chapter 1, which describes the conditions under which combustion instability may occur. Starting from the expression given by Rayleigh [87], the description of the source term in thermo-acoustic configurations has since been discussed and extended (e.g. [16, 75, 40]).

6.1.1 Mathematical Formulation

The study presented here is based on the energy corollary by Myers [72] and extended by Karimi et al. [53] as derived in section 2.3.2. It is recalled that this energy balance reads:

$$\frac{\partial E_2}{\partial t} + \frac{\partial W_2}{\partial x} = D_2 \tag{6.1}$$

with E_2 the first-order disturbance energy density, W_2 the first-order disturbance energy flux vector and D_2 the dissipation rate of first-order disturbance energy per unit volume. For an inviscid flow where vorticity can be neglected, these terms read (cf. section 2.3.2):

$$E_2 = \frac{p_1^2}{2\rho_0 c_0^2} + \frac{\rho_0 u_1^2}{2} + \rho_1 u_0 u_1 + \frac{\rho_0 T_0 s_1^2}{2c_{p_0}} \tag{6.2}$$

$$W_2 = \frac{u_0}{\rho_0} p_1 \rho_1 + p_1 u_1 + u_0^2 \rho_1 u_1 + u_0 \rho_0 u_1^2 + \rho_0 u_0 T_1 s_1 \tag{6.3}$$

$$D_2 = -s_1(\rho_1 u_0 + \rho_0 u_1)\frac{dT_0}{dx} + s_1 \rho_0 u_0 \frac{dT_1}{dx} + T_1 \left(\frac{q_1}{T_0} - \frac{q_0 T_1}{T_0^2} \right) \tag{6.4}$$

The above expressions show that the situation is considerably more complex when Mach number effects are taken into account: 8 out of the 14 terms contained in the definitions of E_2, W_2 and D_2 are related to the mean flow velocity. Furthermore, it should be noted that the term D_2 is composed of five different contributions, which may act both as source or sink terms. The contributions are evaluated separately lateron, and therefore noted as $D_{2,1}$ to $D_{2,5}$:

$$D_2 = \underbrace{-s_1 \rho_1 u_0 \frac{dT_0}{dx}}_{D_{2,1}} \underbrace{-s_1 \rho_0 u_1 \frac{dT_0}{dx}}_{D_{2,2}} \underbrace{+s_1 \rho_0 u_0 \frac{dT_1}{dx}}_{D_{2,3}} \underbrace{+T_1 \frac{q_1}{T_0}}_{D_{2,4}} \underbrace{-\frac{q_0 T_1^2}{T_0^2}}_{D_{2,5}} \tag{6.5}$$

The terms $D_{2,1}$ and $D_{2,3}$ depend directly on the mean flow velocity and describe hence effects linked to the convection of perturbations. $D_{2,1}$ can be added to $D_{2,2}$ to give $(-s_1 m_1 \mathrm{d}T_0/\mathrm{d}x)$, with m_1 the fluctuating mass flow rate, This term expresses thus an interaction of entropy fluctuations s_1 with mass flow rate fluctuations m_1 in regions of varying mean temperature $\mathrm{d}T_0/\mathrm{d}x$, such as the flame. $D_{2,4}$ and $D_{2,5}$ express the contribution of the fluctuating and the mean heat release rate, respectively.

Using the eigenvectors computed by the 1D LEE solver, the temporal signals of pressure, velocity and entropy fluctuations can be reconstructed by re-establishing the harmonic waveforms they represent. The relation $\phi'(x,t) = \Re(\hat{\phi}(x)\exp(-i\omega t))$ gives this temporal form from the mode shape $\hat{\phi}(x) = |\hat{\phi}(x)|\exp(i\arg\phi(x))$ and complex frequency ω. Based thereupon, the separate terms of Eq. (6.2) to (6.4) can be computed. This reconstruction of the disturbance energy balance allows for one to verify the accuracy of the numerical results, in the sense that a closed balance corroborates the eigenmodes found by the LEE solver. Besides, the computation of the individual terms of the energy balance allows to identify the role of each term and thereby judge the importance of separate mechanisms.

The expression for the disturbance energy of Eq. (6.1) is then integrated in time over one period of oscillation T and in space over the domains volume V, which yields:

$$\int_V E_2 \mathrm{d}x\big|_{t=T} - \int_V E_2 \mathrm{d}x\big|_{t=0} + \int_T W_2 \mathrm{d}t\big|_{x=L} - \int_T W_2 \mathrm{d}t\big|_{x=0} - \int_V \int_T D_2 \mathrm{d}x\mathrm{d}t = 0 \quad (6.6)$$

In the following, a compact notation will be used, where angle brackets $< \cdot >$ denote the time integration from $t = 0$ to $t = T$ and the overbar $\bar{\cdot}$ stands for the space integration from $x = 0$ to $x = L$. Setting the energy density initially contained in the domain as a reference value to $\overline{E_2^{t=0}} = 1$, one obtains the scaled balance:

$$\overline{E_2^{t=T}} + [< W_2 >]_{x=0}^{x=L} - \overline{< D_2 >} = 1 \quad (6.7)$$

This integrated balance states hence that the amount of energy contained in the domain after one period of oscillation, $\overline{E_2^{t=T}}$, differs from the initial value $\overline{E_2^{t=0}} = 1$ by the amount of energy lost at the boundaries during this time $[< W_2 >]_{x=0}^{x=L}$ and by the amount of energy added by the source term $\overline{< D_2 >}$. This integrated balance is furthermore directly related to the notion of stability of the modes, in the sense that an unstable mode is characterised by increasing energy density $\overline{E_2^{t=T}} - 1 > 0$. More precisely, $\overline{E_2^{t=T}} = \exp(2\omega_i T)$ holds for each of the modes, and thus $\overline{E_2^{t=T}} > 1$ for an unstable mode with $\omega_i > 0$, and $\overline{E_2^{t=T}} < 1$ for a stable mode with $\omega_i < 0$.

6.1.2 Results for a 1D Configuration

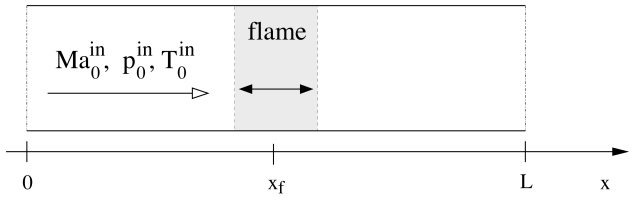

Figure 6.1: Configuration used for the analysis of the disturbance energy budget.

The analysis of the budget of disturbance energy is carried out for the quasi 1D configuration introduced in section 4.2.2. The flame covers a rather big length of $\delta_f = 0.15L$ here, in order to avoid problems due to insufficient discretization: some of the source terms exist only inside the flame region, which makes it important to well capture this zone. However, the grid being composed of a series of equidistantly spaced points, it is not possible to refine locally. Therefore, a good tradeoff between reasonable number of grid points and sufficient precision requires a long flame.

6.1.2.1 Case without Unsteady Heat Release Rate: $\hat{q} = 0$

At first, the configuration is analyzed without the unsteady heat release rate, i.e. the results of section 4.2.2.2 are revisited. As has been mentioned in that section, an interesting aspect in this configuration is the impact of losses of disturbance energy across the domain's borders and their evolution with growing Mach number: depending on the formulation of the boundary conditions, a flux of acoustic energy may or may not occur at the domain inlet and outlet, which can have considerable effects on the modes' growth rates.

The computation is therefore conducted with the two sets of the boundary conditions introduced in chapter 4, i.e. the set of "simple" boundary conditions, that allow acoustic flux across the domain boundaries; and the set of boundary conditions that block the acoustic flux at inlet and outlet, while however allowing entropy fluctuations to be convected out of the domain. The conditions are recalled here and read as follows:

- "simple" boundary conditions:

$$\begin{aligned} x = 0: &\quad \hat{u} = 0 \quad \text{and} \quad \hat{s} = 0 \\ x = L: &\quad \hat{p} = 0 \end{aligned} \tag{6.8}$$

- "no acoustic flux" boundary conditions:

$$\begin{aligned} x = 0: &\quad \hat{u} + \tfrac{u_0}{\rho_0 c_0^2}\hat{p} = 0 \quad \text{and} \quad \hat{s} = 0 \\ x = L: &\quad \hat{p} + \rho_0 u_0 \hat{u} = 0 \end{aligned} \tag{6.9}$$

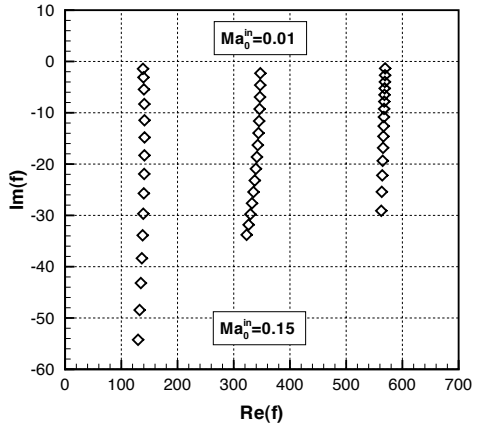

(a) Boundary Conditions that allow acoustic flux, cf. Eqs. (6.8)

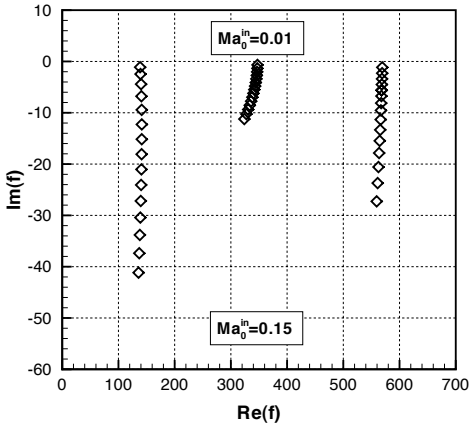

(b) Boundary Conditions that impede acoustic flux, cf. Eqs. (6.9)

Figure 6.2: Frequencies of the first three eigenmodes for $M_0^{in} = 0.01$ to $M_0^{in} = 0.15$; $\delta_f = 0.15L$

		'simple' BC	'no acoustic flux' BC
$M_0^{in} = 0.01$	1	$138.52 - 1.43i$	$138.52 - 1.11i$
	2	$347.26 - 2.30i$	$347.28 - 0.67i$
	3	$569.23 - 1.35i$	$569.23 - 1.15i$
$M_0^{in} = 0.15$	1	$129.80 - 54.25i$	$135.75 - 41.16i$
	2	$322.86 - 33.79i$	$323.87 - 11.22i$
	3	$562.38 - 29.10i$	$559.31 - 27.27i$

Table 6.1: Frequencies of the first three eigenmodes at $M_0^{in} = 0.01$ and $M_0^{in} = 0.15$, cf. Fig. 6.2

The evolution of the eigenfrequencies of the first three modes with increasing inlet Mach number is plotted for both sets of boundary conditions in Fig. 6.2, and the values obtained at the highest and lowest Mach number considered here are regrouped in Table 6.1. The plots shown in Fig. 6.2 correspond to the results presented in Fig. 4.13 for the boundary conditions allowing acoustic flux, and to those presented in Fig. 4.16 for the boundary conditions impeding acoustic flux. However, in difference to the case discussed in section 4.2.2.2, the flame covers a larger zone in the configuration discussed here, with $\delta_f = 0.15L$ instead of $\delta_f = 0.05L$.
As discussed in section 4.2.2.2, the modes are all marginally stable when the mean flow is at rest and tend towards stable modes when the mean flow velocity increases. This indicates that loss and source terms are balanced or zero at low Mach number, whereas the losses outweigh the gain at higher mean flow speed. At the same time, the damping rates obtained at $M_0^{in} = 0.15$ are higher when acoustic flux across the boundaries is allowed, an issue that is especially noticeable for the second mode (cf. Fig. 6.2(a)), which has been explained by higher losses at the domain inlet and outlet than in the case where acoustic flux is prohibited.

It is therefore the second mode of this configuration that is analysed in the following, with the separate terms of the integrated energy balance of Eq. (6.7) being computed for the two types of boundary conditions, each time at low and high Mach number.

	'simple' BC		'no acoustic flux' BC	
	$M_0^{in} = 0.01$	$M_0^{in} = 0.15$	$M_0^{in} = 0.01$	$M_0^{in} = 0.15$
f [Hz]	$347.26 - 2.30i$	$322.86 - 33.79i$	$347.28 - 0.67i$	$323.87 - 11.22i$
$\overline{E_2^{t=T}}$	0.92	0.27	0.98	0.65
$[< W_2 >]_{x=0}^{x=L}$	0.05	2.12	0.00	1.70
$\overline{< D_2 >}$	-0.02	1.40	-0.02	1.36
$\sum$ cf. Eq. (6.7)	0.99	0.99	1.00	0.99

Table 6.2: Terms of time and space integrated disturbance energy balance Eq. (6.7) for the 2^{nd} eigenmode at low and high Mach number

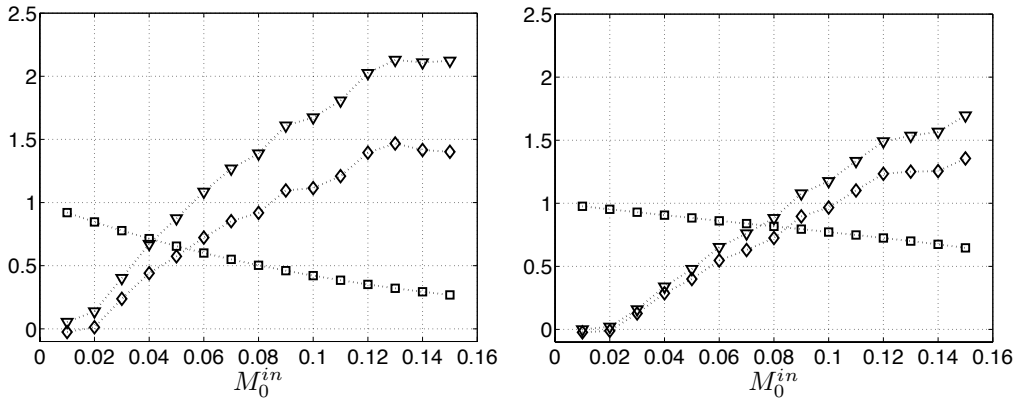

(a) Boundary Conditions that allow acoustic flux, cf. Eqs. (6.8)

(b) Boundary Conditions that impede acoustic flux, cf. Eqs. (6.9)

Figure 6.3: 2^{nd} eigenmode: Terms of the time and space integrated disturbance energy balance Eq. (6.7) for $M_0^{in} = 0.01$ to $M_0^{in} = 0.15$. $\square$ $\overline{E_2^{t=T}}$: space integrated energy density after one period of oscillation, $\triangledown$ $[< W_2 >]_{x=0}^{x=L}$: time integrated flux of energy density at inlet and outlet, $\diamond$ $\overline{< D_2 >}$: time and space integrated source term

The results obtained from this computation are gathered in Table 6.2. First of all, it should be noted that the integrated balance of Eq. (6.7) is satisfied for all the cases: The sum of all terms adds up to one, the error of 1% being acceptable. Secondly, it can easily be verified that the value of disturbance energy contained in the domain after one period of oscillation, $\overline{E_2^{t=T}}$, reflects the growth rate of the corresponding mode. In all cases, the relation

$$\overline{E_2^{t=T}} = \exp\left(2\omega_i T\right) = \exp(\frac{4\pi f_i}{f_r})$$

is satisfied. As all modes are stable, the energy after one period of oscillation is smaller than the reference value at $t = 0$ that was set to $\overline{E_2^{t=0}} = 1$.
The results of Table 6.2 confirm that at low Mach number, the two sets of boundary conditions are equivalent and produce the same effect: the flux term as well as the source term are close to zero, leading to marginally stable modes. At higher Mach number, both flux and source terms are non zero, as they contain terms linked to the mean flow speed (cf. Eqs. (6.3) and (6.4)). However, while the source term at $M_0^{in} = 0.15$ reaches about the same value irrespective of

	'simple' BC		'no acoustic flux' BC	
	$M_0^{in} = 0.01$	$M_0^{in} = 0.15$	$M_0^{in} = 0.01$	$M_0^{in} = 0.15$
f [Hz]	$569.23 - 1.35i$	$562.38 - 29.10i$	$569.23 - 1.15i$	$559.31 - 27.27i$
$\overline{E_2^{t=T}}$	0.97	0.52	0.97	0.54
$[< W_2 >]_{x=0}^{x=L}$	0.00	1.68	0.00	1.71
$\overline{< D_2 >}$	-0.03	1.23	-0.03	1.28
$\sum$ cf. Eq. (6.7)	1.00	0.97	1.00	0.97

Table 6.3: Terms of time and space integrated disturbance energy balance Eq. (6.7) for the 3^{rd} eigenmode at low and high Mach number

the boundary conditions ($\overline{< D_2 >} = 1.40$ and $\overline{< D_2 >} = 1.36$ for simple and no acoustic flux conditions respectively), the value for the acoustic energy flux is considerably different for the two sets of boundary conditions.
An interesting aspect can be observed when comparing the flux of disturbance energy across the domain boundaries for the two sets of boundary conditions: In the case where acoustic energy flux is not allowed across the boundaries, the flux term of Eq. (6.3) is reduced to its last component, the integrated term reading

$$[< W_2 >]_{x=0}^{x=L} = \int_{t=0}^{t=T} (\rho_0 u_0 T_1 s_1)_{x=L} \, \mathrm{d}t.$$

Even though the loss of disturbance energy is in this case only due to entropy hot spots being convected out of the domain, the value of $[< W_2 >]_{x=0}^{x=L}$ is rather high, reaching about 80% of the flux term that is observed when using the "simple" boundary conditions. This suggests that damping effects due to losses of disturbance energy by convection of hot spots out of the domain can be considerable.

For a more detailed picture, the evolution of the different terms of the integrated energy balance of Eq. (6.7) with growing Mach number are shown in Fig. 6.3. The plots show that in agreement with the continuous decrease in ω_i, the energy term evolves smoothly towards lower values of $\overline{E_2^{t=T}}$ with higher Mach number. At the same time, both flux and source term increase with the Mach number. However, this increase is not necessarily proportional to the mean flow velocity as has been shown in [119]. The important factor is that flux and source terms evolve in the same way. It can be noticed from Fig. 6.3 that the observations made for $M_0^{in} = 0.15$ in Table 6.2 are valid for the complete span of mean flow Mach numbers: in all cases, the source term is only little influenced by the boundary conditions, whereas the flux at the boundaries is reduced significantly when acoustic energy flux across the domain limits is prohibited by the boundary conditions.

However, the choice of boundary conditions does not always have an impact on the damping rate: As shown in Fig. 6.2, the third mode is virtually not influenced by the set of boundary conditions that are chosen. The growth rate, i.e. the rate of change in energy density, is about the same for the simple as for the flux-blocking boundary conditions. The individual terms of the energy balance are gathered in Table 6.3. They indicate that for the third mode, not only the source term, but also the flux term is little influenced by the boundary conditions.

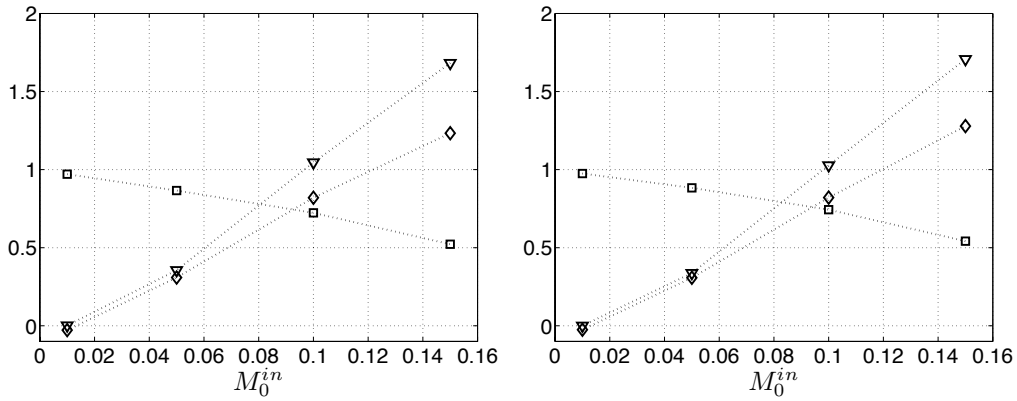

(a) Boundary Conditions that allow acoustic flux, cf. Eqs. (6.8)

(b) Boundary Conditions that impede acoustic flux, cf. Eqs. (6.9)

Figure 6.4: 3^{rd} eigenmode: Terms of the time and space integrated disturbance energy balance Eq. (6.7) for $M_0^{in} = 0.01$ to $M_0^{in} = 0.15$. $\square$ $\overline{E_2^{t=T}}$: space integrated energy density after one period of oscillation, $\triangledown$ $[< W_2 >]_{x=0}^{x=L}$: time integrated flux of energy density at inlet and outlet, $\diamond$ $\overline{< D_2 >}$: time and space integrated source term

This observation is underlined by Fig. 6.4, that shows a nearly identical evolution of flux and source terms with Mach number for the two sets of boundary conditions. As mentioned before, the observation that the flux term is only little affected by a change in boundary conditions suggests that the loss of disturbance energy at the domain's boundaries is essentially caused by convection of entropy perturbations, and that this aspect should thus be taken into account in the description of thermo-acoustic instability.
For a better understanding of the difference between the second and the third mode, the shapes of these two modes at $M_0^{in} = 0.15$ are plotted in Fig. 6.5 for both boundary conditions. The figure shows that the shape of the second mode (Fig. 6.5(a) ,(c), (e)) is much more influenced by the choice of boundary conditions than that of the third mode (Fig. 6.5(b) ,(d), (f)). The values of $|\hat{p}|$ and $|\hat{u}|$ at the domain outlet differ considerably for the two sets of boundary conditions for the second mode, indicating the flux of acoustic energy is clearly non zero if permitted by the boundary conditions. Besides, the losses due to flux of acoustic energy are accompanied by higher losses due to convection of entropy in the case of the second mode.

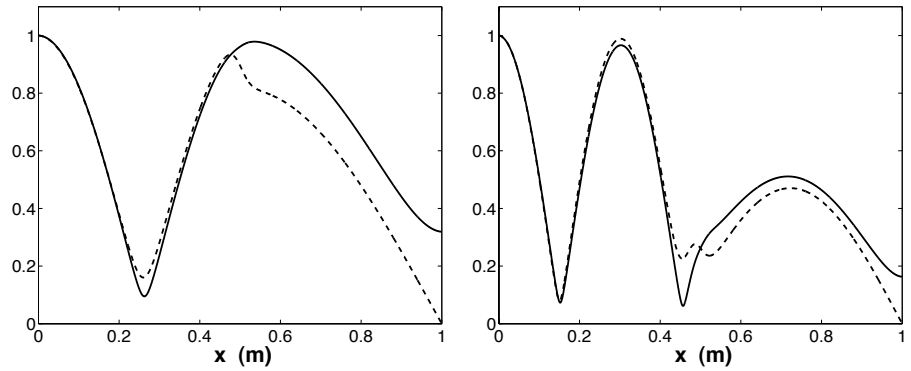

(a) Mode 2, $|\hat{p}(x)|$ (b) Mode 3, $|\hat{p}(x)|$

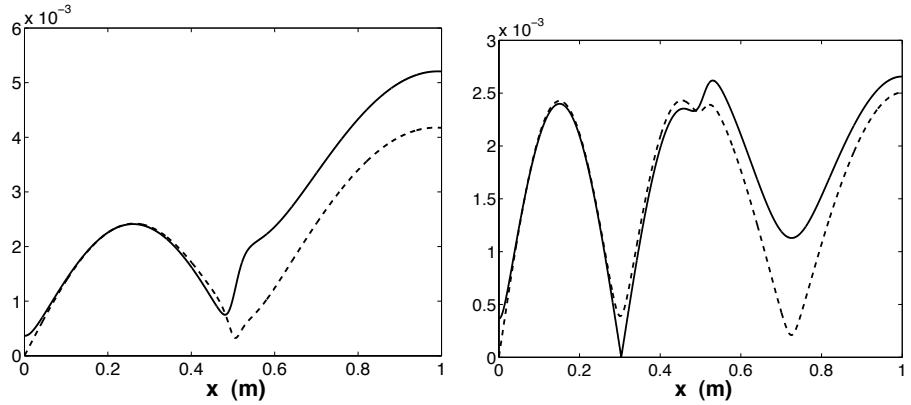

(c) Mode 2, $|\hat{u}(x)|$ (d) Mode 3, $|\hat{u}(x)|$

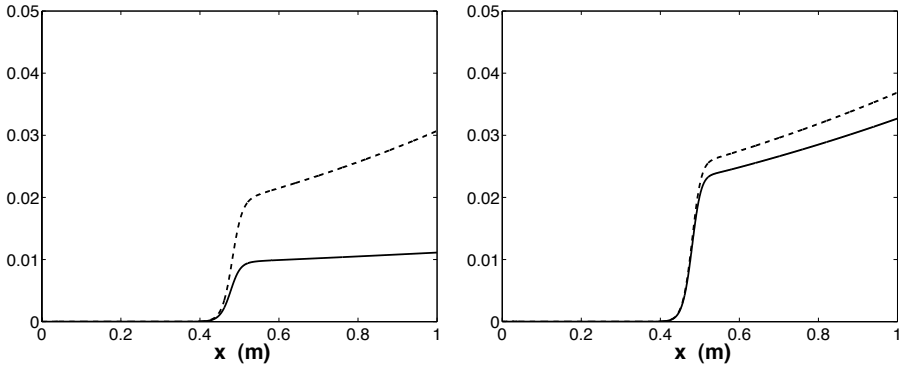

(e) Mode 2, $|\hat{s}(x)|$ (f) Mode 3, $|\hat{s}(x)|$

Figure 6.5: Comparison of Modeshape at high Mach number $M_0^{in} = 0.15$ for the two types of boundary conditions. Left column: 2^{nd} mode. Right Column: 3^{rd} mode. Normalisation is such that $|\hat{p}(0)| = 1$.
—— : Boundary Conditions that impede acoustic flux, cf. Eqs. (6.9) ;
– – – : Boundary Conditions that allow acoustic flux, cf. Eqs. (6.8)

6.1.2.2 Case with Unsteady Heat Release Rate: $\hat{q} \neq 0$

In the following section, the source term of Eq. (6.4) is analysed in more detail. To this end, the configuration of Fig. 6.1 is studied now including an unsteady heat release rate. The parameters of the unsteady heat release model are set to $n = 1$ and $\tau = 0.5$ms, and the flame covers a zone of $\delta_f = 0.15L$. In terms of boundary conditions the present computations are carried out imposing $\hat{u} = \hat{s} = 0$ at the inlet and $\hat{p} = 0$ at the outlet.
The parameters being chosen this way, the eigenfrequencies of the second mode evolve from unstable to stable when the Mach number is increased (see Fig. 6.6).

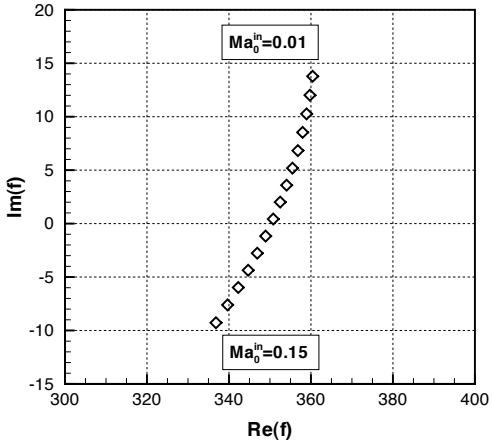

Figure 6.6: Eigenfrequency of the 2nd mode for $n = 1$, $\tau = 0.5$ms, and $\delta_f = 0.15L$.

The shape of this mode at $M_0^{in} = 0.01$ and $M_0^{in} = 0.15$ is plotted in Fig. 6.7. One observes that pressure and velocity fluctuations are only little influenced by the change in mean flow velocity, while the entropy fluctuations are significantly stronger. This suggests that convection of entropy outside of the domain has a strong stabilizing effect on the mode at $M_0^{in} = 0.15$. At the same time of course acoustic flux contributes to energy losses at the boundaries when the Mach number is not zero.

The separate contributions to the integrated energy balance of Eq. (6.7) corresponding to these two and intermediate Mach numbers are given in Table 6.4 and plotted in Fig. 6.8. As in the case without unsteady heat release rate, the term $[< W_2 >]_{x=0}^{x=L}$ is zero when the mean flow is at rest and increases with the mean flow speed. Again, this increase is not linear or even monotone - at $M_0^{in} = 0.14$ the flux is slightly smaller than at $M_0^{in} = 0.13$. This is due to the fact that the flux term is composed of several products of fluctuating quantities, that are each assumed to be harmonic in time. For a phase shift of $\pi/2$ between two of these signals, the time integral of their product is zero. This means that the value of the integrated flux term depends not only on the mean flow velocity and amplitude of the perturbations, but also on the relations between the separate quantities, and is therefore not straightforward to predict. The same is of course the case for the source term, which evolves with the mean flow Mach number in a way similar to the flux term. As shown in Fig. 6.8, the source term is however clearly non zero at low Mach number, leading to an unstable mode. At about $M_0^{in} = 0.1$, the loss term becomes more important than the source term, leading to a stable mode.

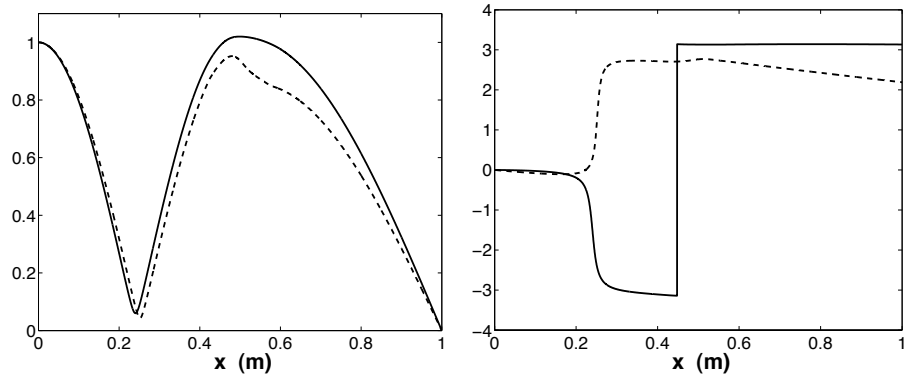

(a) $|\hat{p}(x)|$ (b) $\arg(\hat{p}(x))$

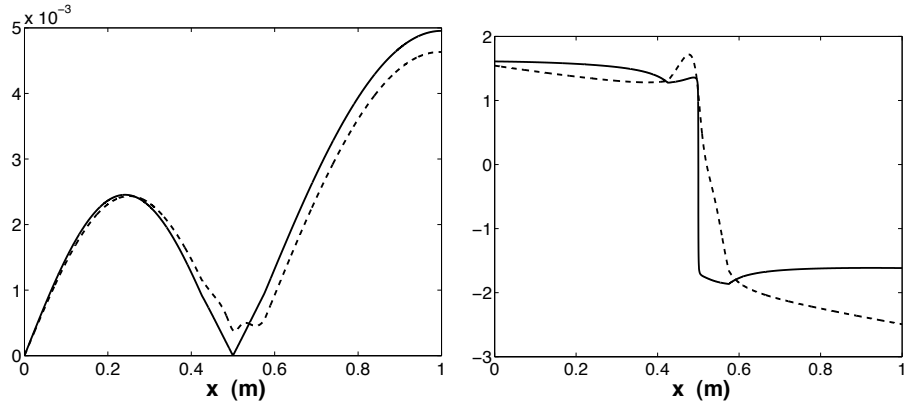

(c) $|\hat{u}(x)|$ (d) $\arg(\hat{u}(x))$

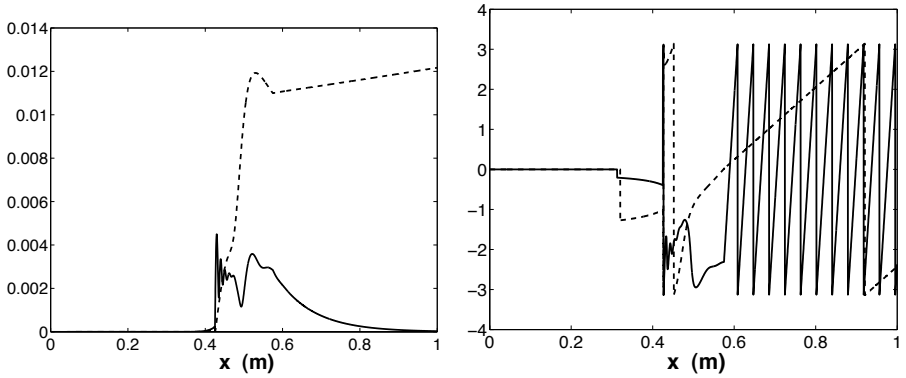

(e) $|\hat{s}(x)|$ (f) $\arg(\hat{s}(x))$

Figure 6.7: Structure of the 2nd Eigenmode at low and high Mach numbers.
—— : $Ma_0^{in} = 0.01$ ($f = 360.4 + 13.8i$Hz) --- : $Ma_0^{in} = 0.15$ ($f = 336.8 - 9.3i$Hz).

When fluctuations in heat release rate are involved, all the five source terms of Eq. (6.4) contribute to the energy balance. It can then be of interest to evaluate the different terms separately in order to get information about their order of magnitude and the nature of their contribution. This includes the overall impact of a term as either a source or a sink term as well as the spatial distribution of the separate source terms and of course the evolution of the separate terms with

	$\mathrm{M}_0^{\mathrm{in}} = 0.01$	$\mathrm{M}_0^{\mathrm{in}} = 0.05$	$\mathrm{M}_0^{\mathrm{in}} = 0.10$	$\mathrm{M}_0^{\mathrm{in}} = 0.15$
f [Hz]	$360.4 + 13.8i$	$356.8 + 6.8i$	$348.9 - 1.2i$	$336.8 - 9.3i$
$\overline{E_2^{t=T}}$	1.62	1.27	0.96	0.71
$[< W_2 >]_{x=0}^{x=L}$	0.07	0.50	1.34	1.80
$\overline{< D_2 >}$	0.69	0.82	1.33	1.53
$\overline{< D_{2,1} >} = \int\int(-s_1\rho_1 u_0 \mathrm{d}T_0/\mathrm{d}x)\mathrm{d}x\mathrm{d}t$	-0.01	0.21	0.90	1.18
$\overline{< D_{2,2} >} = \int\int(-s_1\rho_0 u_1 \mathrm{d}T_0/\mathrm{d}x)\mathrm{d}x\mathrm{d}t$	0.10	0.07	0.07	0.08
$\overline{< D_{2,3} >} = \int\int(s_1\rho_0 u_0 \mathrm{d}T_1/\mathrm{d}x)\mathrm{d}x\mathrm{d}t$	0.02	0.28	0.81	0.99
$\overline{< D_{2,4} >} = \int\int(T_1 q_1/T_0)\mathrm{d}x\mathrm{d}t$	0.66	0.47	-0.08	-0.23
$\overline{< D_{2,5} >} = \int\int(-q_0 T_1^2/T_0^2)\mathrm{d}x\mathrm{d}t$	-0.07	-0.21	-0.37	-0.49

Table 6.4: Active Flame: Terms of time and space integrated disturbance energy balance Eq. (6.7), separate contributions of source term: cf. Eq (6.4)

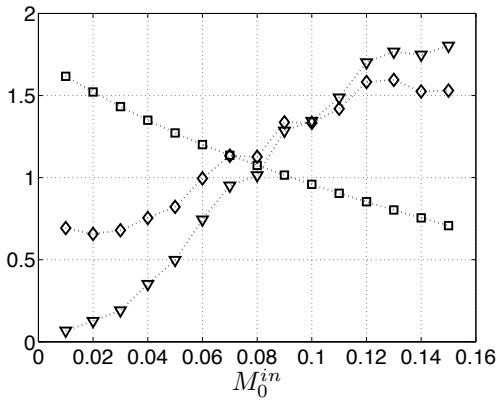

Figure 6.8: 2^{nd} eigenmode: Terms of the time and space integrated disturbance energy balance Eq. (6.7) for $M_0^{in} = 0.01$ to $M_0^{in} = 0.15$. $\square$ $\overline{E_2^{t=T}}$: space integrated energy density after one period of oscillation, $\triangledown$ $[< W_2 >]_{x=0}^{x=L}$: time integrated flux of energy density at inlet and outlet, $\diamond$ $\overline{< D_2 >}$: time and space integrated source term

the mean flow velocity.
The integrated values of the different source terms for $M_0^{in} = 0.01; 0.05; 0.10$ and 0.15 are summarized in Table 6.4. These figures show that at low Mach number, the contribution due to unsteady heat release rate, i.e. $\overline{< D_{2,4} >}$ is by far the most important - during one cycle of oscillation it generates about 66% of the energy initially contained in the system and therefore accounts almost entirely for the mode being unstable. This term reminds in its construction of the Rayleigh criterion (see chapter 1) and has been shown to be the equivalent of the Rayleigh term in cases where entropy fluctuations are considered [75].
The only other term not involving the mean flow velocity is $\overline{< D_{2,2} >}$, which describes the interaction of entropy fluctuations s_1 with velocity fluctuations u_1 in regions of varying mean entropy dT_0/dx. However, in the case presented here, this term contributes considerably less to the energy balance at low Mach number than the unsteady heat release term.
The remaining terms are directly related to u_0 and are therefore only of importance at non zero

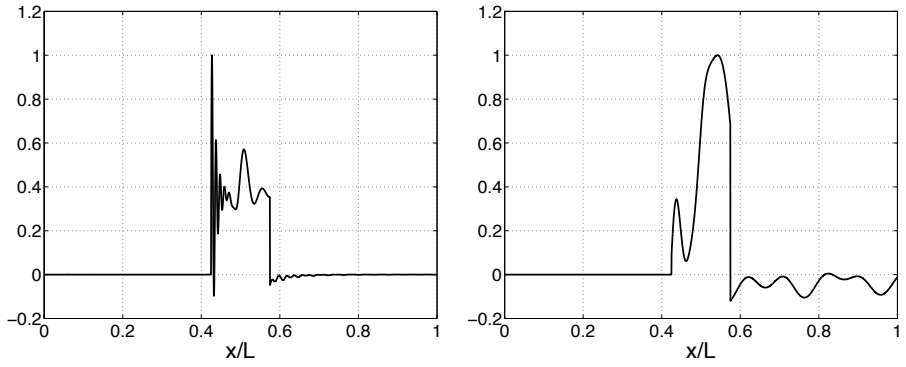

(a) $M_0^{in} = 0.01$ (b) $M_0^{in} = 0.05$

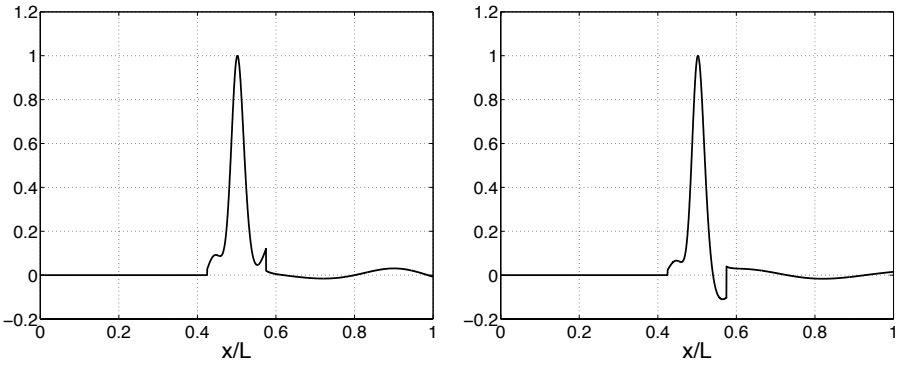

(c) $M_0^{in} = 0.10$ (d) $M_0^{in} = 0.15$

Figure 6.9: Spatial distribution of the time integrated source term $< D_2(x) >$ with increasing mean flow Mach number.

Mach number: $\overline{< D_{2,1} >}$ and $\overline{< D_{2,3} >}$ describe effects due to the convection of entropy fluctuations. $\overline{< D_{2,1} >}$ can thereby be combined with $\overline{< D_{2,2} >}$ to give $\int\int(-s_1 m_1 \mathrm{d}T_0/\mathrm{d}x)\mathrm{d}x\mathrm{d}t$, with m_1 being fluctuations in flow rate. Finally, $\overline{< D_{2,5} >}$ describes the contribution of the mean heat release rate, which is itself defined as $q_0 = \rho_0 u_0 c_p \mathrm{d}T_{t,0}/\mathrm{d}x$. By definition, the term $\overline{< D_{2,5} >}$ is always negative, i.e. the mean heat release of the flame has a stabilizing effect.

The values in Table 6.4 indicate that the integrated values of the source terms that depend on u_0 effectively get more important with the mean flow Mach number. The increasing stabilizing effect of the mean heat release term is thereby outbalanced by the energy gain due to $\overline{< D_{2,1} >}$ and $\overline{< D_{2,3} >}$, which leads to an overall increasing source term. At the same time, the unsteady heat release term inverses its behaviour and contributes as a sink term at $M_0^{in} = 0.10$ and 0.15.

In order to illustrate these observations, the spatial distribution of the time- (but not space-) integrated source term $< D_2(x) >$ is plotted in Fig. 6.9, and that of the separate contributions $< D_{2,1}(x) >$ to $< D_{2,5}(x) >$ in Table 6.5 for $M_0^{in} = 0.01;\ 0.05;\ 0.10$ and 0.15.
As first aspect, the plots underline that only one of the source terms, namely $< D_{2,3}(x) >$, is non zero outside of the flame, the others being related to either the mean temperature gradient or the unsteady heat release rate. As this term $< D_{2,3}(x) >$ accounts for the convection of entropy perturbations, it is represented by structures downstream that get smaller in scale with decreasing Mach number: entropy perturbations have a wavelength that is related to those

of the acoustic waves by $\lambda_e/\lambda_{ac} \approx u/c = M$, i.e. at low convection velocity they lead to structures far smaller than the acoustic wave length.
As a second aspect, one may note that all the separate terms except $< D_{2,5}(x) >$ get locally negative for at least one of the Mach numbers, meaning that the terms may act as a source term in one location and as a sink term in another. This effect is especially present for the unsteady heat release term, which inverses its overall role from a source of disturbance energy at low Mach number to a sink term at high Mach number, while locally still contributing as a source term.

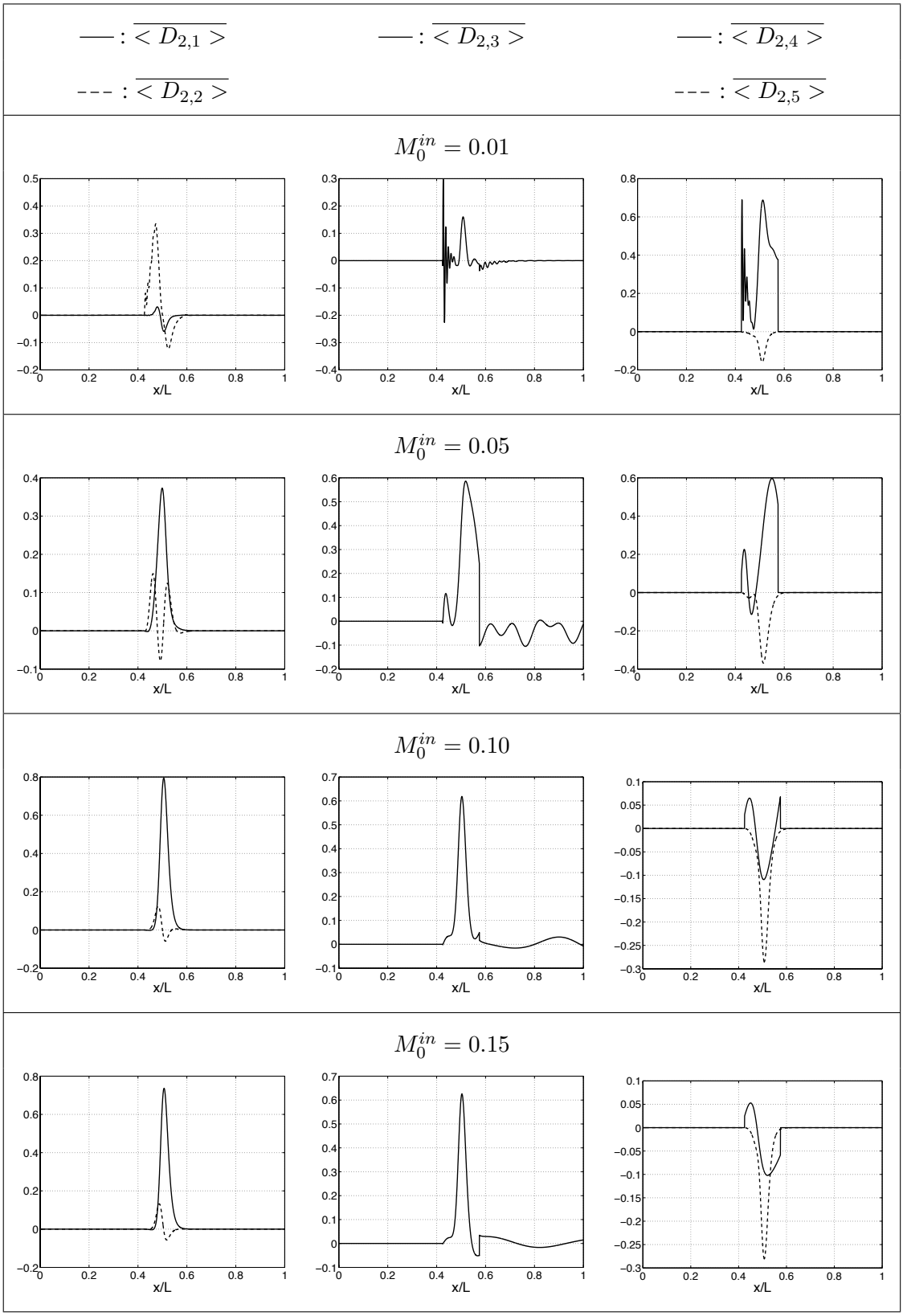

Table 6.5: Active Flame: Terms of time and space integrated disturbance energy balance Eq. (6.7), separate contributions of source term: cf. Eq (6.4)

6.2 Assessing Non-normal Effects

The following section addresses the aspect of the non orthogonality of eigenvectors of the system, and is included here in the form of an article. This work has been carried out in co-operation with co-authors from SNECMA, UM2 and TUM and presented at the "International Workshop on Non-Normal and Nonlinear Effects in Aero- and Thermoacoustics" held on May, 17th -21st, at TU Munich, Germany. An updated version is in preparation for submission to "Physics of Fluids".

The objective of this work is to show the possibility and effects of non normal interaction in thermoacoustic systems. The chapters presented before show how these systems can be described in terms of eigenmodes based on linear theory, which allows to judge their stability. However, if the eigenvectors are not orthogonal, they may interact in a way that short term transient growth may occur even if the system is found to be linearly stable. This effect can be illustrated by superimposing two vectors - either orthogonal or not orthogonal - that are decaying in amplitude, and by following the temporal evolution of their sum (see Fig. 6.10): If the vectors that are superimposed are orthogonal and decay in amplitude, the result vector will also decay in amplitude. However, if the vectors are not orthogonal, the vector resulting from their superposition may initially increase in amplitude, even though the separate vectors decrease. On the long run, of course, the result vector will exhibit decreasing behaviour as well.

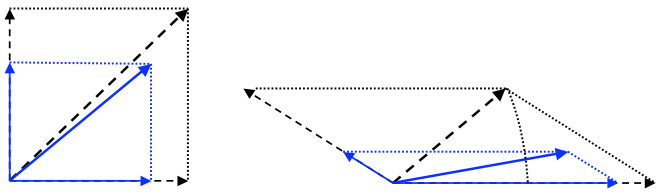

Figure 6.10: Temporal evolution of vectors resulting from linear combination of linearly stable vectors. - - - : vectors at $t = 0$; —— : vectors at $t > 0$. Left: orthogonal case - individual vectors and result vector of linear combination decay. Right: non orthogonal case - individual vectors decay, but result vector of linear combination grows transiently.

Nevertheless, this short term transient growth can be of interest: It indicates that even in a linearly stable system, perturbation amplitudes may be higher than predicted by linear theory. Strong perturbations however might have devastating effects on the system or trigger non linear instability. In this sense, the analysis of non normal effects allows to evaluate the limits of linear analysis: Even if the eigenvalue approach does not allow to predict the actual amplitude of perturbations, nor does the present study take into account non linear effects, the observation of strong transient growth may point out potential problems, i.e. situations where the use of linear theory alone might not be sufficient anymore.

The theory of non normal interaction, initially developed in the domain of classical fluid mechanics [114, 95], has only recently been adapted to the field of thermoacoustics [6, 73, 99]. In these studies, the system is typically described as a first order system in a time domain formulation of the form

$$\frac{\mathrm{d}u}{\mathrm{d}t} + Au = 0,$$

where u is a state vector of fluctuating quantities and A a system matrix, that allow to express the conservation equations. Using a Galerkin technique as described by Culick [20] and expanding the fluctuating quantities as series of orthogonal basis functions allows to obtain a matrix A, whose size corresponds to the number of basis functions that are used. The analysis of the degree of non-normality of the system is then based on a singular value decomposition of the matrix A.
The problem is that for geometrically complex configurations that include heat release and may present non trivial boundary conditions, it is not straightforward to find such a set of orthogonal basis functions that satisfy all conditions. This is why in the following study, the analysis of non normal effects is carried out using a novel approach, which is based on the eigenvectors of the system. Using finite volume techniques, eigenvectors can be computed for very complex configurations [42, 102], but have in turn been shown to be non orthogonal [74].

The paper that follows describes how the theory of non normal interaction can be applied to the numerically computed eigenvectors of the system. The transient growth of energy in the system is analysed based on results of the 1D LEE solver using the configurations described before in sections 4.2.2 and 4.2.3. Special attention is put on the description of Mach number effects and the impact of flame-acoustic interaction. A link to the disturbance energy considerations of section 6.1 is established by showing that the definition of an energy term that describes the strength of the perturbations is a crucial step in this kind of analysis.

ASSESSING NON-NORMAL EFFECTS IN THERMOACOUSTIC SYSTEMS WITH NON ZERO BASELINE FLOW

K. Wieczorek[1], C. Sensiau[2], W. Polifke[3], F. Nicoud*[4]

[1] CFD-Team, CERFACS, 42 Ave Coriolis, 31057 Toulouse, France
[2] SNECMA Villaroche, France
[3] Lehrstuhl für Thermodynamik, TU Munich, 85747 Garching, Germany
[4] I3M, University Montpellier 2, CC51, 34057 Montpellier Cedex 5, France
* Corresponding author: franck.nicoud@univ-montp2.fr

In this paper, the theory of non-normal interaction is applied to eigenmodes of a thermoacoustic system that include mean flow effects. When the mean flow is taken into account, the energy associated to the eigenmodes contains not only contributions of the acoustic field, but also those of convected entropy and vorticity modes. The notion of maximum transient energy growth is therefore extended from an energy expression based on the classical acoustic energy to a form based on the generalized disturbance energy.
The approach is applied to a 1D configuration that consists in a duct including a 1D flame followed by a choked isentropic nozzle. It is shown that for such a case it is essential to include the contribution of entropy perturbations in the calculation of the optimal initial perturbation and the maximum transient energy growth.

1 Introduction

Over the last decades, thermoacoustic instabilities have been the subject of intense research activity with the aim to better understand and eventually predict/avoid them at the design level. Except when the equations are solved in the time domain (e.g. when Large Eddy Simulation is used), the analysis most often relies on a modal approach, where the first eigenmodes/eigenfrequencies of the thermoacoustic system are sought for. Since these modes are not orthogonal in general because of boundary conditions and/or flame coupling [17], the associated frequencies only provide information about the long term evolution of the system, which is linearly stable if and only if all its modes are damped. However, if non-normality is present, linear modes may interact and transient energy growth can be observed even for stable systems. This effect was demonstrated theoretically by Balasubramanian & Sujith [2] who translated ideas initially developed for classical fluid mechanics [13, 22, 26].
The maximum energy growth that can appear depends only on the thermoacoustic system of interest. Calling $\mathscr{U}$ the state vector (typically the components of $\mathscr{U}$ are the fields of acoustic density, pressure and velocity), the relevant equations for describing the time evolution of the perturbations read formally:

$$\frac{\partial \mathscr{U}}{\partial t} + \mathscr{A}(\mathscr{U}) = 0, \tag{1}$$

where $\mathscr{A}$ is a differential operator which is linear when linear thermoacoustics is considered. Eq. (1) is nothing but a set of partial differential equations which can be reduced to a set of ordinary differential equations when an appropriate discretization method is used. The thermoacoustic system of interest is

then represented by a first order dynamical system which reads:

$$\frac{d\mathbf{u}}{dt} + \mathbf{A}\mathbf{u} = 0, \tag{2}$$

where $\mathbf{u}$ is the discretized counterpart of $\mathscr{U}$. If Eq. (2) is obtained from Eq. (1) using a Galerkin technique, i.e. by expanding the fluctuating quantities as series of orthogonal basis functions [5], the vector $\mathbf{u}$ contains the weights of those basis functions. On the other hand, if a finite difference/finite volume technique is used, $\mathbf{u}$ contains the nodal values of the state vector $\mathscr{U}$. Of course, the square matrix $\mathbf{A}$ depends on the discretization technique, both in its size and structure. Typically, a Galerkin method produces a dense matrix of small size, as the expansion requires usually only few basis functions (e.g.: [16]). In difference to that, a finite volume approach produces a large but sparse matrix (e.g.: [19]).
In any case, some of the characteristics of the thermoacoustic system can be studied by analyzing the matrix $\mathbf{A}$ instead of the differential operator $\mathscr{A}$. Notably, the maximum transient energy growth at time t, $G(t)$, is related to the largest singular value of the exponential matrix $\exp(-\mathbf{A}t)$ [22]. This property was used in several recent studies in order to quantify the non-normal effects in simple thermoacoustic systems such as the Rijke tube [2] or a laminar diffusion flame [1]. This allowed assessing the maximum transient growth $G_{max} = \max[G(t)]$, the maximum value being taken over all the possible values of t. Unfortunately, we believe that this approach based on a Singular Value Decomposition (SVD) of the matrix $\mathbf{A}$ is not very suitable for complex systems for two main reasons:

1. **time delay:** In practical cases, the flame response to upstream acoustic perturbations is time lagged, the time delay τ being potentially related to several fluid mechanics and/or chemical processes relevant to the flame unsteadiness. In thermo-acoustic simulations based on linearized equations this time lag behaviour has to be included explicitely in the system of equations via the flame model. As a consequence, the system cannot be described by Eq. (1), but an expression of the form
$$\frac{\partial \mathscr{U}}{\partial t} + \mathscr{A}(\mathscr{U}(t)) + \mathscr{B}(\mathscr{U}(t-\tau)) = 0, \tag{3}$$
must be used instead. Unfortunately, generalizing the SVD approach described above to Eq. (3) is not straightforward and may involve additional simplifications like assuming the time delay τ to be small compared to the first mode's period [16].

2. **boundary conditions:** if the Galerkin method is used to degrade Eq. (1) into Eq. (2), the knowledge of an orthogonal set of basis functions which meet the actual boundary conditions of the thermoacoustic problem is required. Because they convey useful information about the configuration, the acoustic eigenmodes are good candidates (e.g.: [5]) for this purpose. Unfortunately, they are not orthogonal as soon as the boundary conditions correspond to a finite, complex valued impedance [17], a situation which is not rare. If a finite difference/finite volume type of approach is used instead for degrading Eq. (1), the size of the discretized problem, Eq. (2), is large (typical finite volume grids contain $10^5 - 10^6$ elements) so that performing a SVD in order to assess $G(t)$ may be CPU demanding. Thus, maximizing $G(t)$ over all the values of time t to obtain G_{max} might not be affordable in practice.

Recently, Selimefendigil et al. [23] proposed a method to handle delayed systems and overcome the first issue mentioned. In their view, Eq. (3) is recast into an equivalent non-delayed problem for which the pseudospectra can be computed. The concept of pseudospectra (first mentioned by Landau [11]) was introduced by Trefethen [25] in order to quantify the sensitivity of eigenvalues to uncertainties/ perturbations in the data or discretization. The property exploited by Selimefendigil et al. [23] is that the geometry of pseudospectra can be used to obtain a lower bound of $G_{\max}$ (Kreiss theorem). Still, computing pseudospectra becomes very CPU demanding when the size of the problem increases so that this approach does not address the second issue mentioned. Besides, as far as the authors know, analyzing the pseudospectra can only give information about the maximum transient growth and not about the shape of the optimal perturbation.
The first objective of this paper is to assess a strategy which is potentially suitable for assessing non-normal effects in 3D complex configurations and not CPU demanding. It relies heavily on the knowl-

edge of the first few thermoacoustic eigenmodes of the system of interest. Indeed, even if non-normality is present and eigenmodes only provide information about the long term evolution, they convey relevant information about the system. For example, their individual stability dictates the overall stability of the system if non-linear effects are not considered. Numerical strategies have been proposed in the past in order to compute such modes by solving an Helmholtz type of equation with a forcing term representing the flame [9, 17, 24]. The view considered in this paper was initially proposed by Schmid & Henningson [22] for investigating classical fluid mechanics configurations. It consists in looking for the optimal perturbation (the one which generates the largest transient growth) in the linear space spanned by the thermoacoustics modes. In other words, assessing the non-normality effect appears as a post-processing of the results of the classical modal characterization of the configuration. As we will demonstrate, this is virtually done at no additional cost. Of course, since only a finite number of eigenmodes are considered, all the possible perturbations cannot be generated by combining these modes and only a lower bound of $G_{\max}$ can be obtained. However, since the eigenmodes convey a lot of information regarding the system of interest, it is expected that keeping only a few of them is sufficient to obtain a reasonable assessment of the maximum transient growth. The same idea justifies the Galerkin methods where often only a few (of order 10 say) basis functions are necessary to reach good accuracy. However, contrary to the Galerkin method, the orthogonality of the modes is not required in the present approach so that the method is also suitable for complex 3D configurations with finite valued boundary impedance.

All the previous studies dealing with non-normal effects in thermoacoustic systems relied on the zero mean flow assumption although the effect of the approximation $M \simeq 0$ is not well understood [6] and the neglected convective terms may introduce additional non-normality [7]. In the case of a premixed 1D flame, only a moderate non-normal effect was found in the literature [2], the maximum transient energy growth ($G_{\max}$) being close to 7. The second objective of this paper is then to investigate if larger values of $G_{\max}$ can be observed when the baseline flow is not assumed at rest. In this case, the evolution of the perturbations are described by the Linearized Euler Equations instead of a simple Helmholtz equation for the acoustic pressure. Also, the state vector contains one more component (the density or entropy say) on top of the acoustic pressure and velocity fields. Thus this situation is quite different from what has been considered so far in the literature and the presented analysis also serves as an illustration of the flexibility of the method and its ability to handle complex situations.

The formalism of the method is detailed in sections 2.2 and 2.3 in the case of a generic 3D thermoacoustic system written under the zero Mach number assumption and described in section 2.1. In this case, the state vector contains only the acoustic pressure and velocity fields and non-trivial boundary conditions (finite, complex valued impedance) can be considered. The formalism is then extended in section 2.4 to the case where the perturbations are obtained from the LEE and the state vector contains one more component. The method is then illustrated by analyzing the simple case of a 1D flame stabilized within a straight duct. Note however that this situation is more complex than several previous studies since **a)** a time delayed n-τ type of model is used for describing the acoustic-flame coupling and **b)** complex boundary conditions are applied at the boundaries of the duct. The corresponding results are discussed in section 3 where the maximum transient growth related to two types of energies is considered, i.e. the classical acoustic energy and the energy of the fluctuations.

2 Formalism

2.1 The thermoacoustic model

The phenomenon of thermoacoustic instability results from a coupling between combustion processes and the acoustic eigenmodes of the configuration (among many others: [12]). Assuming vanishing Mach number for the mean flow, this coupling can be modeled in the linear regime by the following wave equation :

$$\frac{1}{\gamma(\mathbf{x})\,p_0}\frac{\partial^2 p'(\mathbf{x},t)}{\partial t^2} + \nabla\cdot\frac{1}{\rho_0(\mathbf{x})}\vec{\nabla}p'(\mathbf{x},t) = \frac{\gamma(\mathbf{x})-1}{\gamma(\mathbf{x})\,p_0}\frac{\partial q'(\mathbf{x},t)}{\partial t}, \tag{4}$$

where $p'(\mathbf{x},t)$ stands for the acoustic pressure at position $\mathbf{x}$ and time t; $\gamma(\mathbf{x})$ and $\rho_0(\mathbf{x})$ are the time averaged isentropic coefficient and density of the fluid; p_0 is the homogeneous background pressure.
Eq. (4) states that heat release fluctuations $q'(\mathbf{x},t)$ may influence the acoustics in the domain. It is common practice to model the feedback effect, viz. the influence of acoustic fluctuations on combustion, via an $n-\tau$ type of model [3, 4, 21]. This model assumes that the heat release fluctuations are proportional to the time-lagged velocity fluctuations at a reference point located upstream of the flame:

$$q'(\vec{x},t) = \frac{q_{tot}}{u_{bulk}} H_q(\mathbf{x})\, \mathbf{u}'(\mathbf{x}_{ref}, t-\tau)\cdot\mathbf{n}_{ref}, \tag{5}$$

where $H_q(\mathbf{x})$ is the amplitude of the flame response and can be related to the parameter n of $n-\tau$-models [19], $\tau(\mathbf{x})$ is the time delay and $\mathbf{n}_{ref}$ is a unit vector. Assuming time-harmonic perturbations of pulsation ω, one may write $p'(\mathbf{x},t) = \Re\big(\hat{p}(\mathbf{x})e^{-i\omega t}\big)$ and $q'(\vec{x},t) = \Re\big(\hat{q}(\mathbf{x})e^{-i\omega t}\big)$. The acoustic field can then be expressed in terms of eigenmodes that are solution of a Helmholtz equation written for the complex amplitude of pressure $\hat{p}$:

$$\gamma(\mathbf{x})p_0\nabla\cdot\left(\frac{1}{\rho_0(\mathbf{x})}\vec{\nabla}\hat{p}(\mathbf{x})\right) + \omega^2\hat{p}(\mathbf{x}) = \frac{q_{tot}}{i\omega\rho_{ref}u_{bulk}} H_q(\mathbf{x})\; e^{i\omega\tau(\mathbf{x})}\;\vec{\nabla}\hat{p}(\mathbf{x}_{ref})\cdot\mathbf{n}_{ref} \tag{6}$$

As the problem has been written in frequency domain, the reflection of low frequency waves at the boundaries can be handled easily with a complex valued impedance at the boundary, noted Z. The appropriate boundary condition to impose to $\hat{p}$ takes the following form:

$$\vec{\nabla}\hat{p}(\mathbf{x})\cdot\mathbf{n}_{BC} - i\frac{\omega}{c_0(\mathbf{x})Z(\omega)}\hat{p}(\mathbf{x}) = 0, \tag{7}$$

where $\mathbf{n}_{BC}$ is a unit vector normal to the boundary and $c_0(\mathbf{x})$ is the speed of sound. Solving the eigenproblem given by Eq. (6) and Eq. (7) allows to determine the thermoacoustic pressure eigenmodes $\hat{p}(\mathbf{x})$, and their corresponding eigenfrequencies ω. The velocity eigenmodes $\hat{\mathbf{u}}(\mathbf{x})$ can then be deduced using the linearised Euler equation written in the frequency domain for time harmonic fluctuations:

$$i\omega\rho_0\,\hat{\mathbf{u}}(\mathbf{x}) = \vec{\nabla}\hat{p}(\mathbf{x}). \tag{8}$$

2.2 Non-orthogonality of the eigenfunction

Non-normality arises from the fact that the thermoacoustic eigenmodes are not orthogonal. Thus, it is important to specify how orthogonality is defined or, equivalently, what is the appropriate inner product. The formalism used throughout this paper is therefore stated in the following.
An acoustic perturbation is defined as a vector composed of pressure and velocity fluctuations p' and $\mathbf{u}'$ that are assumed to be harmonic in time. This allows to write:

$$v'(\mathbf{x},t) = \begin{bmatrix} p'(\mathbf{x},t) \\ \mathbf{u}'(\mathbf{x},t) \end{bmatrix} = \begin{bmatrix} \Re(\hat{p}(\mathbf{x})e^{-i\omega t}) \\ \Re(\hat{\mathbf{u}}(\mathbf{x})e^{-i\omega t}) \end{bmatrix} = \Re(\hat{v}(\mathbf{x})e^{-i\omega t}) \tag{9}$$

where the vector $\hat{v}(\mathbf{x})$ contains the complex amplitudes of pressure and velocity fluctuations, this latter being composed of three components $\hat{\mathbf{u}}(\mathbf{x}) = (\hat{u}_x(\mathbf{x}), \hat{u}_y(\mathbf{x}), \hat{u}_z(\mathbf{x}))$ and $\omega = \omega_r + i\omega_i$ is a complex frequency.
The following considerations are set in the complex space, i.e. the return to a real valued vector is dropped. The solutions of the thermoacoustic system are considered in the form of complex valued vectors

$$v(\mathbf{x},t) = \hat{v}(\mathbf{x})e^{-i\omega t} = \hat{v}(\mathbf{x})e^{-i\omega_r t}e^{\omega_i t} \qquad \text{with} \qquad \hat{v}(\mathbf{x}) = \begin{bmatrix} \hat{p}(\mathbf{x}) \\ \hat{\mathbf{u}}(\mathbf{x}) \end{bmatrix} = \begin{bmatrix} \hat{p}(\mathbf{x}) \\ \hat{u}_x(\mathbf{x}) \\ \hat{u}_y(\mathbf{x}) \\ \hat{u}_z(\mathbf{x}) \end{bmatrix} \tag{10}$$

a complex eigenvector.
Considering $v_1(\mathbf{x},t)$ and $v_2(\mathbf{x},t)$ two complex vectors that are solution of Eqs. (6), (7) and (8), a weighted

inner product can be defined as follows:

$$\left\langle v_1(\mathbf{x},t)\middle| v_2(\mathbf{x},t)\right\rangle_W = \int_V \left(v_1(\mathbf{x},t)^H\, W\, v_2(\mathbf{x},t)\right) dV \tag{11}$$

with $v_1(\mathbf{x},t)^H = \hat{v}(\mathbf{x})^H e^{i\omega_r t} e^{\omega_i t}$ the conjugate transpose of $v_1(\mathbf{x},t)$, V the volume of the domain that is considered and W a weight matrix.
If W is the identity matrix I, the inner product defined in Eq. (11) applied to an eigenvector $\hat{v}(\mathbf{x})$ yields simply its L_2-norm:

$$\left\langle \hat{v}(\mathbf{x})\middle| \hat{v}(\mathbf{x})\right\rangle_I = \int_V \hat{v}^H(\mathbf{x})\, I\, \hat{v}(\mathbf{x})\, dV = ||\hat{v}(\mathbf{x})||_2^2$$

By defining the matrix W in an appropriate way, the product of Eq. (11) can be linked to an equivalent of the acoustic energy associated to the mode $v(\mathbf{x}) = \hat{v}(\mathbf{x})e^{-i\omega t}$. For an eigenvector $\hat{v}(\mathbf{x})$ as defined in Eq. (10), a weight matrix

$$W_{ac} = \begin{pmatrix} \frac{1}{2\gamma p_0(\mathbf{x})} & \frac{u_{0x}}{2c_0^2} & \frac{u_{0y}}{2c_0^2} & \frac{u_{0z}}{2c_0^2} \\ \frac{u_{0x}}{2c_0^2} & \frac{\rho_0(\mathbf{x})}{2} & 0 & 0 \\ \frac{u_{0y}}{2c_0^2} & 0 & \frac{\rho_0(\mathbf{x})}{2} & 0 \\ \frac{u_{0z}}{2c_0^2} & 0 & 0 & \frac{\rho_0(\mathbf{x})}{2} \end{pmatrix} \tag{12}$$

allows to define an equivalent acoustic energy of the form:

$$\begin{aligned} E_{ac}(t) &= \left\langle v(\mathbf{x},t)\middle| v(\mathbf{x},t)\right\rangle_{W_{ac}} \\ &= \int_V \left(\hat{v}(\mathbf{x})^H e^{i\omega_r t} e^{\omega_i t}\, W_{ac}\, \hat{v}(\mathbf{x}) e^{-i\omega_r t} e^{\omega_i t}\right) dV \\ &= e^{2\omega_i t} \int_V \left(\frac{1}{2\gamma p_0(\mathbf{x})}|\hat{p}(\mathbf{x})|^2 + \frac{\rho_0(\mathbf{x})}{2}|\hat{\mathbf{u}}(\mathbf{x})|^2 + \frac{|\hat{p}(\mathbf{x})|}{c_0(\mathbf{x})^2}|\mathbf{u_0}(\mathbf{x})\cdot\hat{\mathbf{u}}(\mathbf{x})|\right) dV \end{aligned} \tag{13}$$

The term $E_{ac}(t)$ is a real valued energy that is defined based on complex quantities. It shares the same coefficients as the classical acoustic energy. Still, it differs from the latter in the sense that the classical acoustic energy is based on the real parts of the complex signals and will hence be noted $E_{ac,\Re}(t)$ in the following:

$$E_{ac,\Re}(t) = \int_V \left(\frac{1}{2\gamma p_0(\mathbf{x})} p'(\mathbf{x},t)^2 + \frac{\rho_0(\mathbf{x})}{2}\mathbf{u}'(\mathbf{x},t)^2 + \frac{p'(\mathbf{x},t)}{c_0(\mathbf{x},t)^2}\mathbf{u}_0(\mathbf{x})\cdot\mathbf{u}'(\mathbf{x},t)\right) dV \tag{14}$$

Please note that the energy terms of Eq. (13) and (14) do not follow the same temporal evolution. The term of Eq. (13) is defined in a way as to describe the energy of a linear combination of several modes, which inhibits time averaging over one period of oscillation. Complete equivalence between the terms of Eq. (13) and (14) may be established by time averaging. However, in the present case the short term transient behaviour is to be evaluated. Therefore, it does not make sense to introduce a time average.

The orthogonality of the eigenmodes can now be discussed using the inner product introduced in Eq. (11) together with the weight matrix of Eq. (12). The projection of $\hat{v}_1(\mathbf{x})$ onto $\hat{v}_2(\mathbf{x})$ can be expressed analytically and leads (after some algebra) to the following equation:

$$\left\langle \hat{v}_1\middle| \hat{v}_2\right\rangle_{W_{ac}} = \frac{1}{2}\frac{1}{\omega_1 - \omega_2^*}\left[\int_S \frac{1}{\rho_0}\left(\hat{p}_1 \frac{\vec{\nabla}\hat{p}_2^*}{\omega_2^*} - \hat{p}_2^* \frac{\vec{\nabla}\hat{p}_1}{\omega_1}\right) dS + i\int_V \frac{\gamma-1}{\gamma p_0}\left(\hat{p}_1\hat{q}_2^* + \hat{p}_2^*\hat{q}\right) dV\right], \tag{15}$$

where S and V denote the surface and the volume of the domain and * stands for complex conjugates. (The dependency of the complex variables on $\mathbf{x}$ is omitted for clarity, and the mean flow speed is neglected.)
The expression of Eq. (15) is an extension of the result by Nicoud et al. [17], who were considering only pressure fluctuations in their analysis of the eigenmodes' orthogonality, instead of the complete mode structure composed of pressure and velocity terms. Eq. (15) shows that two eigenmodes $\hat{v}_1$ and $\hat{v}_2$ are

orthogonal when a) boundary impedances are trivial , i.e. they correspond to pressure or velocity nodes with $\hat{p} = 0$ or $\vec{\nabla}\hat{p} = 0$ respectively; and b) no heat release fluctuations occur ($\hat{q} = 0$). However the conditions for orthogonality will most probably never be met in an actual experimental setup, so that non-normality should be considered as the rule for practical thermoacoustic systems.
As a consequence, even if all the eigenmodes are found stable ($\omega_i < 0$) there is a possibility for the equivalent acoustic energy of Eq. (13) to exhibit a transient growth before it eventually vanishes as predicted by the linear modal analysis. The amplitude of the acoustic fluctuations may become significant during this transient phase and the linear assumption is possibly not valid anymore. In particular, it has been shown [20] that gain and phase of the flame transfer function may depend significantly on the amplitude of the velocity fluctuations. This is the reason why non-normality is sometimes related to complex effects such as non-linear triggering [2].
The focus of the present study is however limited to the assessment of non-normality effects in complex configurations and non-linearity is not considered.

2.3 The maximum possible amplification

For complex time-dependant signals of pressure and velocity $q(\mathbf{x}, t)$, a maximum possible amplification $G_{ac}(t)$ can be defined as

$$G_{ac}(t) = \max \frac{E_{ac}(t)}{E_{ac}(0)} = \max_{q(\mathbf{x},0)\neq 0} \frac{\left\langle q(\mathbf{x},t) \middle| q(\mathbf{x},t) \right\rangle_{W_{ac}}}{\left\langle q(\mathbf{x},0) \middle| q(\mathbf{x},0) \right\rangle_{W_{ac}}} \tag{16}$$

This quantity should be thought of as the upper bound of the envelop of the equivalent acoustic energy. Starting from any perturbation with a unit energy norm, the equivalent acoustic energy term will always remain smaller than or equal to this coefficient: $E_{ac}(t) < G_{ac}(t),\ \forall t$. Still, there is no reason why the optimal perturbation, which maximizes E_{ac} at time t_1, should also maximize E_{ac} at time $t_2 \neq t_1$, thus the envelop.
Schmidt & Henningson [22] provide a procedure to assess this maximum possible amplification for complex signals $q(\mathbf{x}, t)$ that can be expressed as a linear combination of m complex eigenmodes:

$$q(\mathbf{x}, t) = \sum_{j=1}^{m} k_j \hat{v}_j(\mathbf{x}) e^{-i\omega_j t} \tag{17}$$

This expansion of $q(\mathbf{x}, t)$ as a linear combination of eigenmodes can be rewritten in a compact matrix notation as

$$q(\mathbf{x}, t) = \hat{V}(\mathbf{x}) e^{-i\Omega t} \mathbf{k} \tag{18}$$

where the j^{th} column of the matrix $\hat{V}(\mathbf{x})$ contains the complex valued eigenvector $\hat{v}_j(\mathbf{x})$, the diagonal matrix $\Omega = \text{diag}(\omega_1, \omega_2, ..., \omega_m)$ contains the complex frequencies of the m eigenvectors used for the expansion and the vector $\mathbf{k}$ stores the coefficients k_j of the linear combination Eq. (17).
Introducing Eq. (18) into the definition of the equivalent acoustic energy of Eq. (13), one obtains:

$$\begin{aligned} E_{ac}^{m}(t) &= \left\langle q(\mathbf{x},t) \middle| q(\mathbf{x},t) \right\rangle_{W_{ac}} \\ &= \int_V q(\mathbf{x},t)^H \, W_{ac} \, q(\mathbf{x},t) dV \\ &= \int_V \left(e^{-i\Omega t}\mathbf{k}\right)^H \hat{V}(\mathbf{x})^H \, W_{ac} \, \hat{V}(\mathbf{x}) e^{-i\Omega t}\mathbf{k} dV \\ &= \left(e^{-i\Omega t}\mathbf{k}\right)^H M_{ac} \left(e^{-i\Omega t}\mathbf{k}\right) \end{aligned} \tag{19}$$

where the matrix M contains the inner products of the m selected eigenvectors:

$$M_{ac} = \int_V \left(\hat{V}(\mathbf{x})^H \, W_{ac} \, \hat{V}(\mathbf{x})\right) dV = \left\langle \hat{V}(\mathbf{x}) \middle| \hat{V}(\mathbf{x}) \right\rangle_{W_{ac}} \tag{20}$$

The element kl of this matrix reads:

$$M_{ac}^{kl} = \int_V \left(\hat{v}_k(\mathbf{x})^H \, W_{ac} \, \hat{v}_l(\mathbf{x})\right) dV \tag{21}$$

Since $\left\langle \cdot \middle| \cdot \right\rangle_{W_{ac}}$ is an inner product, M_{ac} is a positive Hermitian matrix so that its Cholesky decomposition exists and yields the square matrix F_{ac} of size m such that $F_{ac}^H F_{ac} = M_{ac}$. Introducing the decomposition of M_{ac} into the acoustic energy term of Eq. (19) one obtains:

$$E_{ac}^m(t) = \left(F_{ac} e^{-i\Omega t}\mathbf{k}\right)^H \left(F_{ac} e^{-i\Omega t}\mathbf{k}\right) \tag{22}$$

This equation shows that $E_{ac}(t)$ is nothing but the L_2-norm of the vector $F_{ac} e^{-i\Omega t}\mathbf{k}$. Note that in difference to the energy term defined for one single mode (Eq. (13)), the equivalent acoustic energy term for a superposition of several modes is function not only of ω_i, but also of ω_r (via the matrix Ω).
Finally, noting that the Cholesky factor F_{ac} is not singular, the maximum possible amplification at time t takes the following form:

$$G_{ac}^m(t) = \max \frac{E_{ac}^m(t)}{E_{ac}^m(0)} = \max \frac{\|F_{ac} e^{-i\Omega t}\mathbf{k}\|_2^2}{\|F_{ac}\mathbf{k}\|_2^2} = \max_{F_{ac}\mathbf{k}} \frac{\|F_{ac} e^{-i\Omega t} F_{ac}^{-1} F_{ac}\mathbf{k}\|_2^2}{\|F_{ac}\mathbf{k}\|_2^2} \tag{23}$$

By definition, this quantity is the L_2-norm of the operator $F_{ac} e^{-i\Omega t} F_{ac}^{-1}$. In other words, the maximum amplification at time t is given by the largest singular value of $F_{ac} e^{-i\Omega t} F_{ac}^{-1}$. The optimal initial perturbation is given by the corresponding right singular vector of $F_{ac} e^{-i\Omega t} F_{ac}^{-1}$.
On the LHS of Eq. (23), the superscript m indicates that this expression gives the maximum energy amplification at time t for all the perturbations which can be obtained by combining the m selected eigenvectors (this notation is sufficient if one assumes that the m vectors selected correspond to the m lowest eigenfrequencies). In the same way, the maximum transient growth, which can be obtained by combining these m eigenvectors, can be obtained by maximizing $G_{ac}^m(t)$ over time and shall be noted:

$$G_{max,ac}^m = \max_t G_{ac}^m(t). \tag{24}$$

In the case where the eigenmodes are orthogonal and all damped, the matrices M_{ac} and F_{ac} are both diagonal. Then, Eq. (23) shows that the maximum growth rate equals unity (because $F_{ac} e^{-i\Omega t} F_{ac}^{-1}$ reduces to $e^{-i\Omega t}$) as it is expected when non-normality is not present. As a last comment, we stress the fact that the singular value decomposition is performed on a matrix of size m (which is the number of eigenmodes used to generate the signal), making the above approach computationally inexpensive.

2.4 Extension to non isentropic modes

When the LEE equations are solved instead of the Helmholtz equation for pressure only, the thermoacoustic modes contain one more component, in the presented case the fluctuating entropy. Any mode can thus be represented with the following compact notation :

$$v(\mathbf{x}, t) = \hat{v}(\mathbf{x}) e^{-i\omega t} = \hat{v}(\mathbf{x}) e^{-i\omega_r t} e^{\omega_i t} \qquad \text{with} \qquad \hat{v}(\mathbf{x}) = \begin{bmatrix} \hat{p}(\mathbf{x}) \\ \hat{\mathbf{u}}(\mathbf{x}) \\ \hat{s}(\mathbf{x}) \end{bmatrix} = \begin{bmatrix} \hat{p}(\mathbf{x}) \\ \hat{u}_x(\mathbf{x}) \\ \hat{u}_y(\mathbf{x}) \\ \hat{u}_z(\mathbf{x}) \\ \hat{s}(\mathbf{x}) \end{bmatrix} \tag{25}$$

To describe the energy contained in this kind of modes, the corollary for disturbance energy derived by Myers [15] and extended by Karimi et al. [10] is appropriate. Thus, instead of the classical acoustic energy of Eq. (14), the following term should be used to determine the total energy of the disturbances:

$$E_{tot,\Re} = \int_V \left(\frac{1}{2\gamma(\mathbf{x}) p_0} \, p'(\mathbf{x}, t)^2 + \frac{\rho_0(\mathbf{x})}{2} \, \mathbf{u}'(\mathbf{x}, t)^2 + \frac{\rho_0(\mathbf{x}) T_0(\mathbf{x})}{2 C_p(\mathbf{x})} \, s'(\mathbf{x}, t)^2 + \rho'(\mathbf{x}, t) \mathbf{u}_0(\mathbf{x}) \cdot \mathbf{u}'(\mathbf{x}, t) \right) dV \tag{26}$$

The weight matrix W_{tot} that relates the inner product of Eq. (11) to a complex based equivalent of the total disturbance energy of Eq. (26) reads

$$W_{tot} = \begin{pmatrix} \frac{1}{2\gamma p_0} & \frac{u_{0x}}{2c_0^2} & \frac{u_{0y}}{2c_0^2} & \frac{u_{0z}}{2c_0^2} & 0 \\ \frac{u_{0x}}{2c_0^2} & \frac{\rho_0}{2} & 0 & 0 & -\frac{\rho_0 u_{0x}}{2C_p} \\ \frac{u_{0y}}{2c_0^2} & 0 & \frac{\rho_0}{2} & 0 & -\frac{\rho_0 u_{0y}}{2C_p} \\ \frac{u_{0z}}{2c_0^2} & 0 & 0 & \frac{\rho_0}{2} & -\frac{\rho_0 u_{0z}}{2C_p} \\ 0 & -\frac{\rho_0 u_{0x}}{2C_p} & -\frac{\rho_0 u_{0y}}{2C_p} & -\frac{\rho_0 u_{0z}}{2C_p} & \frac{\rho_0 T_0}{2C_p} \end{pmatrix} \tag{27}$$

The resulting energy term reads then

$$\begin{aligned} E_{tot}(t) &= \left\langle v(\mathbf{x},t) \middle| v(\mathbf{x},t) \right\rangle_{W_{tot}} \\ &= e^{2\omega_i t} \int_V \left(\frac{1}{2\gamma p_0} |\hat{p}|^2 + \frac{\rho_0}{2} |\hat{\mathbf{u}}|^2 + \frac{\rho_0 T_0}{2C_p} |\hat{s}|^2 + \left(\frac{\hat{p}}{c_0^2} - \frac{\rho_0}{C_p} \hat{s} \right) |\mathbf{u_0} \cdot \hat{\mathbf{u}}| \right) dV \end{aligned} \tag{28}$$

where the dependencies on $\mathbf{x}$ were omitted for clarity.
The energy term based on complex quantities (Eq. (28)) is formally equivalent to the one based on real valued quantities (Eq. (26)), as the last term of the RHS integral can be rewritten using the linearized state equation

$$\hat{\rho} = \frac{\hat{p}}{c_0^2} - \frac{\rho_0}{C_p} \hat{s}.$$

It can be shown [8] that the matrix W_{tot} defined in Eq. (27) is definite positive as long as the local mean flow Mach number is smaller than a critical value, more precisely if $Ma = \sqrt{\mathbf{u_0} \cdot \mathbf{u_0}}/c_0 < 1/\gamma$. Since this condition is well satisfied for practical combustion systems, the following integral:

$$\left\langle \hat{v}_1(\mathbf{x}) \middle| \hat{v}_2(\mathbf{x}) \right\rangle_{W_{tot}} = \int_V \left(\hat{v}_1(\mathbf{x})^H \, W_{tot} \, \hat{v}_2(\mathbf{x}) \right) dV \tag{29}$$

defines an inner product. Thus, the analytical development described in section 2.3 remains valid in the non-isentropic case and the maximum growth at time t can be written as:

$$G_{tot}^m(t) = \max \frac{E_{tot}^m(t)}{E_{tot}^m(0)} = \max_{F_{tot}\mathbf{k}} \frac{\| F_{tot} e^{-i\Omega t} F_{tot}^{-1} F_{tot} \mathbf{k} \|_2^2}{\| F_{tot} \mathbf{k} \|_2^2} = \| F_{tot} e^{-i\Omega t} F_{tot}^{-1} \|_2^2 \tag{30}$$

where the Cholesky factorisation of the matrix

$$M_{tot} = \int_V \left(\, \hat{V}(\mathbf{x})^H \, W_{tot} \, \hat{V}(\mathbf{x}) \, \right) dV = F_{tot}^H F_{tot}$$

has been introduced. This decomposition obviously exists when W_{tot} is symmetric positive definite, i.e. when $Ma < 1/\gamma$ [8]. It might also exist even if the latter condition is not met locally, in a chocked nozzle say, where the local mean Mach number is obviously greater than the critical value. This is due to the volume integral in the definition of M_{tot}, which allows some compensation between low and large Mach number regions. Similarly to the isentropic case of section 2.3, the maximum energy at time t is given by the largest singular value of $F_{tot} e^{-i\Omega t} F_{tot}^{-1}$ and the corresponding initial perturbation is given by the right principal singular vector. Besides, the maximum transient growth which can be obtained by combining m eigenvectors is:

$$G_{max,tot}^m = \max_t G_{tot}^m(t). \tag{31}$$

As in the isentropic case of section 2.3, we may remark that :

- Eq. (30) produces $G_{max,tot}^m = 1$ when the eigenmodes are orthogonal and damped,
- the requested SVD is still to be made on a matrix of size m, thus not very CPU-demanding

The theoretical results established in sections 2.3 and 2.4 are now used to study an academic configuration where Mach number effects are present.

3 Results

3.1 Configuration

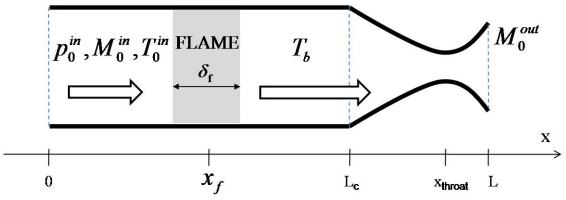

Figure 1: The numerical setup to assess non-normality with non-zero mean flow (from Nicoud and Wieczorek [19]).

L (m)	L_c (m)	x_{throat} (m)	x_f (m)	δ_f (m)	γ	r (S.I)
1.1	1.0	1.0863	0.5	0.15	1.4	287
p_0^{in} (Pa)	$T_0^{\text{in}} = T_u$ (K)	T_b (K)	M_0^{in}	M_0^{out}	x_{ref} (m)	
101325	300	1200	0.05	1.5	0.42	

Table 1: Main physical parameters used for configuration of Fig. 1.

The numerical setup consists in a constant cross section duct of length L_c with a 1D flame of characteristic thickness δ_f located at $x = x_f$ and connected to a nozzle of length $L - L_c$ (see Fig. 1). The mean flow is assumed isentropic except in the flame region and is constructed from analytical expressions of the temperature profile in the combustion chamber and the Mach number distribution in the isentropic nozzle (see Eqs. (4.3) and (4.1) in [19]). The mean flow is then entirely determined by the choice of three independent inlet quantities (for example p_0^{in}, T_0^{in}, M_0^{in}), the outlet Mach number M_0^{out} and relevant geometrical parameters δ_f, x_f, L_c, x_{throat} and L.
The mean profiles depicted in Fig. 2 correspond to the numerical values gathered in Table 1 and used throughout the course of this study. T_u and T_b are the temperature of unburnt and burnt gas respectively. Note that in the presented case, the gain of the flame transfer function H_q of Eq. (5) is set to zero, i.e. unsteady heat release is not considered. However, there is still interaction of the acoustic field with the heat source, as acoustic perturbations generate entropy waves in the flame zone, which are then convected downstream and may in turn create acoustic waves in the nozzle.

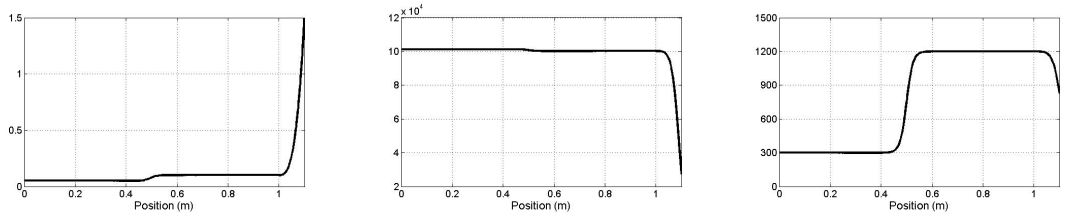

(a) Mach number (b) Static pressure (Pa) (c) Static temperature (K)

Figure 2: Mean flow fields for the configuration of Fig. 1.

The first eigenmodes of the configuration are computed following the procedure described in [19] where the Linearized Euler Equations written in the frequency space are discretized on a staggered

mesh. The first three modes are displayed in Fig. 3 where the modulus of the complex amplitudes of pressure, velocity and entropy are plotted.

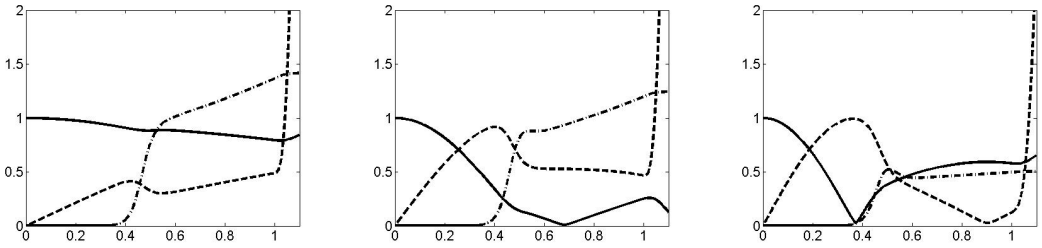

(a) Mode 1 at $59. - 8.3i$ Hz (b) Mode 2 at $169.6 - 9.4i$ Hz (c) Mode 3 at $231.7 - 4.3i$ Hz

Figure 3: The first 3 modes in the configuration of Fig. 1. —— : $|\hat{p}(x)|$; − − − : $|\hat{u}(x)|$; —·— : $|\hat{s}(x)|$. The fluctuating quantities are scaled by γp_0, c_0 and $10 \times C_v$ respectively.

3.2 Transient Energy Growth & Optimal Initial Perturbation

Based on the first six eigenmodes obtained from solving the Linearized Euler Equations, the optimal initial perturbation and the transient energy growth that it may cause are then determined. These quantities are calculated using the two approaches introduced in section 2, i.e. the transient energy growth based on the classical acoustic energy $G^m_{ac}(t)$ as noted in Eq. (23), and the transient energy growth based on the total disturbance energy $G^m_{tot}(t)$ as in Eq. (30).
As the configuration allows for the presence of entropy fluctuations, the optimal initial perturbation may include acoustic and entropy fluctuations in both cases (see Fig. 5). The difference between $G^m_{ac}(t)$ and $G^m_{tot}(t)$ consists in the fact that the contribution of entropy fluctuations to the energy term are considered negligible in the former approach, whereas they are taken into account in the latter.

The temporal evolution of the terms $G^6_{ac}(t)$ and $G^6_{tot}(t)$ is shown in Fig. 4. In this plot, the time is scaled by the period of the first eigenmode which has a frequency of $f_1 = 59. - 8.3i$ Hz (cf. Fig. 3(a)); the possible transient energy growth is plotted using a log-scale.
It is obvious that the two quantities behave very differently, their maximal values being $G^6_{max,ac} \approx 6000$ and $G^6_{max,tot} \approx 6$. In both cases, however, the maximum possible amplification is reached at a reduced time of $t'_{max} \approx 0.5$, i.e. after half a period of the first mode. It should also be noted that the two approaches lead to similar results at very low Mach numbers, with values of $G^m_{max,tot} \approx G^m_{max,ac} \approx 1$.

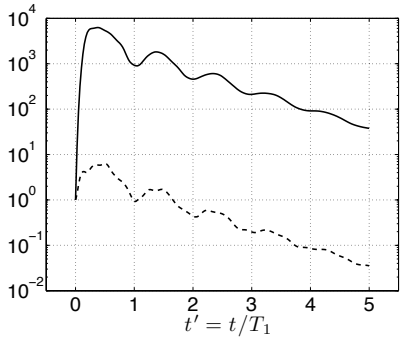

Figure 4: Temporal evolution of the maximum possible amplification as obtained from the first six eigenmodes. —— $G^6_{ac}(t)$; − − − $G^6_{tot}(t)$. Time is scaled by the period of the first eigenmode $t' = \frac{t}{T_1}$ with $f_1 = 59. - 8.3i$ Hz.

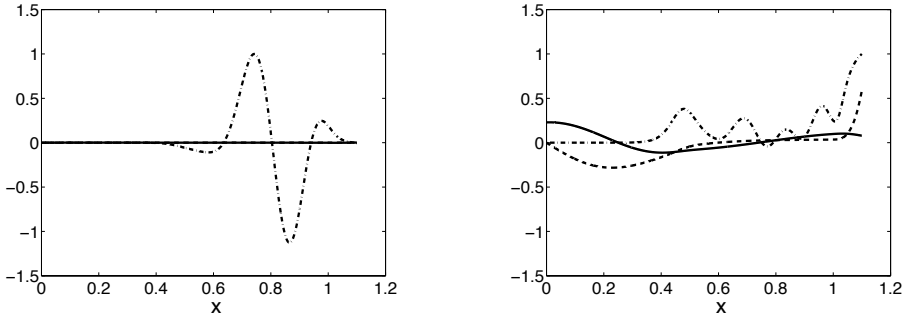

(a) optimal perturbation for $G^6_{\mathrm{ac}}(0)$ (b) optimal perturbation for $G^6_{\mathrm{tot}}(0)$

Figure 5: Spatial distribution of the optimal initial perturbation at $t = 0$: —— $p'(x,t)$; – – – $u'(x,t)$; —·— $s'(x,t)$. The fluctuating quantities are scaled by γp_0, c_0 and C_v respectively.

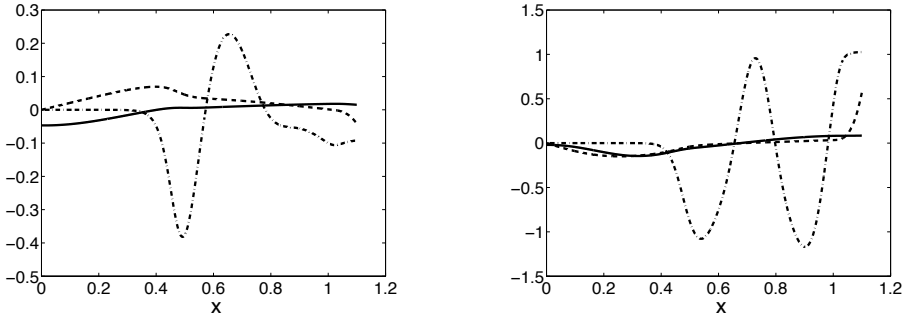

(a) optimal perturbation for $G^6_{\mathrm{ac}}(t_{max})$ (b) optimal perturbation for $G^6_{\mathrm{tot}}(t_{max})$

Figure 6: Spatial distribution of the optimal perturbation at $t = t_{max}$. —— $p'(x,t)$; – – – $u'(x,t)$; —·— $s'(x,t)$. The fluctuating quantities are scaled by γp_0, c_0 and C_v respectively.

The optimal initial perturbations that allow to obtain the maximum possible amplifications $G^6_{ac}(t)$ and $G^6_{tot}(t)$ are shown in Fig. 5 for $t = 0$. Figure 6 shows the same perturbations at the moment of maximum possible amplification, i.e. at $t = t_{max}$.
In the optimal initial perturbation obtained using the total energy approach (see Fig. 5(b)), fluctuations of entropy, pressure and velocity are equally present. At the time of maximum growth $t = t_{\max}$, the entropy contribution to the disturbance energy term E_{tot} has increased significantly, although the acoustic mode persists (see Fig. 6(b)). The situation is rather different for the optimal perturbation computed based on the acoustic energy only. At the initial time, the optimal perturbation contains mainly entropy fluctuations, the acoustic contribution being virtually zero (see Fig. 5(a)). However, at $t = t_{max}$ the entropy fluctuations have decreased, while the acoustic part has increased significantly (see Fig. 6(a)). This means that energy has been transferred from entropy towards acoustic fluctuations. However, as entropy fluctuations were not taken into account in the computation of the energy term, this also means that energy term E_{ac} appears to be enormously amplified as it passes from an initial value close to zero to a non-zero value at $t = t_{max}$.
This observation is consistent with the fact that a large value of $G^6_{max,ac}$ is observed in Fig. 4, while the value of $G^6_{max,tot}$ is a lot smaller.

To better understand the physical background of the difference between $G^m_{max,ac}$ and $G^m_{max,tot}$, the convergence of these quantities with respect to the number of eigenmodes m used for the analysis is displayed in Fig. 7.
From Fig. 7(a) one may conclude that the maximum transient amplification is well predicted with only 5-6 modes, when the total energy of the disturbances is considered. Adding more modes to the analysis

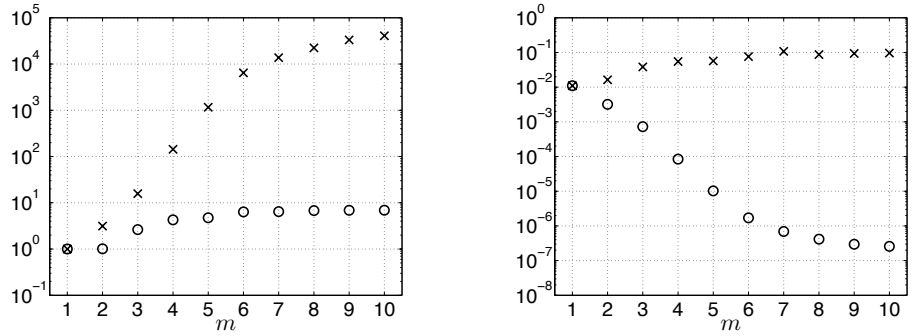

(a) Evolution of the maximum possible amplification terms:
∘-symbols: $G^m_{max,tot}$; ×-symbols: $G^m_{max,ac}$

(b) Contribution of the acoustic energy to the optimal initial perturbation for $G^m_{max,ac}$.
∘-symbols: $\sigma(t=0)$; ×-symbols: $\sigma(t=t_{max})$

Figure 7: Convergence in terms of the number of eigenmodes m used for the analysis.

does not have a huge impact on the result for $G^m_{max,tot}$. By contrast, for the growth rate based on the acoustic energy $G^m_{max,ac}$ convergence is hardly reached when 10 modes are used. It seems as if the values of $G^m_{max,ac}$ can still increase for larger numbers of eigenmodes.
This observation is confirmed by Fig. 7(b), which shows the contribution of acoustic fluctuations to the optimal initial perturbation for computations based on the acoustic energy (cf. Figs. 5(a) and 6(a)). For this plot, the value $\sigma(t)$ has been defined as the ratio of acoustic energy to total disturbance energy:

$$\sigma(t) = \frac{E_{ac}(t)}{E_{tot}(t)}, \tag{32}$$

where $E_{ac}(t)$ and $E_{tot}(t)$ are the terms defined in Eq. (13) and (28) respectively. Values of $\sigma(t)$ close to one indicate hence preponderance of acoustic fluctuations and negligible influence of entropy fluctuations, while values of $\sigma(t)$ near zero denote huge contributions of entropy fluctuations in the signal.
For the optimal perturbation corresponding to $G^m_{max,ac}$ at $t=0$, the contribution of the acoustic energy to the total energy clearly tends to zero for increasing m (∘-symbols). At the same time, the contribution of acoustic energy to the perturbation at $t=t_{max}$ remains of the same order of magnitude (×-symbols). The acoustic transient growth $G^m_{ac}(t) = \max E_{ac}(t)/E_{ac}(0)$ is hence virtually unlimited for increasing values of m, as $E_{ac}(t_{max})$ does not decrease in the same way as $E_{ac}(0)$.
This behaviour is possible since the entropy mode of fluctuations can feed the acoustic mode when the mean flow is accelerated [14]. Another path from entropy to acoustic was discussed by Nicoud and Poinsot [18] in the case where the thermal diffusivity is not zero. The very large value of $G^6_{max,ac}$ displayed in Fig. 4 is just and only the consequence of these physical phenomena. In other words, non-normality effects cannot be characterized by the acoustic transient growth when either mean flow or thermal diffusivity are present; the total transient growth based on the complete energy of the fluctuations should be used instead.

4 Conclusion

This article evaluates non-normal effects for a system that contains both a source of entropy fluctuations and a zone of accelerated mean flow. Rather than using a singular value decomposition approach, the determination of the maximum transient energy growth and the corresponding initial perturbation are based on an expansion in eigenmodes. These modes are obtained by solving the Linearized Euler Equations using a finite volume technique, a method that allows to take into account mean flow effects and is at the same time suitable for complex geometries.
It is shown that the eigenmodes of thermo-acoustic configurations are, in general, not orthogonal, which allows for a transient growth of disturbance energy. However, it is pointed out that for the analy-

sis of non-normal effects of such a configuration the definition of the norm, or equivalently the proper choice of the energy term, is crucial. Two approaches are presented in this paper, the first one being based on an energy term that is equivalent to the classic acoustic energy; the second one being based on the total disturbance energy and therefore including the contribution of entropy fluctuations. It is shown that the use of the acoustic energy concept may cause misleading results in configurations that include mean flow effects: When the energy of entropy fluctuations is neglected in the analysis, any energy transfer from entropy to acoustic fluctuations will lead to spurious values for transient (acoustic) energy growth.
For the presented configuration, a linear combination of five to six eigenmodes is sufficient to determine the maximum possible amplification and the optimal initial perturbation. A maximum possible amplification of $G^6_{max,tot} \approx 6$ is found for a case with a moderate mean flow speed and where unsteady heat release is not taken into account.

Acknowledgments

KW and CS are grateful to the European Community for funding their PhD and PostDoc work under the projects AETHER (Contract No. FP6 - MRTN-CT-2006-035713) and MyPLANET (Contract No. FP7-PEOPLE - 2007-1-1-ITN -210781), respectively. This work was also performed in the framework of the project MICCA funded by the Agence Nationale pour la Recherche (Contract No. ANR-08-BLAN-0027-01).

References

[1] K. Balasubramanian and R. I. Sujith. Non-normality and nonlinearity in combustion acoustic interaction in diffusion flames. *J. Fluid Mech.* , 594:29–57, 2008.

[2] K. Balasubramanian and R. I. Sujith. Thermoacoustic instability in a rijke tube: Non-normality and nonlinearity. *Phys. Fluids*, 20:044103–1–11, 2008.

[3] L. Crocco. Aspects of combustion instability in liquid propellant rocket motors. part i. *J. American Rocket Society* , 21:163–178, 1951.

[4] L. Crocco. Aspects of combustion instability in liquid propellant rocket motors. part ii. *J. American Rocket Society* , 22:7–16, 1952.

[5] F. E. C. Culick. Combustion instabilities in liquid-fueled propulsion systems- an overview. In *AGARD 72B PEP meeting*, 1987.

[6] A. P. Dowling. The calculation of thermoacoustic oscillations. *J. Sound Vib.* , 180(4):557–581, 1995.

[7] T. Gebhardt and S. Grossmann. Chaos transition despite linear stability. *Physical Review E*, 50(5):3705–3714, 1994.

[8] A. Giauque, T. Poinsot, M. Brear, and F. Nicoud. Budget of disturbance energy in gaseous reacting flows. In *Proc. of the Summer Program*, pages 285–297. Center for Turbulence Research, NASA Ames/Stanford Univ., 2006.

[9] E. Gullaud, S. Mendez, C. Sensiau, F. Nicoud, and T. Poinsot. Effect of multiperforated plates on the acoustic modes in combustors. *C. R. Acad. Sci.Mécanique*, 337(6-7):406–414, 2009.

[10] N. Karimi, M. Brear, and W. Moase. Acoustic and disturbance energy analysis of a flow with heat communication. *J. Fluid Mech.* , 597:67–89, 2008.

[11] H. J. Landau. On szegö's eigenvalue distribution theorem and non-hermitian kernels. *J. Analyse Math.*, 28:335–357, 1975.

[12] T. Lieuwen and V. Yang. Combustion instabilities in gas turbine engines. operational experience, fundamental mechanisms and modeling. In *Prog. in Astronautics and AeronauticsAIAA*, volume 210, 2005.

[13] J. Lim and J. Kim. A singular value analysis of boundary layer control. *Phys. Fluids*, 16(6), 2004.

[14] F. E. Marble and S. Candel. Acoustic disturbances from gas nonuniformities convected through a nozzle. *J. Sound Vib.* , 55:225–243, 1977.

[15] M. K. Myers. Transport of energy by disturbances in arbitrary steady flows. *J. Fluid Mech.* , 226:383–400, 1991.

[16] S. Nagaraja, K. Kedia, and RI Sujith. Characterizing energy growth during combustion instabilities: Singularvalues or eigenvalues? *Proceedings of the Combustion Institute*, 32(2):2933–2940, 2009.

[17] F. Nicoud, L. Benoit, C. Sensiau, and T. Poinsot. Acoustic modes in combustors with complex impedances and multidimensional active flames. *AIAA Journal* , 45:426–441, 2007.

[18] F. Nicoud and T. Poinsot. Thermoacoustic instabilities: should the rayleigh criterion be extended to include entropy changes ? *Combust. Flame* , 142:153–159, 2005.

[19] F. Nicoud and K. Wieczorek. About the zero mach number assumption in the calculation of thermoacoustic instability. *International Journal of Spray and Combustion Dynamic*, 1:67–112, 2009.

[20] N. Noiray, D. Durox andT. Schuller, and S. Candel. A unified framework for nonlinear combustion instability analysis based on the flame describing function a unified framework for nonlinear combustion instability analysis based on the flame describing function. *J. Fluid Mech.* , 615:139–167, 2008.

[21] T. Poinsot and D. Veynante. *Theoretical and Numerical Combustion*. R.T. Edwards, 2nd edition, 2005.

[22] P. J. Schmid and D. S. Henningson. *Stability and Transition in Shear Flows*. Springer, New York, 2001.

[23] F. Selimefendigil, R.I. Sujith, and W. Polifke. Identification of heat transfer dynamics for non-modal analysis of thermoacoustic stability. *Applied Mathematics and Computation*, under consideration, 2009.

[24] C. Sensiau, F. Nicoud, and T. Poinsot. A tool to study azimuthal and spinning modes in annular combustors. *Int. Journal Aeroacoustics*, 8(1):57–68, 2009.

[25] L. N. Trefethen. Computation of pseudospectra. *Acta Numerica*, pages 247–295, 1999.

[26] L. N. Trefethen, A. E. Trefethen, S. C. Reddy, and T. A. Driscoll. Hydrodynamic stability without eigenvalues. *Science*, 261:578–584, 1993.

Chapter 7

Conclusion and Perspectives

The objective of this work is to contribute to an improved prediction of thermo-acoustic instability in gas turbine combustion chambers. A challenging aspect of the numerical description of this kind of phenomena is to reach a compromise between a realistic representation of complex configurations and a rapid yet correct prediction of their behaviour. This thesis follows therefore the strategy of solving a simplified system of acoustic equations using a finite volume technique: this allows to take into account complex geometries and mean flow configurations, while the computational time remains rather low compared to LES.
The present thesis extends prior work undertaken at CERFACS in this domain: Based on experience that has been gained during the development of a Helmholtz solver, this work is concerned with the developement of a code that solves the linearized Euler equations and therefore allows to take into account the impact of the mean flow velocity on the acoustic field. The scope of this work is thus twofold:

- First, the impact of the mean flow velocity on the resonant frequencies, growth rates and shape of the acoustic modes present in the domain is addressed. This includes an evaluation of different source and loss terms and their contribution to the energy balance at different operating conditions - such as losses due to convection that become more pronounced as the mean flow velocity increases, or unsteady heat release, that may act as source or sink term depending on flow conditions.

- Secondly, it is discussed how the mathematical description of the system is affected when mean flow terms are retained. This concerns the system of equations itself, that must be suitable to describe thermo-acoustic instability in non zero Mach number mean flow; and furthermore any problems and particularities that occur during the solution of this system of equations.

The first issue has primarily been covered using a Quasi-1D solver for the linearized Euler equations. This tool, developed using the software Matlab, was a first step towards the realization of the finite volume code developed subsequently. Intended as a means to get to know the particularities of the mathematical system, it showed to be very useful for parametric studies on simple test cases in order to investigate Mach number effects. The main results of this study can be summarized as follows:

- The frequency of oscillation of the resonant modes tends to decrease with increasing Mach number, an effect that originates from the change in propagation velocity of downstream and upstream travelling acoustic waves. While this effect is small in simple duct

configurations, it can become considerable as the situation gets more complex, e.g. when flames and nozzles are involved.

- The growth rate of the modes may considerably change due to the mean flow velocity. Among the most important effects in simplified configurations are losses caused by convection of disturbance energy outwards and the stabilizing effect of the flame's mean heat release rate. Another aspect is the role of the flame's unsteady heat release rate that may change from driving to damping and vice versa as the mean flow configuration changes.

The effects of the mean flow on the growth rate being non negligible even at small Mach numbers, the findings indicate that the knowledge of the correct mean flow field is essential in order to fully exploit the potential of a linearized Euler equation solver.

The second issue of this study concerning the mathematical description and solution of the system has mainly been dealt with in the context of the 2D solver. The development of this code allowed to demonstrate the feasibility of the proposed concept, but also showed the constraints associated to it. The most noteworthy observations are the following:

- The discretized system of equations allows for point-to-point instability. As means to avoid this phenomenon, two approaches have been studied: a staggered grid discretization in 1D, and the introduction of an artificial viscosity term in the more complex context of the 2D solver. The results of the 2D solver show that in the context of this study, which is concerned with resonance rather than with propagation of acoustic waves over large distances, the use of artificial viscosity does not negatively impact the results.

- The discretized eigenvalue problem that results from the frequency domain formulation of the linearized Euler equations has a large number of non-physical solutions. In particular, non-physical eigenvalues with a norm of virtually zero complicate the task of locating the correct solutions using an iterative eigenvalue solver based on the Arnoldi algorithm: this algorithm is designed to determine a small number of eigenvalues of a large problem, with the solutions being those eigenfrequencies located at the extrema of the frequency spectrum. This method will hence converge towards the non-physical solutions close to zero, or alternatively to the high frequency modes that are of less interest in the context of this study. At the same time, the first non-zero solutions that are actually sought for are left aside. In order to direct the Arnoldi algorithm towards the solutions of interest, it is therefore applied to the shifted and inverted problem. However, this requires an additional inversion of a large matrix (or equivalently the solution of a large linear system of equations).

This latter issue being rather complex, it is the point where further development is most urgently required in order for the method to be applicable to real scale configurations: So far, the finite volume solver is limited to relatively simple 2D configurations as the parts of the code required for the shift and invert method are implemented in a way that is not suitable for very large problems. Two aspects have to be addressed in particular: firstly, the solution of the large linear system should be dealt with using an iterative method rather than the direct one implemented at present. Secondly, the use of parallel computation, an issue not addressed in this study, may contribute to handle more complex problems.

Another issue needing improvement arises from the non-physical solutions that are permitted by the system of equations. Even though the use of the shift and invert method allows to avoid those close to zero, it has been found that non-physical solutions may exist at higher frequencies and need to be distinguished from resonant modes of the chamber efficiently.

Finally, an efficient application of the linearized Euler equation solver requires - in addition to a correct mean flow field - an appropriate description of the flame acoustic interaction as well as of the boundary conditions for the acoustic field. Even though in the present study these issues are addressed satisfyingly for academic test cases, more complex applications might require improvement, such as the use of an extended flame model or boundary conditions representing arbitrary impedances.

Bibliography

[1] J. A. Adeff and T. J. Hofler. Design and Construction of a Solar-Powered, Thermoacoustically Driven, Thermoacoustic Refrigerator. *J. Acous. Soc. Am.*, 107(6):L37–L42, 2000.

[2] A. Agarwal and P. J. Morris. Calculation of Sound Propagation in Nonuniform Flows: Suppression of Instability Waves. *AIAA Journal*, 42(1):80–88, 2004.

[3] W. Arnoldi. The Principle of Minimized Iteration in the Solution of the Matrix Eigenproblem. *Quarterly of Applied Mathematics*, 9:17–29, 1951.

[4] C. Bailly and D. Juvé. Numerical solution of acoustic propagation problems using linearized Euler equations. *AIAA journal*, 38(1):22–29, 2000.

[5] F. Bake, U. Michel, I. Röhle, C. Richter, F. Thiele, M. Liu, and B. Noll. Indirect combustion noise generation in gas turbines. In *11th AIAA/CEAS Aeroacoustics Conference, Monterey, CA*, volume 2830, 2005.

[6] K. Balasubramanian and R. I. Sujith. Thermoacoustic instability in a rijke tube: Non-normality and nonlinearity. *Phys. Fluids*, 20:044103–1–11, 2008.

[7] M. Barrère and F. A. Williams. Comparison of Combustion Instabilities Found in Various Types of Combustion Chambers. *Proc. Combust. Inst.*, 12:169–181, 1968.

[8] R. Becker and R. Günther. The transfer function of premixed turbulent jet flames. In *Symposium (International) on Combustion*, volume 13, pages 517–526. Elsevier, 1971.

[9] L. Benoit. *Prédiction des Instabilités Thermo-acoustiques dans les Turbines à Gaz*. Phd thesis, University Montpellier II, 2005.

[10] C. Bogey, C. Bailly, D. Juvé, et al. Computation of flow noise using source terms in linearized Euler's equations. *AIAA journal*, 40(2):235–243, 2002.

[11] S. Candel. Combustion Instabilities Coupled by Pressure Waves and their Active Control. In *24th Symp. (Int.) on Combustion*, pages 1277–1296. The Combustion Institute, Pittsburgh, 1992.

[12] S. Candel, D. Durox, S. Ducruix, A.L. Birbaud, N. Noiray, and T. Schuller. Flame dynamics and combustion noise: progress and challenges. *International Journal of Aeroacoustics*, 8(1):1–56, 2009.

[13] R. H. Cantrell and R. W. Hart. Interaction between Sound and Flow in Acoustic Cavities: Mass, Momentum, and Energy Considerations. *J. Acous. Soc. Am.*, 36(4):697 – 706, April 1964.

[14] M. Caraeni, RK Devaki, M. Aroni, M. Oswald, and D. Caraeni. Efficient Acoustic Modal Analysis for Industrial CFD. In *47th AIAA Aerospace Sciences Meeting Including the New Horizons Forum and Aerospace Exposition*. AIAA, 2009.

[15] CERFACS. *The AVBP Handbook - http://cerfacs.fr/∼ avbp/AVBP_V6.X/HANDBOOK*.

[16] B. T. Chu. On the Energy Transfer to Small Disturbances in Fluid Flow (Part I). *Acta Mechanica*, pages 215–234, 1965.

[17] D.G. Crighton. Basic principles of aerodynamic noise generation. *Progress in Aerospace Sciences*, 16(1):31–96, 1975.

[18] L. Crocco. Aspects of combustion instability in liquid propellant rocket motors. part i. *J. American Rocket Society* , 21:163–178, 1951.

[19] L. Crocco. Aspects of combustion instability in liquid propellant rocket motors. part ii. *J. American Rocket Society* , 22:7–16, 1952.

[20] F. E. C. Culick. Combustion instabilities in liquid-fueled propulsion systems - an overview. In *AGARD 72B PEP meeting*, 1987.

[21] F. E. C. Culick. Some recent results for nonlinear acoustics in combustion chambers. *AIAA Journal*, 32(1):146–169, 1994.

[22] N. A. Cumpsty and F. E. Marble. The interaction of entropy fluctuations with turbine blade rows; a mechanism of turbojet engine noise. *Proc. R. Soc. Lond. A*, 357:323–344, 1977.

[23] N. Curle. The influence of solid boundaries upon aerodynamic sound. *Proceedings of the Royal Society of London. Series A, Mathematical and Physical Sciences*, 231(1187):505–514, 1955.

[24] A. P. Dowling. The Calculation of Thermoacoustic Oscillations. *J. Sound Vib.*, 180(4):557–581, 1995.

[25] A. P. Dowling. Nonlinear Self-Exited Oscillations of a Ducted Flame. *J. Fluid Mech.*, 346:271–290, 1997.

[26] A.P. Dowling. The challenges of lean premixed combustion. *Combustion*, 2(1), 2003.

[27] A.P. Dowling and A.S. Morgans. Feedback control of combustion oscillations. *Annual Reviews of Fluid Mechanics*, 37:151– 182, 2005.

[28] S. Ducruix, D. Durox, and S. Candel. Theoretical and experimental determinations of the transfer function of a laminar premixed flame. *Proceedings of the Combustion Institute*, 28(1):765–773, 2000.

[29] S. Ducruix, T. Schuller, D. Durox, and S. Candel. Combustion Instability Mechanisms in Premixed Combustors. In *Combustion Instabilities in Gas Turbine Engines*. AIAA, 2005.

[30] D. Durox, T. Schuller, and S. Candel. Combustion dynamics of inverted conical flames. *Proceedings of the combustion Institute*, 30(2):1717–1724, 2005.

[31] J. D. Eldredge and A. P. Dowling. The absorption of axial acoustic waves by a perforated liner with bias flow. *J. Fluid Mech.*, 485:307–355, 2003.

[32] S. Evesque and W. Polifke. Low-Order Acoustic Modelling for Annular Combustors: Validation and Inclusion of Modal Coupling. In *International Gas Turbine and Aeroengine Congress & Exposition, ASME Paper*, volume GT-2002-30064, 2002.

[33] R. Ewert and W. Schröder. Acoustic perturbation equations based on flow decomposition via source filtering. *Journal of Computational Physics*, 188(2):365–398, 2003.

[34] J.E. Ffowcs Williams and D.L. Hawkings. Sound generation by turbulence and surfaces in arbitrary motion. *Philosophical Transactions for the Royal Society of London. Series A, Mathematical and Physical Sciences*, 264(1151):321–342, 1969.

[35] V. Fraysse, L. Giraud, S. Gratton, and J. Langou. A Set of GMRES Routines for Real and Complex Arithmetics on High Performance Computers. Technical report, CERFACS, 1998.

[36] A. Frohn. *Einführung in die Technische Thermodynamik*. Wittwer Hochschulskripten, 1998.

[37] T. Gebhardt and S. Grossmann. Chaos transition despite linear stability. *Physical Review E*, 50(5):3705–3714, 1994.

[38] A.M.G. Gentemann, A. Fischer, S. Evesque, and W. Polifke. Acoustic transfer matrix reconstruction and analysis for ducts with sudden change of area. In *9th AIAA/CEAS Aeroacoustics Conference and Exhibit, Hilton Head*, 2003.

[39] A. Giauque. *System identification and disturbance energies in reacting flows - TH/CFD/07/15*. PhD thesis, Institut National Polytechnique de Toulouse, France - TyFEP - Dynamique des fluides, 2007.

[40] A. Giauque, T. Poinsot, M. Brear, and F. Nicoud. Budget of disturbance energy in gaseous reacting flows. In *Proc. of the Summer Program*, pages 285–297. Center for Turbulence Research, NASA Ames/Stanford Univ., 2006.

[41] A. Giauque, T. Poinsot, W. Polifke, and F. Nicoud. Validation of a flame transfer function reconstruction method for complex turbulent configurations. In *14th AIAA/CEAS Aeroacoustics Conference*, Vancouver, Canada, 2008.

[42] E. Gullaud, S. Mendez, C. Sensiau, F. Nicoud, and T. Poinsot. Effect of multiperforated plates on the acoustic modes in combustors. *C. R. Acad. Sci.Mécanique*, 337(6-7):406–414, 2009.

[43] H. Hassan. Scaling of combustion-generated noise. *J. Fluid Mech.*, 49:445–453, 1974.

[44] B. Higgins. *Journal of Natural Philosophy and Chemical Arts*, 1:129, 1802.

[45] C. Hirsch. *Numerical Computation of Internal and External Flows*. John Wiley, New York, 1988.

[46] M.S. Howe. Contributions to the theory of aerodynamic sound, with application to excess jet noise and the theory of the flute. *Journal of Fluid Mechanics*, 71(04):625–673, 1975.

[47] M.S. Howe. The dissipation of sound at an edge. *Journal of Sound and Vibration*, 70(3):407–411, 1980.

[48] HSL. *The Harwell Subroutine Library - http://www.hsl.rl.ac.uk/catalog.html*.

[49] A. Huber and W. Polifke. Dynamics of practical premixed flames, part I: model structure and identification. *International Journal of Spray and Combustion Dynamics*, 1(2):199–228, 2009.

[50] Z.M. Ibrahim, F.A. Williams, and S.G. Buckley. A review of previous studies of oscillatory combustion in gas turbines. 2005.

[51] U. Ingard and V.K. Singhal. Effect of flow on the acoustic resonances of an open-ended duct. *The Journal of the Acoustical Society of America*, 58:788, 1975.

[52] R. Kaess, W. Polifke, T. Poinsot, N. Noiray, D. Durox, T. Schuller, and S. Candel. CFD-based mapping of the thermo-acoustic stability of a laminar premix burner. In *Proceedings of the Summer Program*, page 289, 2008.

[53] N. Karimi, M. Brear, and W. Moase. Acoustic and Disturbance Energy Analysis of a Flow with Heat Communication. *J. Fluid Mech.*, 597:67–89, 2008.

[54] A. Kaufmann, F. Nicoud, and T. Poinsot. Flow forcing techniques for numerical simulation of combustion instabilities. *Combust. Flame*, 131:371–385, 2002.

[55] V.N. Kornilov, K. Schreel, and LPH De Goey. Experimental assessment of the acoustic response of laminar premixed Bunsen flames. *Proceedings of the Combustion Institute*, 31(1):1239–1246, 2007.

[56] L. S. G. Kovásznay. Turbulence in Supersonic Flow. *Journal of the Aeronautical Sciences*, 20(10):657 – 674, 1953.

[57] N. Lamarque. Ecriture et validation d'un code permettant le calcul de l'impédance d'entrée d'une tuyère. Rapport de stage de fin d'études ENSEEIHT WN/CFD/04/51, CERFACS, June 2004.

[58] N. Lamarque. *Schémas numériques et conditions limites pour la simulation aux grandes échelles de la combustion diphasique dans les foyers d' hélicoptère - TH/CFD/07/117*. PhD thesis, Institut National Polytechnique de Toulouse, France - Dynamique des Fluides, 2007.

[59] N. Lamarque and T. Poinsot. Boundary conditions for acoustic eigenmodes computation in gas turbine combustion chambers. *AIAA Journal*, 46(9):2282–2292, 2008.

[60] R. Lehoucq and D. Sorensen. ARPACK: Solution of Large Scale Eigenvalue Problems with Implicitly Restarted Arnoldi Methods. www.caam.rice.edu/software/ARPACK. User's guide, 1997.

[61] M. Leyko, F. Nicoud, S. Moreau, and T. Poinsot. Numerical and analytical investigation of the indirect noise in a nozzle. In *Proceedings of the Summer Program*, pages 343–354, Center for Turbulence Research, NASA AMES, Stanford University, USA, 2008.

[62] T. Lieuwen and A. Banaszuk. Background noise effects on combustor stability. *J. Prop. Power*, 21(1):25–31, 2005.

[63] M. J. Lighthill. On Sound Generated Aerodynamically. I. General Theory. *Proc. R. Soc. Lond. A, Mathematical and Physical Sciences*, 211(1107):564–587, 1952.

[64] M. J. Lighthill. On Sound Generated Aerodynamically. II. Turbulence as a source of sound. *Proc. R. Soc. Lond. A, Mathematical and Physical Sciences*, 222(1107):1–32, 1954.

[65] K. Mahesh, G. Constantinescu, and P. Moin. A numerical method for large-eddy simulation in complex geometries. *J. Comput. Phys.*, 197(1):215–240, 2004.

[66] F. E. Marble and S. Candel. Acoustic Disturbances from Gas Non-Uniformities Convected Through a Nozzle. *J. Sound Vib.*, 55:225–243, 1977.

[67] C. Martin, L. Benoit, Y. Sommerer, F. Nicoud, and T. Poinsot. LES and Acoustic Analysis of Combustion Instability in a Staged Turbulent Swirled Combustor. *AIAA Journal*, 44(4):741–750, 2006.

[68] K. McManus, T. Poinsot, and S. Candel. A review of active control of combustion instabilities. *Prog. Energy Comb. Sci.*, 19:1–29, 1993.

[69] P. Merkli and H. Thomann. Thermoacoustic Effects in a Resonance Tube. *J. Fluid Mech.*, 70(1):161–177, 1975.

[70] C. L. Morfey. Acoustic Energy in Non-Uniform Flows. *J. Sound Vib.*, 14(2):159–170, 1971.

[71] P.J. Morris and F. Farassat. Acoustic analogy and alternative theories for jet noise prediction. *AIAA journal*, 40(4):671–680, 2002.

[72] M. K. Myers. Transport of Energy by Disturbances in Arbitrary Steady Flows. *J. Fluid Mech.*, 226:383–400, 1991.

[73] S. Nagaraja, K. Kedia, and R.I. Sujith. Characterizing energy growth during combustion instabilities: Singularvalues or eigenvalues? *Proc. Combust. Inst.*, 180(9):1588–1612, 2008.

[74] F. Nicoud, L. Benoit, C. Sensiau, and T. Poinsot. Acoustic modes in combustors with complex impedances and multidimensional active flames. *AIAA Journal*, 45:426–441, 2007.

[75] F. Nicoud and T. Poinsot. Thermoacoustic Instabilities: Should the Rayleigh Criterion be Extended to Include Entropy Changes? *Combust. Flame*, 142:153–159, 2005.

[76] F. Nicoud and K. Wieczorek. About the zero mach number assumption in the calculation of thermoacoustic instability. *International Journal of Spray and Combustion Dynamic*, 1:67–112, 2009.

[77] N. Noiray, D. Durox, T. Schuller, and S. Candel. A Unified Framework for Nonlinear Combustion Instability Analysis based on the Flame Describing Function. *J. Fluid Mech.*, 615:139–167, 2008.

[78] C. Pankiewitz and T. Sattelmayer. Time Domain Simulation of Combustion Instabilities in Annular Combustors. *ASME Journal of Engineering for Gas Turbines and Power*, 125(3):677–685, 2003.

[79] A. D. Pierce. *Acoustics: an introduction to its physical principles and applications*. McGraw Hill, New York, 1981.

[80] J. Pieringer, T. Sattelmayer, and F. Fassl. Simulation of Combustion Instabilities in Liquid Rocket Engines with Acoustic Perturbation Equations. *Journal of propulsion and power*, 25(5):1020–1031, 2009.

[81] T. Poinsot and S. Lele. Boundary conditions for direct simulations of compressible viscous flows. *J. Comput. Phys.*, 101(1):104–129, 1992.

[82] T. Poinsot and D. Veynante. *Theoretical and Numerical Combustion*. R.T. Edwards, 2nd edition, 2005.

[83] W. Polifke, C. Paschereit, and K. Döbbeling. Constructive and destructive interference of acoustic and entropy waves in a premixed combustor with a choked exit. *Int. J. Acoust. Vib.*, 6:135–146, 2001.

[84] W. Polifke, A. Poncet, C.O. Paschereit, and K. Döbbeling. Reconstruction of acoustic transfer matrices by instationary computational fluid dynamics. *Journal of Sound and Vibration*, 245(3):483–510, 2001.

[85] P. P. Rao and P. J. Morris. Use of Finite Element Methods in Frequency Domain Aeroacoustics. *AIAA Journal*, 44(7):1643–1652, July 2006.

[86] L. Rayleigh. The Explanation of Certain Acoustic Phenomena. *Nature*, July 18:319–321, 1878.

[87] L. Rayleigh. *The Theory of Sound*. Mac Millan (reprinted by Dover, New York, 1945), 1894.

[88] S. W. Rienstra and A. Hirschberg. *An Introduction to Acoustics*. Eindhoven University of Technology, 2002.

[89] P.L. Rijke. Notiz über eine neue Art, die Luft in einer an beiden Enden offenen Röhre in Schwingungen zu versetzen. *Annalen der Physik*, 183(6):339–343, 1859.

[90] N. Rott. Damped and Thermally Driven Acoustic Oscillations in Wide and Narrow Tubes. *Zeitschrift für Angewandte Mathematik und Physik*, 20(2):230–243, 1969.

[91] Y. Saad. *Numerical methods for large eigenvalue problems*. Manchester Universtity Press, 1992.

[92] Y. Saad. *Iterative methods for sparse linear systems*. PWS Publishing Company, 1996.

[93] T. Sattelmayer. Influence of the combustor aerodynamics on combustion instabilities from equivalence ratio fluctuations. In *International Gas Turbine and Aeroengine Congress and Exhibition*, Munich, 2000. ASME Paper.

[94] H. Schlichting and K. Gersten. *Grenzschicht-Theorie*. Springer, 2006.

[95] P. J. Schmid and D. S. Henningson. *Stability and Transition in Shear Flows*. Springer, New York, 2001.

[96] T. Schuller, D. Durox, and S. Candel. A Unified Model for the Prediction of Laminar Flame Transfer Functions: Comparisons between Conical and V-flames Dynamics. *Combust. Flame*, 134:21–34, 2003.

[97] T. Schuller, D. Durox, and S. Candel. Self-induced combustion oscillations of laminar premixed flames stabilized on annular burners. *Combust. Flame*, 135:525–537, 2003.

[98] G. Searby, A. Nicole, M. Habiballah, and E. Laroche. Prediction of the Efficiency of Acoustic Damping Cavities. *Journal of Propulsion and Power*, 2007.

[99] F. Selimefendigil, R.I. Sujith, and W. Polifke. Identification of heat transfer dynamics for non-modal analysis of thermoacoustic stability. *Applied Mathematics and Computation*, under consideration, 2009.

[100] L. Selle, G. Lartigue, T. Poinsot, R. Koch, K.-U. Schildmacher, W. Krebs, B. Prade, P. Kaufmann, and D. Veynante. Compressible large-eddy simulation of turbulent combustion in complex geometry on unstructured meshes. *Combust. Flame*, 137(4):489–505, 2004.

[101] C. Sensiau. *Simulations numériques des instabilités thermoacoustiques dans les chambres de combustion aéronautiques - TH/CFD/08/127*. PhD thesis, Université de Montpellier II, - Institut de Mathématiques et de Modélisation de Montpellier, France, 2008.

[102] C. Sensiau, F. Nicoud, and T. Poinsot. A tool to study azimuthal and spinning modes in annular combustors. *Int. Journal Aeroacoustics*, 8(1):57–68, 2009.

[103] C. Silva, M. Leyko, E. Gullaud, F. Nicoud, and T. Poinsot. Development of an acoustic tool for combustion noise analysis in confined domains. In *2ème colloque INCA*, CORIA, Rouen, France, 2008.

[104] J. C. Sisco, Y. C. Yu, V. Sankaran, and W. E. Anderson. Examination of Mode Shapes in an Unstable Model Combustor. *Journal of Sound and Vibration*, 330(1):61–74, 2011.

[105] C. Sondhauß. Über die Schallschwingungen der Luft in erhitzten Glasröhren und in gedeckten Pfeifen von ungleicher Weite. *Annalen der Physik und Chemie*, 79:1–34, 1859.

[106] R.C. Steele, L.H. Cowell, S.M. Cannon, and C.E. Smith. Passive control of combustion instability in lean premixed combustors. *Journal of Engineering for Gas Turbines and Power*, 122:412, 2000.

[107] S. R. Stow and A. P. Dowling. Modelling of Circumferential Modal Coupling Due to Helmholtz Resonators. In *ASME Paper 2003-GT-38168*, Atlanta, Georgia, USA, 2003.

[108] S.R. Stow and A.P. Dowling. A time-domain network model for nonlinear thermoacoustic oscillations. *Journal of Engineering for Gas Turbines and Power*, 131:031502, 2009.

[109] S. M. Stringer and K. W. Morton. Artificial viscosity for the cell vertex method. Technical report, Oxford University Computing Laboratory, 1996.

[110] G. W. Swift. Thermoacoustic Engines and Refrigerators. *Physics Today*, 48(7):22–28, 1995.

[111] O. G. Symko, E. Abdel-Rahman, Y. S. Kwon, M. Emmi, and R. Behunin. Design and Development of High-Frequency Thermoacoustic Engines for Thermal Management in Microelectronics. *Microelectronics Journal*, 35:185–191, 2002.

[112] N. Tran, S. Ducruix, and T. Schuller. Damping combustion instabilities with perforates at the premixer inlet of a swirled burner. *Proc. Combust. Inst.*, In Press, 2009.

[113] L. N. Trefethen and D. Bau. *Numerical Linear Algebra*. SIAM Philadelphia, 1997.

[114] L. N. Trefethen, A. E. Trefethen, S. C. Reddy, and T. A. Driscoll. Hydrodynamic stability without eigenvalues. *Science*, 261:578–584, 1993.

[115] K. Truffin and T. Poinsot. Comparison and extension of methods for acoustic identification of burners. *Combust. Flame*, 142(4):388–400, 2005.

[116] K. Truffin, B. Varoquié, and T. Poinsot. Measurements of transfer functions in reacting flows using large eddy simulations. In *10th International Congress on Sound and Vibration*, number P-38, pages 785–793, Stockholm, Sweden, 2003.

[117] B. Varoquié, J.-P. Légier, F. Lacas, D. Veynante, and T. Poinsot. Experimental analysis and large eddy simulation to determine the response of non-premixed flame submitted to acoustic forcing. *Proc. Combust. Inst.*, 29:1965–1970, 2002.

[118] J. Wheatley, T. Hofler, G. W. Swift, and A. Migiori. An Intrinsically Irreversible Thermoacoustic Heat Engine . *J. Acous. Soc. Am.*, 74(1):153–170, 1983.

[119] K. Wieczorek and F. Nicoud. Thermoacoustic instabilities in non zero Mach number mean flow configurations. In *European Combustion Meeting, Vienna, April 14th-17th*, 2009.

[120] K. Wieczorek and F. Nicoud. Prediction of Thermoacoustic Instabilities: Numerical Study of Mach Number Effects. In *16th AIAA/CEAS Aeroacoustics Conference, Stockholm, Sweden, June 7th-9th*, 2010.

[121] P. Wolf, G. Staffelbach, L.Y.M. Gicquel, T. Poinsot, V. Moureau, and C. Bérat. Massively parallel LES of azimuthal thermo-acoustic instabilities in annular gas turbines. In *2ème colloque INCA*, CORIA, Rouen, France, 2008.

[122] Y. Yu, J. Sisco, W. E. Anderson, and V. Sankaran. Examination of Spatial Mode Shapes and Resonant Frequencies Using Linearized Euler Solutions. In *37th AIAA Fluid Dynamics Conference and Exhibit, Miami, Florida*, 2007.

[123] B. T. Zinn and T. C. Lieuwen. Combustion Instabilities: Basic Concepts. In *Combustion Instabilities in Gas Turbine Engines*. AIAA, 2005.

List of Figures

List of Tables